Measurement of Neutral Pion with Respect to the Azimuthal Angle in Au+Au Collisions at $\sqrt{s_{NN}} = 200$ GeV

Yoki Aramaki

Department of Physics
Graduate School of Science
The University of Tokyo

A Dissertation Submitted in Partial Fulfillment of the
Requirements for the Degree of Doctor of Science

Abstract

Quantum chromodynamics (QCD) is the gauge theory to describe the strong interaction among quarks and gluons. Theoretical calculations based on QCD predict that quarks deconfine and the nuclear matter transits to the quark gluon plasma (QGP) under the energy density of the above 1 GeV/fm^3 and the temperature of the above 150–200 MeV.

The high temperature and/or density state is expected to have been realized in the early universe. On earth, the high-energy heavy-ion collisions are a unique tool to realize such an extreme state. One of the powerful probes is a hard scattered parton produced at the early stage of the collisions. The scattered partons pass through the created matter and fragment into hadrons. Therefore, this probe is sensitive to research the nature of the created matter.

The production of π^0 in ^{197}Au+^{197}Au collisions at the center-of-mass energy per nucleon pair ($\sqrt{s_{NN}}$) of 200 GeV has been measured at the PHENIX experiment at Relativistic Heavy Ion Collider in Brookhaven National Laboratory (BNL). The observed yield of π^0 in Au+Au collisions is suppressed by a factor of 5 compared to that in the superposition of nucleon-nucleon collisions. This suppression will depend on the average path length which partons pass through the created matter. Since the path length depends on the azimuthal direction of the parton propagation in non-central heavy-ion collisions, one should expect the hadron suppression caused by parton energy loss to depend on the azimuthal angle with respect to the reaction plane. Thus, the measurement of the azimuthal anisotropy of hadrons plays a crucially important role of the precise study of parton energy loss. For that reason, the azimuthal anisotropy of neutral pion are measured in $\sqrt{s_{NN}} = 200$ GeV Au+Au collisions. The transverse momenta of the azimuthal anisotropy of π^0 reached up to 14 GeV/c. It was found that the yield of π^0 has the strong azimuthal angular dependence even at high p_T.

Several parton energy loss formalisms in the three dimensional hydrodynamic simulation are proposed and predict different azimuthal angular dependence of the yield suppression for each parton energy loss formalism. The models can reproduce p_T and centrality dependence for the yield of π^0 in Au+Au, while they fail to reproduce the azimuthal angular dependence. In this thesis, it is pointed out that energy loss models based on perturbative QCD (pQCD) can't explain the data.

Contents

List of Figures

List of Tables

Chapter 1

Introduction

1.1 QCD and QGP

Quantum Chromodynamics (QCD) is a local $SU(3)$ gauge theory and is recognized as the theory of strong interaction among quarks and gluons. The two important features of QCD are color confinement and asymptotic freedom. Quarks and gluons have the degree of color, and they are confined in color-singlet hadrons in low energy. The strong coupling constant, α_s, can be expressed as follows:

$$\alpha_s(Q^2) \simeq \frac{12\pi}{(33 - 2N_f)\ln(\frac{Q^2}{\Lambda^2_{\mathrm{QCD}}})}, \tag{1.1}$$

where Q^2 is the transferred momentum, N_f is the number of quark flavors, and the typical QCD scale, Λ_{QCD}, is approximately 0.2 GeV. As described in Eq. 1.1, α_s decreases with an increase of momentum transfer in high-energy collisions [1, 2]. Eventually, the color confinement may be broken with the increase of the temperature and/or density in a many-body system consisted of hadrons which could result in a phase transition from the confined nuclear matter (ordered phase) to the deconfined state (disordered phase). The deconfined state is called "Quark Gluon Plasma (QGP)."

The lattice QCD calculations predict that the phase transition to the QGP state occurs at a critical temperature, T_c, of 150–200 MeV [3]. Figure 1.1 shows the calculation of the energy density scaled by the fourth power of the temperature, ϵ/T^4, as a function of temperature scaled by the critical temperature, T/T_c [4]. The energy density increases drastically around at T_c of $\sim$200 MeV due to the increase of the degree of freedom by deconfinement.

A schematic phase diagram of QCD matter including QGP is shown in Fig. 1.2. The horizontal axis is the baryon chemical potential and the vertical axis is the temperature. QGP is considered to have existed in high-temperature circumstances of the early universe on the microsecond time scale after the Big Bang.

High-energy heavy-ion collisions provide a possibility to create QGP in the laboratory. The first fixed target experiment with high-energy heavy-ion collisions began at Bevalac

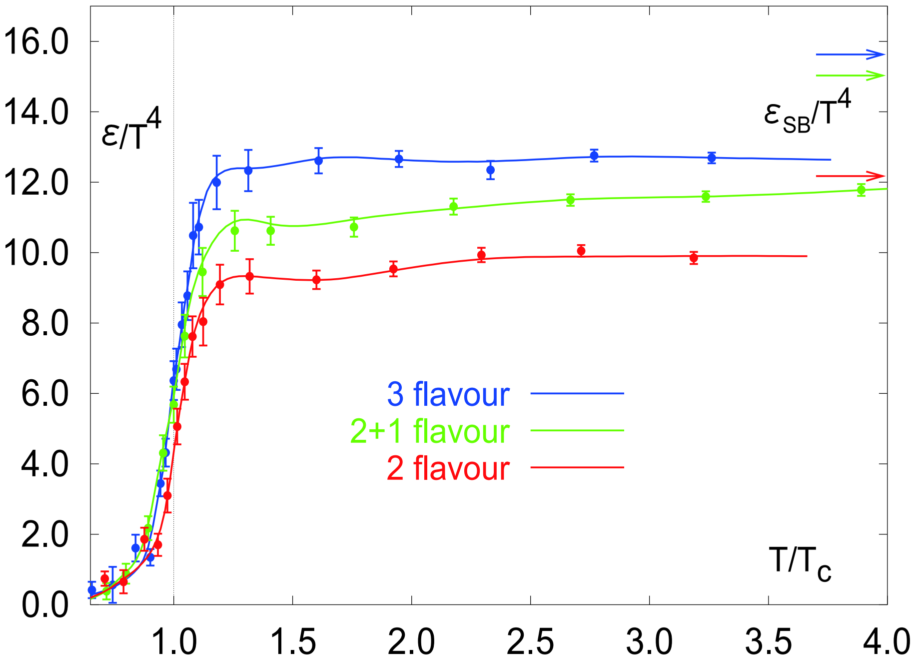

Figure 1.1: The energy density (ϵ) scaled by T^4 as a function of temperature scaled by the critical temperature (T_c) calculated in the lattice QCD [4]. The arrows on the right side indicate the values of ϵ/T^4 for Stefan-Boltzmann limit.

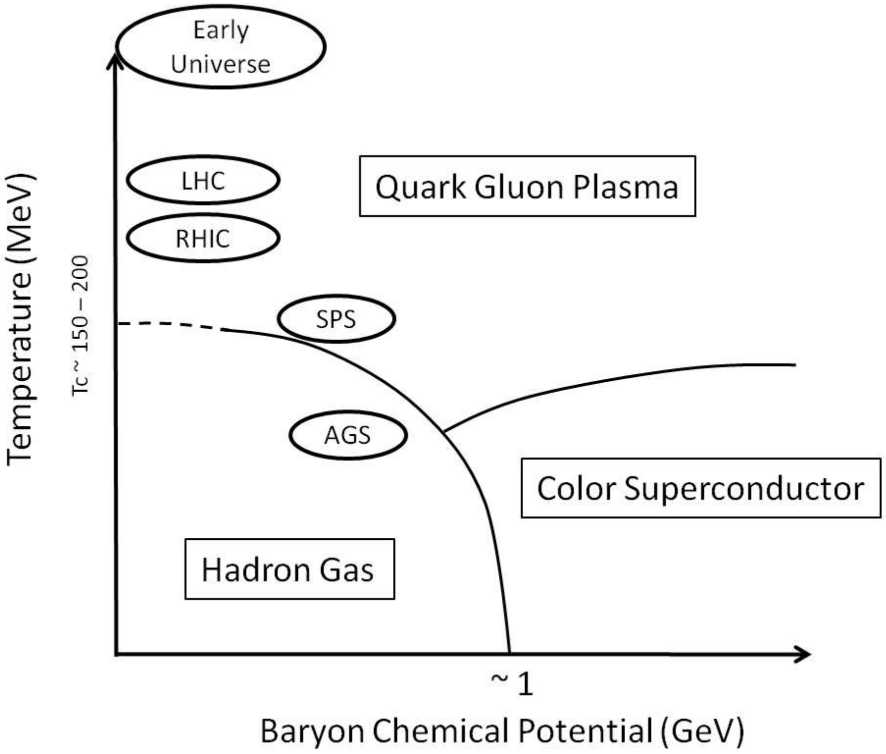

Figure 1.2: A schematic phase diagram of QCD matter.

at Lawrence Berkley Laboratory (LBL) with $\sim$ 2A GeV beams in the middle of 1970's. In 1986, heavy-ion experiments with higher energy started at Alternating Gradient Synchrotron (AGS) in Brookhaven National Laboratory (BNL) with $\sim$14A GeV beams and at Super Proton Synchrotron (SPS) in European Organization for Nuclear Research (CERN) with $\sim$160A GeV beams.

The Relativistic Heavy Ion Collider (RHIC) at BNL is the first colliding-type accelerator which can collide heavy nuclei up to gold (^{197}Au) at the center-of-mass energy per nucleon pair of $\sqrt{s_{NN}} = 200$ GeV and started its operation in 2000. The energy density achieved by the collisions at RHIC is expected to be above the critical temperature.

1.2 Hard Scattered Parton as Probes of QGP

Since the observed particles come from various processes in the heavy-ion collisions, it is difficult to measure the properties of QGP directly. One of the powerful probes is a hadron with a large transverse momentum (p_T). High-p_T hadrons are mainly the leading particles from the fragmentation of quarks and gluons, scattered with a large momentum transfer Q^2. The hadron production in heavy-ion collisions can be estimated from that in nucleon-nucleon collisions with nuclear medium effects. The cross section of high-p_T hadron production is well reproduced by the calculation with three factorized processes; initial distribution of partons in the colliding species, the elementary parton-parton cross section, and the fragmentation process of partons into hadrons.

Since hard scatterings of parton have small cross section, one can regard the nuclei as an incoherent superposition of point-like partons. It has been predicted that the hard scattered partons lose their energy while passing through the high-dense matter. Energy loss of the hard scattered partons is primary due to the gluon radiation, as similar to the electromagnetic bremsstrahlung radiation. For that reason, the hard scattered partons are sensitive to the density of the created medium and its nature. Therefore, the hard scattered parton are expected as one of powerful probes for searching the properties of QGP. The detailed explanation of this probe is described in Sec 2.2.

1.3 Motivation of This Study

Parton energy loss models predict that the magnitude of the energy loss in the medium depends on the path length L which partons pass through, as described in Sec. 2.6. Thus, the measurement of the energy loss with respect to the path length is expected to enable us to obtain the detail information about parton energy loss mechanism.

The path length is strongly associated with the azimuthal angle from the reaction plane in the collisions, since the matter created in the non-central heavy-ion collision is almond shape as shown in Fig. 2.13.

If the azimuthal angular distribution of emitted particles is written in the form Fourier expansion, the second harmonic coefficient is expressed as the strength of the azimuthal anisotropy v_2. The collective flow is dominant for the azimuthal anisotropy v_2 at low-p_T

region, while the v_2 with high p_T is expected to have the information about the initial collision geometry such as the path length. In order to reduce the effect of the colletive flow, the azimuthal anisotropy with high p_T should be measured. Since the angle of the reaction plane plays a important role to measure the v_2, several new detectors to determine the angle of the reaction plane were installed in PHENIX.

In this thesis, the data in RHIC Year-7 Au+Au run was analyzed, and the π^0 measurement with respect to the azimuthal angle was improved larger than the early one (RHIC Year-4 Au+Au run).

1.4 Organization of This Thesis

Production of neutral pion in ^{197}Au+^{197}Au collisions at $\sqrt{s_{NN}} = 200$ GeV in the RHIC Year-7 run has been studied at the PHENIX experiment at RHIC. The neutral pion has been measured with the decay of $\pi^0 \rightarrow 2\gamma$ at mid-rapidity ($|y| < 0.35$).

The organization of this thesis is as follows: Chapter 2 introduces the theoretical and experimental background for the parton energy loss in high-energy heavy-ion collisions. In chapter 3, the RHIC accelerator complex and the PHENIX detectors are described. In chapter 4, the conditions of beam and trigger at RHIC Year-7 Au+Au run are summarized. In chapter 5 the analysis of the π^0 via decay photons is explained. In chapter 6, the obtained results are described. In chapter 7, the obtained results are compared to the parton energy loss models. Chapter 8 concludes this thesis.

1.5 Major Contributions

The author studied the production of neutral pion in Au+Au collisions at $\sqrt{s_{NN}} =$ 200 GeV as a collaborator of the PHENIX experiment at RHIC. The author carried out out the measurements of the invariant yield and the azimuthal anisotropy of π^0 via two photons at the PHENIX experiment and the data taking of the RHIC Year-7 run used in this analysis. The author carried out the energy calibration of electromagnetic calorimeters which are primary detectors to identify photons. The paper entitled as “Azimuthal anisotropy of neutral pion production in Au+Au collisions at $\sqrt{s_{NN}} = 200$ GeV:Path length dependence of jet quenching and the role of initial geometry” [6] was published in Physical Review Letters.

Chapter 2

Physics Background

Several basic information related to this thesis is described in this chapter. First of all, the overview of high-energy heavy-ion collisions is described. High-energy heavy-ion collision is a unique tool to create the extreme condition with high temperature and energy density. Secondly, observables to study the properties of the created matter are described. Thirdly, the results in early heavy-ion experiments related to the energy loss are introduced. In the last part, the motivation of this thesis and the author's contribution are described.

2.1 Relativistic Heavy-ion Collisions

High-energy heavy-ion collisions have been used to realize an extreme state with high temperature and energy density which is required for the QGP formation.

2.1.1 Collision Geometry

The geometrical aspects of high-energy heavy-ion collisions play an important role in collision dynamics. Since the de Broglie wavelength of the nuclei in high-energy nucleus-nucleus collisions is much smaller than the size of the nucleus, the collision is characterized by the impact parameter, $\mathbf{b}$, of the colliding nuclei. Figure 2.1 shows the central collision and peripheral collision of nuclei with radii of R. As shown in Fig. 2.2, the nucleons in high-energy heavy-ion collisions are classified into two parts: the participants and spectators. Since the spectators keep longitudinal velocity of their parent nuclei and emerge at nearly zero degree in the collisions, it is easy to experimentally separate the spectators and the participants. The shape between participants and spectators is determined by the impact parameter $\mathbf{b}$. Information about the impact parameter $\mathbf{b}$ can be obtained by measuring the number of the spectators and/or the participants.

The relation among impact parameter (b), the number of binary nucleon-nucleon collisions (N_{coll}), and the number of participants (N_{part}) can be evaluated using the Glauber model [7]. The Glauber model describes the collisions between a nucleus (A) and a nucleus (B). The nucleons in each colliding nucleus are assumed to obey the Woods-Saxon

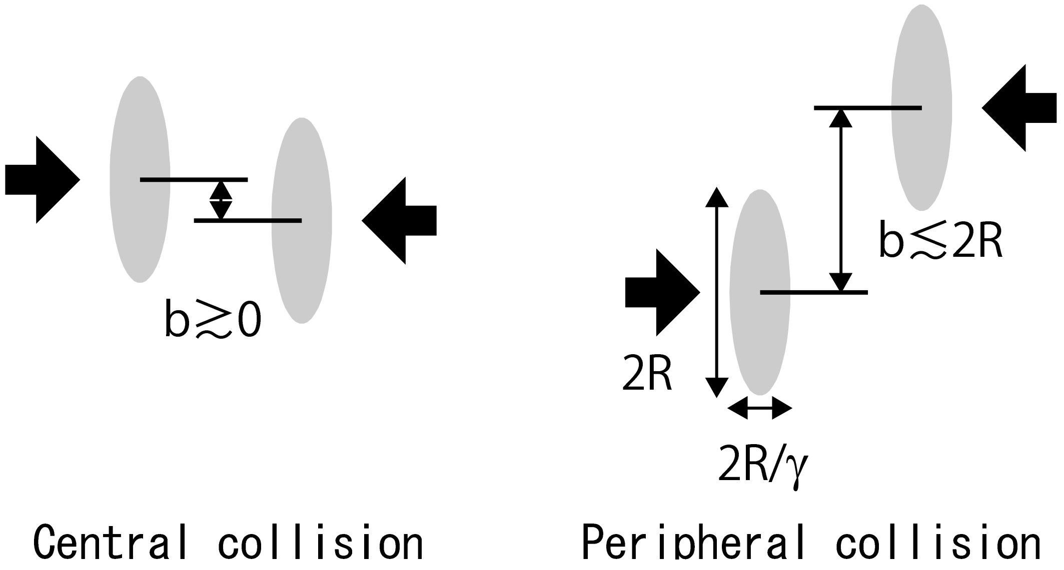

Figure 2.1: A schematic of central (left) and peripheral (right) collisions.

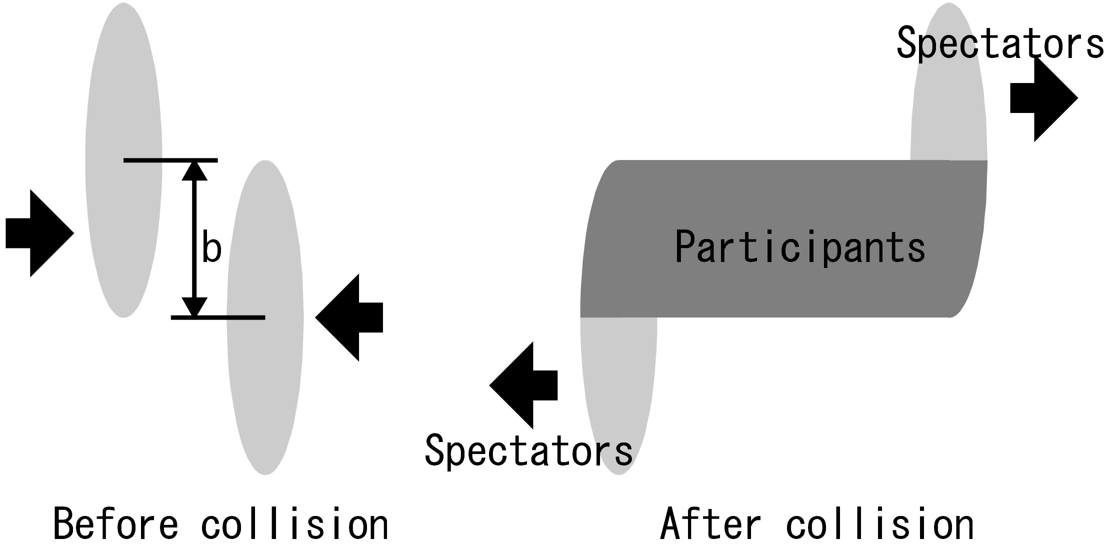

Figure 2.2: A schematic of before and after a collision of nuclei.

distribution in case of heavy nuclei,

$$\rho(r) = \frac{\rho_0}{1 + \exp(\frac{r-R}{d})}, \tag{2.1}$$

where ρ_0 is the normal nuclear density, R is a radius of the nucleus, and d is the diffuseness parameter. The occurrence probability of a nucleon-nucleon collision between the nuclei A and B along to the $z-$axis at the impact parameter $\mathbf{b}$ is expressed by the following integral formula,

$$T_{AB}(\mathbf{b})\sigma_{NN} = \int\int d\mathbf{b}_A dz_A \rho_A(\mathbf{b}_A, z_A) d\mathbf{b}_B dz_B \rho_B(\mathbf{b}_B, z_B) t(\mathbf{b} - \mathbf{b}_A - \mathbf{b}_B)\sigma_{NN}, \tag{2.2}$$

where σ_{NN} is a nucleon-nucleon inelastic cross section and $t(\mathbf{b})$ is the probability for having a nucleon-nucleon collision within the transverse element $d\mathbf{b}$ when the nuclei A and B collide with a given impact parameter $\mathbf{b}$. The probability having multiple (n) nucleon-nucleon collisions can be expressed using binomial relation,

$$p(n, \mathbf{b}) =_{AB} \mathrm{C}_n [T_{AB}(\mathbf{b})\sigma_{NN}]^n [1 - T_{AB}(\mathbf{b})\sigma_{NN}]^{AB-n}. \tag{2.3}$$

The probability for having at least one nucleon-nucleon collision in the collision of nuclei A and B at a given impact parameter $\mathbf{b}$ is expressed as,

$$\frac{d\sigma_{AB}}{d\mathbf{b}} = \sum_{n=1}^{AB} p(n, \mathbf{b}) = 1 - p(0, \mathbf{b}) = 1 - [1 - T_{AB}(\mathbf{b})\sigma_{NN}]^{AB}. \tag{2.4}$$

Therefore, the total inelastic cross section σ_{AB} integrated over $\mathbf{b}$ is described as follows:

$$\sigma_{AB} = \int d\mathbf{b}\big(1 - [1 - T_{AB}(\mathbf{b})\sigma_{NN}]^{AB}\big). \tag{2.5}$$

The average number of inelastic nucleon-nucleon collisions N_{coll} at the impact parameter $\mathbf{b}$ is expressed as follows:

$$N_{coll}(\mathbf{b}) = \langle n(\mathbf{b}) \rangle \sum_{n=1}^{AB} n p(n, \mathbf{b}) = AB \cdot T_{AB}(\mathbf{b})\sigma_{NN}. \tag{2.6}$$

2.1.2 Space-time Evolution

High-energy heavy-ion collisions create a complicated process with various phases from the initial collision through the hadronic phase. J.D. Bjorken proposed one scenario to describe the space-time evolution of the heavy-ion collisions [8].

Figure 2.3 shows the schematic of the space-time evolution of the matter created in high-energy heavy-ion collision at RHIC. The longitudinal and transverse coordinates in the picture are z and the time coordinate t, respectively. It is assumed that the space-time

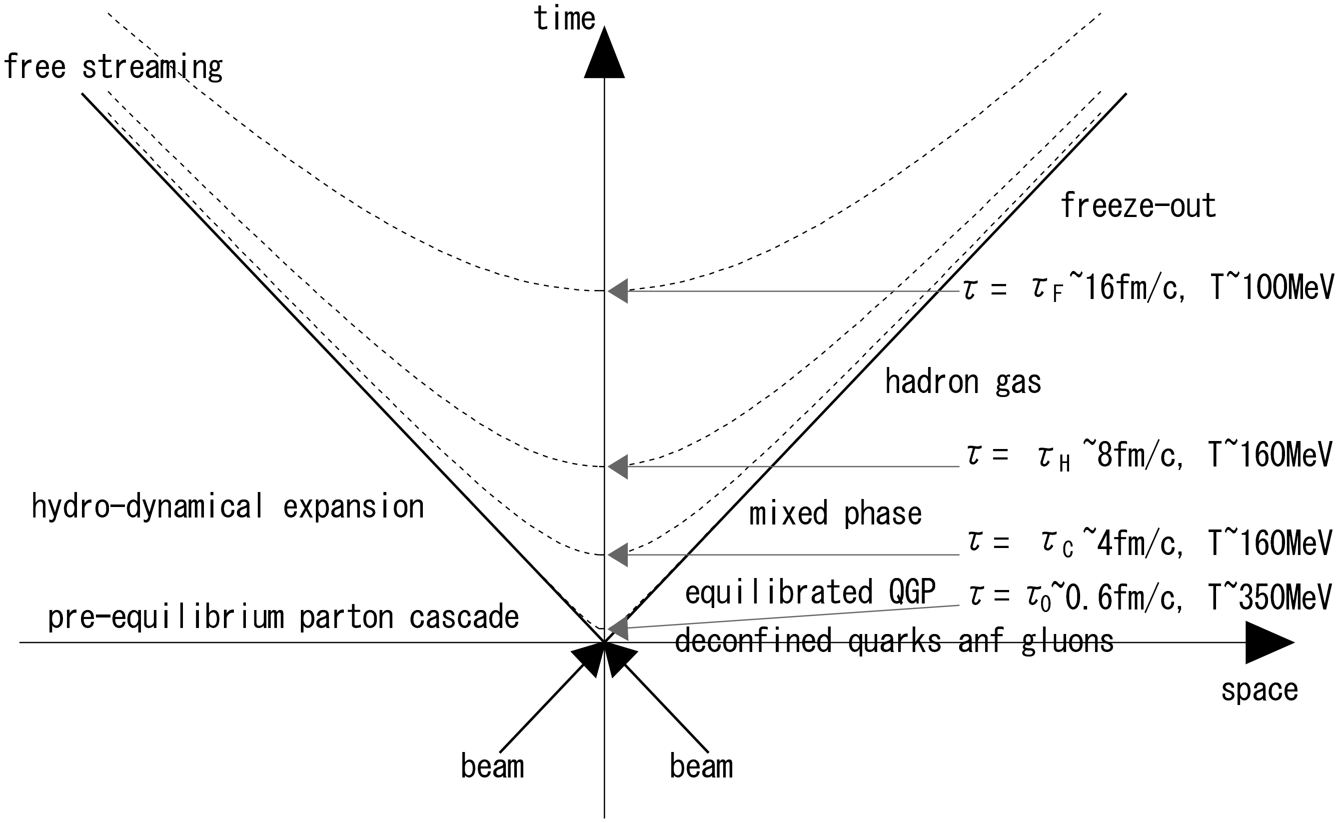

Figure 2.3: A schematic of the space-time evolution in a nucleus-nucleus collision. The times and temperatures at each phase are obtained from Ref. [8] based on the hydrodynamic model. Mixed phase would exist only if the transition is first order.

evolution depends solely on the proper time, $\tau = \sqrt{t^2 - z^2}$, which is a good approximation in the high-energy limit.

At the proper time $\tau = 0$, a huge amount of energy is released in a tiny volume. Free partons, mainly gluons, are produced by a collision between the two Lorentz contracted nuclei. In a high-energy heavy-ion collision, nuclei look like pancakes due to the Lorentz contraction ($\gamma \sim 106$ at $\sqrt{s_{NN}} = 200$ GeV) in the center-of-mass system of the collision. Once a high-energy heavy-ion collision occurs, the two colliding pancakes pass through each other, and many inelastic nucleon-nucleon collisions occur in a very short time. The system is not initially in thermal equilibrium and the dynamics may be described as a cascade of colliding partons. The subsequent multiple-parton scattering brings the matter to local equilibrium.

If the energy deposit is large enough and exceeds the critical energy density, the QGP might be formed at the proper time $\tau = \tau_0$. After the formation of the QGP, the system would evolve such as fluid, and expand and cool down according to hydrodynamics.

At $\tau = \tau_C$, the system reaches to the critical temperature T_c between the QGP and ordinary hadrons. If the transition is the first order, the system passes through the mixed phase which consisting of the QGP and hadron phase.

At $\tau = \tau_H$, the system finishes the hadronization and produces hadrons which keep interacting with each other until the temperature drops to the freeze-out temperature.

At $\tau = \tau_F$, hadrons cease to interact with each other and move away, which is called kinetic freeze-out.

2.1.3 Initial Energy Density

If we agree to Bjorken's scenario [8], the energy density achieved at the formation time, τ_0, can be estimated from the physics observables: particle multiplicity, and transverse energy. In an overlap region with the longitudinal thickness, Δz, and the transverse area, S at $z = 0$ and at $t = \tau_0$, the particle density is given as,

$$\frac{\Delta N}{S\Delta z} = \frac{1}{S}\frac{dN}{dy}\frac{dy}{dz}\Big|_{y=0} \tag{2.7}$$

$$= \frac{1}{S}\frac{dN}{dy}\frac{1}{\tau_0 \cosh y}\Big|_{y=0}, \tag{2.8}$$

where y is a rapidity, as defined in Appendix A and the particle energy in a given rapidity y is $m_T \cosh y$, where m_T is a transverse mass of the particle (Appendix A).

The energy density, ϵ_0, is estimated as follows:

$$\epsilon_0 = m_T \cosh y \cdot \frac{\Delta N}{S\Delta z} \tag{2.9}$$

$$= \frac{m_T}{S\tau_0}\frac{dN}{dy}\Big|_{y=0} \tag{2.10}$$

$$= \frac{1}{S\tau_0}\frac{dE_T}{dy}\Big|_{y=0}, \tag{2.11}$$

where E_T is a transverse energy in a collision.

If $\tau_0 = 1$ fm/c is used in central collisions, the energy density from Bjorken's scenario is estimated to be ~ 3.2 GeV/fm^3 in Pb+Pb collisions at SPS ($\sqrt{s_{NN}} = 17.3$ GeV) [9] and ~ 5.4 GeV/fm^3 in Au+Au collisions at RHIC ($\sqrt{s_{NN}} = 200$ GeV) [10]. It exceeds the critical energy density ϵ_c of 1 GeV/fm^3 required for the phase transition.

2.2 Hard Scattering and Jet Quenching

The space-time evolution of the system after the heavy-ion collisions is complicated. Since observed particles are produced by the interaction with various phases, it is hard to measure the observables from the only QGP phase. For that reason, the measurement has to rely on the indirect observables which are sensitive to the matter at early stage of collisions.

As one of the probes to investigate the matter at early stage of collisions, high-p_T hadrons produced by the hard scattering have been proposed. Since a hard scattering is a point-like (distance scale of $1/p_T \leq 0.1$ fm), the cross section of high-p_T hadrons in the relativistic heavy-ion collisions can be regarded as that in $p+p$ collisions after multiplied by the number of collisions. If there is a difference between the measurement and the expectation from $p+p$ collisions, it can be attributed to the effect of interactions with the matter.

As described in Sec. 2.5.2, the PHENIX experiment at RHIC in $\sqrt{s_{NN}} = 200$ GeV Au+Au collisions has been observed the yield suppression of high-p_T hadrons compared to that in $p+p$ collisions. As illustrated in Fig. 2.4, the hard scattered partons which pass through the hot and dense matter radiate the gluons by the interaction with soft partons in the matter. As a consequence of parton energy loss, the yield of high-p_T hadrons (jets) is expected to be suppressed in the extreme state of the matter, such as QGP. This phenomena is called "Jet Quenching". The detailed explanation about parton energy loss mechanism is described in Sec. 2.6. Since the initial gluon density of the matter can be evaluated by the quantity of the energy loss, a jet quenching is a good probe to investigate the property of the matter.

2.3 High-p_T Hadron Production

One of the striking feature of QCD is asymptotic freedom [1] due to the anti-screening feature of the QCD vacuum. The strong coupling constant decreases with the increase of momentum transfer squared, Q^2. One consequence is that interactions with Q^2 larger than a few GeV^2 can be calculated using the perturbative theory of QCD (pQCD). The cross section of a high-p_T hadron in nucleon-nucleon scattering is described in pQCD as the convolution of partonic reactions $a + b \rightarrow c + d$ with the density function as shown in

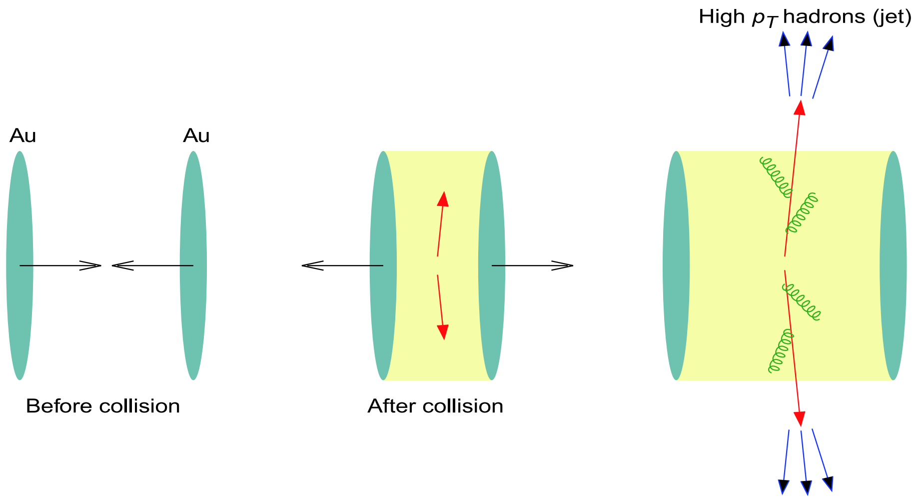

Figure 2.4: A schematic of Au+Au collision and jet quenching for central collision ($\mathbf{b}$ = 0 fm). Fast partons scattered by nucleon-nucleon collisions transverse in the medium and lose their energy by mainly gluon bremsstrahlung.

Fig. 2.5:

$$\sigma^{ab\to hX} = \sum_{abcd} \int dx_a dx_b dz_c f_{a/A}(x_a, Q^2) f_{b/B}(x_b, Q^2) \sigma(ab \to cd) D^0_{h/cd}(z_{cd}, Q^2), \quad (2.12)$$

where $f_{a/A}(x_a, Q^2)$ and $f_{b/B}(x_b, Q^2)$ are the parton distribution functions (PDFs) of the "a" and "b" partons in the hadron "A" and "B", respectively, $D^0_{h/cd}(x_{cd}, Q^2)$ is a fragmentation function (FF) from the "c" or the "d" parton to the hadron, $x(z)$ is a momentum fraction of the initial parton (final hadron) in the initial hadron (final parton), $\sigma(ab \to cd)$ is a cross section of the parton-parton interaction. It should be noted that only term of parton-parton scattering in Eq. 2.12, $\sigma(ab \to cd)$, is perturbatively computable, while other terms (PDF and FF) are obtained from parameterizations based on the experimental data.

Since the PDF can not be obtained from the pQCD calculation due to the incoherent non-perturbative effect of a binding state in QCD, the PDF is calculated by theoretical groups using measured nuclear structure function $F_2(x, Q^2)$ [12]. A structure function of parton has been measured by deep inelastic scattering (DIS) of leptons in many experiments at SLAC and DESY. For example, CTEQ group provides the parameterized PDF as shown in Fig. 2.6.

A fragmentation function, $D^0_{h/p}(z, Q^2)$, has been determined using the processes of $e^+ + e^- \to \gamma^*$ or $Z \to h + X$ in $\sqrt{s}$ =3–183 GeV lepton-pair collisions.

The next-to-leading order (NLO) pQCD calculations succeed in describing the production of high-p_T particles in high-energy nucleon-nucleon collisions. Figure 2.7 shows the p_T-spectra of π^0 measured by PHENIX in $p + p$ collisions at $\sqrt{s} = 200$ GeV and the NLO pQCD calculations [13]. The calculations are consistent with the data, indicating

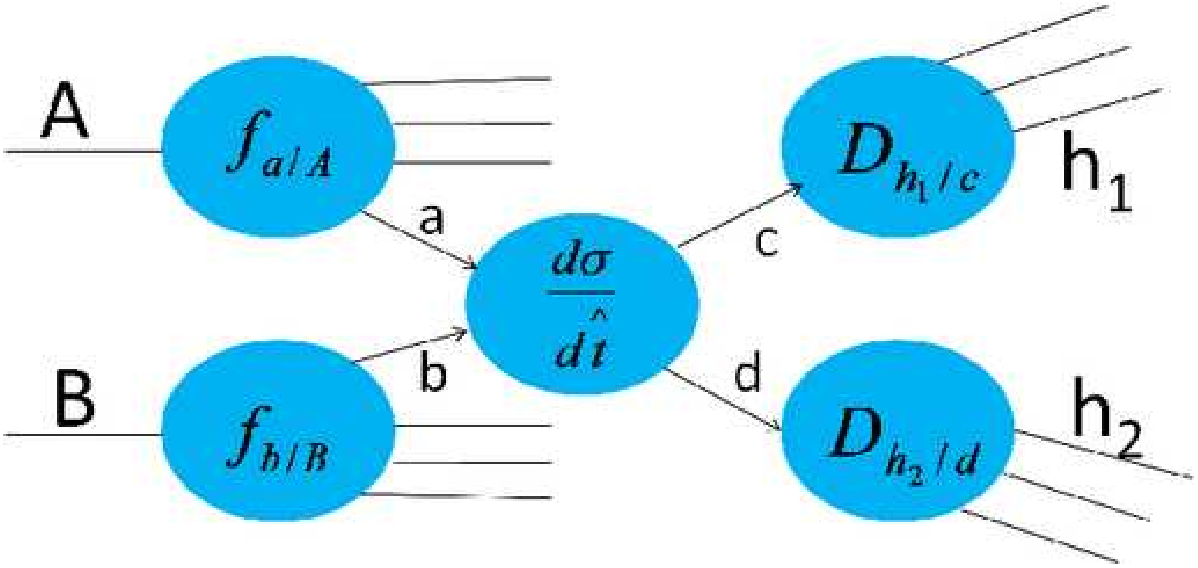

Figure 2.5: A diagram of the calculation on a hard scattering.

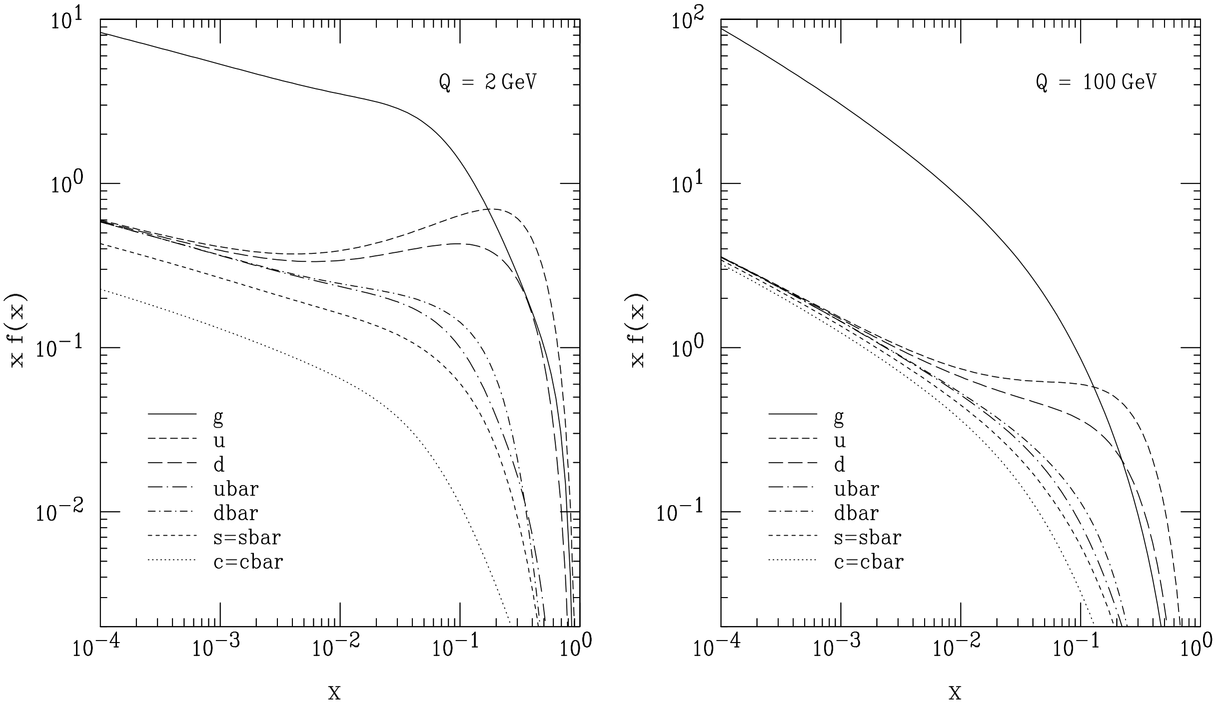

Figure 2.6: The parton distribution function calculated by the CTEQ group as a function of x at Q =2 and 100 [11].

that the particle production at high-p_T region is dominated by the fragmentation of hard scattered partons, and the production rate is well reproduced.

2.4 High-p_T Hadron Production in Heavy-ion Collisions

2.4.1 Nuclear Modification Factor (R_{AA})

The amount of nuclear effect can be quantified using a nuclear modification factor (R_{AA}). The R_{AA} is expressed as a ratio of the measured yield in Au+Au collisions to the expected yield in $p+p$ collisions, and the R_{AA} is defined as follow:

$$R_{AA} = \frac{d^2N_{AA}/dp_Td\eta}{T_{AA}(b) \cdot d^2\sigma_{NN}/dp_Td\eta}, \tag{2.13}$$

where the numerator is the invariant yield per unit rapidity, the denominator is the cross section in the $p+p$ collisions scaled with the thickness function, $T_{AA}(b)$, in nucleus-nucleus collisions, and $T_{AA}(b)$ is a Glauber scaling factor, and $T_{AA}(b)$ is defined as follows:

$$T_{AA}(b) = \int d^2\mathbf{r}T_A(\mathbf{r}) \cdot T_A(\mathbf{r} - b), \tag{2.14}$$

where $T_A(\mathbf{r}) = \int dz\rho_A(\mathbf{r}, z)$. The average number of binary nucleon-nucleon collisions ($\langle N_{coll}\rangle$) at an impact parameter b is given as $T_A(b) = \langle N_{coll}(b)\rangle/\sigma_{NN}$, where σ_{NN} is the total inelastic cross section. If a hard scattered parton penetrates the matter without any nuclear effect, the R_{AA} should be equal to one after the correction of the well-known nuclear effect described in Sec. 2.4.2.

2.4.2 Initial State Effect

A production of high-p_T hadrons in nucleon-nucleon collisions includes both an initial state effect and a final state effect. In this thesis, the final state effect is defined as jet quenching, while the well-known initial state effects are defined as Cronin effect and nuclear shadowing. The initial state effects should be taken into account before we conclude that the yield suppression is the final state effect. The well-known initial state effects is explained in subsequent sections.

Cronin Effect

It was observed in 1974 by J.W. Cronin *et al.* that the differential cross section does not simply scale with the number of the target nucleus, A, in a p+A collisions [14]. The differential cross section in p+A collisions for a given p_T is parameterized as,

$$E\frac{d^3\sigma}{dp^3}(p_T, A) = E\frac{d^3\sigma}{dp^3}(p_T, 1) \cdot A^{\alpha(p_T)}. \tag{2.15}$$

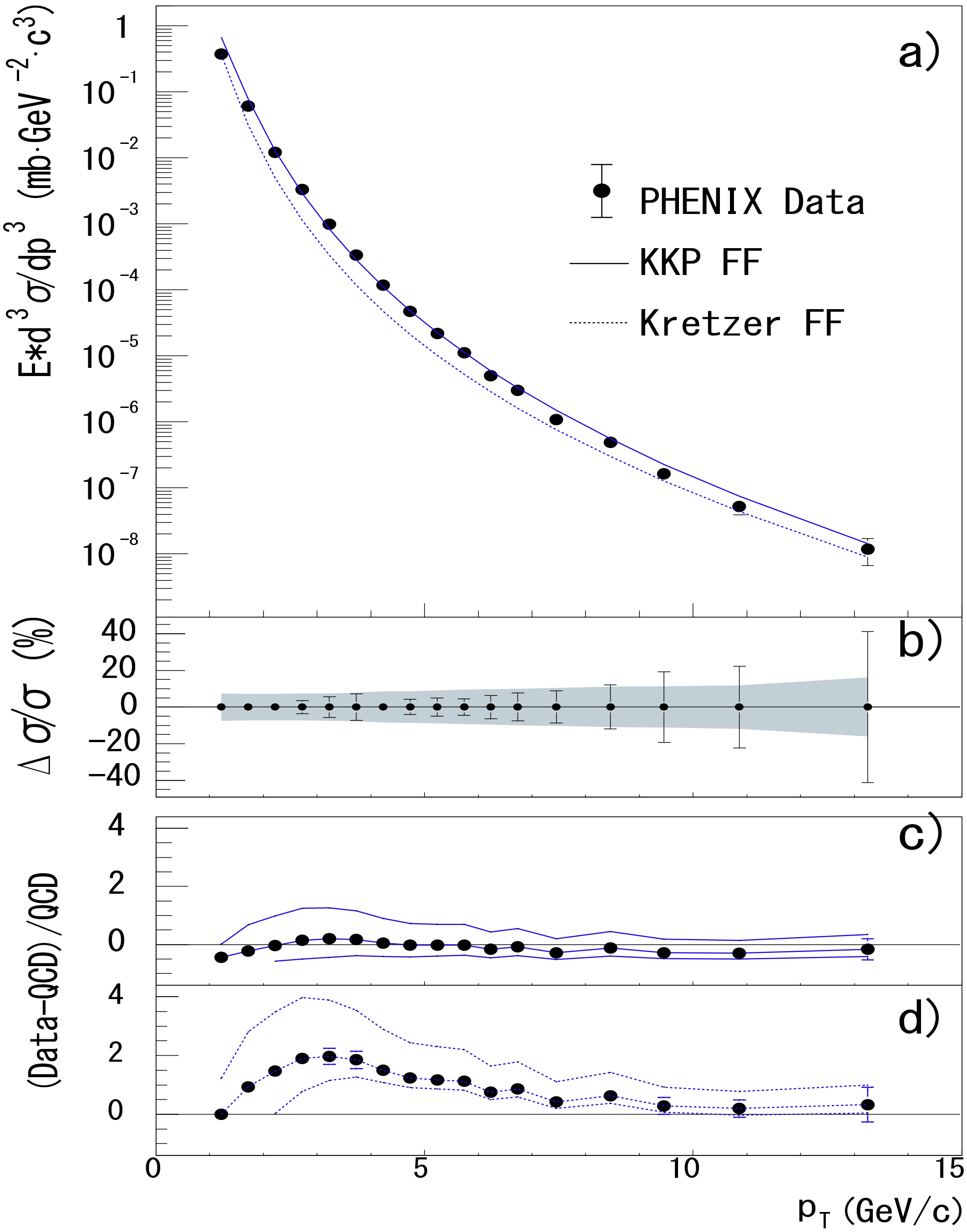

Figure 2.7: (a) The data is the invariant differential cross section of the inclusive π^0 production. Solid and dashed lines are NLO pQCD calculations with equal renormalization and factorization scales of p_T using the Kniehl-Kramer-Pötter and Kretzer, respectively. (b) The bars and bands are the relative statistical and systematic uncertainties, respectively. (c), (d) The relative difference between the data and the theory using KKP (c) and Kretzer (d) fragmentation functions with scales of $p_T/2$. The Lower and upper curves are p_T and $2p_T$. The normalization error of 9.6 % is not shown in all figures [13].

As shown in Fig. 2.8, α becomes larger than 1 at the p_T region below 1 GeV/c. Compared to the expectation from $p+p$ collisions, the enhancement of the particle production was observed. The enhancement is explained as the multiple scattering of the incident partons while passing through the nucleus A before the hard collisions which smear the axis of the hard scattering relative to the axis of the incident beam. Therefore, this effect is called "k_T smearing", where k_T is the transverse momentum of a parton.

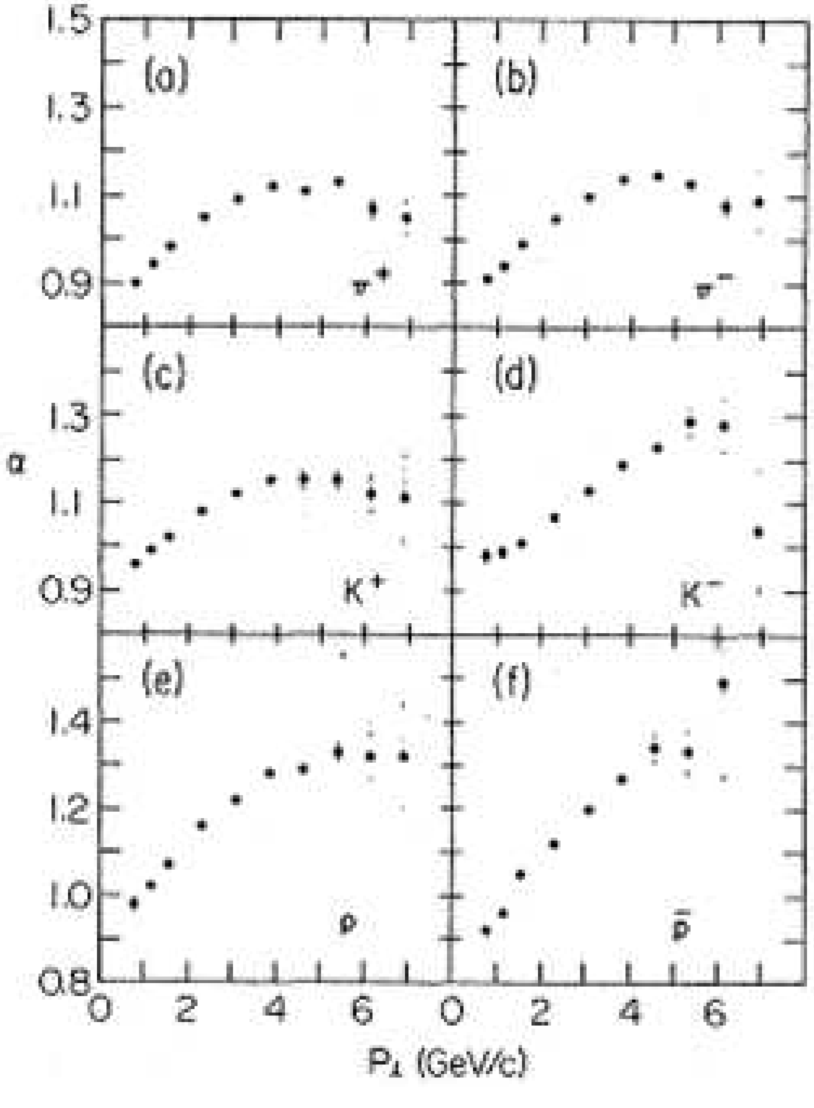

Figure 2.8: The α of hadrons as a function of p_T [14]. The hadrons are produced by 400 GeV proton to nucleus at Fermi National Accelerator laboratory (Fermilab.).

The k_T in $p+p$ collisions at $\sqrt{s} = 200$ GeV has been measured by RHIC-PHENIX experiment using the method of two-particle azimuthal-angular correlations which worked well at Intersecting Storage Rings (ISR) energies ($\sqrt{s} \leq 63$ GeV) at CERN [15]. The extracted value, $\sqrt{\langle k_T^2 \rangle} = 2.68 \pm 0.35$ GeV/c, is comparable with the past measurements at lower $\sqrt{s}$ energies.

Nuclear Shadowing

It was observed in 1982 by the EMC group that a structure function $F_2(x, Q^2)$ of Fe differs significantly from that of a free nucleon [16].

Comparing with nuclear structure functions, deuterium is often referred as a weak-bounded system and has an spine-averaged nuclear structure function. The initial nuclear effects are qualified as the ratios of the structure functions of parton, $F_2^A(x, Q^2)/F_2^D(x, Q^2)$. These effects are summarized in Table 2.1. Figure 2.9 shows the ratios of F_2 for different nuclei [17]. The x in Fig. 2.9 is a momentum fraction of the initial parton.

Nuclear Effect	x Region	Fraction
Shadowing	$x \leq 1$	$F_2^A/F_2^D \leq 1$
Anti-shadowing	$0.1 \leq x \leq 0.3$	$F_2^A/F_2^D \geq 1$
EMC Effect	$0.3 \leq x \leq 0.7$	$F_2^A/F_2^D \leq 1$
Fermi Motion	$x \leq 0.7$	$F_2^A/F_2^D \geq 1$

Table 2.1: Summary table for various nuclear effects at each x region.

The relevant $x-$region of the scattered parton can be estimated using p_T of the leading hadron. The x at mid-rapidity is approximately described as follows:

$$x \sim \frac{2p_T}{\sqrt{s_{NN}}}. \tag{2.16}$$

The p_T region of $1 < p_T < 20$ GeV/c for the hadrons in the mid-rapidity ($y \approx 0$) at RHIC energy corresponds to the x-region of $0.01 < x < 0.2$, where nuclear shadowing should be considerable for the initial nuclear effect.

2.5 Measurement of Neutral Pion at Heavy-ion Collisions

Several high-energy heavy-ion experiments at SPS and RHIC for different center-of-mass energies have been performed. In this section, the results related to the parton energy loss are introduced.

2.5.1 Several Experiments at SPS Energies

Neutral pion in heavy-ion collisions was measured in S+S and S+Au at $E_{\mathrm{lab}} = 200$A GeV ($\sqrt{s_{NN}} = 19.4$ GeV) in WA80 [18], in Pb+Au at $E_{\mathrm{lab}} = 158$A GeV ($\sqrt{s_{NN}} = 17.3$ GeV) in CERES and in Pb+Pb at $E_{\mathrm{lab}} = 158$A GeV in WA98 [19]. Figure 2.10 shows the R_{AA} of pion in nucleus-nucleus collisions at $\sqrt{s_{NN}} \leq 31$ GeV. These results show that the R_{AA} monotonically increase with p_T. It is interpreted as the consequence of Cronin effect.

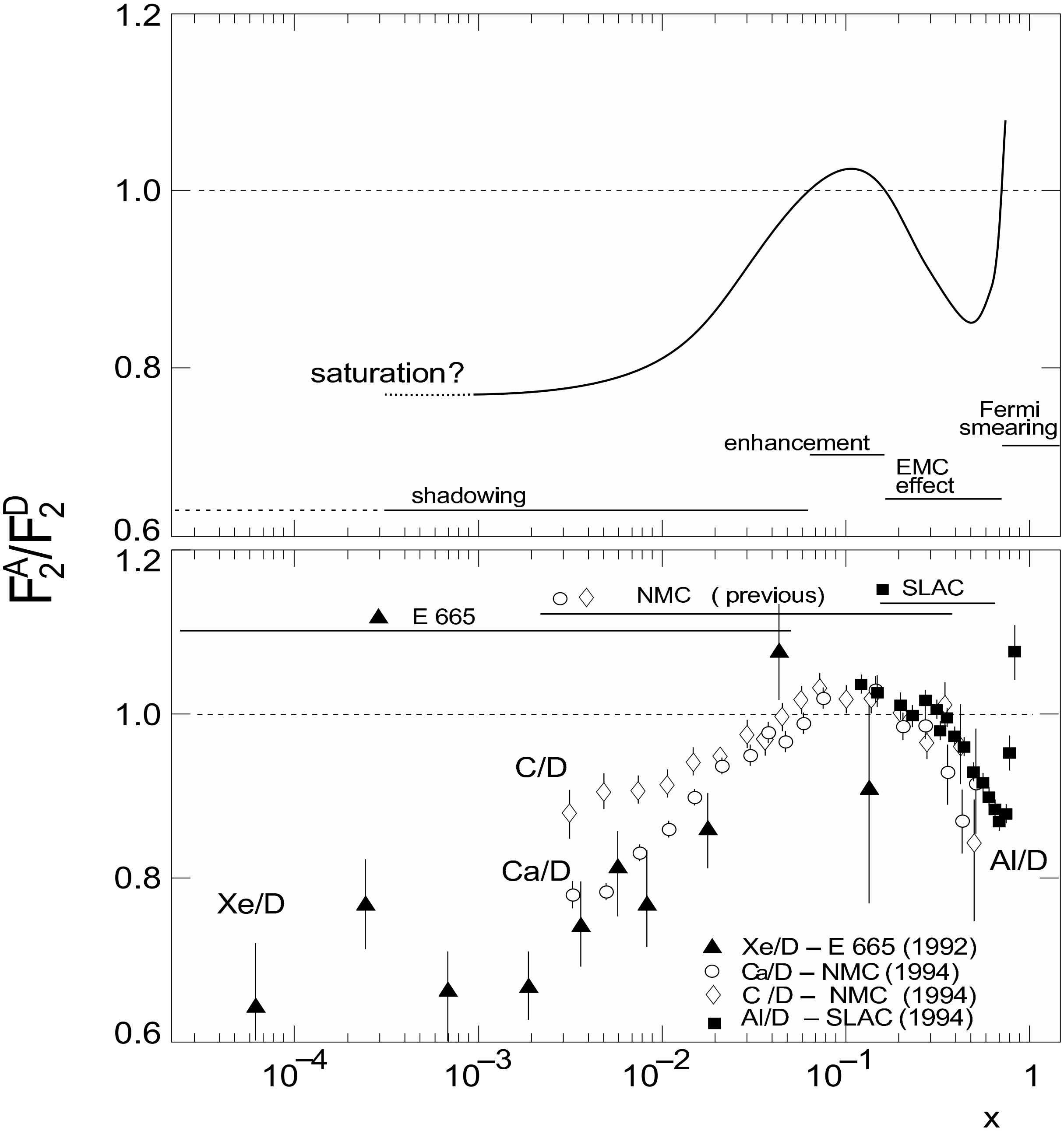

Figure 2.9: The ratio of F_2 structure functions of various nuclei to that of deuterium [17].

Based on the difference between the measurement and theoretical expectation where the initial state effects are taken into account, X.N. Wang estimated that the energy loss of the hard scattered partons is $dE/dx < 0.02$ GeV/fm on the assumption of no modification in fragmentation function (FF) [20].

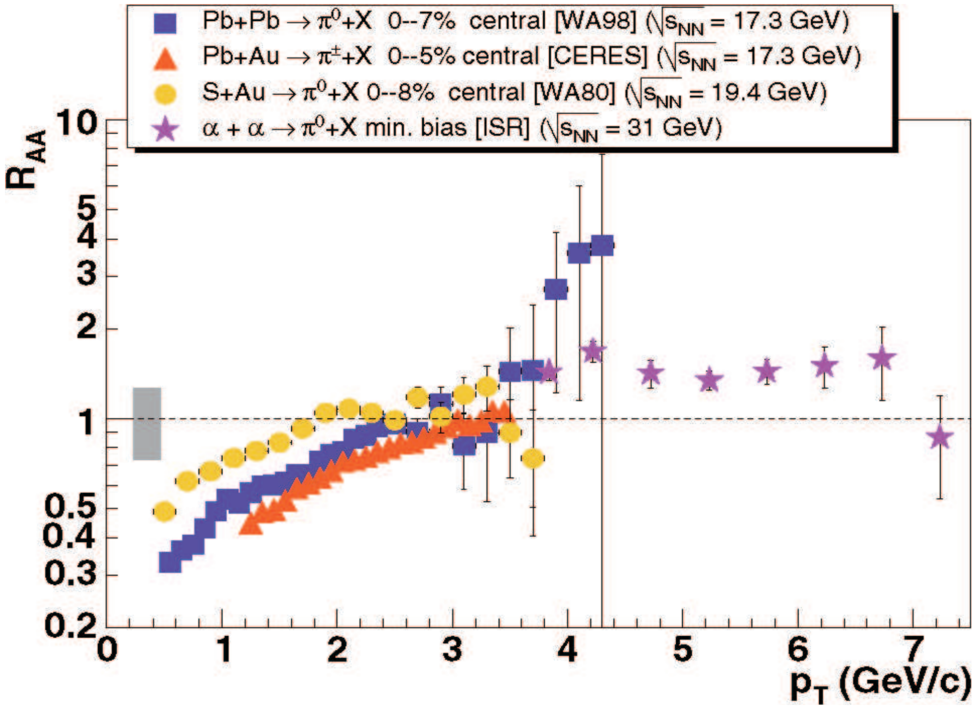

Figure 2.10: Nuclear modification factors of neutral pion production at CERN-SPS in central Pb+Pb, Pb+Au, and S+Au collisions at $\sqrt{s_{NN}} \approx 20$ GeV and π^0 production at CERN-SPS in minimum bias $\alpha + \alpha$ collisions at $\sqrt{s_{NN}} = 31$ GeV [21]. The R_{AA} at SPS are obtained using the $p + p$ parameterization proposed in Ref. [22]. The shaded band around R_{AA} =1 represents the overall fractional uncertainty of the SPS data including the quadric sum of the uncertainty of 25 % from the $p + p$ reference and the uncertainty of 10 % from the Glauber calculation of $\langle N_{coll} \rangle$. There is an additional overall uncertainty of ±15 % for the CERES data not shown in this figure [23].

2.5.2 PHENIX Experiment at RHIC Energy

In contrast to the results at SPS, the results at RHIC show the yield suppression of high-p_T hadrons in central Au+Au collisions at $\sqrt{s_{NN}} = 200$ GeV compared to the binary scaled $p + p$ collisions at the same center-of-mass energy. Figure 2.11 shows the R_{AA} of neutral pion in central and peripheral Au+Au collisions, together with R_{AA} in minimum bias d+Au collisions at $\sqrt{s_{NN}} = 200$ GeV [24, 25]. The yield of neutral pion is strongly suppressed in central Au+Au collisions, while the yield of π^0 is not suppressed in d+Au collisions [26]. It is concluded that the large suppression is not due to the initial state effects such as nuclear shadowing and Cronin effect and shadowing. This observation has led to the extensive theoretical studies [27, 28, 29, 30]. Most of these studies are based on the prediction [31, 32, 33] that multiple gluon radiations are induced from the scattered fast partons in the hot and dense matter, leading to a suppression of the fragmented products of high-p_T hadron ("Jet Quenching").

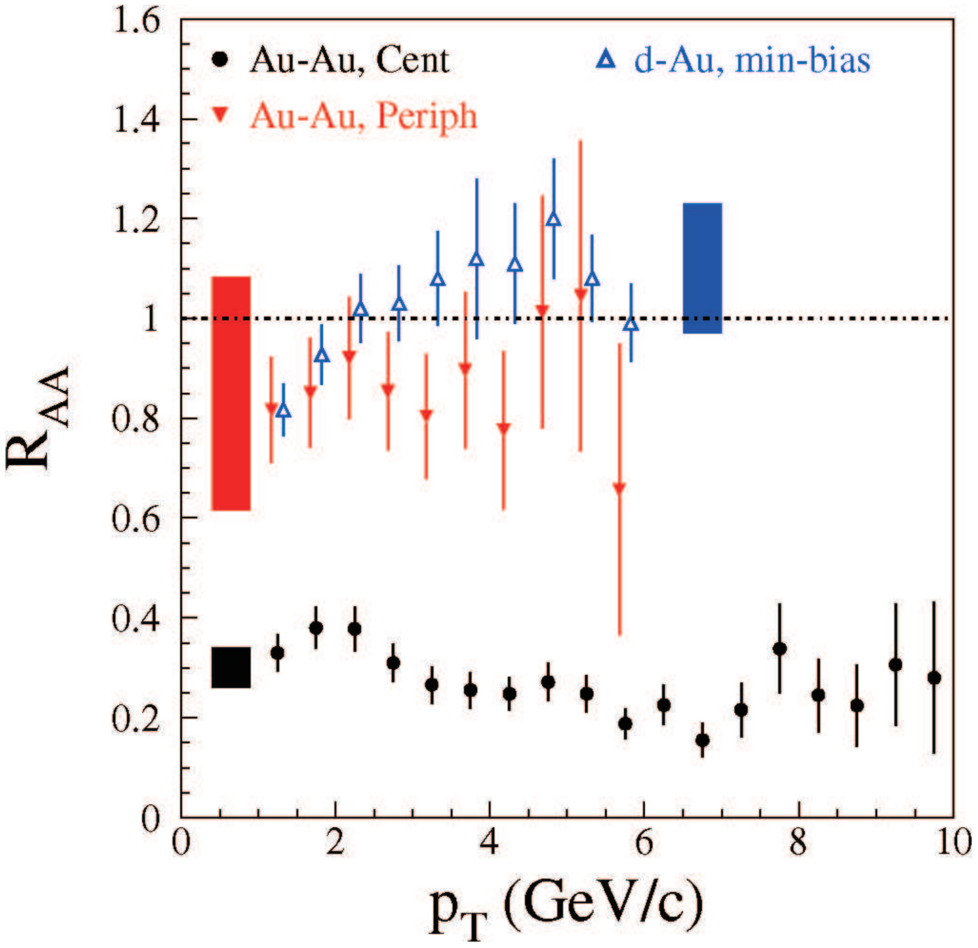

Figure 2.11: Nuclear modification factor of π^0 in the central and peripheral $\sqrt{s_{NN}} =$ 200 GeV Au+Au collisions compared to that in d+Au collisions at the same center-of-mass energy measured by the PHENIX experiment. The band around the data points indicates the normalization uncertainty [23].

2.6 Parton Energy Loss Mechanism

An energetic charged particle passing through the matter loses its energy due to collisions with electrons and nuclei via electromagnetic interactions. There are two main processes on energy loss: a collisional process and radiative process such as a bremsstrahlung.

Taking the analogy that charged particles lose their energy in charged medium, colored partons would lose their energy in colored medium. If an energetic parton propagates through a colored medium, it is predicted to lose its energy by the strong interaction with soft partons in the matter. In 1982, it was considered that an energetic parton might lose its energy by elastic scatterings with other partons in QGP [34]. It was subsequently turned out that the energy loss by the radiation of soft gluons would be dominant effect rather than the elastic scatterings [35]. Thus, the theoretical treatment of the parton energy loss has to consider a destructive interference effect of the emitted gluons if the formation time of the gluon is longer than its collision time in the medium [36]. It is analogous to the photon in electromagnetic interaction. The interaction probability of photon bremsstrahlung in high-density medium is smaller than that in low-density medium, and it is known as Landau-Pomeranchuk-Modally (LPM) effect [37]. Based on the analogy, M. Gyulassy *et al* first pointed out that the occurrence probability of gluon radiation would become low in the colored medium with high density [36]. R. Baier also proposed parton energy loss models with different formalism which takes into account LPM effect in QCD [37, 38, 39]. The energy loss of hard-scattered partons propagating in an infinite medium is expressed as follows:

$$\frac{dE}{dx} \propto N_c \alpha_s \sqrt{E \frac{\mu^2}{\lambda}} \ln \frac{E}{\lambda \mu^2}, \tag{2.17}$$

where L is larger than $L_{c\tau}$, where $L_{c\tau}\sqrt{\lambda E/\mu^2}$, N_c is equal to 3, E is a parton energy, μ^2 is a Debye screening mass for the effective parton scatterings, and λ is a mean free path of parton in the medium. For an energetic parton in the finite-length medium ($L_{c\tau} > L$), the energy loss becomes almost independent of E and can be related to the total p_T broadening acquired by the multiple scatterings, and the energy loss is given as,

$$-\frac{dE}{dx} = \frac{N_c \alpha_s}{8} (\Delta p_T)^2 = \frac{N_c \alpha_s}{8} (\delta p_T)^2 \frac{L}{\lambda}, \tag{2.18}$$

where $(\delta p_T)^2$ is a squared transverse momentum which one parton acquires during the propagating in the medium, and L is the total path length which a parton passes through in the medium. Since the energy loss per unit path length is proportional to L, the total energy loss of parton is proportional to L^2.

Since $L_{c\tau}$ involves the two unknown parameters, λ and μ^2, it is difficult to calculate the quantity of the energy loss if L is larger than $L_{c\tau}$. Accordingly, X.-N. Wang studied the phenomenological consequences in the inclusive single particle spectrum to realize more applicable for the system of the hot and dense matter produced in heavy-ion collisions. He assumed that the energy loss is proportional to $\sqrt{E/E_0}$, where E_0 is assumed to be 20 fm^2/GeV or 5 fm^2/GeV, and the mean free path λ_q is 1 fm [40].

The left panel in Fig. 2.12 shows the modification factors calculated by pQCD [41]. In the calculation, the energy loss $-dE/dx$ is taken to be 1 GeV/fm and 2 GeV/fm, which is independent of the path length x. The mean free paths are assumed to be two cases of 1 fm and 0.5 fm. The right panel in Fig. 2.12 shows the expected nuclear modification

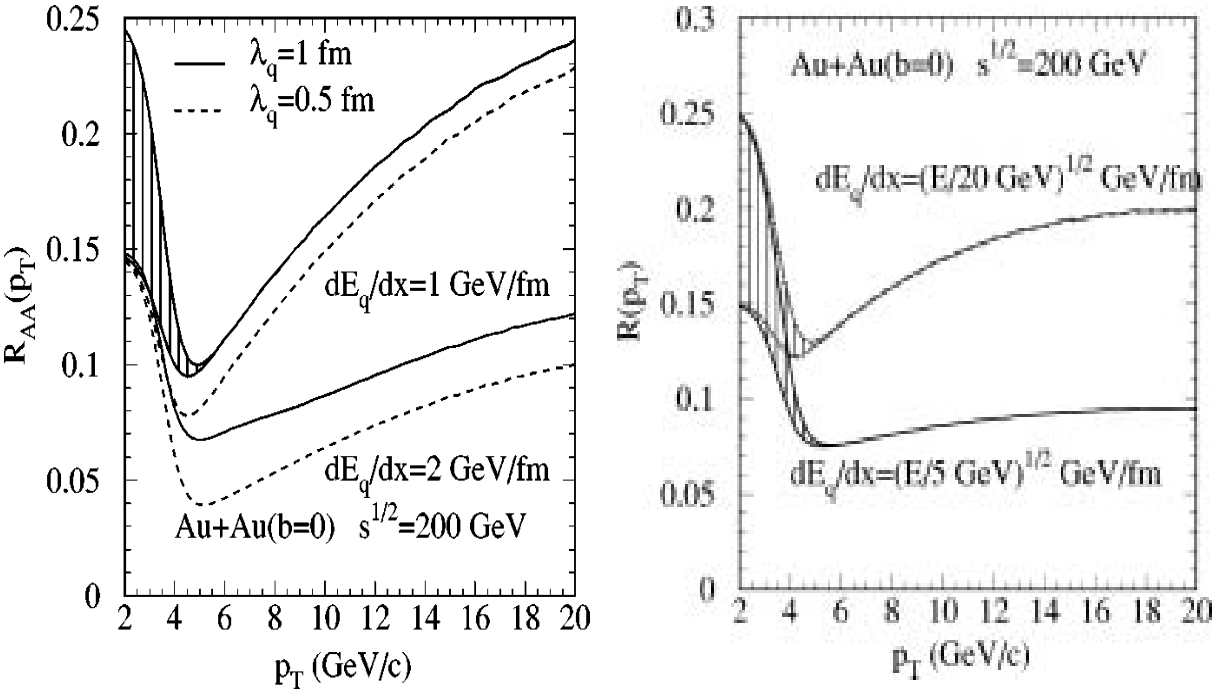

Figure 2.12: Left: The nuclear modification factors as a function of p_T in Au+Au collisions at $\sqrt{s_{NN}} = 200$ GeV [41]. These predictions are assumed to be constant dE/dx (1 GeV/fm and 2 GeV/fm) and the mean free path (λ_q =1 and 0.5 fm). Right: The expected nuclear modification factor of charged particles in Au+Au collisions at $\sqrt{s_{NN}} = 200$ GeV. The energy dependence of parton, $dE/dx = \sqrt{E/E_0}$, and the mean free path, $\lambda_q = 1$ fm, are assumed. Both of shade areas in two panels indicate the uncertainty of the effective mass number scaling of low-p_T spectra depending on the interaction of soft and hard processes.

factors which depend on the parton energy as a function of p_T with two different scaling factors (E_0).

The calculation shown in Fig. 2.12 is assumed to be a static medium. However, the expansion of the system created by heavy-ion collisions would lead to a rapid decrease of the color-charge density. Therefore, the proper-time dependence should be involved in the energy loss model.

The proper-time dependence of color-charge density can be obtained as $\rho(\tau) \propto T^3(\tau) \propto \tau^{-1}$ from the Landau hydrodynamical model [42] under the assumption of a longitudinal expanding of a fireball [43]. The energy-loss calculation assumes that a color-charge density, $\rho(\tau)$, decreases with the proper time τ:

$$\rho(\tau) = \frac{\tau_0}{\tau}\rho(\tau_0), \tag{2.19}$$

where

$$\rho(\tau_0) = \frac{1}{\tau_0 \pi R^2}\frac{dN^g}{dy}. \tag{2.20}$$

Many theoretical calculations of parton energy loss in the hot and dense matter have been performed, and it is found that the high-p_T hadron spectra in relativistic heavy-ion collisions are quite sensitive to how the energetic partons interact with the hot and dense medium and lose their energy before they fragment into hadrons, leading to the suppression of high-p_T particles. Furthermore, the modification factor as a function of p_T is sensitive to the parton-energy dependence predicted in the models. The non-linear path-length dependence of the energy loss leads to stronger suppression as suggested by R. Baier *et al* [44]. If the energy loss "dE/dx" is independent of the path length, the suppression should be small at high-p_T region. The precise measurement of high-p_T hadrons makes it possible to constrain the proposed energy-loss mechanisms, and it gives the information for the understanding of the created matter.

2.7 Relation of Path Length and Azimuthal Angle

In non-central heavy-ion collisions, the initial overlap of two nuclei in the transverse reaction plane becomes almond shape as shown in Fig. 2.13. Thus, if the energy loss is assumed to depend on the path length, the quantity of the energy loss is associated with the azimuthal angle of emitted particles.

One example to understand the relation is the correlation of standard eccentricity, ϵ_{std}, and impact parameter ($\mathbf{b}$). Let the standard eccentricity be defined as follows:

$$\epsilon_{\mathrm{std}} = \frac{< y^2 > - < x^2 >}{< y^2 > + < x^2 >}, \tag{2.21}$$

where x and y denote each position of the nucleons, and ϵ_{std} represents the asymmetry of the particle distribution on the transverse reaction plane. Both the standard eccentricity

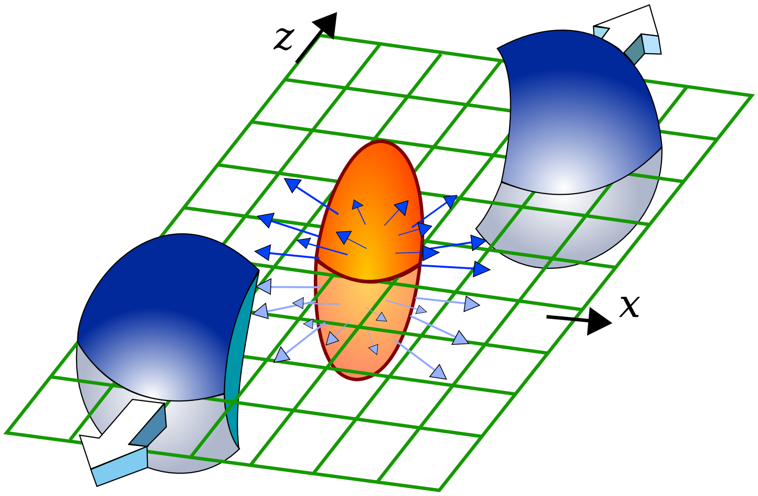

Figure 2.13: A schematic view of the collective flow at RHIC. The collective flow is created by the strong pressure gradient along the azimuthal angle with respect to the reaction plane.

and impact parameter are observables to characterize the initial collision geometry. Even though the observables can not be measured directly, these can be estimated by the Glauber calculation. Figure 2.14 shows the average standard eccentricity as a function of the average impact parameter. Figure 2.14 certainly shows that the standard eccentricity is strongly associated with the impact parameter.

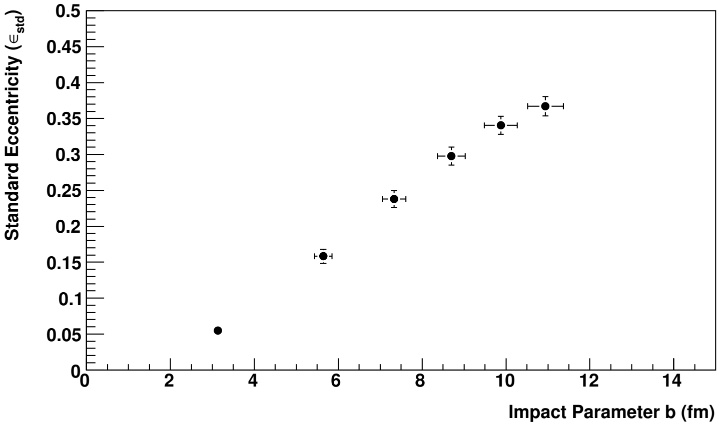

Figure 2.14: The standard eccentricity as a function of impact parameter in Au+Au collisions from the Glauber calculation.

2.7.1 Azimuthal Distribution of Emitted Particles

If the mean free path is larger than the size of the system, the azimuthal angular distribution of emitted particles should be isotropic. On the other hand, if the mean free path is much smaller than the size of the system, the geometry of the system should be reflected to the azimuthal distribution of emitted particles. It is assumed that a spatial anisotropy at the early stage of the heavy-ion collisions is converted into an azimuthal anisotropy of the emitted particles in momentum-space by the strong graduation of the pressure along the azimuthal angle with respect to the reaction plane. Therefore, the azimuthal anisotropy is expected to be sensitive to the early stage of heavy-ion collisions. The reaction plane is defined as the plane where the directions of beam and the vector connecting the center of both nuclei (impact parameter) and is determined by event-by-event The azimuthal anisotropy of emitted particles is quantitatively evaluated with Fourier expansion series as follows:

$$E\frac{d^3N}{dp^3} = \frac{1}{2\pi p_T}\frac{dN}{dp_T dy}\Big(1 + 2v_1\cos\big(\phi_{\rm lab} - \Psi\big) + 2v_2\cos\big(2[\phi_{\rm lab} - \Psi]\big) + \ldots\Big), \tag{2.22}$$

where $\phi_{\rm lab}$ is the azimuthal angle of emitted particles in the fixed laboratory frame, Ψ is the azimuthal angle of the reaction plane, and v_n is the magnitude of each harmonics [45]. Particularly, the second harmonic term in Eq.2.22 corresponds to the magnitude of the azimuthal anisotropy (v_2).

2.7.2 High-p_T Azimuthal Anisotropy v_2

The large azimuthal anisotropy has been observed at RHIC. Figure 2.15 shows the v_2 of the identified charged hadron, $\pi^\pm$, $K^\pm$, p, and $\bar{p}$ as a function of p_T in $\sqrt{s_{NN}} = 200$ Au+Au collisions at PHENIX. The closed red circles, green squares, and blue triangles are proton and anti-proton, $K^\pm$, and $\pi^\pm$, respectively. The colored lines are the expectations from the hydrodynamical calculation. At low-p_T region below 1.5 GeV/c, the v_2 increase with p_T and show the mass dependence which is described by the hydrodynamics calculation [46], while the difference between the model and the data is significant at high-p_T region. The model is assumed that the initial local equilibrium is thermalized at 0.6 fm/c, and the phase transition is the first-order phase transition with a freeze-out temperature of 120 MeV. In the model, it is predicted that the viscosity of the created matter is quite small. Therefore, the matter created in Au+Au collisions is assumed to be a perfect fluid.

The azimuthal anisotropy v_2 with low p_T behaves as hydro, while the v_2 with high p_T is assumed that the effect of the collective flow decrease. Thus, in order to extract the information about initial geometry, the azimuthal anisotropy v_2 should be measured at high-p_T region.

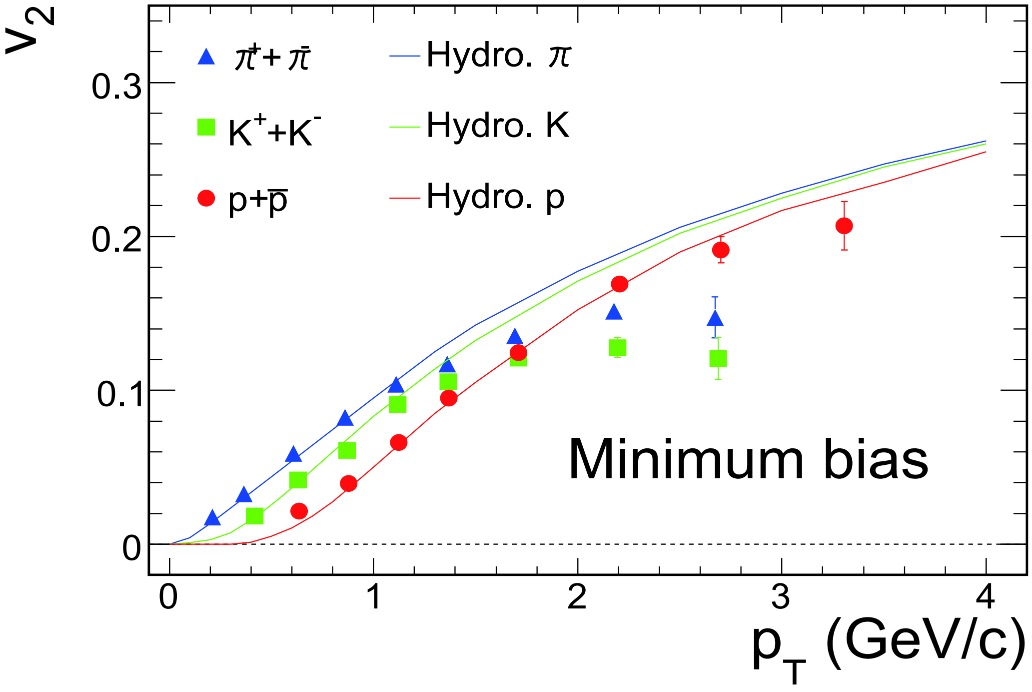

Figure 2.15: The azimuthal anisotropy v_2 of charged hadrons as a function of p_T at $|y| < 0.35$ in $\sqrt{s_{NN}} = 200$ GeV minimum bias Au+Au collisions at PHENIX [46].

Chapter 3

Experimental Setup

The Relativistic Heavy Ion Collider (RHIC) [47] was initially proposed in 1983 and built at Brookhaven National Laboratory (BNL) in the United States of America. The Pioneering High Energy Nuclear Interaction eXperiment (PHENIX) for heavy ion physics at RHIC has started in the early summer of 2000.

3.1 The Relativistic Heavy Ion Collider

The aim at the RHIC is to realize the nuclear matter under extreme condition. The RHIC is designed to accelerate heavy ion at the maximum energy per nucleon of 100 GeV. Heavy ions are produced at the negative-ion source and accelerated through Tandem-Van-de-Graaff, and the three synchrotrons': the booster accelerator, the Alternating Gradient Synchrotron (AGS), and the RHIC. The RHIC ring has the total length of 3.8 km with the maximum bunches of 120 and the designed luminosities, $2{\times}10^{26}$ cm^{-2}s^{-1}, for Au ions. Beam parameters and performances achieved by the RHIC complex accelerator are summarized in Table 3.1. The RHIC collides the two beams of Au ions head-on when they are traveling at nearly the 99.5 % speed of light. Figure 3.1 shows a schematic layout of the RHIC accelerator complex. The RHIC was also used to study the spin structure of the nucleon. The designed luminosity for polarized protons is $2{\times}10^{32}$ cm^{-2}s^{-1}, and their maximum energy is 250 GeV.

3.2 The PHENIX Experiment

PHENIX is a large experiment located at one of the six interaction points of the RHIC [49]. Figure 3.2 shows the setup of the PHENIX detectors viewed from beam and side direction. In this thesis, the coordinate of the PHENIX detectors is defined as shown in Fig. 3.3. The beam is along the z-axis, and the pseudo-rapidity is determined with the polar angle θ as defined in Appendix A. For the central region, two arms are symmetrically-located on azimuthal angle. The pseudo-rapidity coverage of the central arms is ± 0.35 and two

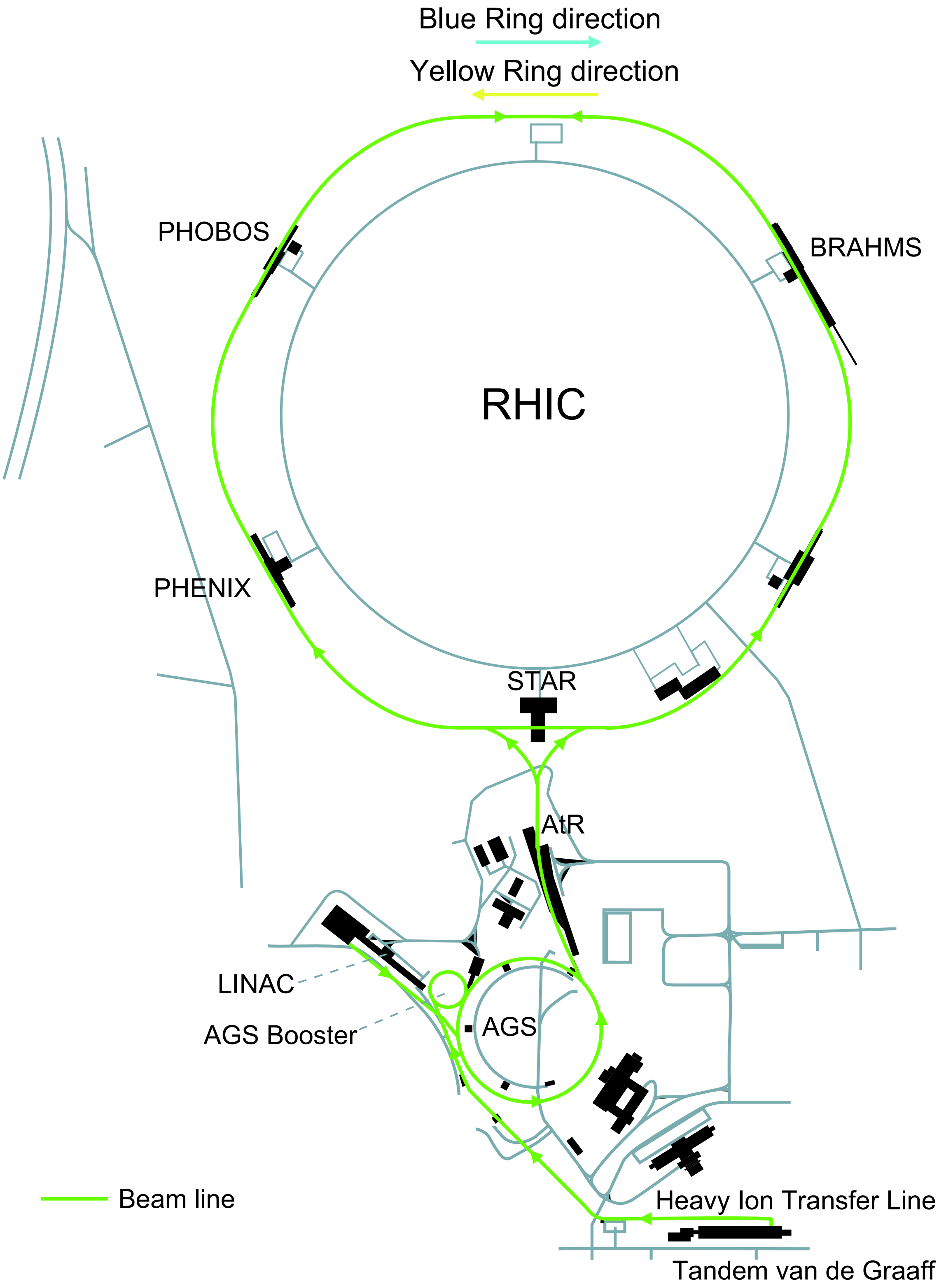

Figure 3.1: The RHIC accelerator complex and the arrangement of experiments [47].

Injection Energy	$\gamma = 10.25$ ($p = 9.5$ GeV/c/nucleon)
Storage Energy	$\gamma = 107.4$ ($p = 100.0$ GeV/c/nucleon)
Peak Luminosity	30×10^{26} cm^{-2}s^{-1}
Ions/Bunch	1.1×10^{9}
Number of bunches	111
Emittance	17–35 μm
Interaction diamond length (maximum)	20 cm
Crossing angle, nominal (maximum)	0(<1.7) mrad
Bunch length	15 cm
Bunch radius	0.2 mm ($\beta^* = 1$)
Luminosity life time	3 hours

Table 3.1: Archieved beam parameters and performance of heavy ion runs at RHIC-PHENIX experiment [48].

muon arms at forward region is ± 1.2–2.4. The coverage and features in each arm are summarized in Table 3.2.

Since the focus in this thesis is the measurement of neutral pions with the Electromagnetic Calorimeter (EMCal) in the central arms, the EMCals will be explained in detail, after brief overview of the PHENIX detectors.

3.2.1 PHENIX Trigger Counter

Beam-Beam Counter

Beam Beam Counter (BBC) is used for event trigger, and used to measure the beam property such as the luminosity and centrality [50]. The BBCs are two arrays of 64 Cherenkov counters, each of which is located at both the north and south positions of 1.44 m from the nominal collision. The BBCs cover the pseudo-rapidity of 3.0–3.9. Figure 3.4 shows (a) one counter, (b) an array and (c) BBC mounted.

Each counter is composed of 3 cm thick quartz as a Cherenkov radiator equipped with 1 inch diameter mesh-dynode photomultiplier tube (Hamamatsu R6178). The BBC is designed to measure the number of charged particles produced in the collisions, the vertex position of collision, and the start time for the time-of-flight system. The BBC plays an important role for the centrality determination. Due to the limited acceptance coverage, the trigger efficiency of 93 % and 50 % in the inelastic collisions can be achieved for Au+Au and $p + p$ collisions at the center-of-mass 200 GeV, respectively. The start time, T_0, and the Z-vertex position, z_{vtx}, along the beam axis are obtained as follows:

$$T_0 = \frac{T_N + T_S}{2} - \frac{z_{N-S}}{c} \tag{3.1}$$

$$z_{vtx} = \frac{|T_N - T_S|}{2} \cdot c, \tag{3.2}$$

Subsystem	Rapidity	Azimuth	Purpose and Features
Central Magnet	$\lvert\eta\rvert <0.35$	2π	Up to 1.5 T·m.
Muon Magnet	$1.1< \eta <2.5$		0.72 T·m at $\lvert\eta\rvert < 2$,
			0.36 T·m at $\lvert\eta\rvert < 1.3$.
Beam Beam Counters (BBC)	$3.1< \lvert\eta\rvert <3.9$	2π	trigger,
			start timing,
			Z-Vertex determination,
			reaction plane determination.
Zero Degree Calorimeter (ZDC)	±2 mrad		trigger.
Muon Piston Calorimeter (MPC)	$3.0 < \lvert\eta\rvert < 4.0$	2π	reaction plane determination.
Reaction Plane Detector (RXNP)	$1.0 < \lvert\eta\rvert < 2.8$		
Drift Chamber (DC)	$\lvert\eta\rvert <0.35$	$\pi/2\times2$	momentum determination,
			$\delta p/p = 0.4$ % at $p = 1$ GeV/c.
Pad Chamber (PC)		$\pi/2\times2$	track matching.
Time Expansion Chamber (TEC)		$\pi/2$	track matching.
Ring Imaging CHerenkov (RICH)		$\pi/2\times2$	Electron ID.
Aerogel Detector (AGEL)		$\pi/8$	High-p_T $\pi/K/p$ ID.
Time of Flight (TOF)		$\pi/4$	Hadron ID.
Lead Scintillator (PbSc)	$\lvert\eta\rvert <0.35$	$\pi/2+\pi/4$	Energy and Position,
Lead Glass (PbGl)		$\pi/4$	photon ID.
Muon Tracker (MuTr)	$1.15< \lvert\eta\rvert <2.44$	2π	muon/hadron separation.
Muon Identifier (MuID)			tracking for muons.

Table 3.2: Summary of the PHENIX detectors [49].

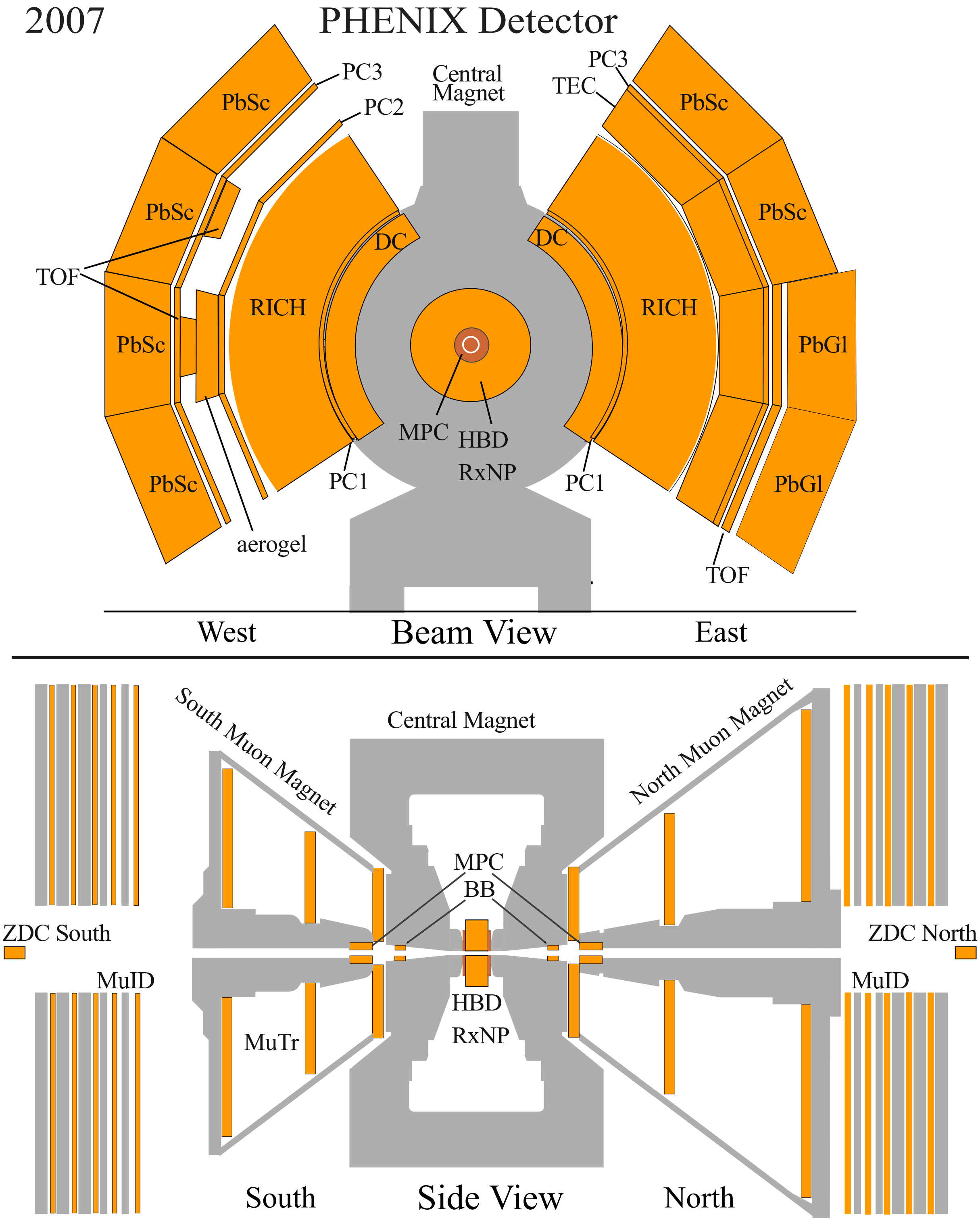

Figure 3.2: A layout of the PHENIX detectors in 2007. Upper panel shows a beam view. Two central arms and central magnet are shown. Lower panel shows a side view. Two muon arms, central magnet and muon magnet are shown.

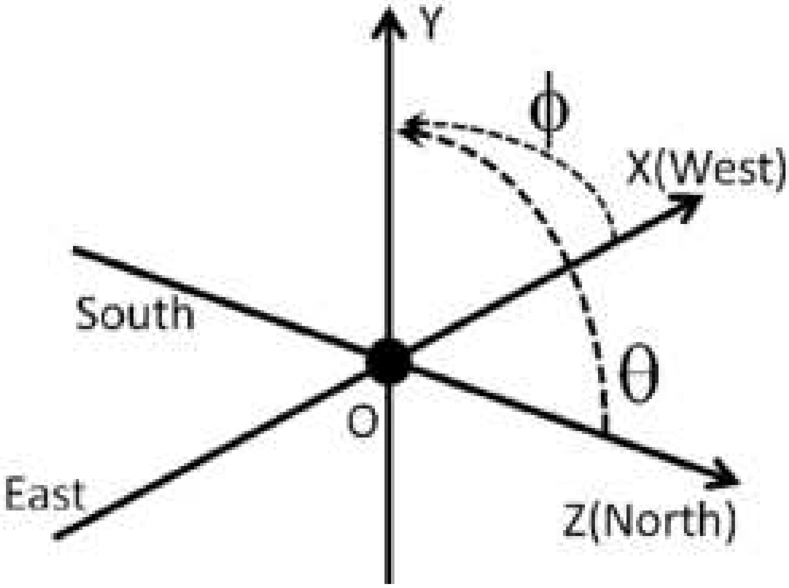

Figure 3.3: A definition of global coordinate system used in the PHENIX experiment.

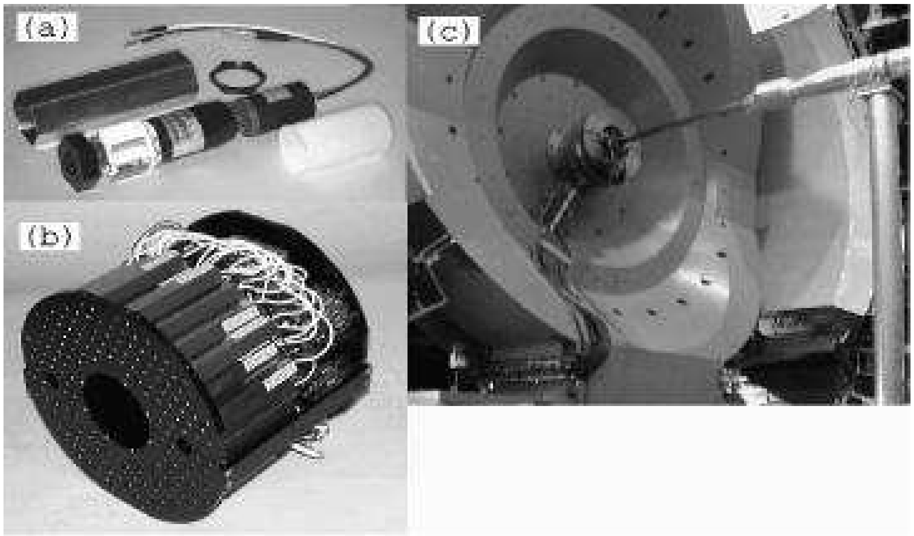

Figure 3.4: (a) Single BBC consisting of a 1 inch mesh dynode phototube mounted on a 3 cm quartz radiator; (b) A BBC array comprising 64 BBC elements; and (c) The BBC mounted on the PHENIX detectors is shown. The beam pipe shown in the middle of the picture. The BBC is installed on the mounting structure behind the central spectrometer magnet [50].

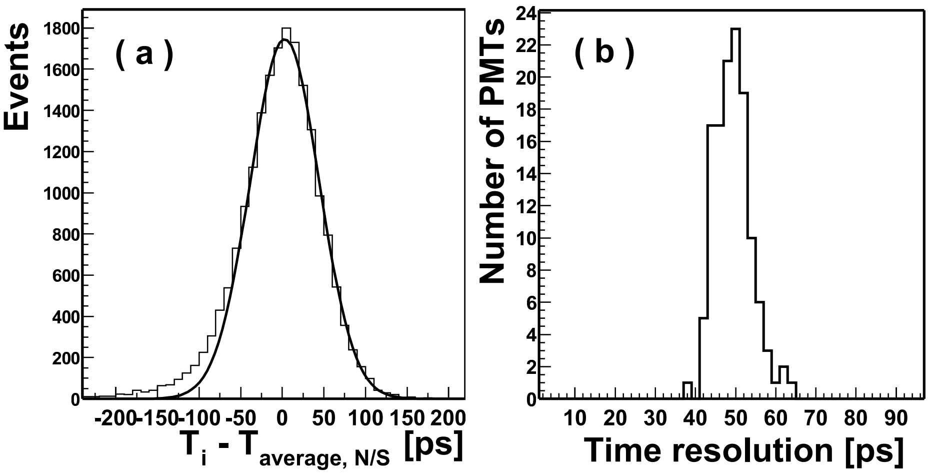

Figure 3.5: (a) The distribution of the timing deviation for a typical BBC element from the averaged hit timing of all BBC element. (b) The profile of the timing resolution for each BBC element [50].

where z_{N-S} represents a distance between the BBCs located at north and south sides, T_N and T_S are the measured average time of arriving particles at north and south sides, respectively. Figure 4.2 shows the distribution of Z-vertex positions reconstructed by the BBCs. As shown in Fig. 3.5, the timing resolution of a single BBC element is 52±4 ps (RMS) under the real experimental conditions.

Zero-Degree Calorimeter

The Zero-Degree Calorimeter (ZDC) are the common trigger device among the four RHIC experiments [51]. The ZDC is a hadron calorimeter designed to detect neutrons and measure their total deposited energy. Figure 3.6 shows the layout of the ZDC. Two ZDCs are placed at $z_{ZDC} = \pm 18.25$ m from the interaction point and just behind the DX dipole magnet. The angular acceptance of the ZDC is $|\theta < 2|$ mrad. The DX dipole magnets serve to bend the incoming beams to the colliding region and the outgoing beams to the collider beam line. Since the DX dipole magnet can bend charged particles, only the neutron can reach to each ZDC. Therefore, each ZDC provides the energy measurement of the forward neutrons which are not bounded by Coulomb excitation or evaporated from unstable spectators produced by heavy-ion collisions.

Each ZDC is mechanically subdivided into three identical modules with two interaction lengths each. The mechanical design of one module is shown in Fig. 3.7. The active medium is clear PMMA fibers ($\phi = 0.5$ mm) interleaved with 45 degrees along to the beam to align the optical fibers with the Cherenkov angle for forward particles in the shower. The fibers are connected to a phototube (Hamamatsu R329-2). Taking the correlation between the north and south sided ZDC provides the background rejection due to single

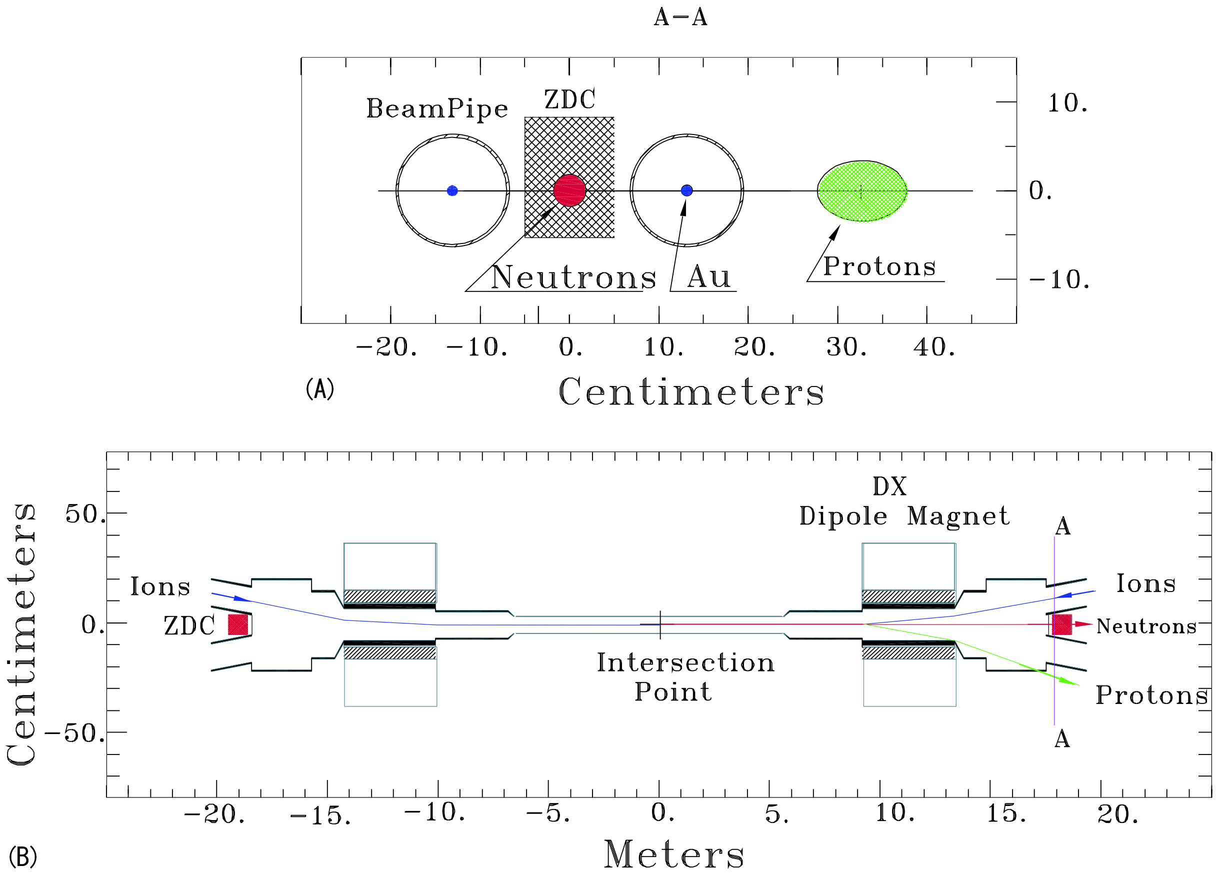

Figure 3.6: A plan view of the collision region and (section A-A) a beam view of the ZDC location indicating deflection of protons and charged fragments with Z/A∼1 downstream of the DX dipole magnet.

beam interaction with the residual gas in the beam pipe. The energy resolution of the ZDC for 100 GeV neutrons is about 21 %. The time resolution is about 120 ps and it corresponds to the Z-vertex resolution of about 2.5 cm for 100 GeV neutrons.

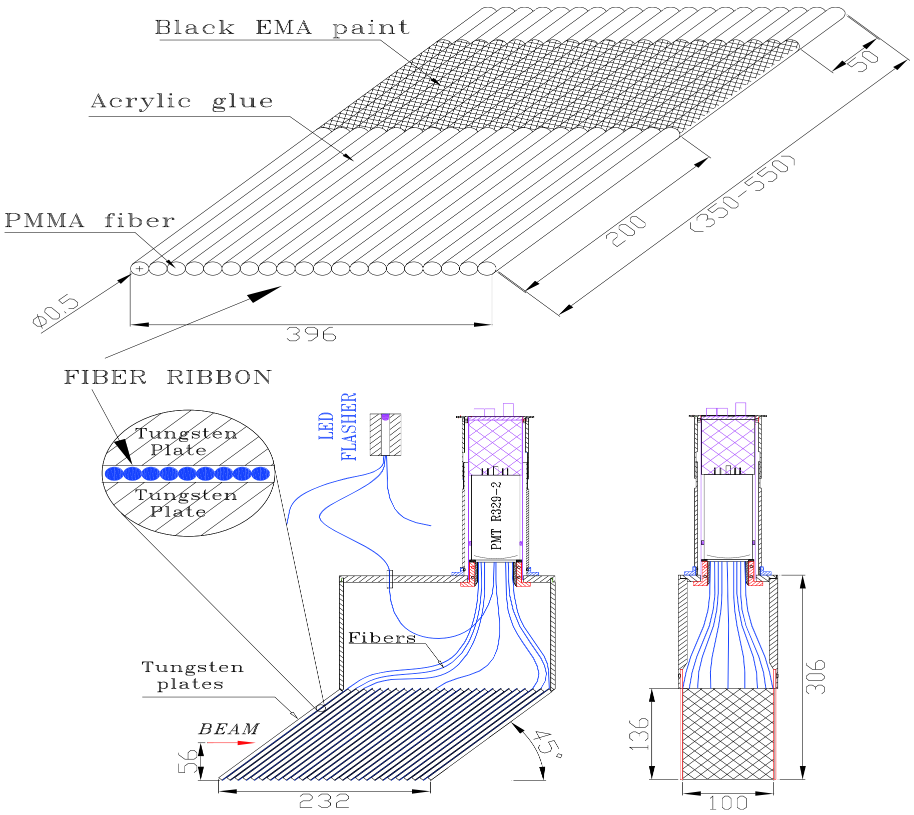

Figure 3.7: Mechanical design of the production tungsten module. The unit is a millimeter.

3.2.2 PHENIX Central Arm

Each of the two central arms covers the pseudo-rapidity range of $|\eta| < 0.35$ and 90 degrees in azimuthal angle. As shown in the upper panel of Fig. 3.2, each arm consists of the layers of subsystems for tracking, particle identification and calorimetry. The west arm is composed of drift chambers (DC), pad chambers (PC1), ring imaging Cherenkov detectors (RICH), pad chamber (PC2), Aerogel detectors (AGEL), Time-Of-Flight (TOF), pad chambers (PC3) and lead-scintillator calorimeters (PbSc). The east arm is composed of similar detectors as the west arm. There are no PC2 and AGEL, but in addition, two sectors of Time-Of-Flight (TOF) systems, four layer of time expansion chambers (TEC), two sectors of PbSc and two sectors of lead-glass calorimeters (PbGl). The radial distances from the beam line for each detector are summarized in Table 3.3 and 3.4.

West Arm	Radial Distance
DC	2.02–2.46 m
PC1	2.47–2.52 m
RICH	2.5–4.1 m
PC2	4.15–4.21 m
AGEL	4.3–4.5 m
PC3	4.91–4.98 m
PbSc	5.07–6.0 m

Table 3.3: Radial distances from the beam line for a west arm.

East Arm	Radial Distance
DC	2.02–2.46 m
PC1	2.47–2.52 m
RICH	2.5–4.1 m
TEC	4.1–4.8 m
TOF	5.06 m
PC3	4.91–4.98 m
PbSc (PbGl)	5.07 m (5.4 m)

Table 3.4: Radial distances from the beam line for a east arm.

A magnetic field is produced by the Central Magnet for measuring momentum of the charged particles. Two concentric coils can provide an axial magnetic field of $\int Bdl$ =0.43–1.15 T·m. In order to reduce the influence of the magnetic field on the several detector components, such as the photomultiplier tube, the exterior distance at the radial distance of $r > 2$ m from the vertex is required to be small. This requirement is satisfied with an appropriate arrangement of the flux return yoke, less than $\int Bdl$ =0.01 T×m at $\eta = 0$. The characteristics of each subsystem (tracking, particles identification and calorimetry) are discussed briefly in the following sections.

3.2.3 Tracking System

For the analysis of charged particle, the reconstruction of tracking starts at the DC. The DC measures the deflection of charged particles in the magnet field with a position resolution of about 150 μm in the $r - \phi$ plane. It provides a momentum resolution of $\delta p/p$ =0.7%⊕1.0 %×p (GeV/c) for charged pions.

The tracking information obtained using the DC is utilized for pattern recognition through the detectors of the central arms, such as the PC and TEC. The PCs are multi-wire proportional chambers and the TEC is composed of a set of 24 large multi-wire tracking chambers. Detailed technical information of the tracking subsystems are summarized in Ref. [52].

3.2.4 Charged Particle Identification

One of the main feature of the PHENIX detectors is excellent capability of electron identification up to high p_T. The RICH plays a major role for the electron identification with velocities larger than the speed of light in the gaseous radiator where Cherenkov photons are emitted with a light cone. The light cone is appeared as a ring shape on the RICH mirror system, and the Cherenkov light is reflected onto photomultipliers. With CO_2 gas at atmospherical pressure and 20 $^\circ C$ (its index is 1.000410), a charged particle with $\beta\gamma > 35$ emits Cherenkov photons. Its threshold corresponds to the momentum of 18 MeV/c for electrons and 4.9 GeV/c for pions.

The TOF has timing resolution of about 100 ps, which allows to distinguish at momenta up to 4 GeV/c between kaons and protons with 4 σ separation and at momenta up to 2.4 GeV/c between pions and kaons with 4 σ separation. Since the TOF system is installed only in front of the lead-glass calorimeter, the identification of charged particles is also made with a time-of-flight measurement in the lead-scintillator calorimeter which has a nominal timing resolution of approximately 270 ps.

The AGEL consists of $22(z) \times 11(\phi) \times 12(r)$ cm^3 Aerogel with a refractive index of about 1.01, an integration cube and two 3-inch phototubes. The intermediate refractive index of Aerogel enables us to distinguish pion and kaon, kaon and proton. The AGEL covers the region of $\pi/8(\phi) \times 0.7(\eta)$ in the west arm.

The TEC is a transition radiation detector and gives information of charged particle tracking and electron identification by dE/dx and transition radiation information. The TEC covers $\pi/2$ in azimuth and ± 0.35 in pseudo-rapidity. One TEC sector has an active area of 3.1–3.5 m$(z)\times$1.7–1.9 (ϕ) and consists of 6 individual chambers. Each chamber is build in two layers; a lower layer containing window support and radiator foils, and an upper layer containing the active elements of the wire chamber. The upper layer is filled with Xe/CO_2 mixed gas and is composed of a Cu-mylar cathode window, drift space of 3 cm, three wire planes (field, anode, field) oriented parallel to the Z-axis of the detector, and a final Cu-mylar cathode window. Detailed technical information of the particle indentification subsystems are summarized in Ref. [53].

3.2.5 Photon Identification

The two types of electromagnetic calorimeter; lead-scintillator calorimeter (PbSc) and lead-glass calorimeter (PbGl) are located at the end of central arms. With their fine segmentation of $\Delta\eta \times \Delta\phi \approx 0.01 \times 0.01$, both of calorimeters provide a good resolution for energy and position. Since the calorimeters are the main subsystem for the study in this thesis, the detail information of calorimeters are described in Sec. 3.3 and Ref. [54].

3.2.6 Data Acquisition System (DAQ)

The Level-1 trigger (LVL1) is responsible to select interesting events and provide the sufficient rejection of uninteresting events to reduce the data rate up to the level which can be handled by the PHENIX data acquisition (DAQ) system [55]. The DAQ system is accomplished through the pipelined and deadtimeless features of the detectors.

The PHENIX trigger system consists of two separate subsystems; the Local Level-1 (LL1) system and the Global Level-1 (GL1) system. The LL1 system directly communicates with the detectors such as the BBC and the EMCal. The input data from these detectors are processed by the LL1 algorithms to produce a set of reduced-bit input data for each RHIC beam crossing.

The PHENIX data acquisition (DAQ) system processes the signals from each detector subsystem, produces the trigger decision, and stores the triggered data. The size of zero-suppressed events are 160 kbytes for Au+Au collisions. The schematic of the DAQ is shown in Fig. 3.8.

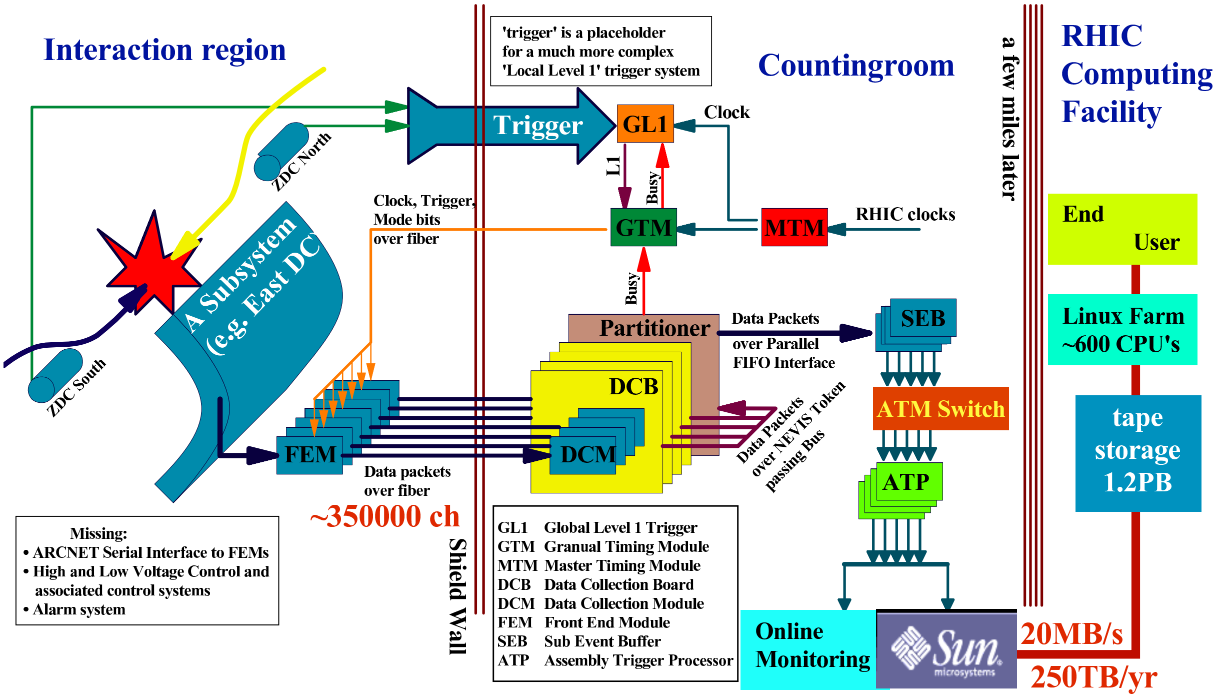

Figure 3.8: A schematic diagram of the PHENIX data acquisition system [55].

Overall control of the DAQ is provided by the Master Timing Module (MTM), the Granule Timing Module (GTM), and the GL1. The MTM receives the RHIC clock of 9.4 MHz and delivers it to the GTM and the GL1. If the LVL1 trigger accepts an event, an signal is sent to the GTM. The "accept" signal generated by the GTM is transmitted to the Front End Modules (FEMs) which are designed to convert the analog response of the detectors into the digitized signal. The GTM equips a fine-delay tuning of the clock with the step of ∼50 ps, in order to compensate the difference of times among the FEMs.

The data are stored up to 40 beam crossings to allow for the time needed to make the decision of the LVL1 trigger. After receiving the signal accepted as an event, each FEM starts to digitize the data. This is carried out for the elements for all detectors at every beam crossing synchronously with the RHIC beam clock.

The signals from each FEM are sent to the Data Collection Modules (DCMs) via optical fiber cables. The DCMs perform the data buffering, the zero suppression, the check of errors, and the data reformatting. The DCM sends the compressed data to the Event Builder (EvB). The EvB is the system which consists of 39 Sub Event Buffers (SEBs), an Asynchronous Transfer Mode (ATM) switch and 52 Assembly Trigger Processors (ATPs). The SEBs transfer the data from granule to the ATPs via the ATMs and perform the assembly of the event. Finally, the data is saved in the disk with the logging rate of 400 Mbytes/s at the maximum, and the data are used for the online monitoring.

3.3 The Electromagnetic Calorimeters

The electromagnetic Calorimeter (EMCal) is the device for detecting photons coming from π^0 The overview of the EMCal system, the detailed specification, and the basic performance are described in this section.

In the PHENIX central arm, two types of different EMCal are installed. The EMCals consist of 6 sectors of lead-scintillator calorimeter (PbSc) and 2 sectors of lead-glass calorimeter (PbGl). The basic parameters are summarized in Table 3.5. One super-modules for PbSc (PbGl) consists of 36 (24) modules, and one sector for PbSc (PbGl) consists of 18 (192) super-modules and total of 8 sectors are installed in the PHENIX central arm.

	PbSc	PbGl
Type	66 Scintillator + Lead	Cherenkov
Radiation length (X_0) [mm]	21	29
Moliere radius [mm]	30	37
Cross section of a channel [mm^2]	55.35×55.35	40×40
Depth [mm (X_0)]	375 (18)	400 (14)
$\Delta\eta$ of a channel	0.011	0.008
$\Delta\phi$ of a channel	0.011	0.008
Number of channels per super-module	144 (12×12)	24 (4×6)
Number of super-module per sector	18 (3×6)	192 (12×16)
Number of total sectors	6	2
Number of total channels	15552	9216

Table 3.5: Summary of the EMCal detectors.

The PbSc is a sampling calorimeter of shashlik type, while the PbGl is a calorimeter of Cherenkov detection. The features are quite different for the granularity, energy resolution, linearity, response to hadrons, timing, and shower shape.

The PbGl has the better granularity and energy resolution, while the PbSc has the better linearity and timing resolution, and the response to hadrons is better understood. The physics results obtained with each EMCal can be cross-checked by themselves due to having the different properties of EMCals. In order to cover various physics programs, measurement of photons and π^0s in p+p and Au+Au collisions and measurement of which includes weak bosons in polarized protons collisions, the EMCal is designed to satisfy the following requirement.

- Coverage of a wide energy range extending from a few hundreds MeV to 80 GeV.
- Energy accuracy within 2 % to measure the cross sections of single photons and π^0s with an accuracy within 10 %
- Fine granularity of $\Delta\eta \times \Delta\phi \approx 0.01 \times 0.01$ to achieve an occupancy of less than 20 % in the central Au+Au collisions

3.3.1 Lead-Scintillator Calorimeter

The PbSc electromagnetic calorimeter is a shashlik-type sampling calorimeter made of alternating tiles of lead and scintillator. As shown in Fig. 3.9, the basic building block is a module consisting of four (optically isolated) towers which are readout individually.

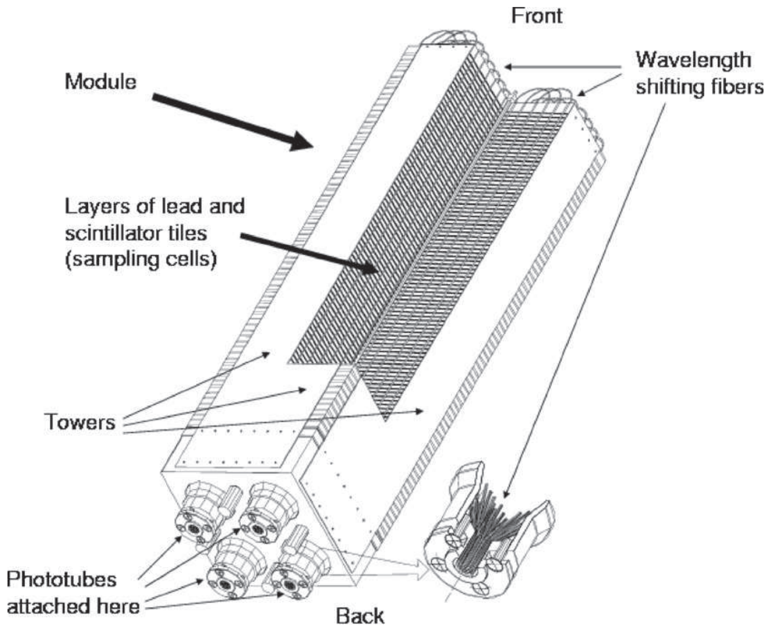

Figure 3.9: A cross section of lead-scintillator calorimeter showing a stack of scintillator and lead plates, readout of wavelength shifting fiber, and leaky fiber inserted in the central hole.

Figure 3.9 shows the interior view of a module block. Each PbSc tower contains 66 sampling cells consisting of alternating tiles of lead (0.4 cm) and scintillator (0.4 cm). The scintillator is made of Polystyrene (1.5 % PT, 0.01 % POPOP). The edge of the tiles are plated with Al. These cells are optically connected with the 36 longitudinally penetrating wavelength shifting fibers to collect light. The collected light is read out by FEU115M phototubes at the back of the towers. The diameter of the phototube is 30 mm. Thirty six modules are attached to a backbone and held together by welded stainless-steel skins on the outside to form a rigid structure called a super-module. Detailed of the design and method of construction of the PbSc are described in Ref. [54].

3.3.2 Calibration and Monitoring System

The calibration and monitoring of the EMCal are performed with a UV laser which supplies light to the calorimeter through a series of optical splitter and fibers.

The block diagram of the monitoring system is schematically shown in Fig. 3.10. The YAG-laser light is split by three steps and delivered into total of 3888 modules. The amplitude of the laser is monitored by a phototube and photo diodes in all the light splitters. Since the operation condition has changed from the time of construction and the gain drift during the data taking should be corrected, this laser calibration system is established to normalize the initial energy calibration, which has been obtained by utilizing the energy deposited by cosmic ray for all towers during construction. The gain of the amplifier for the photo diodes is monitored by test pulses.

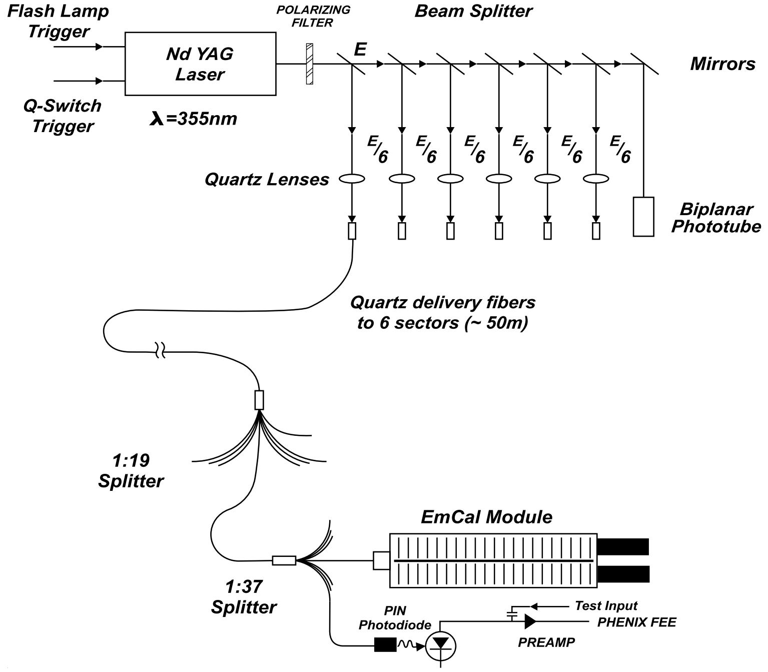

Figure 3.10: A laser light distribution and the monitoring system.

3.3.3 Test Beam Performance of PbSc Calorimeter

Since PbSc is a major detector which is used for the π^0 analysis, the fundamental characteristics is described in this section in detail. The basic performance, energy resolution, linearity, position resolution and hadron rejection has been measured at BNL in the energy range up to 7 GeV. In order to extend the energy range up to 80 GeV, the beam test has been performed at the CERN H6 beam line in 1998.

Linearity and Resolution of Energy

The measured energy divided by the energy of electron beam as a function of the incident beam energy in the calorimeter is shown in Fig. 3.11. The Data are normalized at 1 GeV. The attenuation length of the finite light in the WS fibers is 100 cm, and it is a major contributor to the response non-uniformity at the low energies of the energy scale. Other contributors are the energy leakage from the calorimeter via the front and back surfaces and the fluctuation of the shower depth.

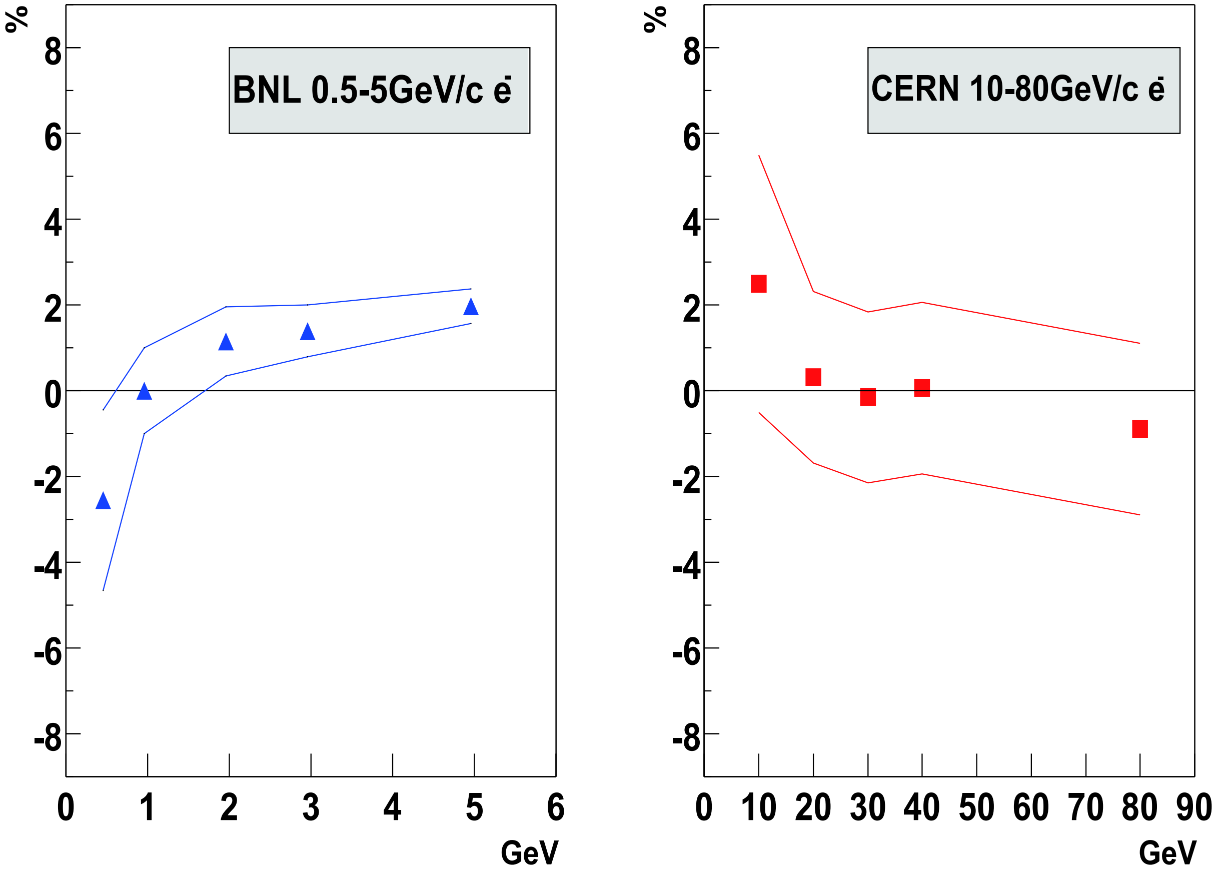

Figure 3.11: The energy linearity of PbSc calorimeter obtained from both of beam tests at BNL (left) and CERN (right). The region between solid lines show the total systematic uncertainties in the measurement.

At high momenta, the positive effect of the light attenuation in the fibers is overcompensated by the negative effect of energy leakage from the back of the calorimeter. As a result, the effect of non-linearity is about a factor of two lower than what one would expect from the effect of light attenuation alone. The non-linearity due to the attenuation in the fibers is corrected with the following form,

$$\exp\Big(\frac{x_0}{\lambda}\ln(E)\Big) = E^{x_0/\lambda}, \tag{3.3}$$

where λ is 120 cm. The correction of both effects are applied to the data. Figure 3.12 shows that the energy resolution is obtained using electron and positron beam tests at CERN and BNL. The data can be fitted with linear or quadratic expressions. Only statistical uncertainties are taken into account in the fits. An additional systematic uncertainty of 1 % is estimated based on the reproducibility of the measurements at each energy range. The energy resolution of one PbSc calorimeter obtained from the fits are given as,

$$\begin{aligned} \frac{\sigma_E}{E} &= 1.2\ \% + \frac{6.2\ \%}{\sqrt{E(GeV)}} \quad \text{(a linear expression), and} && (3.4) \\ &= 2.1\ \% \oplus \frac{8.1\ \%}{\sqrt{E(GeV)}} \quad \text{(a quadric expression),} && (3.5) \end{aligned}$$

where $\oplus$ denotes a square of the quadratic sum, stands for $\alpha \oplus \beta = \sqrt{\alpha^2 + \beta^2}$. The angular dependence of the energy resolution is negligible. They are valid in the energy region of 0.5 GeV to 80 GeV within the systematic uncertainty of 1 %.

Position Resolution

Using electron and positron at the well-known impact position on the surface of the EMCal in the test beam, the position resolution is evaluated with the logarithmic method [56]. In the logarithmic method, the position X is determined by the following formula:

$$X = \frac{\sum_{i=1}^{N} C_i \cdot x_i}{\sum_{i=1}^{N} C_i}, \tag{3.6}$$

where x_i denotes a center of each channel in the horizontal direction. Similarly, Y is defined in the vertical direction. The weight coefficients, C_i, are given as,

$$\begin{aligned} R_i &= Max\Big[0, E_i/E_{\text{total}}\Big], && (3.7) \\ C_i &= Max[0, \log(R_i) + C_0], && (3.8) \end{aligned}$$

where E_{total} is a total energy, $E_{\text{total}} = \sum_{i=1}^{N} E_i$, and C_0 is a constant. A larger value of α and β is expressed by $Max[\alpha, \beta]$.

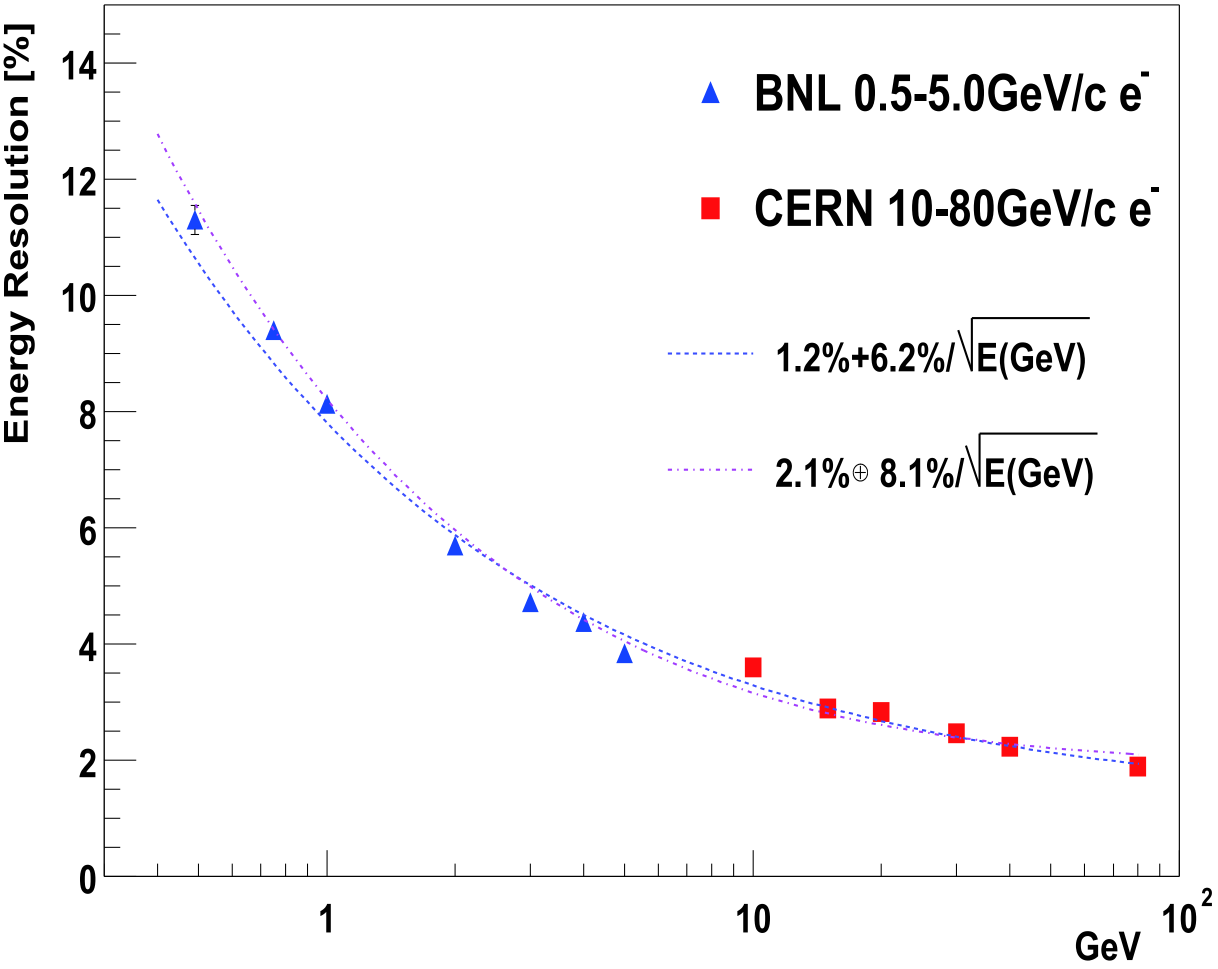

Figure 3.12: The energy resolution of one PbSc calorimeter given by the beam tests. A dashed line and a dash-dotted line show the result obtained by a linear formula and a quadric formula, respectively.

The deviation in a short period shows that the systematic uncertainty is 2 mm in the logarithmic method . The position resolution of one PbSc depends on the incident energy of photon E and incident angle θ, and it is given as,

$$\begin{aligned} \sigma_x(E,\theta) &= \sigma_0(E) \oplus \Delta \times \sin\theta, & (3.9) \\ \sigma_0(E) &= 1.55\ [\mathrm{mm}] \oplus \frac{5.7\ [\mathrm{mm}]}{\sqrt{E(\mathrm{GeV})}}, & (3.10) \end{aligned}$$

where $\sigma_0(E)$ is a position resolution for normal incidence and $\Delta \sim L_{\mathrm{rad}} \sim 19$ mm. If photons hit on the face of the PbSc at the maximum incident angle of 20 degree, $\Delta \times \sin\theta$ is about 6.5 mm, and the position resolution for photon of 1 GeV is about 13 mm.

3.3.4 Lead-glass Calorimeter

The PbGl calorimeters were previously used in the WA98 experiment at CERN, where direct photons were observed for the first time in heavy ion collisions [57]. After the disassemble of the WA98 experiment, 9216 elements from the former LEDA1 calorimeters were transported to BNL and reassembled as two sectors of the EMCal in PHENIX. The PbGl is a Cherenkov detector (55 % PbO and 45 % SiO_2, and defractive index n is 1.648) with critical energy of $E_c = 16$ MeV. Though Cherenkov radiation is a negligible source of energy loss, it is very useful for detecting particles and measuring energy because the number of Cherenkov photons produced per unit length is constant, and the total length of all position and tracks in a shower produced by electrons are proportional to the energy of the primary particle.

Each sector of the lead-glass calorimeters consists of super-modules, each forming a self-contained detector with its own reference system as shown in Fig. 3.13. One super-module is composed of an array of four lead-glass modules, each module with a size of $4\times4\times40$ cm^3 is wrapped in reflecting Mylar foil and shrink tube.

The response of the PbGl calorimeter was studied extensively in test beams at the AGS in BNL and the SPS in CERN to investigate the performance of the device with respect to the energy, position and timing, their variation with energy and position, and incident angle. Figure 3.14 shows the measured energy resolution pf positron showers as a function of incident energy for various incident angles on the surface in the lead-glass calorimter. As a result, each characteristics is parametrized as following:

- Energy resolution

$$\frac{\sigma(E)}{E} = (0.8 \pm 0.1)\ \% \oplus \frac{(5.9 \pm 0.1)\ \%}{\sqrt{E(\mathrm{GeV})}} \tag{3.11}$$

- Position resolution

$$\sigma_x(E) = (0.2 \pm 0.1)\ \mathrm{mm} \oplus \frac{(8.4 \pm 0.3)\ \mathrm{mm}}{\sqrt{E(\mathrm{GeV})}} \tag{3.12}$$

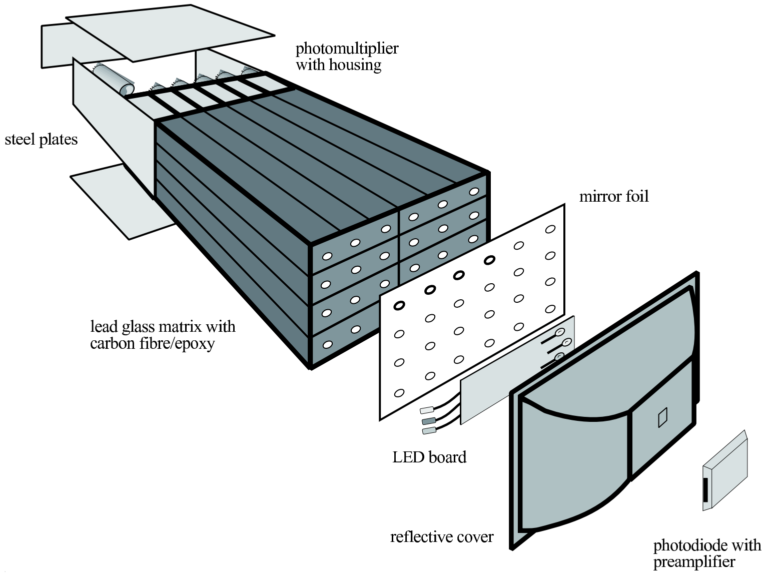

Figure 3.13: A schematic view of a super-module of lead-glass including the reference system.

3.3.5 Calorimeter Frond End Electronics

The readout electronics for the EMCal system conforms to the general PHENIX Frond End Electronics (FEE) scheme [55]; a periodic sampling synchronous with the RHIC Radio Frequency (RF) clock and the readout with pipelined, deadtimeless conversion

A negative-current pulse from each PMT in EMCal is processed as shown in Fig. 3.15.

There is no preamp or shaping stage other than passive integration. The 93 Ω register terminates the signal from the PMT, and the voltage profile at point-A shown in Fig. 3.15 simply follows the current profile from the PMT which is a pulse with less than the rise time of 5 ns. The charge is collected in the 500 pF capacitor and the voltage profile at point-B in Fig. 3.15 follows the integral of the current. The current pulse is a step function with the rise time of ∼100 ns. Each of these ASIC chips services four PMT channels and also contains the circuit of the fast trigger function.

In the measurement of the arrival time, the voltage pulse is discriminated, either in a leading-edge mode or a constant-fraction mode. The discriminator firing starts a voltage ramp generator. The ramp is stopped on the next edge of the RHIC clock providing a common-stop mode TAC for each channel. The ramp voltage is sampled and converted by the AMU/ADC.

The charge signal is put through a Variable Gain Amplifier (VGA), and the gain can be optimized remotely in the range between ×4 and ×12 with 5-bit resolution. The dynamic range of signal from the EMCal is quite large and expected deposit energy are from 0.02 GeV up to 15–30 GeV with a noise contribution from the electronics of no more than 0.1 % for large signals and 5 MeV for small signals. It is impossible to cover this

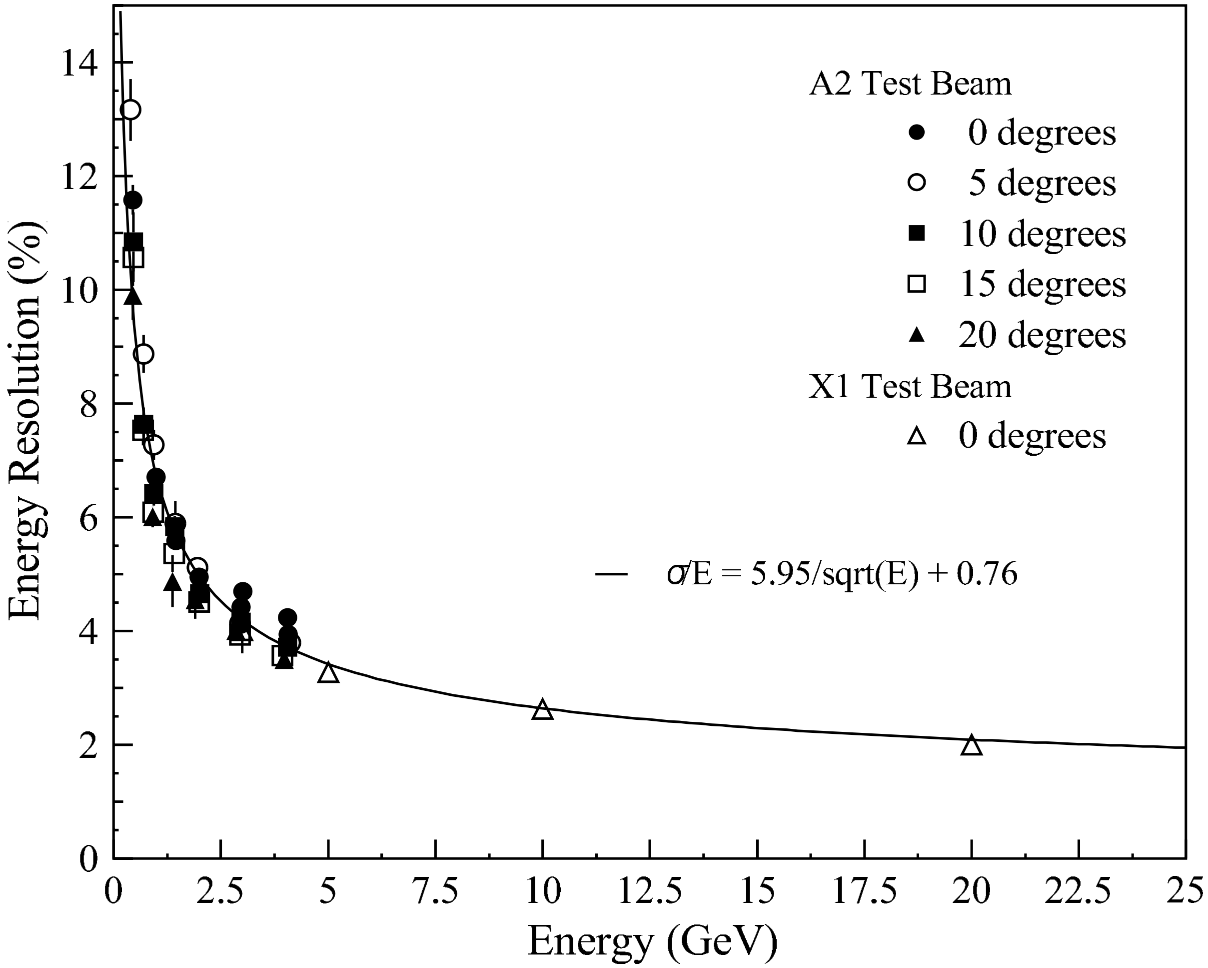

Figure 3.14: The energy resolution of a PbGl calorimeter as a function of incident energy.

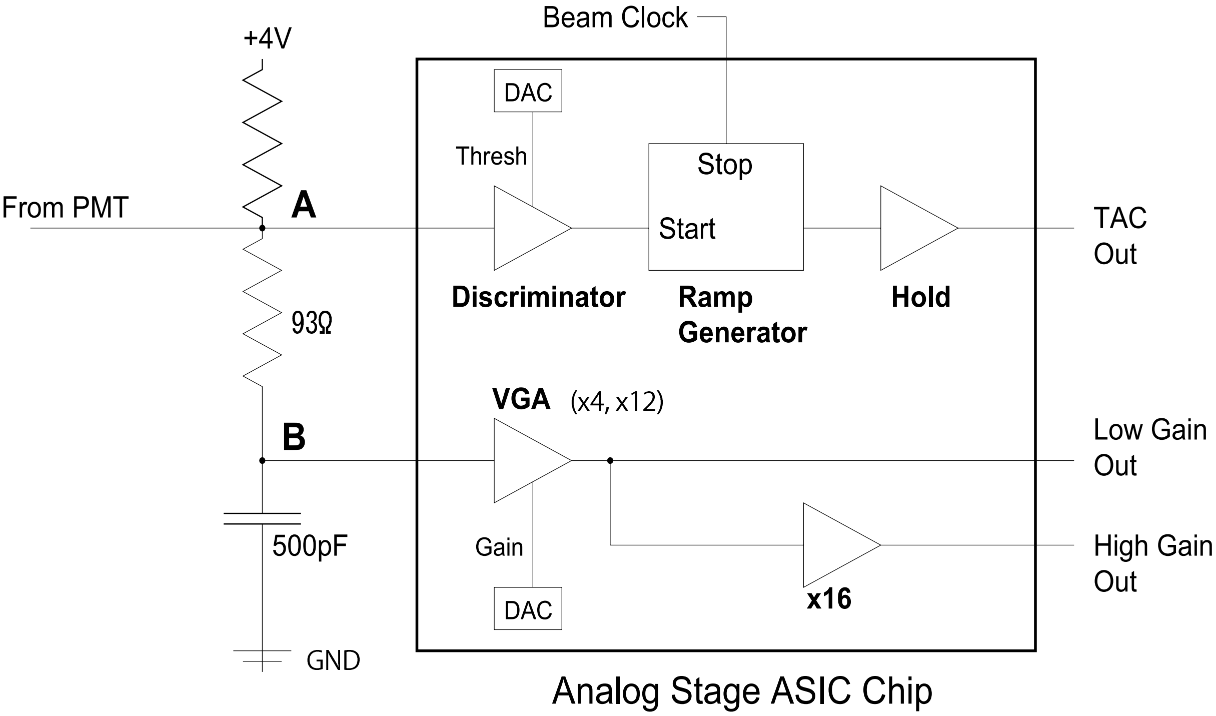

Figure 3.15: A block diagram of the circuit for measuring the energy and timing for EM-Cal. A signal from the PMT is used for timing and charge information with a termination of 93 Ω. All of the following analog processing stages up to ADC and TDC conversion are carried out within an ASIC chip [58].

wide range with a single 12-bit ADC conversion. Thus, the signal is amplified twice with two kinds of different levels of amplification. The signal from the low gain is obtained straight from the VGA and the signal from the high gain is obtained separately after a second stage of ×16 amplification.

The voltage waveforms from the high and low gain energy stages and the TAC for each channel are sampled once per RHIC clock tick and stored in a series of Analog Memory Units (AMU's) [55]. Each waveform is sampled into a ring buffer of 64 AMU's, effectively preserving it for 64 RHIC clock ticks or about 7 μs. Upon receiving a LVL1 accept signal, the FEE identifies the energy and the AMU cells of TAC corresponding to the event. The stored charges are taken out and converted in the ADC. To compensate the constant-offset voltage among AMU cells, two AMU cells are read out with "pre" and "post" in Fig. 3.16, where "pre" corresponds to the time before the signal starts, and "post" corresponds to the time after the integrated signal reaches its maximum. Finally, the integrated charge stored in AMU memory cell is obtained by the subtraction of ADC values in "pre" and "post" cell. The formatted data for each event is sent to a PHENIX Data Collection Module (DCM) via G-LINK.

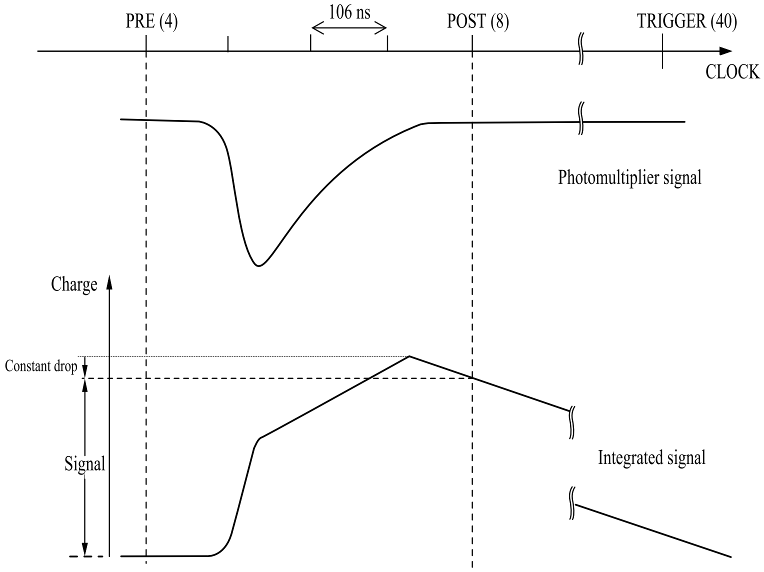

Figure 3.16: A schematic of the AMU sampling against with timing. The upper figure is an input signal and the bottom figure is an integrated charge in an AMU cell.

3.4 The Reaction Plane Detectors

The precise determination of the reaction plane is required for measuring the azimuthal angle of particles emitted at collisions. The PHENIX can utilize several detectors to measure the reaction plane of collisions. Beam Beam Counter (BBC) has been primarily used for the determination of the reaction plane before the installation of Muon Piston

Calorimeter (MPC) and Reaction Plane Detector (RXNP).

3.4.1 Beam Beam Counter

The performance of this detector is described in Section 3.2.1.

3.4.2 Muon Piston Calorimeter

In 2006, Muon Piston Calorimeter (MPC) was installed to measure π^0, η and jet in the forward rapidity region [59]. The MPC is a compact electromagnetic calorimeter installed in the holes of the south and north muon pistons indicated as Fig. 3.17. The MPCs are located at ±220 cm along the beam axis and is covering from 5 cm to 22.5 cm for the radial direction. The MPCs cover the rapidity range of $3.0 < |\eta| < 4.0$. The hole is 45.05 cm in diameter and 43.1 cm depth. There is a steel beam pipe which runs through the center of the hole, as shown in Fig. 3.17. It is 7.62 cm in diameter.

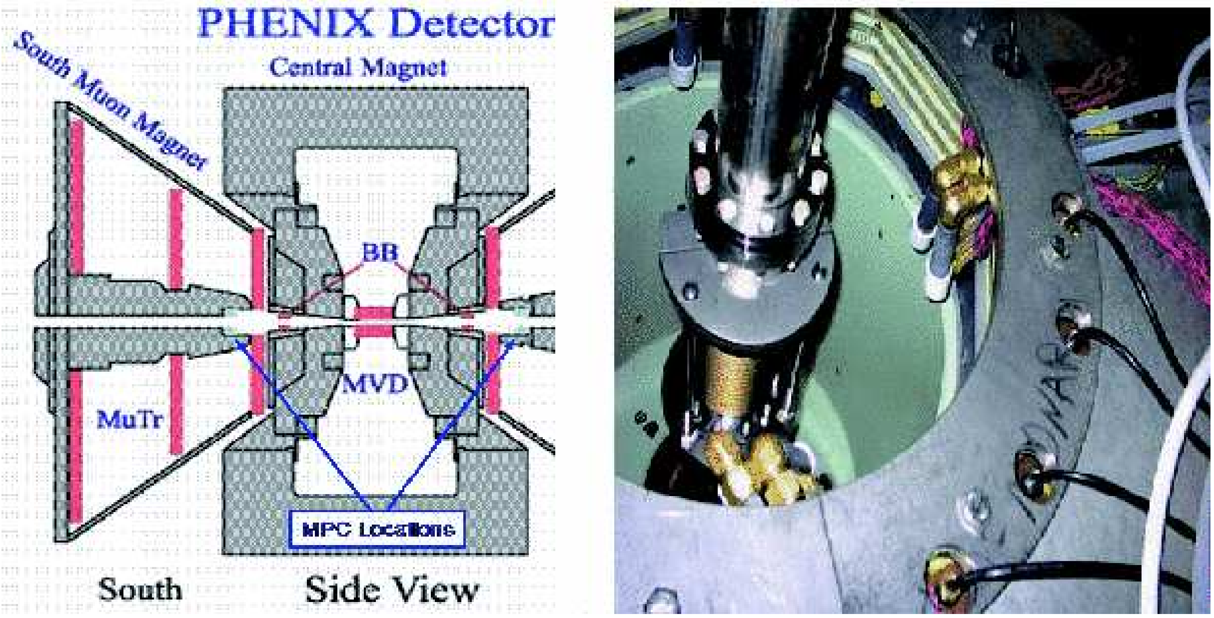

Figure 3.17: A side view of the MPC location in the PHENIX detectors(left). The MPC for each arm is installed in the north and south muon piston hole. The right picture show a muon piston hole.

Properties of MPC

Figure 3.18 shows a schematic of the installed crystals. Figure 3.19 show a lead-tungstate ($PbWO_4$) crystal, an APD, a preamp and its holder. The MPC consist of 240 $PbWO_4$ crystals for each arm. The crystals have been produced to use in the PHOS detector in the LHC-ALICE experiment. The photons from crystals are read out with the Avalanche

Photo-Diode (APD), Hamamatsu S8664-55, which has an active area of 5×5 mm^2 and charge-sensitive pre-amplifiers as used with LHC-ALICE experiment.

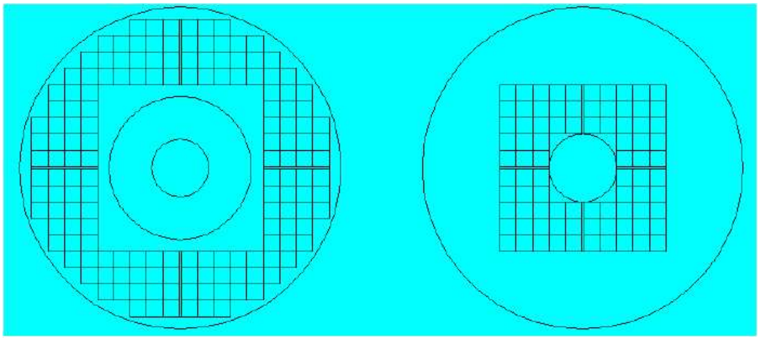

Figure 3.18: A design of the MPC segmentation. The left figure shows the fixed outer detector. The outer circle represents the piston hole, the next hole is the bellows and the smallest circle is the beam pipe. The movable inner part of the MPC is shown on the right [59].

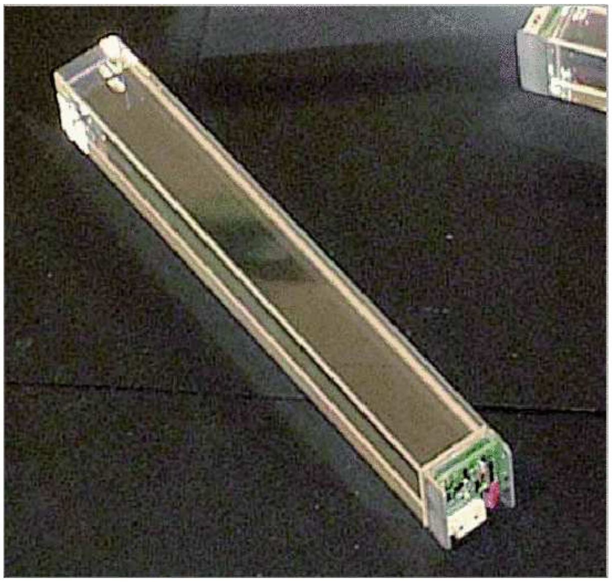

Figure 3.19: A $PbWO_4$ crystal with a attached APD, a preamplifier and a holder [59].

The properties of the crystals are summarized in Table 3.6. The energy resolution is measured by National Synchrotron Light Source (NSLS) in BNL, Hiroshima University group, and Kurchatov University group. The energy resolution of MPC is given as,

$$\frac{\Delta E}{E} = \frac{6\ [\%]}{\sqrt{E(GeV)}} \oplus \frac{230 \sim 330\ [\text{MeV}]}{E(GeV)}, \tag{3.13}$$

where the second term of 230∼330 (MeV)/E comes from the electronics of the MPCs (∼180 MeV) and the physics background (∼50–150 MeV).

Density	8.28 g/cm^3
Size	$2.2 \times 2.2 \times 18$ cm^3
Weight	721.3 g
Moliere radius	2.0 cm
Radiation length	0.89 cm
Interaction length	22.4 cm
Light yield	∼10 p.e./MeV at 25 °C
Refractive Index	2.16

Table 3.6: The properties of a $PbWO_4$ crystal [59].

Online Monotoring and Calibration

The gain of the APD depends on both temperature and bias voltage, and the temperature of $PbWO_4$, and there is the gain variation by about 2 % from the APD. The temperature of the MPC is monitored every 3–4 minites with thermocouples and this cariation is corrected.

A LED calibration system is implemented to correct for the effect of the light absorption which reduce the transmissivity of the crystal due to the crystal structure modified by the radiation damage.

3.4.3 Reaction Plane Detector

Reaction plane detector (RXNP) has been used since 2007. The RXNP cover a pseudorapidity range of $1.0 < |\eta| < 2.8$. The active area is composed of plastic scintillator, BC-412. The scintillator has a thickness of 20 mm and is located at $38 < |z| < 40$ cm. The lead with 20 mm thickness is put in front of the scintillator as a converter. The right panel in Fig. 3.20 shows the front view of the RXNP. The upper-left panel shows a enlarged illustration of the scintillator of the RXNP and the lower panel shows a side view of the scintillator of the RXNP. As shown in Fig. 3.20, the inner edge of the scintillator begin at $r=5$ cm and extend to $r=33$ cm. The RXNP is segmented into 12 sectors in azimuthal angle (ϕ). Each sector is further divided into two radial sections (green and light blue regions) corresponding to the rapidity regions of $1.0 < |\eta| < 1.5$ and $1.5 < |\eta| < 2.8$. In this thesis, the RXNP which is segmented at $1.0 < |\eta| < 1.5$ and $1.5 < |\eta| < 2.8$ is called the $RXNPout$ and $RXNPin$, respectively. Embedded fiber light guides, BCF92, connect the plastic scintillator to the mesh dynode PMTs, Hamamatsu R5924. The PMTs is located to the beam pipe at $r = 110$ cm and $z = 61$ cm.

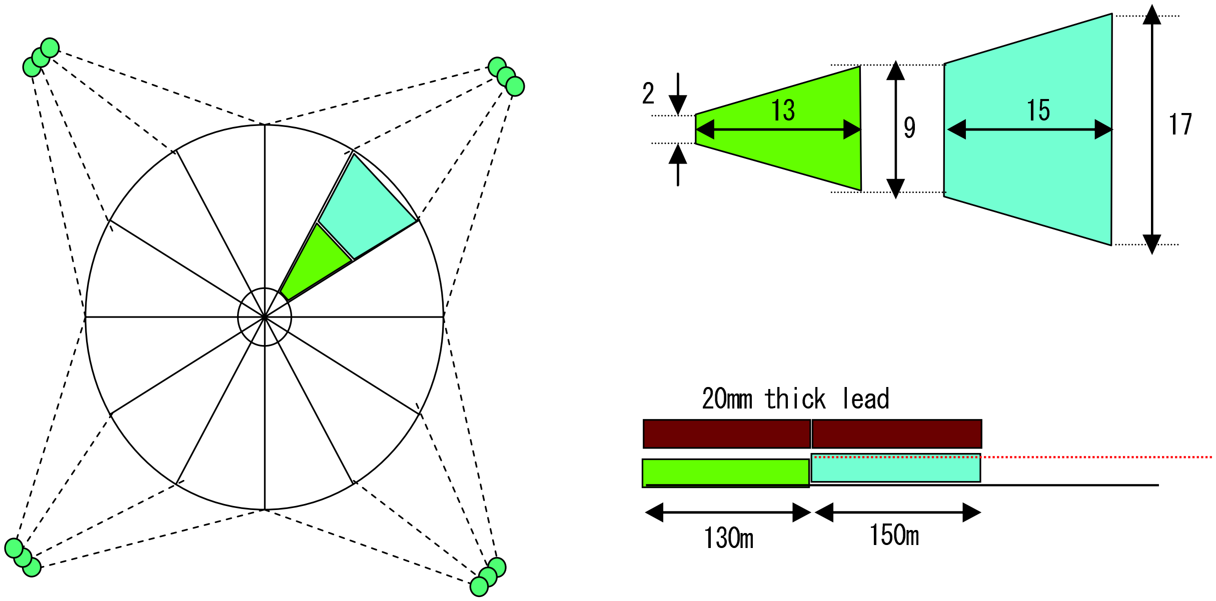

Figure 3.20: A front and side views of the reaction plane detector (RXNP) [60]. The right panel is a bird-eye view of the RXNP. The upper left panel is the front view of the two segmented RXNP and lower left panel is a side view of the RXNP.

Chapter 4

Run Condition

The analysis of π^0 uses the data collected by the PHENIX experiment during RHIC-Year2007 Run (in 2007) in Au+Au collisions at $\sqrt{s_{NN}} = 200$ GeV. The beam and trigger conditions are briefly described in this chapter.

4.1 Collisions of Au+Au at $\sqrt{s_{NN}} = 200$ GeV in 2007

During RHIC-Year2007 Run (Mar. 27, 2007–Jun. 26, 2007), the data in Au+Au collisions at $\sqrt{s_{NN}} = 200$ GeV were collected with the PHENIX detectors. The peak and averaged luminosity were 30×10^{26} $\mathrm{cm^2s^{-1}}$ and 10–14×10^{26} $\mathrm{cm^2s^{-1}}$, respectively. The delivered integrated luminosity as a function of date is shown in Fig. 4.1, and the recorded integrated luminosity is 813 $\mu\mathrm{b}^{-1}$.

4.2 Trigger Condition

4.2.1 Definition of Minimum Bias Trigger

The BBC LL1 trigger (BBCLL1) is an event trigger to record the collision data. The timing information of the BBCs is used to select events which occur in the beam crossing and within nominal interaction region ($|z| < 50$ cm) along the beam axis. The digitized timing information of both north and south of the BBCs is sent to the BBCLL1 modules which makes the trigger decision. PHENIX defines BBCLL1 as the "Minimum Bias" (MB) trigger which is used for taking minimum bias events. The MB trigger logic is defined as follows;

$$\text{Minimum Bias} \equiv (\text{BBCNS} \geq 2) \cap \text{ZDCNS} \cap (\text{Z}-\text{vertex} < 38 \text{ cm}), \tag{4.1}$$

where BBCNS$\geq$2 represents that at least two hits are required in both the north and south of the BBCs. ZDCNS represents that both the north and south of the ZDCs have at least one neutron hit. The Z-vertex obtained from the BBCLL1 trigger is required to be less than 38 cm. The collision vertex along the beam axis is calculated using by the BBC

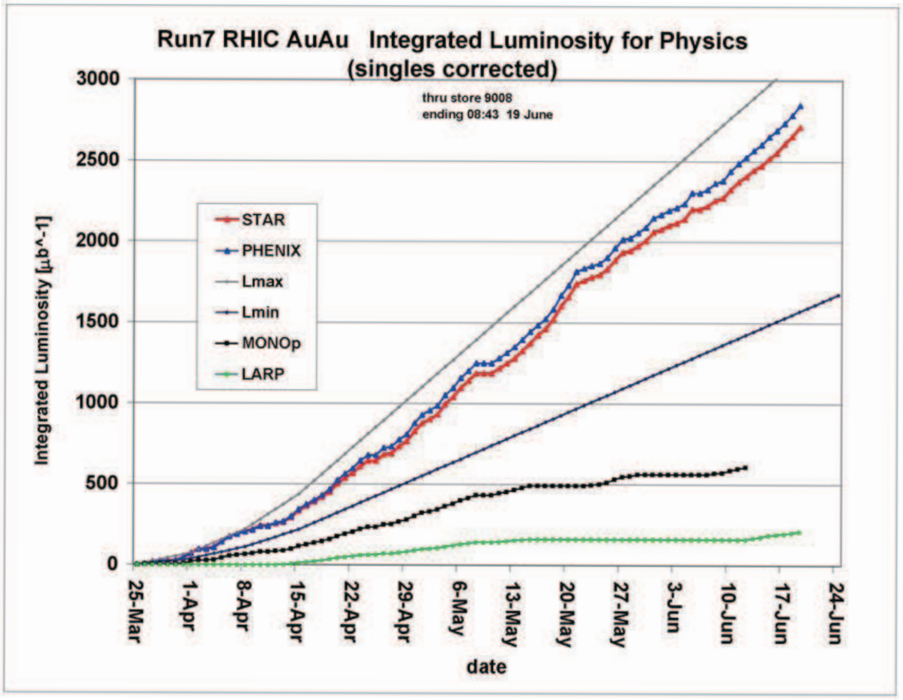

Figure 4.1: The delivered integrated luminosity of Au+Au collisions at $\sqrt{s_{NN}} = 200$ GeV in RHIC Year-2007 Run as a function of date.

information in the offline analysis and the determined position is called as **BbcZvertex**. The **BbcZvertex** distribution in Au+Au collisions at $\sqrt{s_{NN}} = 200$ GeV is shown in Fig. 4.2. Finally, the MB triggered data sample was about 5.1 billion events.

4.2.2 Minimum Bias Trigger Efficiency

The efficiency of inelastic Au+Au collisions for the MB trigger, ϵ_{MB}^{Au+Au}, was estimated by the full detector simulation with the event generators [61, 62] and from the charge distribution of the BBC in the real data using the negative binomial distribution (NBD) with the assumption of N_{part} scaling of the hit distribution of the BBC [63]. The generator, HIJING[64] is used to evaluate the MB trigger efficiency. The detector simulation was carried out with PHENIX Integrated Simulation Application (PISA) which is a simulator[65] of the PHENIX detector based on the GEANT3 libraries. As a result, the efficiency of inelastic Au+Au collisions by the MB trigger is evaluated to be $\epsilon_{\mathrm{MB}}^{\mathrm{Au+Au}} = 92.3 \pm 0.4$ (stat.) ± 1.6 (syst.) %.

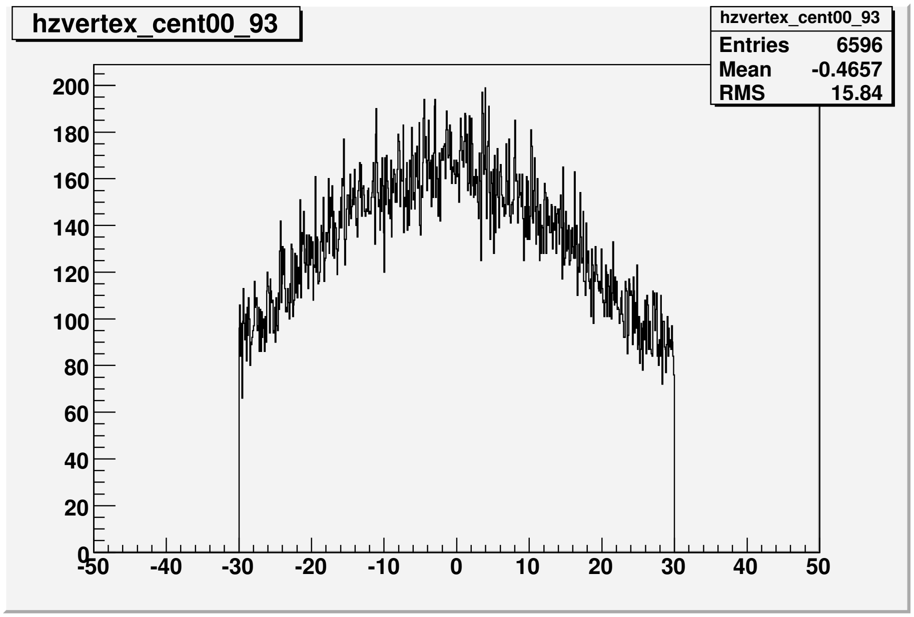

Figure 4.2: A distribution of **BbcZvertex** in the minimum bias Au+Au events at $\sqrt{s_{NN}} =$ 200 GeV in RHIC Year-2007 Run. An on-line vertex cut of $|z_{\mathrm{BBCLL1}}| < 38$ cm and an on-line vertex cut of |**BbcZvertex**| <30 cm is applied.

Chapter 5

Data Analysis

The main part of the data analysis is to obtain the invariant yield of neutral pion in Au+Au collisions at $\sqrt{s_{NN}} = 200$ GeV as function of azimuthal angle from the reaction plane in several centrality bins. The analysis procedure of π^0 will be described in this chapter.

5.1 Invariant Yield and Nuclear Modification Factor

A neutral pion via two photons is identified as a sharp peak in the invariant mass spectrum of the two photons, $M_{\gamma\gamma}$, calculated with the following equation,

$$M_{\gamma\gamma} = \sqrt{\left(\vec{P}_{\gamma}^{(1)} + \vec{P}_{\gamma}^{(2)}\right)^2} = \sqrt{2E_{\gamma}^{(1)} \cdot E_{\gamma}^{(2)} \cdot (1 - \cos\theta_{12})}, \tag{5.1}$$

where $\vec{P}_1$ and $\vec{P}_2$ are four-momenta of photon, θ is an opening angle between the two photons, and $E_{\gamma}^{1,2}$ are the total energy of photons. The opening angle θ is calculated from the hit positions of the two photons on the surface in EMCal.

The invariant cross section of neutral pion with the momentum p is expressed in terms of the rapidity y and the transverse momentum, $p_T \equiv \sqrt{p_x^2 + p_y^2}$, along the beam axis:

$$E\frac{d^3\sigma}{dp^3} = \frac{d^3\sigma}{d\phi dy p_T dp_T} = \frac{1}{2\pi p_T}\frac{d^2\sigma}{dp_T dy}, \tag{5.2}$$

where E and ϕ are a total energy and an azimuthal angle of π^0, respectively.

The invariant cross section of π^0 via the decay mode from two photons can be experimentally extracted as follows:

$$\frac{BR}{2\pi p_T}\frac{d^2\sigma}{dp_T dy} = \frac{1}{2\pi p_T}\frac{N_{\pi^0}(p_T)}{\int Ldt \cdot \epsilon(p_T) \cdot \Delta p_T \cdot \Delta y}, \tag{5.3}$$

where BR is a branching ratio of π^0 to 2γ and its ratio is about 98.8 %, N_{π^0} is the number of π^0 reconstructed by two photons, ϵ is an overall efficiency including the acceptance,

Δy is a rapidity bin width and is set to $\Delta y = 1$, Δp_T is a p_T bin width, and $\int Ldt$ is an integrated luminosity.

The integrated luminosity, $\int Ldt$, can be expressed using the number of minimum bias (MB) triggered events, N_{MB}:

$$\int Ldt = \frac{N_{MB}}{\sigma_{\mathrm{Au+Au}} \cdot \epsilon_{MB}^{\mathrm{Au+Au}}} = \frac{N_{MB}}{\langle N_{coll}^{MB} \rangle \cdot \sigma_{p+p} \cdot \epsilon_{MB}^{\mathrm{Au+Au}}}, \tag{5.4}$$

where $\sigma_{\mathrm{Au+Au}}$ and σ_{p+p} are the cross sections of inelastic Au+Au and $p+p$ collisions, $\epsilon_{MB}^{\mathrm{Au+Au}}$ and $\langle N_{coll}^{MB} \rangle$ are the MB trigger efficiency and the number of binary collisions for MB Au+Au collisions, respectively. The cross section of inelastic $p+p$ collisions triggered by the MB trigger is $\sigma_{p+p} \times \epsilon_{MB}^{p+p} = 23.0 \pm 2.2$ mb [66]. The estimation of $\epsilon_{MB}^{\mathrm{Au+Au}}$ and $\langle N_{coll} \rangle$ for Au+Au collisions is described in Sec. 5.4.2.

The invariant yield of π^0 is defined as,

$$\begin{aligned} \frac{BR}{2\pi p_T}\frac{d^2N_{\pi^0}}{dp_Tdy} &= \frac{1}{2\pi p_T}\frac{N_{\pi^0}(p_T)}{N_{\mathrm{MB}} \cdot \Delta p_T \cdot \Delta y \cdot \epsilon(p_T)} && (5.5) \\ &= \frac{1}{\sigma_{\mathrm{Au+Au}} \cdot \epsilon_{\mathrm{MB}}^{\mathrm{Au+Au}}} \times \frac{BR}{2\pi p_T}\frac{d^2\sigma}{dp_Tdy}, && (5.6) \end{aligned}$$

The integrated yield of π^0 is calculated as follows:

$$BR\frac{dN_{\pi^0}}{dy} = BR\sum_{p_T}\frac{d^2\sigma}{dp_Tdy}\Delta p_T. \tag{5.7}$$

The nuclear modification factor, R_{AA}, is used to quantify the difference between the superposition of nucleon-nucleon collisions and a nucleus-nucleus collisions. The definition of R_{AA} is given as,

$$\begin{aligned} \mathrm{R}_{AA}(p_T) &= \frac{BR\frac{d^2N_{\pi^0}^{\mathrm{Au+Au}}}{dp_Tdy}}{BR\frac{d^2\sigma^{p+p}}{dp_Tdy} \times T_{AA}} = \frac{BR\frac{d^2N_{\pi^0}^{\mathrm{Au+Au}}}{dp_Tdy}}{\langle N_{coll}\rangle BR\frac{d^2N_{\pi^0}^{p+p}}{dp_Tdy}}, && (5.8) \\ \mathrm{R}_{AA} &= \frac{BR\frac{dN_{\pi^0}^{\mathrm{Au+Au}}}{dy}}{BR\frac{d\sigma^{p+p}}{dy} \times T_{AA}} = \frac{BR\frac{dN_{\pi^0}^{\mathrm{Au+Au}}}{dy}}{\langle N_{coll}\rangle BR\frac{dN_{\pi^0}^{p+p}}{dy}}, && (5.9) \\ T_{AA} &\equiv \frac{\langle N_{coll}\rangle}{\sigma^{p+p}}, && (5.10) \end{aligned}$$

where T_{AA} is called as a nuclear overlap function.

The nuclear modification factor R_{AA} is the ratio of the π^0 yield in Au+Au collisions to the yield of π^0 in $p+p$ collisions scaled by the average number of binary collisions. If there is no medium effect such as a jet quenching on the π^0 production in Au+Au collisions, the π^0 production in Au+Au collisions will be described by the superpositions of independent nucleon-nucleon collisions, and the R_{AA} should be unity.

The N_{MB}, $\epsilon(p_T)$ and $N_{\pi^0}^{\mathrm{Au+Au}}$ in Eq. 5.5 are observables to obtain the invariant yield and R_{AA} of π^0. The analysis schemes are summarized as follows:

- The number of MB triggered events
  The N_{MB} is determined by the quality assurance for selecting good runs, and this will be described in Sec. 5.4 and 5.8.

- The number of raw counts of π^0
  The $N_{\pi^0}^{\mathrm{Au+Au}}$ can be measured by the invariant mass method, and the extraction of π^0 will be described in Sec. 5.7.

- Correction factors
  The overall efficiency of detected π^0s, $\epsilon(p_T)$, can be factorized as follows:

  $$\epsilon(p_T) = \epsilon_{\mathrm{reco}} \cdot \epsilon_{\mathrm{acc}} \cdot C_{\mathrm{bin}}, \tag{5.11}$$

  where ϵ_{reco} and ϵ_{acc} are the reconstruction and the acceptance efficiencies of π^0, respectively, and C_{bin} is the correction factor of the bin width of p_T. Since the reconstruction and acceptance efficiencies of π^0 are correlated with each other, these are estimated by the embedded π^0 method as a whole of the detection efficiency of π^0, $\epsilon_{reco} \times \epsilon_{acc}$. The estimation will be described in Sec. 5.10.2. The correction of the bin width for p_T will be described in Sec. 5.10.2.

5.2 Azimuthal Anisotropy

Since an azimuthal angular distribution of emitted particles ($dN/d\phi$) is a periodic function with 2π, it is expanded into Fourier series for azimuthal angle with 2π period, and it is given as,

$$\begin{aligned} \frac{dN}{d\phi} &= \frac{x_0}{2\pi} + \frac{1}{\pi}\sum_{n=1}^{\infty}\Big(x_n\cos(n\phi) + y_n\sin(n\phi)\Big) && (5.12) \\ &= \frac{x_0}{2\pi}\left(1 + 2\sum_{n=1}^{\infty}\Big(\frac{x_n}{x_0}\cos(n\phi) + \frac{y_n}{x_0}\sin(n\phi)\Big)\right), && (5.13) \end{aligned}$$

where the Fourier coefficients, x_n and y_n, can be obtained by integrating $dN/d\phi$. If an observable O is given, the average O is expressed as,

$$\langle O \rangle = \frac{\int d\phi\ O \times dN/d\phi}{\int d\phi\ dN/d\phi}. \tag{5.14}$$

Since the detected particles are finite in an event, the integral of $dN/d\phi$ takes a simple summation of particles observed in the event.

$$\begin{aligned} x_n &= \int_0^{2\pi} d\phi \frac{dN}{d\phi}\cos(n\phi) = \sum_{i=0}^{M} w_i\cos(n\phi_i) \equiv Q_x, && (5.15) \\ y_n &= \int_0^{2\pi} d\phi \frac{dN}{d\phi}\sin(n\phi) = \sum_{i=0}^{M} w_i\sin(n\phi_i) \equiv Q_y, && (5.16) \end{aligned}$$

where i sums all particles, M, which are used to determine the event plane, ϕ_i is the azimuthal angle of the emitted i-th particle, and w_i is the factor weighted by momentum or multiplicity and so on) to minimize the dispersion of event plane. Thus, the event plane resolution is maximized by w_i. The two-dimensional vector Q=(Q_x,Q_y) is defined as "flow vector" in this thesis.

If the azimuthal angle ϕ in Eq. 5.13 is defined as an azimuthal angle from the reaction plane, the azimuthal angular distribution of emitted particles becomes an even function. Using the fact, y_n term can be omitted since the integration in Eq. 5.16 would be zero. Finally, the azimuthal angular distribution is expressed as follows:

$$\frac{dN}{d\phi} = \frac{x_0}{2\pi}\left(1 + 2\sum_{n=1}^{\infty}\frac{x_n}{x_0}\cos(n\phi)\right) = \frac{x_0}{2\pi}\left(1 + 2\sum_{n=1}^{\infty} v_n \cos\big(n[\phi_{\mathrm{lab}} - \Psi]\big)\right), \tag{5.17}$$

where ϕ_{lab} is an azimuthal angle of the fixed orientation in the measurement, Ψ is an azimuthal angle of true reaction plane, v_n and x_n/x_0 are a magnitude of azimuthal anisotropy. Furthermore, Eq. 5.17 is expanded as follows:

$$\begin{aligned}
\frac{dN}{d\phi} &= \frac{x_0}{2\pi}\left(1 + 2\sum_{n=1}^{\infty}\left(\frac{x_n}{x_0}\cos(n\phi_{\mathrm{lab}}) + \frac{y_n}{x_0}\sin(n\phi_{\mathrm{lab}})\right)\right) \\
&= \frac{x_0}{2\pi}\left(1 + 2\sum_{n=1}^{\infty} v_n^{\mathrm{obs}}\cos(n\Psi_n)\cos(n\phi_{\mathrm{lab}}) + v_n^{\mathrm{obs}}\sin(n\Psi_n)\sin(n\phi_{\mathrm{lab}})\right) \\
&= \frac{x_0}{2\pi}\left(1 + 2\sum_{n=1}^{\infty} v_n^{\mathrm{obs}}\cos\Big(n[\phi_{\mathrm{lab}} - \Psi_n]\Big)\right),
\end{aligned} \tag{5.18}$$

where v_n^{obs} and Ψ_n are defined as follows:

$$v_n^{\mathrm{obs}} = \frac{\sqrt{x_n^2 + y_n^2}}{x_0}, \tag{5.19}$$

$$\Psi_n = \frac{1}{n}\tan^{-1}\left(\frac{y_n}{x_n}\right). \tag{5.20}$$

Comparing to Eq. 5.18, one can regard Ψ_n as the angle of true reaction plane. It is reconstructed from the reaction products event-by-event basis. Generally, the reconstructed plane ("event plane") differ by an error of $\Delta\Psi$ from the true reaction plane. Therefore, the measured azimuthal angle of event plane, Ψ_n, is given as,

$$\Psi_n = \Psi + \Delta\Psi, \tag{5.21}$$

where Ψ is the angle of the true reaction plane.

Averaging over events, one can be obtained the following relation between the measured Fourier coefficient, v_n^{obs}, and true Fourier coefficients, v_n [67]:

$$\begin{aligned} v_n^{\mathrm{obs}} &= \big\langle \cos(n[\phi_{\mathrm{lab}} - \Psi_n]) \big\rangle \\ &= \big\langle \cos(n[\phi_{\mathrm{lab}} - \Psi] - n[\Psi_n - \Psi]) \big\rangle \\ &= \big\langle \cos(n[\phi_{\mathrm{lab}} - \Psi]) \cdot \cos(n\Delta\Psi) \big\rangle + \big\langle \sin(n[\phi_{\mathrm{lab}} - \Psi]) \cdot \sin(n\Delta\Psi) \big\rangle \\ &= \big\langle \cos(n[\phi_{\mathrm{lab}} - \Psi]) \big\rangle \big\langle \cos(n\Delta\Psi) \big\rangle \\ &= v_n \big\langle \cos(n\Psi) \big\rangle, \end{aligned} \tag{5.22}$$

where $\phi_{\mathrm{lab}} - \Psi$ and $\Delta\Psi$ are assumed to be independent for line 3 and 4 in Eq. 5.22, and the reflection symmetry of $\phi_{\mathrm{lab}} - \Psi$ and $\Delta\Psi$ is assumed for sine term in the line 3. The average-sine term vanishes under the high-multiplicity ($M \gg 1$) condition such as Au+Au collisions. In last line, the event plane resolution, $\big\langle \cos(n\Delta\Psi) \big\rangle$, is derived, and the resolution should be corrected for the measured azimuthal anisotropy.

For the measurement of azimuthal anisotropy v_2, the v_n^{obs} in Eq. 5.22 is an observable, and the event plane resolution, $\big\langle \cos(n\Delta\Psi) \big\rangle$, should be corrected. The analysis schemes are summarized as follows:

1. The event plane
   The event plane is defined as the reconstructed reaction plane. The azimuthal angle from the event plane is essential for the measurement of the azimuthal anisotropy v_2. It is explained in detail in Sec. 5.5

2. The azimuthal angular distribution of π^0
   The π^0s is reconstructed on an event-by-event basis, and they are categorized for each azimuthal angular bin. The measured azimuthal anisotropy v_2^{obs} is extracted from the azimuthal angular distribution of π^0. It is described the details of this measurement in Sec. 5.9.

3. The event plane resolution
   As described in Eq. 5.22, the measured azimuthal anisotropy v_2 should be corrected with the event plane resolution. The evaluation of the event plane resolution is described in Sec. 5.5.2

5.3 R_{AA} with Respect to the Azimuthal Angle

Figure 5.1 shows a schematic view of the cross section for the created medium in high-energy heavy-ion collisions. The nuclear modification factor R_{AA} of π^0 with respect to the azimuthal angle is given as,

$$R_{AA}(\Delta\phi_i, p_T) = F(\Delta\phi_i, p_T) \cdot R_{AA}(p_T), \tag{5.23}$$

where $F(\Delta\phi_i, p_T)$ is the ratio of the relative yield, and the ratio is given as,

$$F(\Delta\phi_i, p_T) = \frac{N(\Delta\phi_i, p_T)}{\displaystyle\sum_{i=1}^{6} N(\Delta\phi_i, p_T)}, \tag{5.24}$$

where $N(\Delta\phi_i, p_T)$ is the number of detected π^0s in a given azimuthal angle bin and p_T bin. Since the created matter has an almond shape, it is symmetrical to the short or long axis of the matter. The azimuthal angle from the azimuthal angular range of 0 to $\pi/2$ rad are divided into six regions as shown in Fig. 5.1.

Since the detection efficiency and acceptance are corrected for the measurement of the azimuthally integrated R_{AA} of π^0, the $F(\Delta\phi_i, p_T)$ is not needed to correct the efficiency. However, $F(\Delta\phi_i, p_T)$ is needed to correct for the resolution of the reaction plane, since the detector determined the reaction plane has a finite resolution.

The azimuthal anisotropy v_2^{raw} in the raw azimuthal angular distribution of π^0 is corrected with the event plane resolution. The ratio of the relative yield of π^0 is given as,

$$F(\Delta\phi_i, p_T) = \frac{1}{C_{\mathrm{width}}} \cdot F(\Delta\phi_i, p_T)^{\mathrm{meas}} \cdot \left[\frac{1 + 2v_2^{\mathrm{corr}}\cos(2\Delta\phi)}{1 + 2v_2^{\mathrm{raw}}\cos(2\Delta\phi)}\right]. \tag{5.25}$$

where C_{width} is the number of azimuthal angular bins, and C_{width} is equal to 6 in the case. The azimuthal anisotropy and the event plane resolution are described in Sec. 5.2 and 5.5.2.

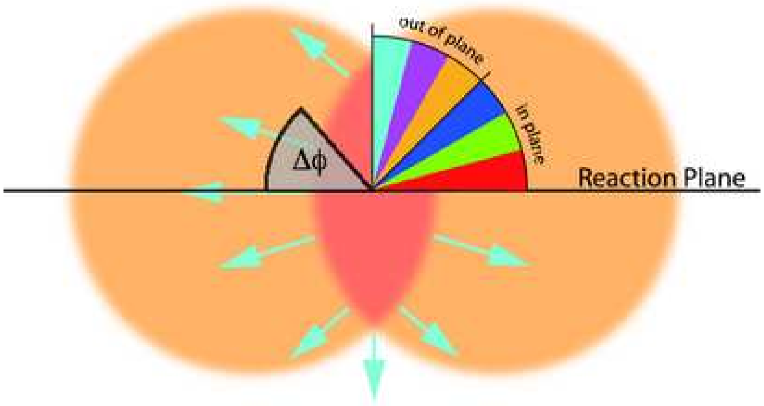

Figure 5.1: A schematic view of the created medium at heavy ion collisions.

5.4 Event Classification

In this section, the event classification method is described. The impact parameter of two colliding nuclei, the number of participant nucleons, and the number of binary nucleon-nucleon collisions characterize the collision. These parameters are calculated with the Glauber model, which is described in Section 5.4.2.

5.4.1 Centrality Determination

Collision centrality of each event in Au+Au collisions is determined by the charge measured by the BBCs. Figure 5.2 shows the distribution of the total charge of the BBC.

The amount of total charge is proportional to the particle multiplicity. The particle multiplicity is correlated to the overlapping area of two colliding nuclei. Therefore, the total charge of the BBC has negative correlation with the impact parameter of the collision. A centrality class of an event is determined by the charge detected in the BBC. As shown in Fig. 5.2, the bin width of the maximum minimum charge detected in the BBC charge are assigned to the centrality of 0 % (the smallest impact parameter) and 93 % (the largest impact parameter), respectively. Intermediate region is sliced with a bin width of 10 %, that is, 0–10 %. 10–20 %, …, 70–80 % and 80–93 %. The most peripheral bin is 80–93 %. Since the charge detected of the BBC depends on the collision vertex position, **BbcZvertex**, the centrality determination was performed for a **BbcZvertex** bin width of 5 cm.

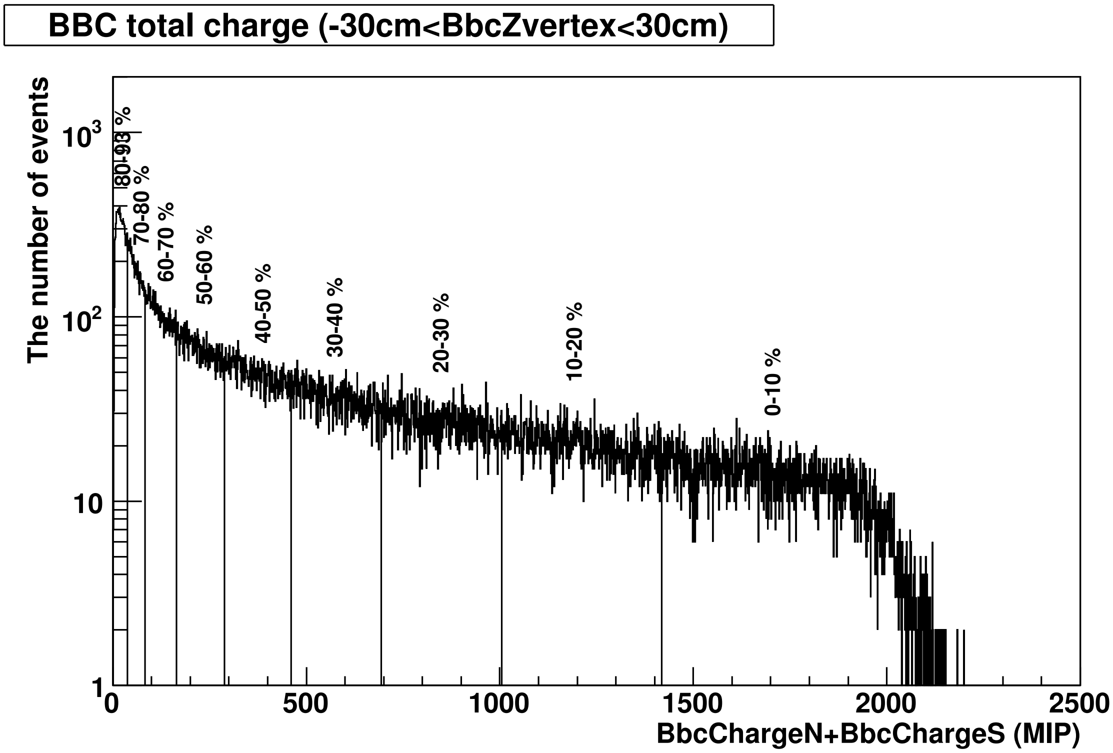

Figure 5.2: A sample distribution of the BBC total charge, **BbcChargeN** and **BbcChargeS**, at the Z-vertex region of -30 cm< **BbcZvertex** <30 cm.

5.4.2 The Glauber Model

As described in Sec. 2.1.1, the Glauber model is a geometrical model of hadronic collisions. The nucleus in each colliding nucleus follows a Woods-Saxon distribution as given in Eq. 2.1. In the case of ^{197}Au+^{197}Au collisions, the following input parameters in Eq. 2.1 and 2.2 are used[63, 68]:

- $R = 6.38$ [fm]

- $d = 0.535$ [fm]
- $\sigma_{NN} = 42$ [mb]

The errors of R, d and σ_{NN} correspond to the systematic uncertainties. The average N_{part}, N_{coll}, T_{AA}, **b** and the systematic uncertainties for each centrality class are summarized in Table 5.2.

5.5 Reaction Plane Measurement

As described in Sec. 2.7.1, the azimuthal angular distribution of emitted particles follows Eq. 5.13. In this section, the event plane determination and calibration are described. Furthermore, the estimation of the event plane resolution is explained.

5.5.1 Event Plane Determination

In the analysis, the MPC and the inner RXNP (RXNin) are used to determine the event plane on a event-by-event basis. The determination of event plane is affected by the non-flow effects such as jets, resonance decay products, and HBT [69, 70]. These effects can be reduced by taking a large rapidity gap [71]. Since the MPC and the RXNin are placed in the forward rapidity, it is expected that the non-flow effects is contributed slightly to the mid-rapidity ($|y| < 0.35$) where the central arm detectors are placed.

The event plane is measured by the following observables;

$$\begin{aligned} 2\Psi^{\mathrm{obs}} &= \tan^{-1}\left(\frac{Q_y}{Q_x}\right), && (5.26) \\ Q_x &= \sum_{i=0} w_i \cos(2\phi_i), && (5.27) \\ Q_y &= \sum_{i=0} w_i \sin(2\phi_i), && (5.28) \end{aligned}$$

where Ψ^{obs} is the observed azimuthal angle of the event plane, Q_x and Q_y are the projection of event plane to x and y axes, respectively, ϕ_i is the azimuthal angle of each PMT, and w_i is the weighting factor. For the RXNin, the amount of the charge detected by PMT is chosen as a weight.

5.5.2 Event Plane Calibration

Since an event plane at heavy-ion collisions is randomly distributed, the distribution of the event plane in azimuth should be also isotropic. However, the measured event plane is not alway azimuthally isotropic due to the azimuthal asymmetric acceptance which is caused by the dead channel in the detector. In order to correct the effect, two calibration procedures have been performed for the measured event plane.

Re-centering Calibration

The re-centering calibration is defined as follows:

$$\begin{aligned}
2\Psi_{corr} &= \tan^{-1}\left(\frac{Q_y^{\rm corr}}{Q_x^{\rm corr}}\right), && (5.29)\\
Q_x^{\rm corr} &\equiv \frac{Q_x - \langle Q_x \rangle}{\sigma_x}, && (5.30)\\
Q_y^{\rm corr} &\equiv \frac{Q_y - \langle Q_y \rangle}{\sigma_y}, && (5.31)
\end{aligned}$$

where $\langle Q_{x,y} \rangle$ are the mean of flow vectors Q_x and Q_y, and $\sigma_{x,y}$ are the width of $Q_{x,y}$. Both the mean and width of the flow vectors are obtained by Q_x and Q_y distributions fitted with Gaussian, and they are parameterized for every centrality classes.

Flattening Calibration

After the re-centering calibration, even though the event plane become almost flat, the small non-flatness of the event plane still remains because higher-harmonic components are not removed by the re-centering calibration. The flattening calibration is performed to remove the non-flat components of the event plane. The flattening calibration is defined as follows:

$$\begin{aligned}
n\Delta\Psi &\equiv \sum_{k=1}^{k_{\rm max}} \left[A_k \cos(kn\Psi^{\rm corr}) + B_k \sin(kn\Psi^{\rm corr})\right] && (5.32)\\
n\Psi &\equiv n\Psi^{\rm corr} + n\Delta\Psi, && (5.33)
\end{aligned}$$

where A_k and B_k are obtained by requiring that k-th Fourier moment of the Ψ distribution vanishes if the Ψ distribution is assumed to be isotropic. Assuming that the correction $\Delta\Psi$ is small,

$$\begin{aligned}
\Psi &= \Psi^{\rm corr} + \Delta\Psi && (5.34)\\
\Delta\Psi &= \sum_k \left[A_k \cos(2k\Psi^{\rm corr}) + B_k \sin(2k\Psi^{\rm corr})\right] && (5.35)\\
A_k &= -\frac{2}{k}\big\langle \sin(2k\Psi^{\rm corr})\big\rangle && (5.36)\\
B_k &= \frac{2}{k}\big\langle \cos(2k\Psi^{\rm corr})\big\rangle, && (5.37)
\end{aligned}$$

where $\Psi^{\rm corr}$ is the corrected event plane and $\Delta\Psi$ is the correction factor obtained from the flattening calibration. The index-k is a degree of Fourier expansion and the brackets denote the average over all particles in all events. One can see that the event plane distribution after the flattening calibration should be flat. We perform the flattening calibration for run-by-run basis.

Each flow vectors measured with MPC and RXNin has been calibrated by the only re-centering method, and the each calibrated flow vector after re-centering is combined for MPC and RXNin, and the combined flow vectors are calibrated with the flattening method. Figure 5.3 shows the azimuthal angular distribution measured by the north and south BBCs after only re-centering calibrations and after re-centering and flattening calibration. As shown in Fig. 5.3, the small distortion of the azimuthal angular distribution is corrected by the flattening calibration. The main distortion is corrected for the re-centering calibration, and the figures of the re-centering calibration for each MPC and RXNin are described in Appendix B.

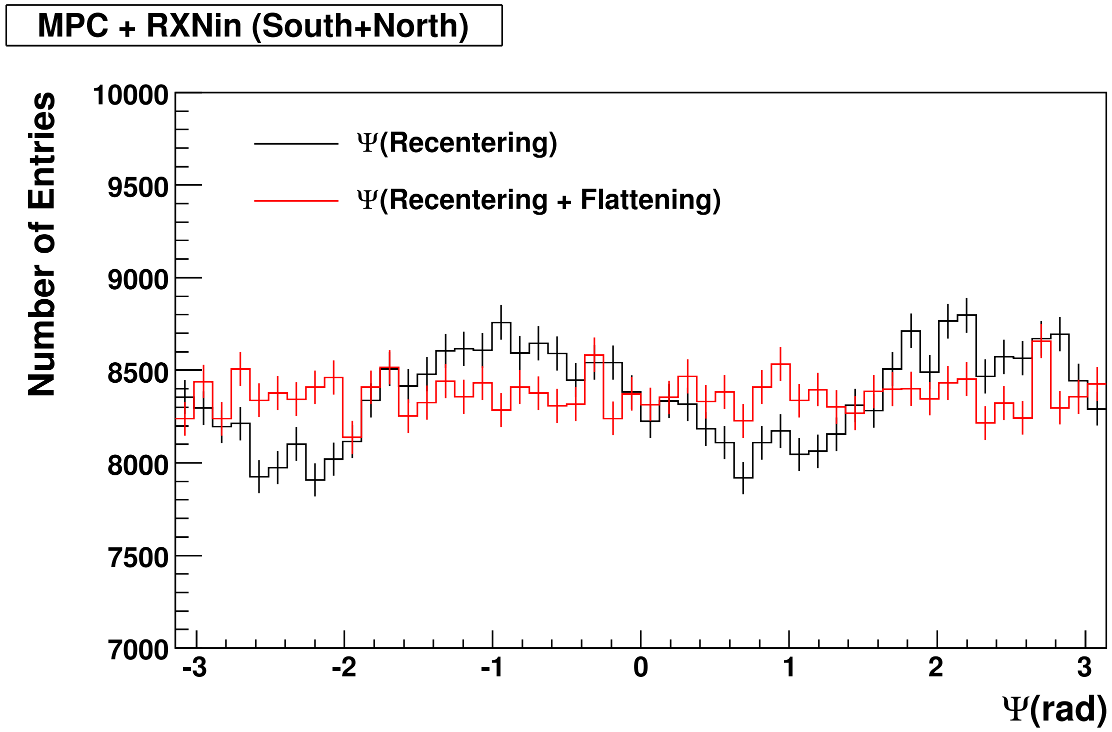

Figure 5.3: The azimuthal angular distribution of the event plane measured by the north and south MPCs and RxNin. Black, red histograms are the azimuthal angular distribution after only the re-centering calibration, and after the re-centering and flattening calibrations, respectively.

Figure 5.4 shows the azimuthal angular correlation of the event plane after the calibrations between the measured north and south side of MPC+RXNin. The strong azimuthal-angular correlation are shown in Fig. 5.4. The event planes are determined by north and south detectors of MPC and RXNin weighted with the average of azimuthal angles from the event plane, and the MPC and RXNin are used for measuring the azimuthal anisotropy v_2.

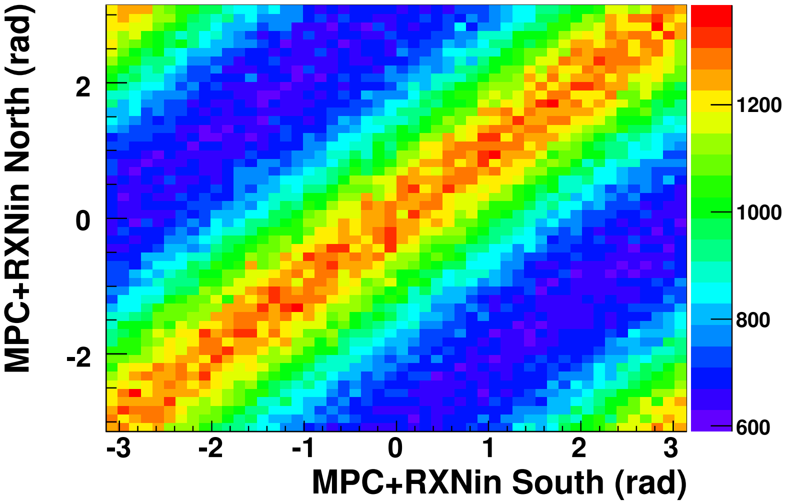

Figure 5.4: A sample of the azimuthal angular correlation of the measured event plane by the north and south MPC+RXNins.

Event Plane Resolution

In general, only finite number of particles is emitted and detected in each event. It includes the fluctuations in determining the azimuthal anisotropy on an event-by-event basis. Even if the distribution of the emitted particles is azimuthally isotropic, the statistical fluctuation can lead to non-zero coefficients v_n. Therefore, the evaluation of the event plane has been performed on the following assumptions: all particles in same event and rapidity are not correlated with each other, the multiplicity is large, and the flow at the same impact parameter does not have a large fluctuation on event-by-event basis. Accordingly, the event plane resolution can be expressed as follows [72]:

$$\big\langle \cos(k\theta_n)\big\rangle = \frac{\sqrt{\pi}}{2}\tilde{\chi}_n e^{-\tilde{\chi}^2/2}\Big[I_{(k-1)/2}\Big(\frac{\tilde{\chi}_n^2}{2}\Big) + I_{(k+1)/2}\Big(\frac{\tilde{\chi}_n^2}{2}\Big)\Big]. \tag{5.38}$$

Since we have two independent event planes measured by the south and north detectors, the event plane resolution can be estimated by measuring the relative azimuthal angle $\Delta\Psi_n \equiv n(\Psi_n^{\mathrm{South}} - \Psi_n^{\mathrm{North}})$.

The method of event plane determination is described in Ref. [72]. The azimuthal anisotropy v_2 is measured by the following equation.

$$v_2 = \frac{\big\langle \cos\big[2(\phi - \Psi)\big]\big\rangle}{\big\langle \cos\big[2(\Delta\Psi)\big]\big\rangle}, \tag{5.39}$$

where $\big\langle \cos[2(\Delta\phi)]\big\rangle$ is the dispersion of second order, and it is called as "event plane resolution" for elliptic plane. Figure 5.5 shows the distributions of the relative azimuthal angle of the event plane, $\Delta\Psi \equiv \Psi(\mathrm{SOUTH}) - \Psi(\mathrm{NORTH})$, between the combined MPC and RXNin on the south side and the north side. The event plane resolution can be estimated with differential of azimuthal angles measured by each sub-detector of the south and north detectors. The relation between event plane resolution and the relative differential of the azimuthal angle is given as,

$$\begin{aligned}\big\langle\cos[2(\Psi_A - \Psi_B)]\big\rangle &= \big\langle\cos 2(\Psi_{true} - \Psi_B) - 2(\Psi_{true} - \Psi_A)\big\rangle \\ &= \big\langle\cos 2(\Psi_{true} - \Psi_A)\cos 2(\Psi_{true} - \Psi_B) \\ &\quad + \sin 2(\Psi_{true} - \Psi A)\sin 2(\Psi_{true} - \Psi_B)\big\rangle \\ &= \big\langle\cos 2(\Psi_{true} - \Psi_A)\big\rangle\big\langle\cos 2(\Psi_{true} - \Psi_B)\big\rangle \\ &= \sigma_A \cdot \sigma_B, \end{aligned} \tag{5.40}$$

where Ψ_A, Ψ_B, and $\Psi_{\rm true}$ are the azimuthal angle from the event plane of emitted particles measured at sub-detectors (A and B), true azimuthal angle from the event plane, respectively, $\Psi_{\rm true} - \Psi_A$ and $\Psi_{true} - \Psi_B$ are assumed to be independent, and σ_A and σ_B are each event plane resolution of south and north detectors. If it is assumed that the correlation is only the flow effect, the hit distributions of the emitted particles satisfies the following equation.

$$\frac{dN}{d(\Delta\phi)} = \frac{e^{-\chi^2}}{2}\Big(\frac{2}{\pi}(1+\chi^2) + z\big[I_0(z) + L_0(z)\big] + \chi^2\big[I_1(z) + L_1(z)\big]\Big), \tag{5.41}$$

where $z \equiv \chi^2\cos(\Delta\Psi)$, $I(z)$ and $L(z)$ are modified Bessel function and modified Struve function, respectively. These functions are applied to the measured azimuthal-angular distribution. The event plane resolution, $\big\langle\cos(2\Delta\phi)\big\rangle$, is derived from the following equation and the obtained χ^2 by the fit in Eq. 5.41.

$$\big\langle\cos(2\Delta\Psi)\big\rangle = \frac{\sqrt{\pi}}{2}\chi^2 e^{-\chi^2/2}\bigg(I_0\Big(\frac{\chi^2}{2}\Big) + I_1\Big(\frac{\chi^2}{2}\Big)\bigg), \tag{5.42}$$

where I_0 and I_1 are modified Bessel functions. Finally, the event plane resolution can be derived from Eq. 5.42. Figure 5.6 shows the event plane resolution with the MPC and RXNin combined and only BBC detector. As shown in Fig. 5.6, the event plane resolution is better than that with BBC by 80 %.

Jet Correlation Effect

As discussed in Sec. 5.5.1, the non-flow effect such as a jet prevents the accurate measurement of the azimuthal anisotropy. Since the fragmented jets are strongly correlated with each other in azimuthal angle and rapidity, the azimuthal angle of the event plane is biased. The bias effect is studied with PYTHIA and HIJING [60]. PYTHIA is used to generate a di-jet, while HIJING is used to reproduce multiplicity of the heavy-ion collisions. Each HIJING event is assigned as a random direction of the event plane, each particle is weighted by the following equation;

$$w = 1 + 2v_2(p_T, \eta)\cos 2(\phi - \Psi), \tag{5.43}$$

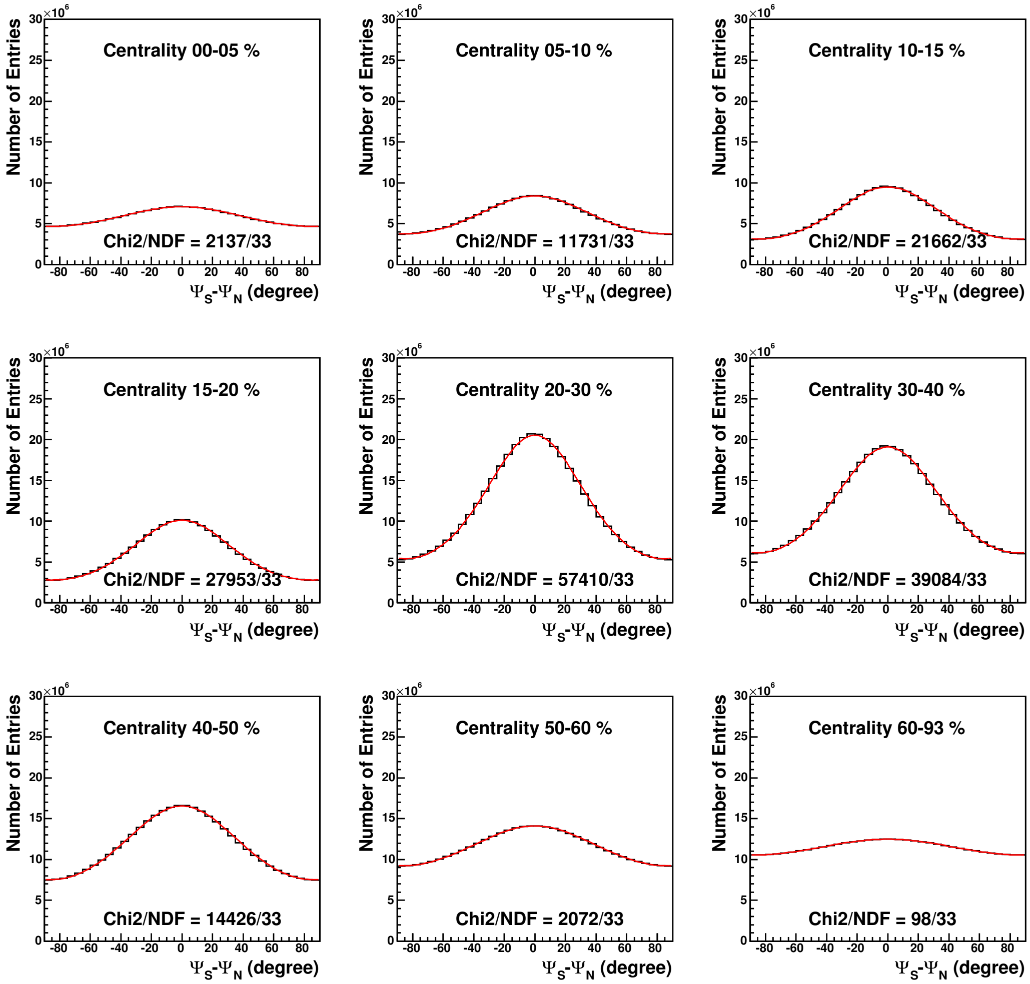

Figure 5.5: The hit distributions of the relative event plane angle for each centrality class.

where η, ϕ, and Ψ are pseudo-rapidity, the azimuthal angle of emitted particles, azimuthal angle of the event plane, respectively. The weight is chosen to reproduce the measured azimuthal anisotropy v_2 of the charged hadron.

Each PYTHIA event is required to have a transverse momentum with above 6 GeV/c, and is also required within PHENIX acceptance ($|\eta| < 0.35$).

Figure 5.8 shows the fake v_2 produced by HIJING and HIJING+PYTHIA as a function of centrality. The event plane is determined by the pseudo-rapidity window from 1.0 to 2.8. The coverage of this pseudo-rapidity window corresponds to the region of both RXNin and RXNout.

Figure 5.9 shows the fake $v2$ at mid-rapidity using the event plane determined with different pseudo-rapidity windows. As shown in Fig. 5.9, the pseudo-rapidity window such as BBC and MPC is negligible for the jet correlation effect, while the fake v_2 determined with RXNout is produced at non-central collisions. The RXNin has small effect (less

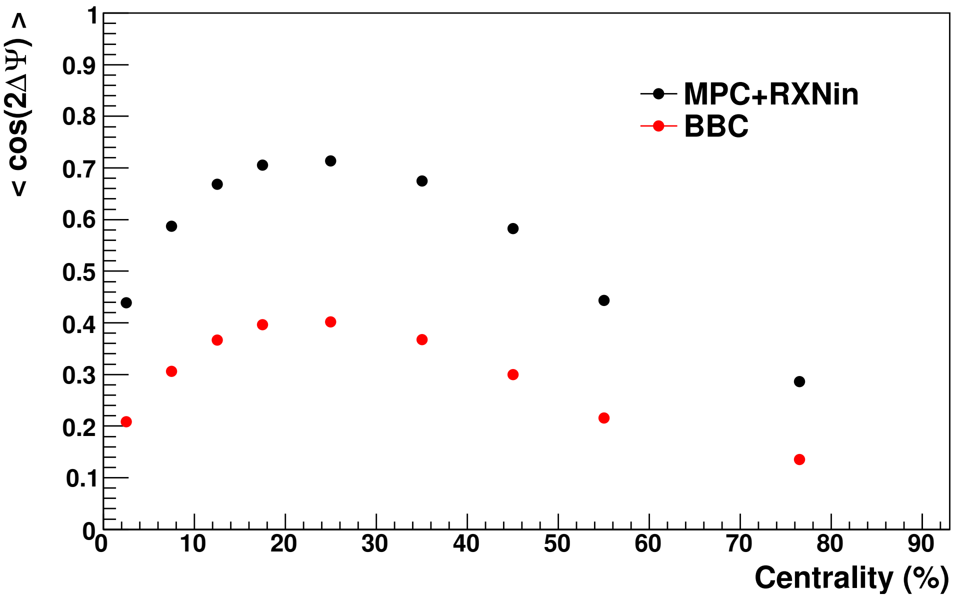

Figure 5.6: The event plane resolution as a function of centrality class. Black and red circles show that the event plane resolutions with the combined MPC and RXNin and only BBC, respectively.

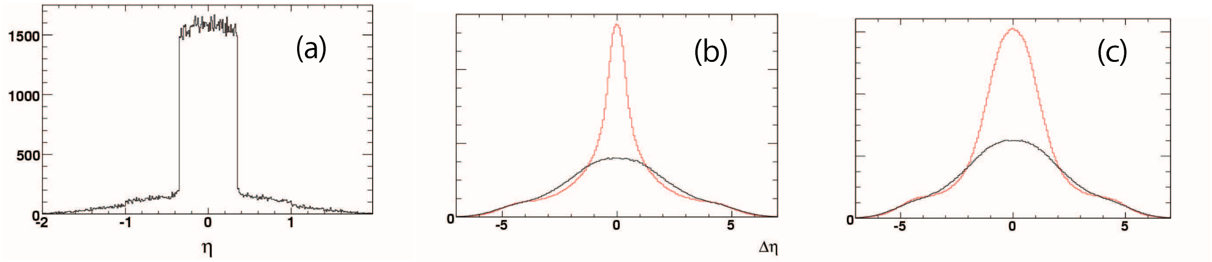

Figure 5.7: (a) Particle distribution with p_T of the above 6 GeV/c as a function of pseudo-rapidity. (b) Triggered particles at the near side in the same event (red) and particles with event mixing technique (black) as a function of pseudo-rapidity. (c) Triggered particles at the away side in the same event (red) and particles with event mixing technique (black) as a function of pseudo-rapidity [60].

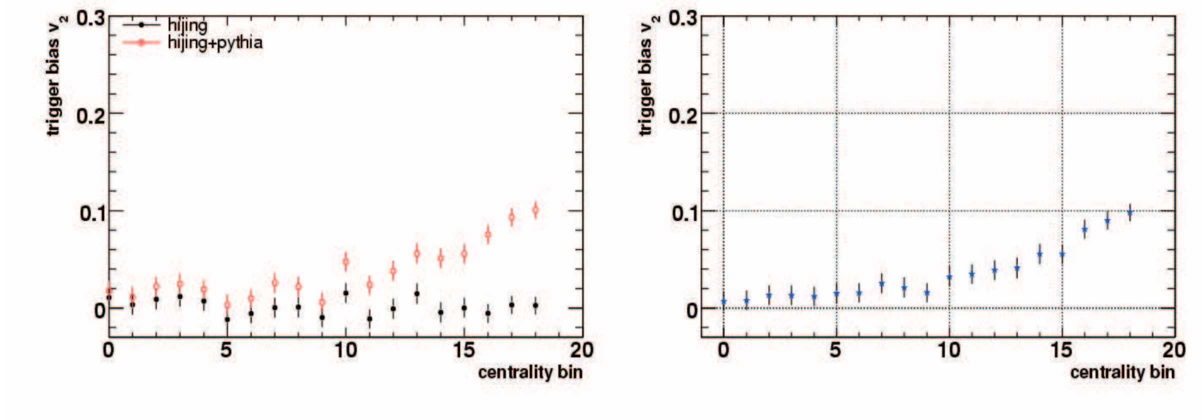

Figure 5.8: Left : Fake v_2 at mid-rapidity with event plane from HIJING (open red circles) and HIJING + PYTHIA (closed black circles) as a function of centrality class. Right: The difference of fake v_2 at mid-rapidity with HIJING and HIJING + PYTHIA as a function of centrality [60].

than a few percent). For the simulation, BBC, MPC , and RXNin should be used for the determination of the event plane.

5.6 Photon Identification with EMCal

The reconstruction of photons is realized by "clustering". Developing electromagnetic shower, the energetic photons and electrons deposit their energy in the EMCals. An electromagnetic shower forms one cluster which consists of one tower with the most highest energy deposit and several surrounding towers with lower energy deposit. For the clustering, all the towers of each sector in the EMCals are scanned to find clusters.

Since a two-dimensional profile of the electromagnetic shower is well understood, a cluster candidate is compared to the predicted shower shape (photon identification).

5.6.1 Overview of Clustering Algorithm

The clustering algorithm of the EMCals is separated into the following procedures.

1. Find towers with the energy deposit above 10 MeV, and form the isolated cluster with 3×3 towers.

2. Find a local maximum tower in the isolated cluster.

3. Form "peak area" made of 5×5 towers around the local maximum tower with the energy deposit above 80 MeV.

4. Select the "core" towers from the "peak area" in order to reduce the overlap effect of the showers.

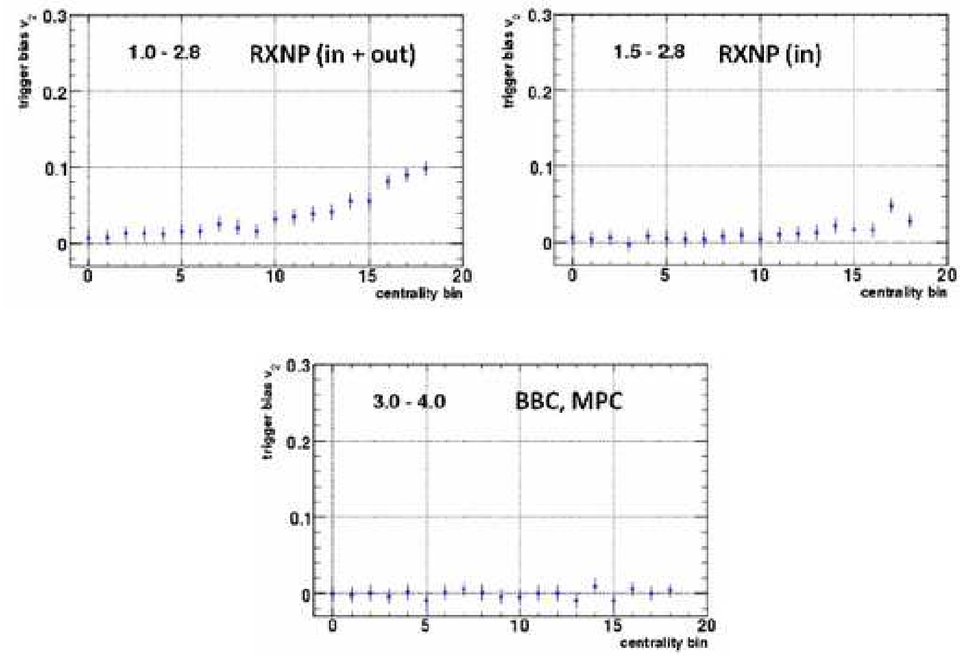

Figure 5.9: Centrality dependence of the fake v_2 using the event plane determined with different pseudo-rapidity windows [60].

5.6.2 Isolated Cluster and Peak Area

First of all, the energy threshold of 10 MeV is applied to all the towers in order to reduce the noise. The neighboring 3×3 towers which are satisfied with the energy threshold are recognized as the "isolated cluster"

If a local maximum tower which has the maximum amplitude in the isolated cluster is found, and the additional energy threshold of 80 MeV is applied to the local maximum tower. The total energy are obtained by the 3×3 towers, the center of gravity are calculated with the position of each tower. This calculation is based on the test-beam results. The towers in 5×5 around the local maximum tower are called "peak area"

5.6.3 Reconstruction of Hit Position

Due to the lateral segmentation of the EMCal, the impact position of a particle is needed to correct with the hit angle. Figure 5.10 shows the definition of the angle and impact position. The hit position of a particle on the surface in EMCal is used with the center of gravity, and it is given as,

$$x_{\mathrm{cent}} = \frac{\sum_i E_i x_i}{E_{\mathrm{tot}}}, \tag{5.44}$$

$$y_{\mathrm{cent}} = \frac{\sum_i E_i y_i}{E_{\mathrm{tot}}}, \tag{5.45}$$

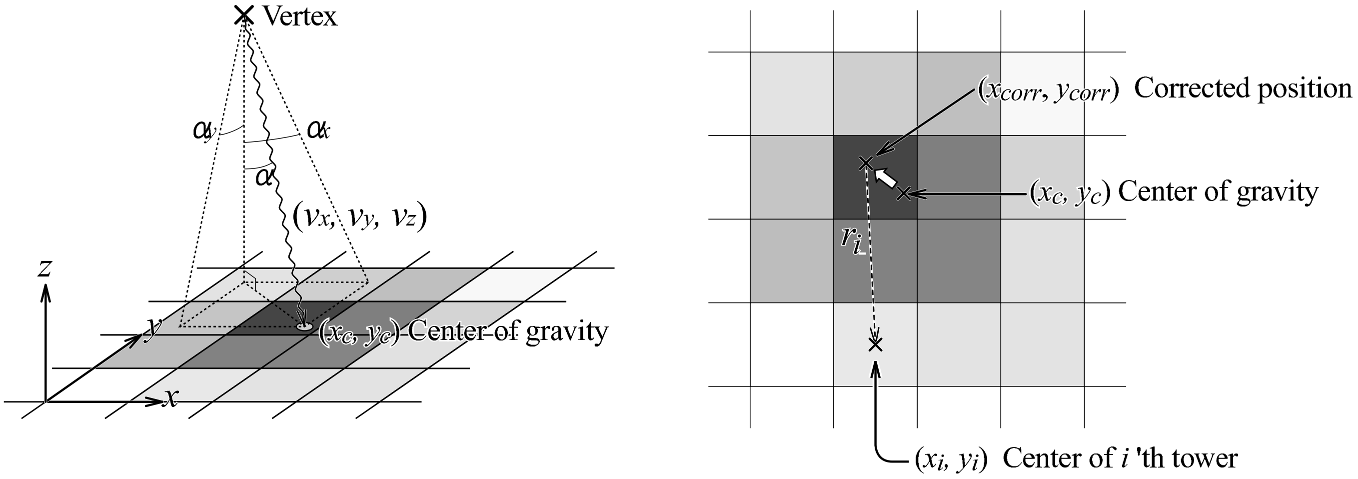

Figure 5.10: A definition of the impact angles (left) and the impact position correction method (right). The matrix shows the towers in EMCal, and the color strength correspond to the amount of deposited energy.

where $x_{\rm cent}$ and $y_{\rm cent}$ are the positions with the center of gravity in the i-th "peak area", E_i is its energy in the "peak area", and $E_{\rm tot}$ is the energy sum in the "peak area". At inclined angle, the projection of the maximum shower on the surface in EMCal does not correspond to the true impact position x_{true}. The positions obtained by the center of gravity of a shower and x_{true} is different due to the finite size of the modules. During the clustering, the center of gravity is corrected with the dependence based on the test-beam results and simulations to the actual impact point on the surface in EMCal assuming that the particle is a photon.

$$\begin{aligned}
x_{\rm true} &= x_{\rm cent}\big(1.05 + 0.12\ln E_{\rm tot}\big)\sin^2\theta_x, && (5.46)\\
y_{\rm true} &= y_{\rm cent}\big(1.05 + 0.12\ln E_{\rm tot}\big)\sin^2\theta_y, && (5.47)\\
\sin\theta_x &= \frac{v_x}{\sqrt{v_x^2+v_y^2}}, && (5.48)\\
\sin\theta_y &= \frac{v_y}{\sqrt{v_y^2+v_y^2}}, && (5.49)
\end{aligned}$$

where (v_x, v_y, v_z) is defined as the vector from the collision vertex to the center of gravity.

5.6.4 Reconstruction of Energy

The showers in each "peak area" overlap in the high-multiplicity condition. In order to reduce the overlap effect, the "core" towers are used instead of the "peak area".

Definition of Core Energy

The hit occupancy of the EMCal is extremely large due to the large multiplicity of charged particles and photons in heavy-ion collisions. The hit occupancy is about 15 % for the

PbSc in the most central Au+Au collisions at $\sqrt{s_{NN}} = 200$ GeV. The occupancy is estimated from the early result for the multiplicity of charged hadrons at RHIC. In high multiplicity environment, the energy deposit in a cluster is smeared by the contribution from other clusters. For instance, the observed ionization energy for the minimum ionizing particles (MIPs) increase by about 6 % in central Au+Au collisions. In order to reduce the bias caused by the high-multiplicity condition, it was proposed to sum only a few towers, instead of taking all towers, for the measurement of energy. A few towers are defined as a "core" tower. In fact, about 80 % of total energy deposits in a single tower if a photon hits at the center of the tower. A "core" tower (E_{core}) in the "peak area" is given as,

$$E_{core} = \sum_i E_i^{\rm meas}, \tag{5.50}$$

where $E_i^{\rm meas}$ is the measured energy in i-th tower, and $\sum_i$ is defined as the sum of the "core" towers. The "core" towers are defined as,

$$\begin{aligned} \frac{E_i^{\rm pred}}{E_{\rm all}^{\rm meas}} &> 0.02 \qquad (5.51) \\ \text{, and} \quad E_{\rm all}^{\rm meas} &= \sum_i^{\rm all} E_i^{\rm meas}, \qquad (5.52) \end{aligned}$$

where $E_{\rm all}^{\rm meas}$ is the energy sum of all the towers in the "peak area", $E_i^{\rm pred}$ is the predicted energy in i-th tower with the shower profile [73].

The deviation of the energy deposit in each tower is parameterized as follows:

$$\sigma_i^2 = q(E_{\rm all}^{\rm meas}) + C \cdot E_i^{\rm pred} \cdot \left(1 - \frac{E_i^{\rm pred}}{E_{\rm all}^{\rm meas}} + f(E_{\rm all}^{\rm meas}, \theta) \cdot \left(1 - \frac{E_i^{\rm pred}}{E_{\rm all}^{\rm meas}}\right)\right), \tag{5.53}$$

where $C = 0.03$ (GeV)^2 is the scale factor of the energy fluctuations in the shower obtained by the test beam results. The deviation σ_i^2 in Eq. 5.53 is used to evaluate the shower profile. The corrections of the incident angle $f(E_{\rm all}^{\rm meas}, \theta)$ is given as $f(E_{\rm all}^{\rm meas}, \theta) = (4/0.03)\sqrt{E}\sin^4\theta$, and the missing energy, $q(E_{\rm all}^{\rm meas})$ used in the clustering algorithm is given as $q(E) = (0.005)^2 + (0.0014)^2 \cdot E^2$ [GeV]^2.

Fraction of Core Energy

The fraction of the E_{core} to the total energy depend on the incident angle, position, and energy. The fraction is parameterized by the results obtained in the beam test:

$$\frac{E_i^{\rm pred}}{E_{\rm all}^{\rm meas}} = p_1(E_{\rm all}^{\rm meas}, \theta) \cdot \exp\left(-\frac{(r/r_0)^3}{p_2(E_{\rm all}^{\rm meas}, \theta)}\right) + p_3(E_\theta^{\rm meas}) \cdot \exp\left(-\frac{(r/r_0)}{p_4(E_{\rm all}^{\rm meas}, \theta)}\right), \tag{5.54}$$

where r is a distance between the center of tower and the center of gravity, r_0 is a size of unit EMCal tower (5.54 cm), θ is an incident angle with respect to a perpendicular on the surface in EMCal, and $p_i(E,\theta)$ are parameterized as follows:

$$\begin{aligned} p_1(E,\theta) &= 0.59 - (1.45 + 0.13\ln E)\sin^2\theta, && (5.55)\\ p_2(E,\theta) &= 0.26 - (0.80 + 0.32\ln E)\sin^2\theta, && (5.56)\\ p_3(E,\theta) &= 0.25 - (0.45 + 0.036\ln E)\sin^2\theta && (5.57)\\ \text{, and}\quad p_4(E,\theta) &= 0.42. && (5.58) \end{aligned}$$

Figure 5.11 shows the energy fraction expected for the case of perpendicular hit of photon at the center of tower. The number of "core "towers is four, and the E_{core} contains about 91.8 % of the total energy in the cluster.

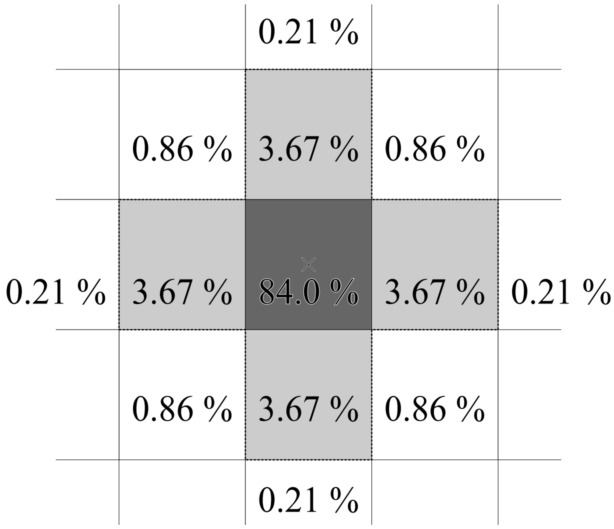

Perpendicular hit on the center of tower.

Figure 5.11: An example of the expected shower energy fraction in towers in the case of perpendicular hit of photon on the center of a tower. Five towers surrounded by dotted line are used for the E_{core} calculation.

Correction of Core Energy

The number of towers used for E_{core} depends on the hit position and the incident angle. Since the E_{core} calculation definitely neglects the contribution from the shower tail, a part of the shower energy are lost. As shown in Fig. 5.11, about 4 % of the shower energy is missing. The fraction of the total energy relative to the expectation of the total energy are estimated with the Monte Carlo simulation parameterized by the test-beam results. The correction of the E_{core} in the clustering algorithm and the input angle is parameterized as:

$$\frac{E_{core}}{E_{core}^{\mathrm{corr}}} = a_1\Big(1 - a_2\sin^4\theta(1 - a_3\ln E_{core})\Big), \tag{5.59}$$

where $a_1 = 0.918$, $a_2 = 1.35$, $a_3 = 0.003$. For later chapters, the corrected E_{core} denotes E_{core}^{corr} in Eq. 5.59.

If the light generated by a shower travels to the PMT via fibers, it is attenuated. Since the depth of the shower varies logarithmically with the energy, the attenuation gives rise to a non-linear response for the energy as shown in Sec. 3.3.3. The non-linearity caused by the attenuation in the fibers are corrected in the following form:

$$\exp(x_0 \ln(E)/\lambda) = E^{x_0/\lambda}, \tag{5.60}$$

where λ is an attenuation length of 120 cm, x_0 is an effective path length of the scintillation light. The shower leakage is estimated as 1 % at 10 GeV and 4 % at 100 GeV. The corrections of these effects are applied to the data.

5.6.5 Cut Parameters for Photon Identification

There are several cuts applied in order to deduce signals of π^0, as listed in this section.

Energy Threshold of Clusters

The small-fragmented clusters which have the energy of ~100 MeV are produced by the clustering algorithm. Since these clusters are the large background source in the measurement of π^0, the energy threshold is applied to reduce the background.

Since this analysis is interested in the only high-p_T events, the applied cut for the deposited energy in clusters is set to $E_T > 5$ GeV. In fact, the measurement of the invariant yield spectra of π^0 at $p_T < 5$ GeV/c has precisely measured at RHIC Year-4 Run, the spectra of yield at low p_T are not measured in this analysis.

Energy Asymmetry

The energy asymmetry cut is applied to reject the combinatorial two photons with high p_T. The energy asymmetry, α, is defined as follows:

$$\alpha \equiv \frac{|E_{core}^{(1)} - E_{core}^{(2)}|}{E_{core}^{(1)} + E_{core}^{(2)}}. \tag{5.61}$$

Since the π^0 decays isotropically in its rest frame, its energy asymmetry distribution should be flat. Figure 5.12 shows the energy asymmetry distribution at $p_T = 10 \pm 0.5$ GeV/c in minimum bias events. The energy asymmetry distribution at the high p_T region has a strong peak near $\alpha = 1$ due to the combinatorial photons, which is made of the broken or mis-identified small-energetic clusters. The energy asymmetry cut is set to $\alpha < 0.8$ to reduce the high-p_T combinatorial background.

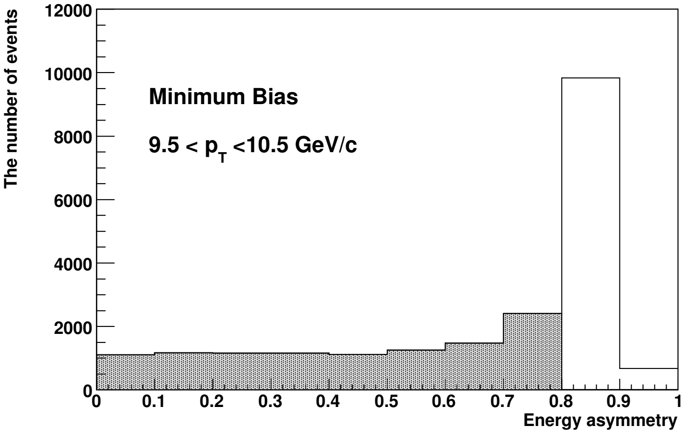

Figure 5.12: A sample of the energy asymmetry distribution at $p_T = 10 \pm 0.5$ GeV/c in minimum bias events.

Opening Angle Between Clusters

An opening angle θ of two decayed photons from the π^0 is expressed as follows:

$$\cos\theta = 1 - 2\left(\frac{M_{\pi^0}^2}{E_{\pi^0}^2}\right)\frac{1}{1-\alpha^2}, \tag{5.62}$$

where M_{π^0} and E_{π^0} are the mass of π^0 and its energy, and α is the energy asymmetry. If the π^0 decays with the extreme energy asymmetry, $\alpha = 0$, the opening angle takes the minimum:

$$M_{\pi^0} = \frac{E_{\pi 0}^2}{2}\left(1 - \cos\theta_{min}\right). \tag{5.63}$$

Therefore, it is assumed that photon clusters with small opening angle contribute to this low-mass region. If the clustering fails and its cluster is divided to two or more number of small-cluster fragments, the π^0 is reconstructed by the clusters with the small opening angle. As a result, the invariant mass is limited at $M_{\gamma\gamma} > 42.5$ MeV to reduce the large combinatorial background produced from the fake clusters.

Distance Between Clusters

The decayed photons from the high-p_T π^0 may be reconstructed as one cluster by the finite size of the EMCal tower and the clustering algorithm. The segment size of a tower in PbSc is 5.5 cm×5.5 cm. Roughly, if the distance between clusters is about 11 cm corresponding to $p_T > 12$ GeV/c for π^0, the clusters are merged. The ΔR is defined as a distance of the projected points of two photons from the same π^0 on the surface in EMCal. The distance ΔR between clusters cut is set to $\Delta R < 8$ cm, since isolated clusters at $\Delta R < 8$ cm are identified as one cluster. Since this cut affect the yield of π^0, the systematic uncertainty for the merging of clusters is evaluated in Sec. 5.10.3.

Exclusion of Bad Towers

In the π^0 analysis, the central tower with the energy deposit in the cluster which is found at the edges of a sector is not used for this analysis. The bad tower is identified at online analysis before reconstructing the data, The towers with higher frequency by 5 σ than the average hit frequency of each tower in one sector are defined as warn at the low energy (< 2 GeV) or hot at the high energy region, while towers with lower frequency by 5 σ than the average hit frequency for each tower in one sector are defined as dead. If warn, hot or dead towers are found at the center of the cluster, the neighboring towers are not used for this analysis. It denotes that the neighboring towers are 3×3 towers centering on a bad tower. The correction of the acceptance loss is taken into account for calculating the detection efficiency of π^0.

Shower Shape

The shower shapes produced by electromagnetic and hadronic particles are quite different so that shower shape profile is often used to distinguish between them. The parameterization is given as,

$$\chi^2 = \sum_i \frac{(E_i^{\mathrm{pred}} - E_i^{\mathrm{meas}})^2}{\sigma_i}, \tag{5.64}$$

where E_i^{meas} is the energy measured in tower i and E_i^{pred} is the predicted energy using the parameterization and the actual measured impact point for an electromagnetic particle of total energy $\sum_i E_i^{\mathrm{meas}}$. The χ^2 value characterizes how electromagnetic a particular shower is, and it can be distinguish between electromagnetic and hadronic particles. used to discriminate against hadrons. Therefore, the χ^2 distribution of 2 GeV/c electrons and pions with the energy deposit above MIP are shown in Fig. 5.13. The arrow marks the χ^2 cut is corresponding to electron efficiency of 90 %.

In the π^0 analysis at high-p_T region, the stronger shower shape cut than the $\chi^2 < 3$ is not necessary, since the background is quite small at high-p_T. In order to evaluate the systematic uncertainty of the photon identification, the yields of π^0 reconstructed with the cuts with $\chi^2 < 3$ and without shower shape cut (NoPID) are compared. The evaluation is described in Sec. 5.10.3.

5.6.6 Energy Calibration

The energy calibration has been performed for tower-by-tower. The π^0 invariant mass method is mainly used for the energy calibration and the energy slope method are used for the only towers where the π^0 mass method fails.

π^0 Invariant Mass Method

Before the energy recalibration, cuts for the photon identification are applied to the cluster and the events.

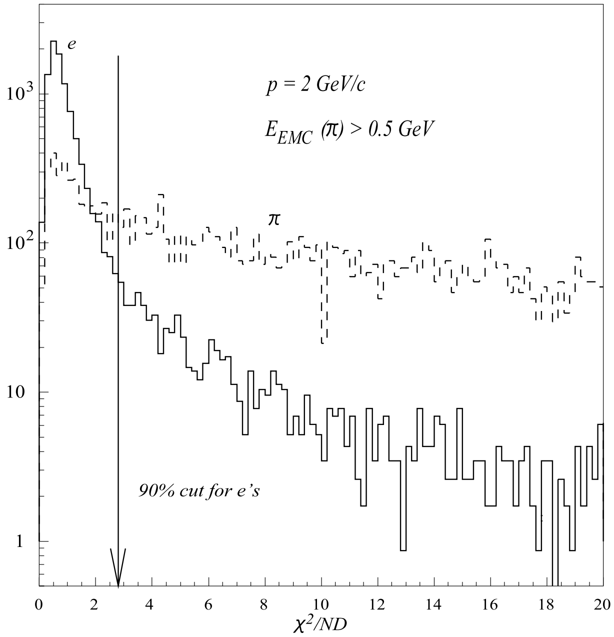

Figure 5.13: The χ^2 distribution of showers induced by 2 GeV/c electrons and pions in the PbSc calorimeter.

- Event selection: Centrality > 40 [%] & |**BbcZvertex**| < 30 [cm]
- Target tower threshold: $p_T > 0.8$ [GeV/c]
- Associated tower threshold: $p_T > 0.2$ [GeV/c]
- Shower shape cut: $\chi^2 < 3$
- Energy asymmetry cut: $\alpha < 0.8$
- Photon-pair cut: $p_T > 1.0$ [GeV/c]

The π^0 are reconstructed using the target and the associated photon candidates in each tower. The reconstructed π^0 is fitted by Gaussian and polynomial function and the π^0 mass is obtained. The obtained $\pi 0^0$ mass for every towers is shifted to 135 MeV (the true π^0 mass). The obtained correction factors are applied to the E_{core} in each tower. These procedures has been performed by four iterations.

Energy Slope Method

The slope method is used to obtain the average E_{core} in a tower. If E_{core} in a tower is assumed to be exponential shape, the average E_{core} is given as,

$$\langle E_{core} \rangle = \frac{\int_0^\infty E_{core}\ e^{-p_1 \cdot E}\ dE}{\int_0^\infty e^{-p_1 \cdot E}\ dE} = \frac{(1/p_1)^2}{1/p_1} = \frac{1}{p_1}, \tag{5.65}$$

where p_1 denotes a free parameter. The measured E_{core} distribution for each tower is fitted by the following function:

$$f(E_{core}) = p_0 \cdot e^{p_1 \cdot E_{core}}, \tag{5.66}$$

where p_0 and p_1 are free parameters. As described in Eq. 5.65, the inverse slope of p_1, corresponds to the average E_{core} in the tower. Figure 5.14 shows that a sample E_{core} distribution for each tower at the momentum range of $1 < p_T < 2$ GeV/c. The average E_{core} for each tower is obtained by the fit function in Eq. 5.66.

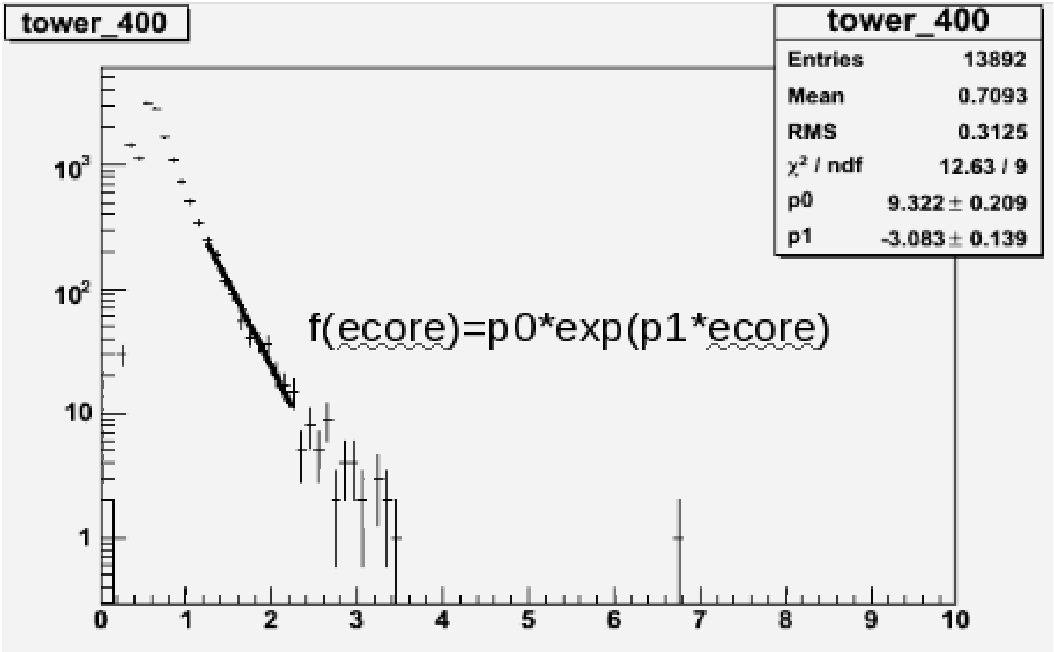

Figure 5.14: A sample E_{core} distribution in a tower and the exponential fit.

5.7 Neutral Pion Identification

The standard cut to identify neutral pion and the background evaluation are described.

5.7.1 Standard Cuts to Extract Neutral Pion

The cut parameters in the below list are used in the π^0 analysis. After applying cuts, the invariant mass spectrum between any photon were calculated to identify π^0.

1. Z-vertex: |**BbcZvertex**| < 30 cm
2. Distance between clusters: $\Delta R < 8$ cm
3. Energy in clusters: $E_T \geq 0.5$ GeV

4. Energy asymmetry: $\alpha < 0.8$
5. Shower shape: $\chi^2 < 3.0$ (PbSc)
6. Opening angle (low mass cut): $M_{\gamma\gamma} < 42.5$ MeV
7. Fiducial cut: 3×3 towers around a dead tower
8. Photon pair: $p_T > 5$ GeV/c

5.7.2 Tight Cut to Extract Neutral Pion

The basic cut parameters are same for the standard cut. The only difference is the shower shape cut. The standard cut is used with $\chi^2 < 3$, while the shower shape cut with the tight cut is given as,

$$\left(0.3 + 4e^{-E_{\rm all}/E_{\rm cent}}\right) \cdot (1.97 - 0.67\chi^2) > 1.4, \tag{5.67}$$

where $E_{\rm cent}$ is the energy in the central tower (the one with the highest energy within the cluster), $E_{\rm all}$ is the sum of the energy measured in all the towers in the "peak" cluster. The tight cut is used to evaluate the systematic uncertainty of photon identification since early photon analysis in PHENIX. The tight cut has the advantage of stronger hadron rejection than standard cut, while the detection efficiency is quite lower than the standard cut [74].

5.7.3 Background Evaluation

It needs to subtract the background from the invariant mass spectra. The background sources are assumed to be the combinatorics which are created by the decay photons from different π^0 and the photon clusters mis-identified with the shower shape cut.

Since the combinatorial photons are independent with each other, they can be evaluated by the event mixing technique. The event mixing technique is used to subtract the uncorrelated-combinatorial photons. It is possible to keep the signal from π^0 and to drastically reduce the combinatorial background using the event mixing technique.

The events are classified based on the centrality (11 classes, 0–5 %, 5–10 %, 10–15 %, 15–20 %, 20–30 %, 30–40 %, 40–50 %, 50–60 %, 60–70 %, 70–80 % and 80–93 %) Z-vertex (12 classes, every 5 cm bins from -30 cm to 30 cm) to perform the event mixing. After the classification, the events are stored in the event buffer with 5 depth. Mixing with the photons identified in one event and the photons in an another event in the event buffer, uncorrelated photons are produced. The produced mixed events are normalized to the mass window which exclude the peak area ($0.085 < M_{\gamma\gamma} < 0.09$ [GeV/c]$^{-2}$, $0.2 < M_{\gamma\gamma} < 0.4$ [GeV/c]$^{-2}$). The normalized mixed events are subtracted to the invariant mass spectrum produced in the same events.

The subtracted invariant mass spectrum may have the residual background from the correlated photons. The correlated photons is thought to be $\pi^0 - \pi^0$ or $\gamma - \gamma$ correlation.

The residual background is evaluated by the second polynomial and Gaussian fit function on the subtracted mass spectrum. Finally, the mass window of π^0 is selected from 0.11 to 0.17 GeV/c^{-2} and the number of π^0 is counted.

The left panel in Fig. 5.15 shows the invariant mass spectrum of two photons (black) and the corresponding mixed event (red) at the momentum range of $7 < p_T < 7.5$ GeV/c in minimum bias (MB, 0–93 % centrality) collisions. The right panel in Fig. 5.15 shows the subtracted invariant mass spectrum. The blue line is the fit function to subtract the remaining background which is produced by the mis-identified photon clusters. The peak of π^0 can be clearly seen and the shaded mass window is counted.

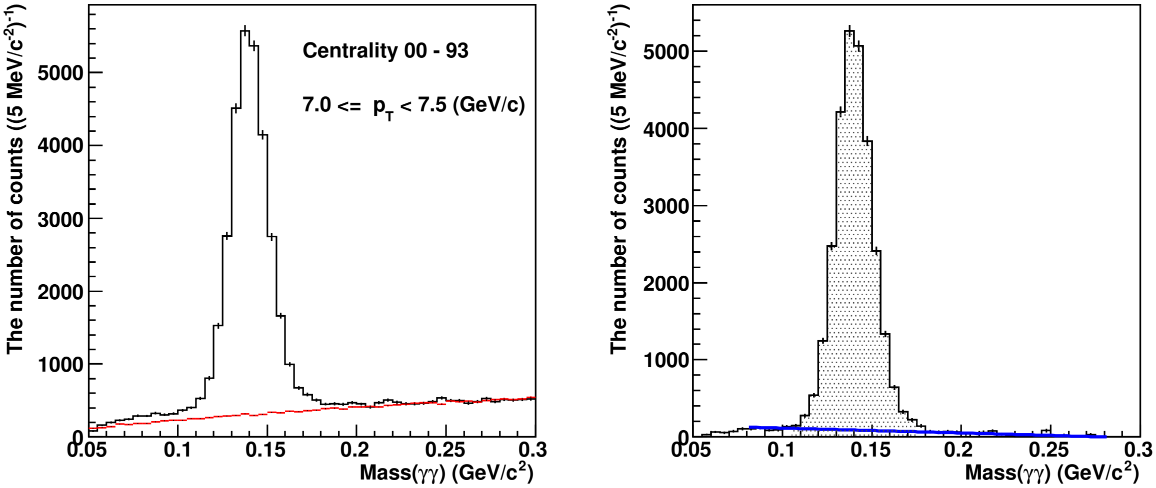

Figure 5.15: Left: Invariant mass spectrum of two photons (black) and the corresponding mixed events (red) at $7 < p_T < 7.5$ GeV/c in minimum bias collisions. Right: The subtracted invariant mass spectrum of two photons at $7 < p_T < 7.5$ GeV/c.

5.8 Quality Assurance for Selecting Good Runs

The quality assurance (QA) of the data has been performed by inspecting π^0 peak and width, the centrality distribution and the reaction plane distribution. The number of the events after the QA was about 3.8 billion.

5.8.1 π^0 Energy QA

The QA for π^0 peak and width has been performed by the minimum bias events at high-p_T region of $p_T > 5$ GeV/c. The shower shape cut ($\chi^2 < 3$) for PbSc is applied for reconstructing π^0s, and any shower shape cut for photon identification is not applied for PbGl. If π^0 mass peak and width are five sigma larger than the average of total runs, the runs are defined as bad and were not used for the further analysis. Figure 5.16 and 5.17 show the π^0 mass peak and width as a function of run number, respectively.

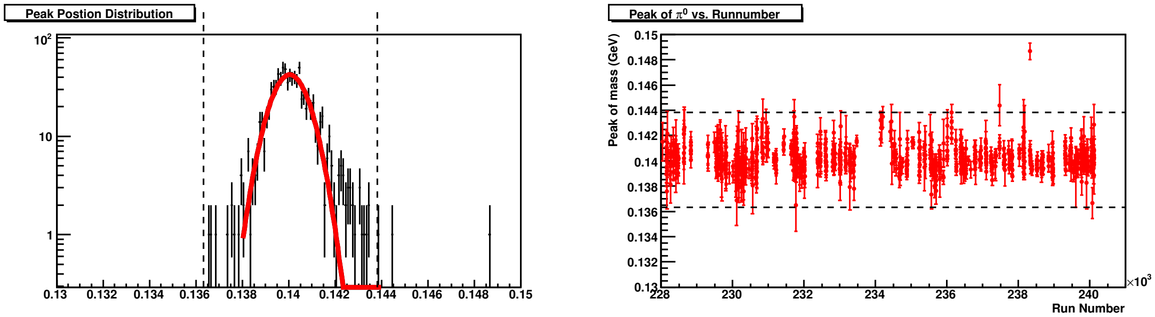

Figure 5.16: The left panel shows the distribution of the π^0 peak in all runs. Black dashed lines show the average peak $\pm 5\sigma$ obtained by Gaussian fit. The right panel shows the π^0 peak as a function of run number. Black dashed lines are same as a left panel.

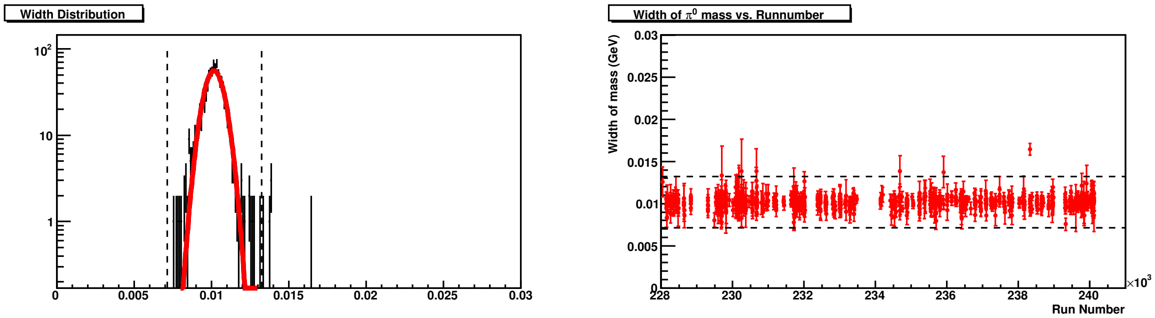

Figure 5.17: The left panel shows the distribution of the width for π^0. Black dashed lines show the average width ± 5 σ obtained from the Gaussian fit. The right panel shows the width for π^0 as a function of run number. Black dashed lines are same as a left figure.

5.8.2 Centrality QA

The QA for the centrality distribution has been performed. The centrality distribution should be flat by definition. The measured centrality distribution is fitted with a straight line. If the χ^2/NDF obtained by the fit is larger than three, the run is defined as bad and is rejected for the further analysis.

5.8.3 Event Plane QA

The QA for the angular distribution of the event plane has been performed with the minimum bias events. The QA is used with BBCs to determine the event plane. The angular distribution of the event plane should be flat by definition so that the angular

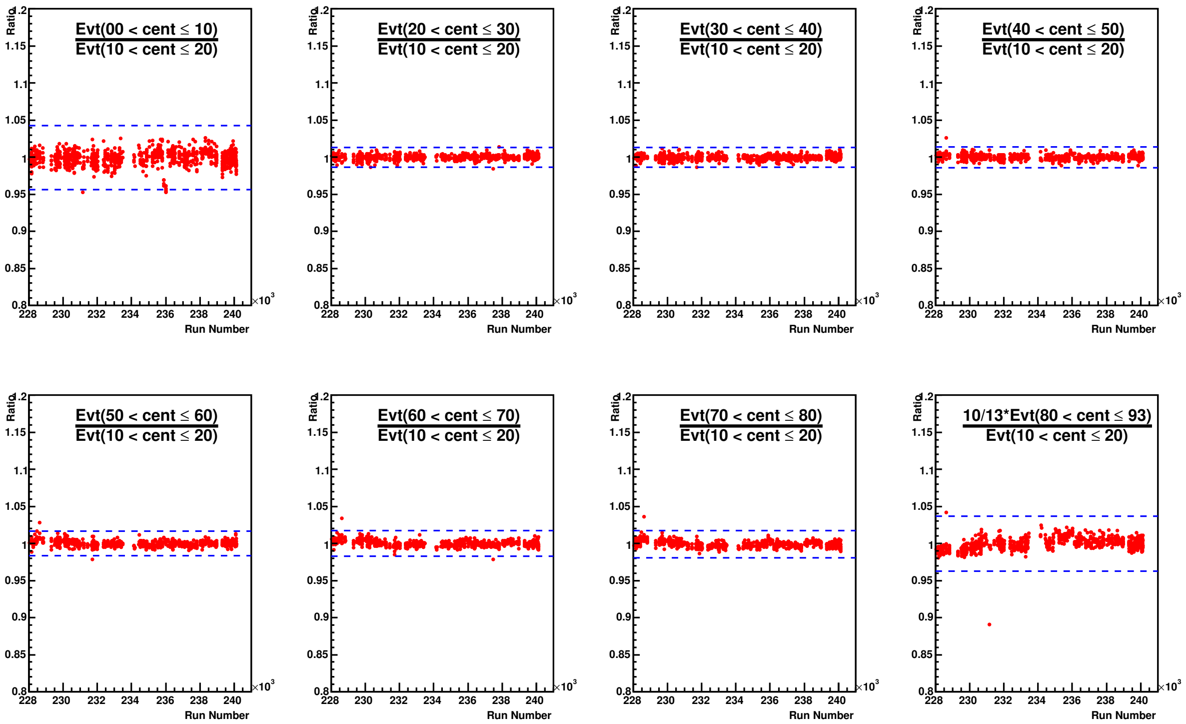

Figure 5.18: The ratios of centrality distribution as a function of a run number. Each 10 % centrality class is divided into the entries of centrality 11-20 %.

distribution is fitted with a straight line. If the χ^2/NDF is larger than three, the run with bad chi-square is not used in the π^0 analysis.

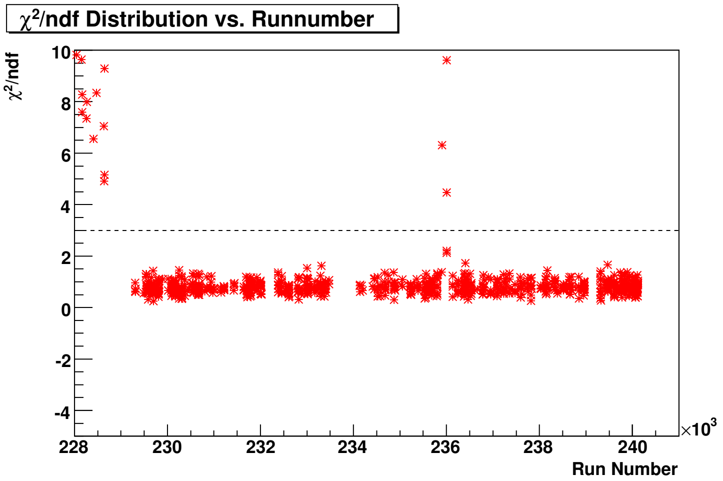

Figure 5.19: The chi-squares per NDF distribution as a function of run number. Black dashed line shows $\chi^2/\text{NDF} = 3$. The fit has been performed at minimum bias events for all runs.

5.9 Azimuthal Anisotropy v_2 Measurement

The azimuthal anisotropy v_2 of π^0 has been measured using the event plane determined by MPC and RXNin.

5.9.1 Azimuthal Angular Distribution of π^0

Figure 5.20 shows the angular distribution of the number of π^0 with respect to the azimuthal angles at centrality 20–30 %. This angle corresponds to the relative angle from the event plane. The reconstructed π^0 for every events are counted for each azimuthal angle bin ($0 < \Delta\phi < \pi/2$). The red curve in Fig. 5.20 are the assumed fit function, and it is given as,

$$f(\phi) = N_0\Big(1 + 2v_2\cos\big(2(\phi - \Psi)\big)\Big), \tag{5.68}$$

where $\phi - \Psi$ is the relative azimuthal angle from the event plane, and N_0 is the amplitude of the azimuthal angular distribution, and v_2 is the measured azimuthal anisotropy. The measured azimuthal anisotropy v_2 is corrected with the event plane resolution estimated in Sec. 5.5.2.

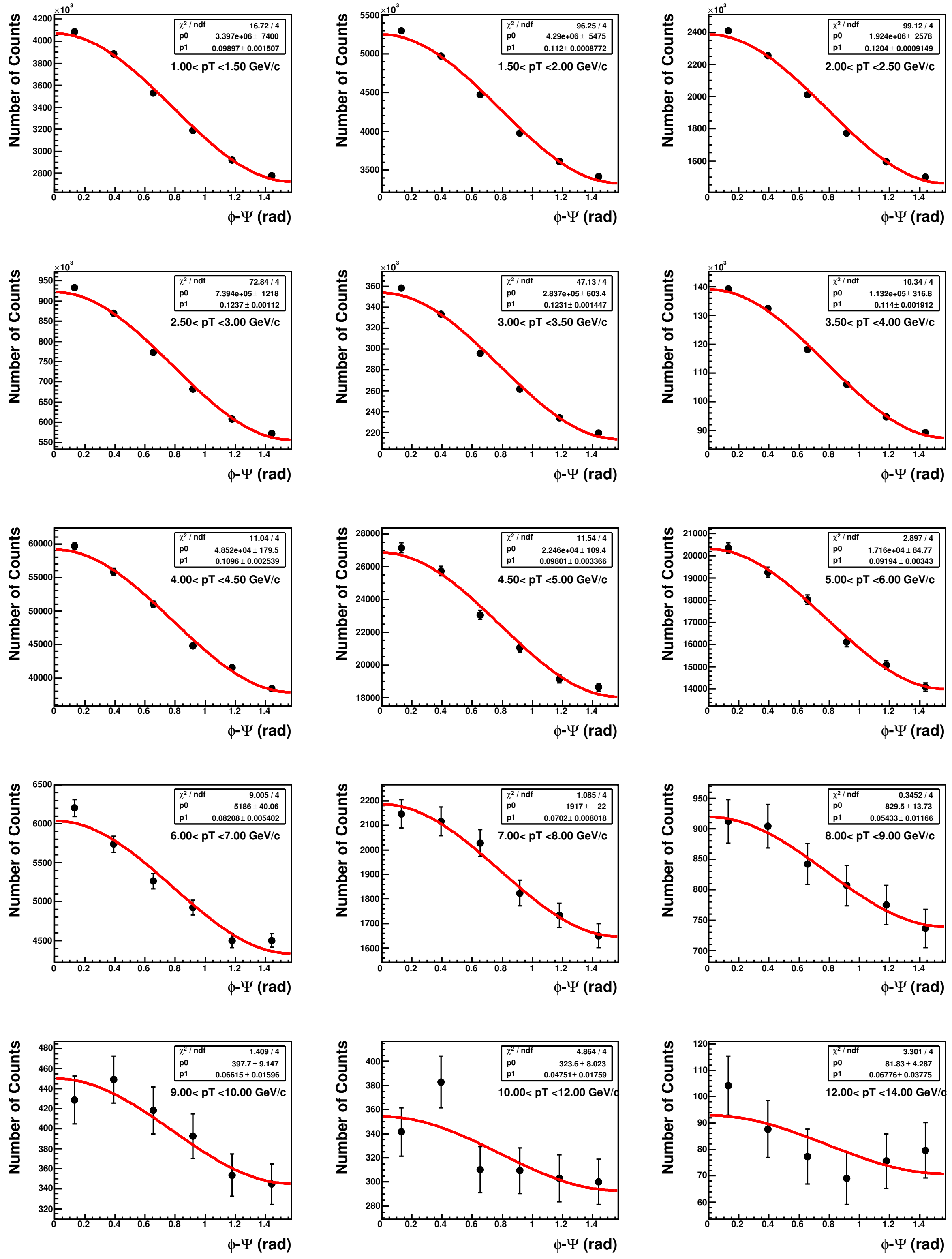

Figure 5.20: The angular distribution of the number of neutral pions with respect to the azimuthal angle bins at centrality 20–30 %.

5.9.2 Systematic Uncertainty for Azimuthal Anisotropy

The main systematic uncertainty sources of the azimuthal anisotropy v_2 are considered the photon identification and the yield extraction. Furthermore, the uncertainty for the determination of the event plane is considered.

Yield Extraction

The uncertainty for the yield extracted is estimated by the two invariant mass windows of the π^0. Figure 5.21 shows the ratios as function of p_T. The numerator is the v_2 from the window with 2.5 σ of the π^0 mass width determined by the Gaussian fit, and the denominator is the v_2 from the fixed window with 0.1 to 0.18 $[\mathrm{GeV}/c]^{-2}$. As shown in Fig.5.21, the difference of the v_2 in the most central (closed black circles) collisions is larger than mid-central (closed red squares) or peripheral (closed blue triangles) collisions.

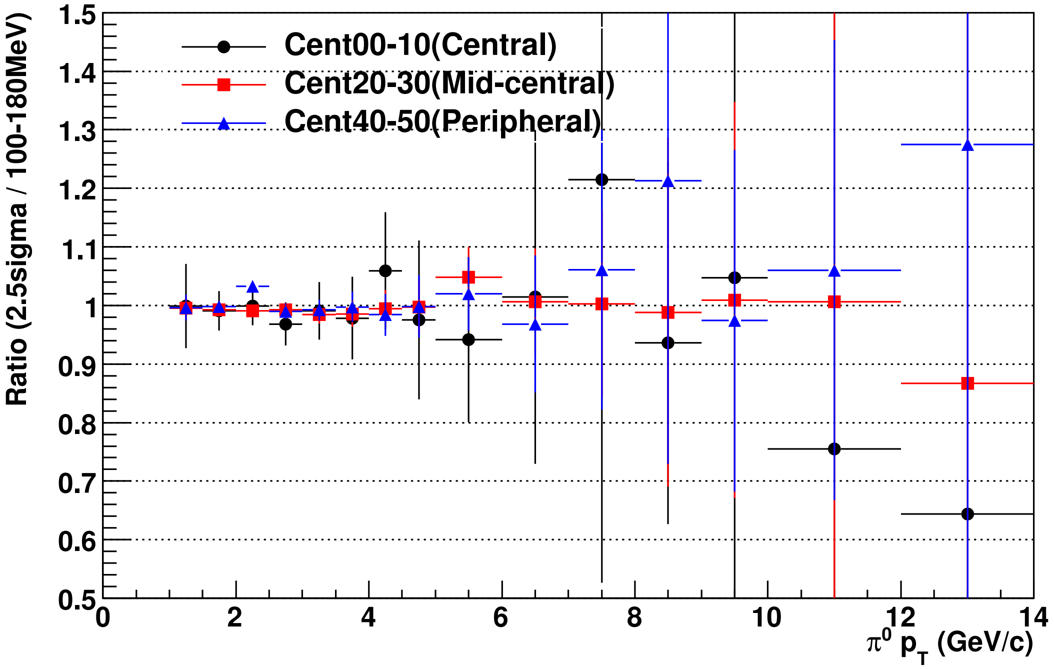

Figure 5.21: The ratios of 2.5 σ mass window to fixed $(0.1 < M_{\gamma\gamma} < 0.18)$ mass window as a function of p_T at central, mid-central, and peripheral collisions.

Photon Identification

The uncertainty from the photon identification is estimated by the tight and standard cut. Figure 5.22 shows the ratios of the v_2 with the tight cut to standard cut as a function of p_T

at central, mid-central, and peripheral collisions. For the central collisions, the difference of the cuts are larger than mid-central or peripheral collisions.

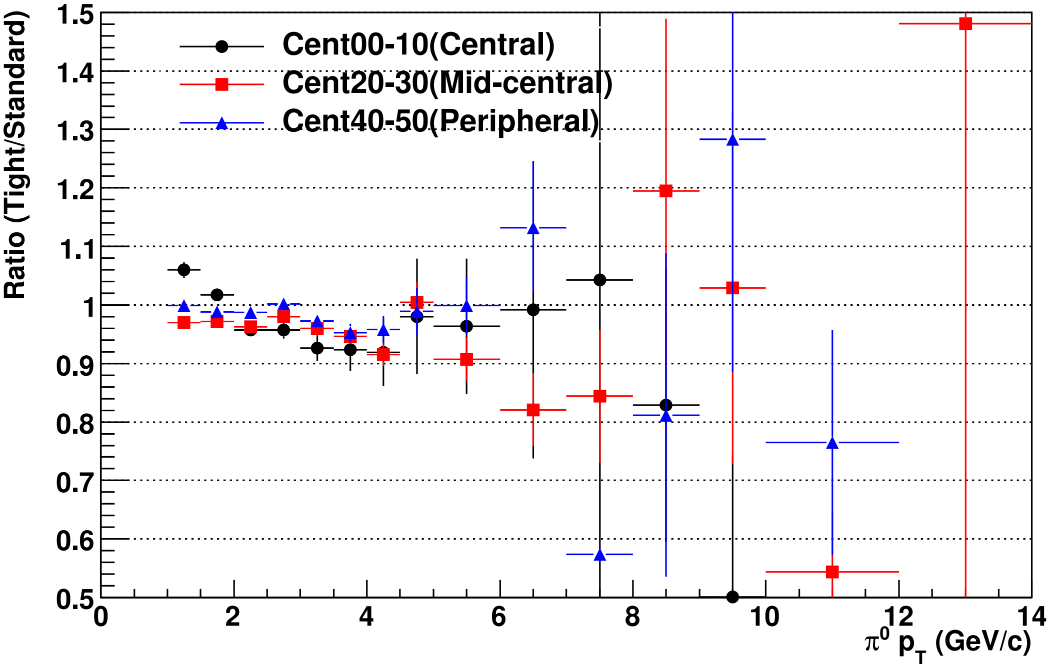

Figure 5.22: The ratios of the v_2 with the tight cut to the standard cut as a function of p_T at the central(closed black circles), mid-central (closed red squares), and peripheral (closed blue triangles) collisions.

Determination of the Event Plane

The uncertainty from the determination of the event plane is estimated from the measurement of v_2 with different reaction plane detectors [6]. In this thesis, the uncertainty for each centrality class is given as about 10 % in the central collision (centrality 0–10 % and 10–20 %) and the peripheral collisions (centrality 40–50 % and 50–60 %), and about 5 % in the mid-central collisions (centrality 20-30 % and 30-40 %).

5.10 Invariant Yield and R_{AA} Measurement

The invariant yield is derived from the raw counts of π^0 and the correction factors in Eq. 5.11, and the R_{AA} can be extracted from Eq. 5.10

5.10.1 Raw yields spectra of π^0 as a function of p_T

After passing through the analysis procedure, the raw spectra of π^0 were measured for each 10 & centrality class, 0–5 % centrality and minimum bias.

5.10.2 Simulation for Detection Efficiency

As described in the beginning of this chapter, the detection efficiency $\epsilon(p_T) \equiv \epsilon_{reco} \cdot \epsilon_{acc}$ is evaluated by the Monte Carlo simulation. However, this is not sufficient for high-multiplicity environment such as Au+Au collisions. In order to reproduce the high-multiplicity environment, the generated single π^0 is embedded in real event.

In this simulation, the same dead channels of EMCal, which are not used with the real data analysis are implemented. The deposited energy of the cluster in the simulation may be smeared due to the fluctuation from the tower-by-tower calibration of E_{core} with the real data. Therefore, the deposited energy were tuned to match the energy scale and the mass width of π^0 in the real data, and the comparison of the fiducial area and the photon identification efficiency between real data and the simulation were also done.

The detection efficiency of π^0 are defined as follows:

$$\epsilon(p_T) = \frac{f(p_T^{\text{out}})}{f(p_T^{\text{in}})}, \tag{5.69}$$

where $f(p_T^{\text{in}})$ is the generated spectrum of π^0 yield, and $f(p_T^{\text{out}})$ is the reconstructed spectrum of π^0 yield. The generated spectrum needs to be weighted with due to the steeply falling shape. The weighting is used with the shape of the previous measured π^0 spectrum at PHENIX [75].

Conditions for Generated Single π^0s

To obtain the detection efficiency of π^0, Monte Carlo simulation of $\pi^0 \rightarrow \gamma\gamma$ has been performed. The condition for the generation of single π^0 is summarized in Table 5.1.

Variables	Range	Conditions
z-vertex	-30 $\leq z \leq$ 30 cm	Uniform
π^0 p_T	$0 \leq p_T \leq 25$ GeV/c	Uniform
Rapidity	-0.5 $\leq y \leq$ 0.5	Uniform
Azimuthal angle	$0 \leq \phi \leq 2\pi$	Uniform

Table 5.1: Summary of initial conditions for the generated π^0.

Embedding Procedure

The information of the reconstructed clusters and the hits of the detectors are recorded in the Data Summary Tape (DST). Parameters which characterize events, such as the

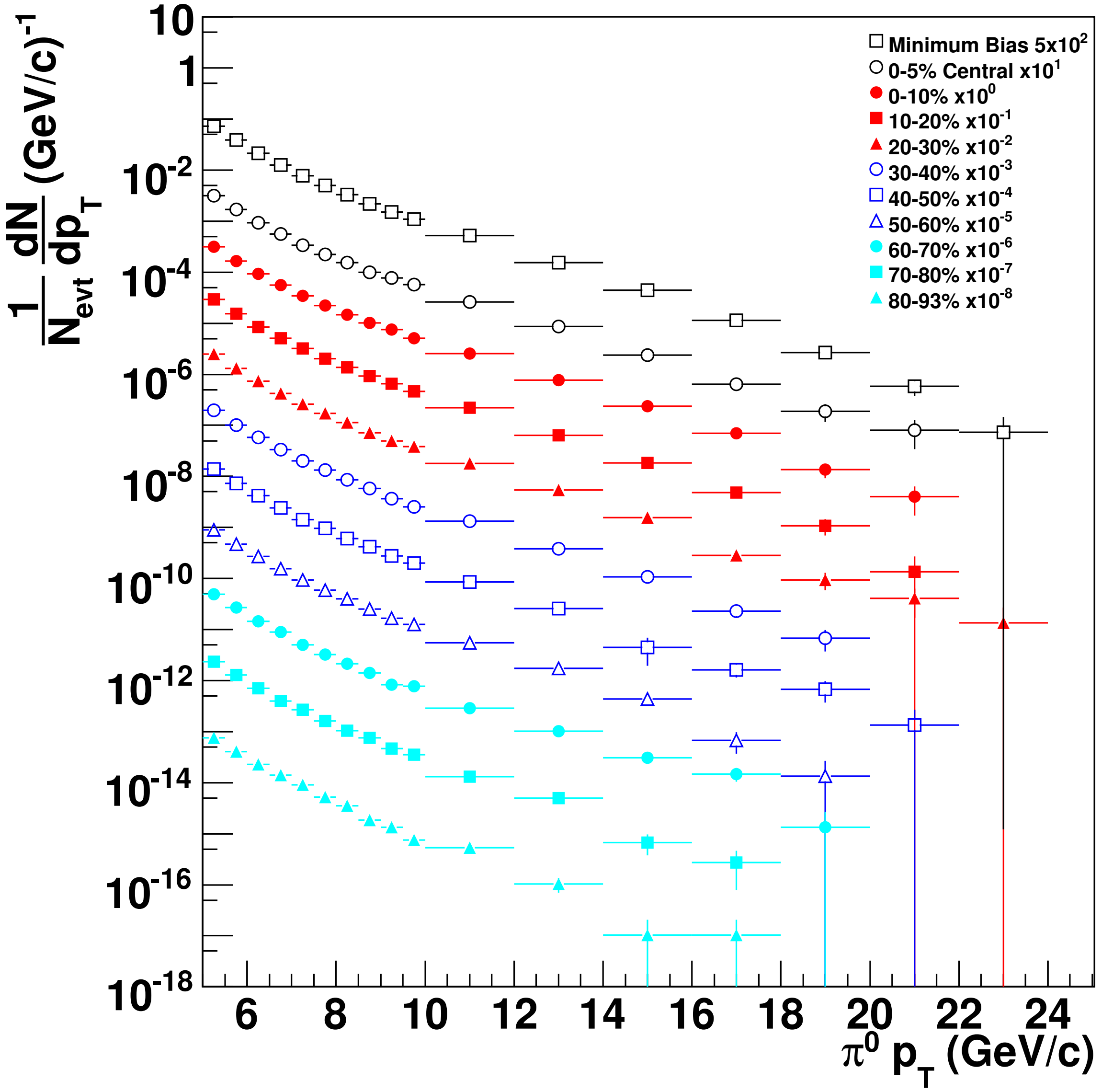

Figure 5.23: Raw yields spectra of π^0 as a function of p_T for every 10 % centrality classes and 0–5 % and minimum bias. The p_T-bin width is 0.5 GeV/c at p_T <10 GeV/c and 2 GeV/c at higher p_T.

collision vertex and centrality, are also recorded in the DST files. In this thesis, simulated and real data files are called as *simDST* and *realDST*, respectively.

The analysis flow chart of the embedding procedure is shown in Fig. 5.24.

The generated π^0s pass through PISA which is implemented with PHENIX geometrical configuration. Since the deposited tower energy in the *simDST* files has ideal values, the energy is smeared to reproduce the energy scale and the width of π^0 with the measured data. The single pi^0 is embedded in the *realDST* which is calibrated the deposited energy in the tower.

The Z-vertex and centrality for the *realDST* are classified for every 5 cm and 10 % and each detection effciency is calculated. The detection efficiency for each Z-vertex and centrality class is weighted by **BbcZvertex** distribution from the real data. The weighted detection efficiency of π^0 is obtained for each sector in EMCal. The detection efficiencies for each sector is averaged for whole of PbSc.

Energy Scale and Width of π^0

The energy scale and width of π^0 measured in real data are compared to those in the simulated data. Figure 5.25 and 5.26 show the energy scale and its width of π^0 as a function of p_T, respectively. Both closed red circles and open black squares show the measured data and simulated data, respectively. The difference of the energy scale between real data and simulation is quite small (less than 0.5 %) and the difference of the width is less than 1 MeV. The difference of the energy scale seriously influences the yield. This difference is assign as systematic uncertainty from the energy scale in the invariant yield of π^0. The evaluation of this uncertainty will be described in Sec. 5.10.3.

The detection efficiency with PbSc is evaluated for each 0.5 GeV/c p_T bin. The 8-th polynomial function is used to connect data points due to the reduction of the statistical fluctuation on the simulation. The difference between the simulated data and the fit function is evaluated as the systematic uncertainty. Figure 5.27 shows the average efficiencies of the measured π^0 with PbSc for three centrality class as a function of p_T. The open black circles, red squares and blue triangles are the detection efficiencies for centrality 0–10, 20-30 and 80-93 %, respectively. The detection efficiency of π^0 increases as p_T up to 12 GeV/c. The detection efficiencies at $p_T > 12$ GeV/c drop steeply due to the finite volume for the towers in EMCal.

Figure 5.28 shows the ratio of the detection efficiencies at $p_T = 10$ GeV/c as a function of centrality. The efficiencies for each centrality is divided by that for centrality 80–93 %. The detection efficiency of π^0 at most central collisions is smaller than that at peripheral collisions due to high multiplicity environment.

Bin Width Correction

A limited energy resolution leads to a re-distribution of the yield in one energy or p_T bin to the neighboring bins. As this is true for any p_T bin, the loss in one bin for a flat input spectrum and constant energy resolution is compensated by the gain from the surrounding bins, leading to identical input and output spectra, therefore an efficiency of one. For a

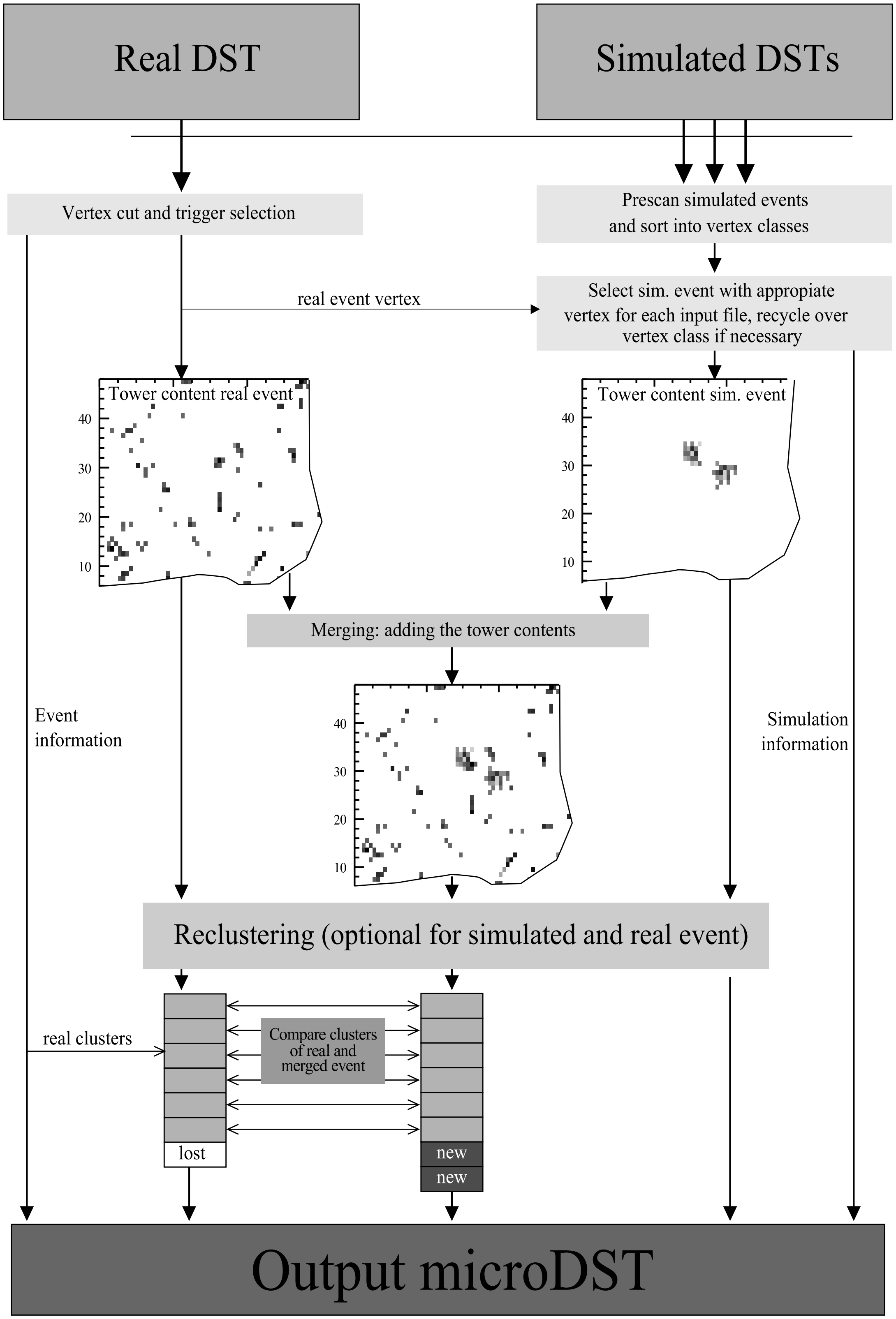

Figure 5.24: Main program flow of the embedding algorithm [76].

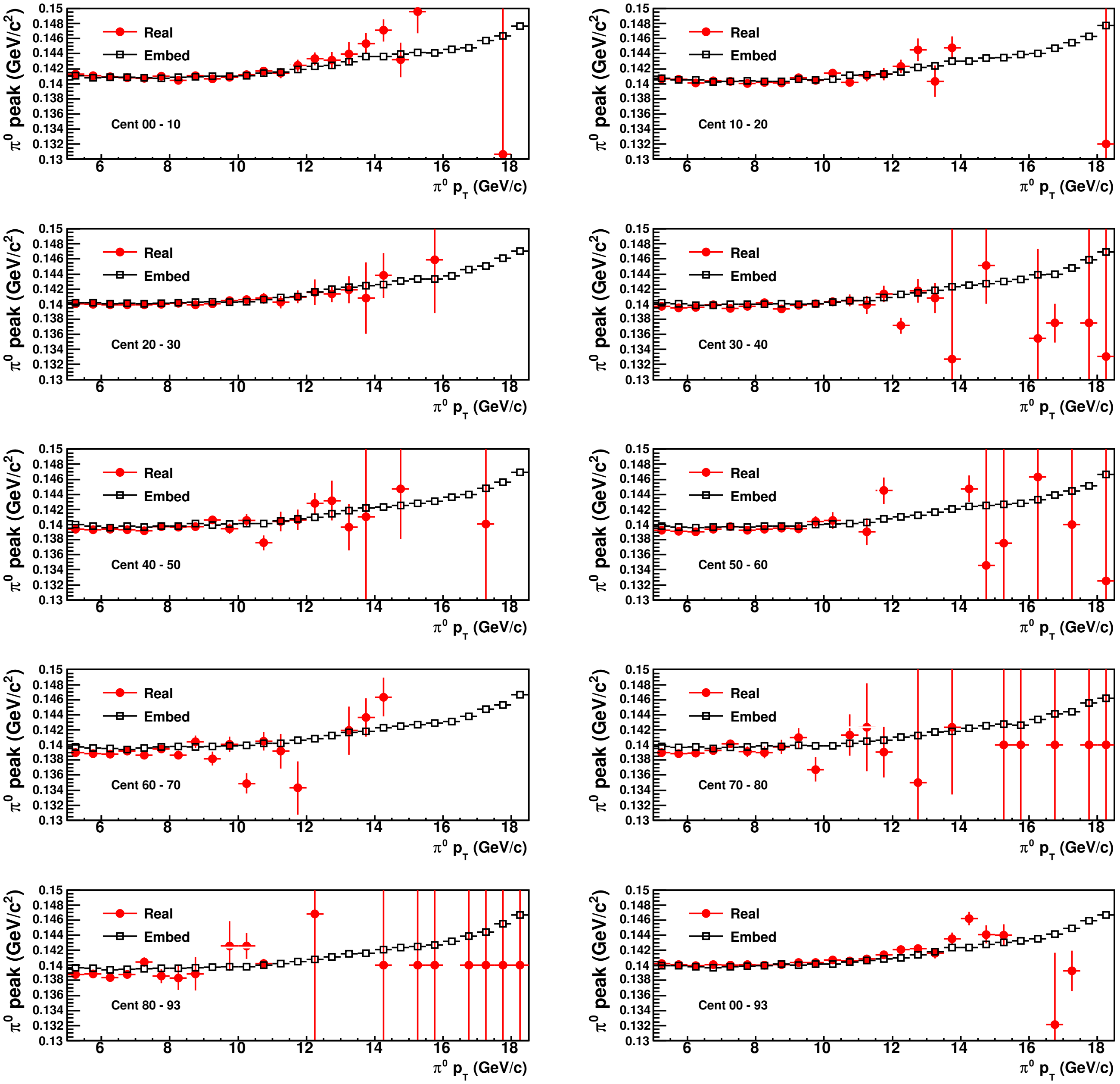

Figure 5.25: The mass of π^0 as a function of p_T for each 10 % centrality class. Red and black points are the measured data and simulation, respectively.

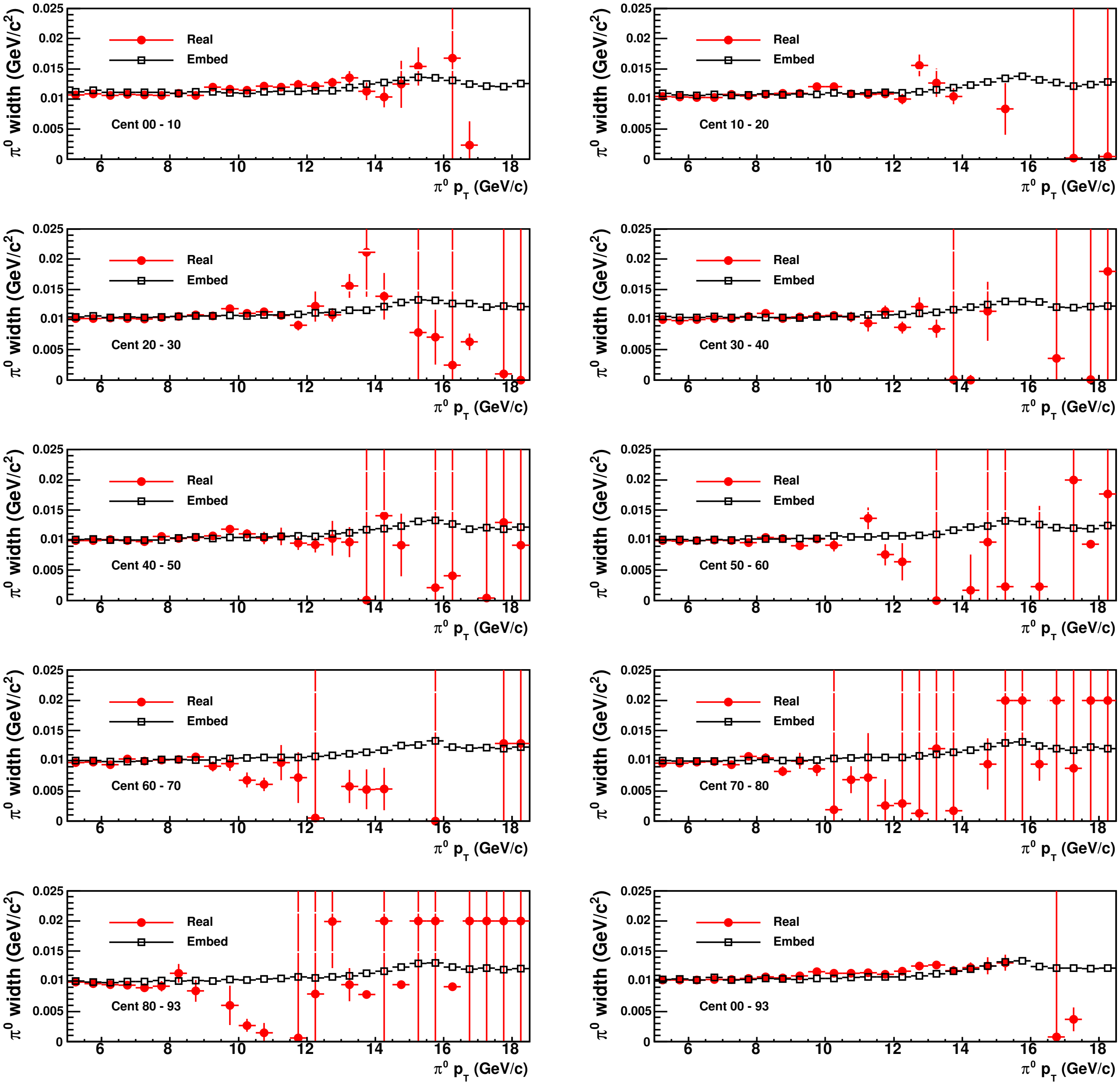

Figure 5.26: The mass widths of neutral pion as a function of p_T for each 10 % centrality class. Red and black points show the measured data and simulated data, respectively.

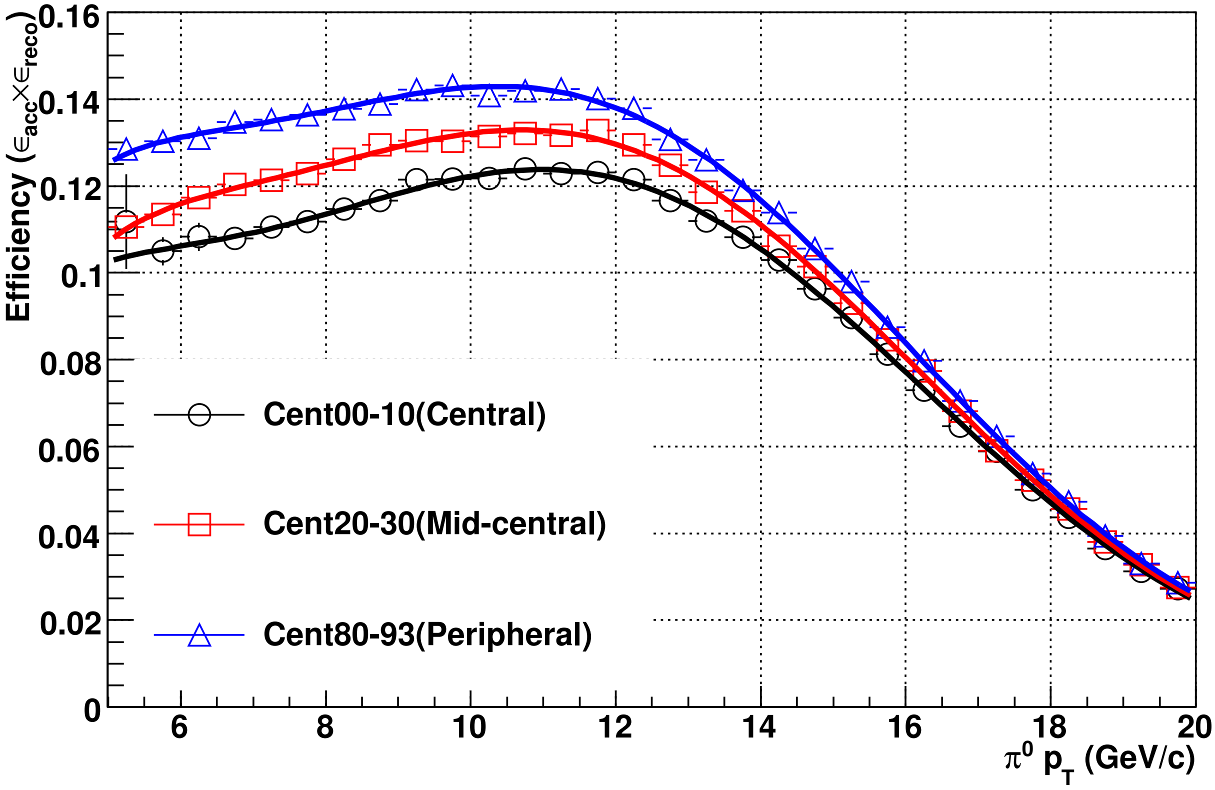

Figure 5.27: Neutral pion efficiency as a function of p_T for 0–10, 20–30 and 80-93 % centrality classes. The shower shape cut ($\chi^2 < 3$) are applied.

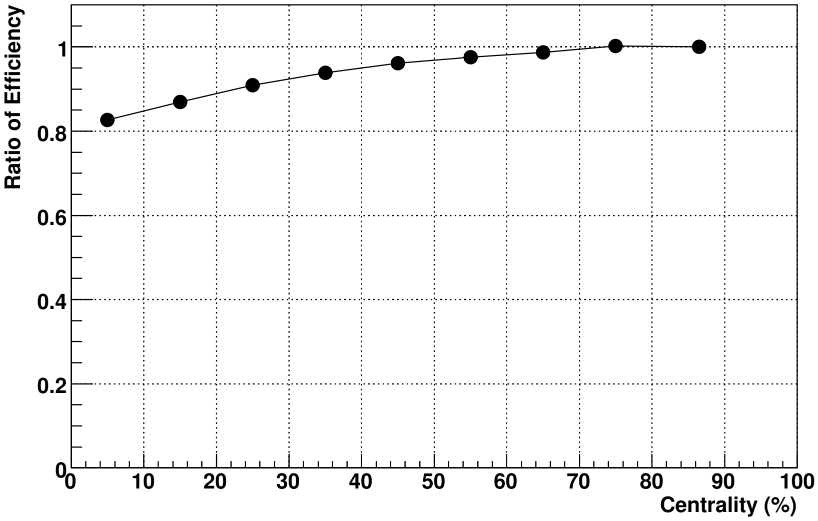

Figure 5.28: Ratio of the efficiency at $p_T = 10$ GeV/c as a function of centrality. The shower shape cut ($\chi^2 < 3$) are applied.

steeply falling spectrum as shown in Fig 5.29, the situation is different. The change of yield in each bin is dominated by the gain from lower p_T, which is larger than the loss for this p_T bin, the feed down from higher p_T bin plays only a minor role. This leads to an overall shift of the yield toward higher p_T bins and an efficiency larger than one. For the case of steely falling spectra, an error is introduced when plotting the extracted yield for a given p_T at the center of the bin, as it does not represent the center of gravity of the distribution within the bin. This effect becomes worse for larger bin widths and steeper falling spectra. The way to overcome this problem is two, shifting the values of p_T horizontally or shifting the values of the yield vertically. If the values of the yield are shifted, the values of p_T do not change.

In order to derive this shift, a pure power-law fit function is fitted to the measured invariant yield spectrum. A pure power-law fit is considered to be a good approximation of the true spectrum of π^0. For this function $f(p_T)$, the average yield in a given central point of the bin width, $f(p_T^c)$, and the bin width, Δp_T, is compared to the value of the function at the central point.

$$r = \frac{\frac{1}{\Delta}\int_{p_T^c-\Delta/2}^{p_T^c+\Delta/2} dp_T f(p_T)}{f(p_T^c)}. \tag{5.70}$$

The corrected yield is given by the following expression,

$$\frac{dN_{\mathrm{corr}}}{dp_T} = \frac{1}{r}\frac{dN_{\mathrm{uncorr}}}{dp_T}, \tag{5.71}$$

where N_{corr} and N_{uncorr} are the number of the corrected and uncorrected yields of π^0, respectively.

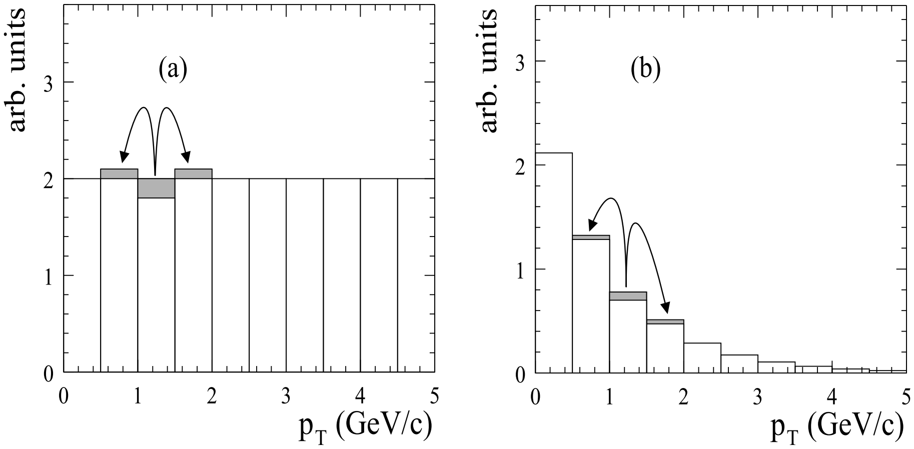

Figure 5.29: Illustration how the efficiency is affected by different shapes of input spectrum [76].

5.10.3 Systematic Uncertainty of Invariant Yield

The systematic uncertainties for this measurement include the following sources. These uncertainty sources are categorized by three types.

- Type-A: p_T-uncorrelated error
  It might be p_T-correlated and the correlation is not known (e.g. points at low p_T might move down while points at high p_T move up.)
- Type-B: p_T-correlated error
  All points move in the same direction.
- Type-C: p_T-correlated error
  All points move by the same factor (scale error)

Yield Extraction

Two kinds of methods are used for this estimation. One is to use the fixed mass window, and the other is to use the two sigma from the peak of π^0 mass obtained by the Gaussian fit. The mass window is fixed for 0.11 to 0.17 $[\mathrm{GeV}/c]^{-2}$ corresponding to about $\pm 3\ \sigma$. Figure 5.30 shows the ratio of the yields with the two sigma to with the fixed mass window as a function of p_T for three centrality classes, and these ratio are correlated with p_T.

Energy Scale

For simulation, the energy scale and its width of π^0 are compared to the measured data. The deposited energy in a tower is smeared to reproduce both the energy scale and its width of π^0 in the real data via the simulation.

As shown in Fig. 5.26, the width of π^0 for all centrality classes reproduce the measured data. As shown Fig 5.25, the difference between the measured and the simulation is about

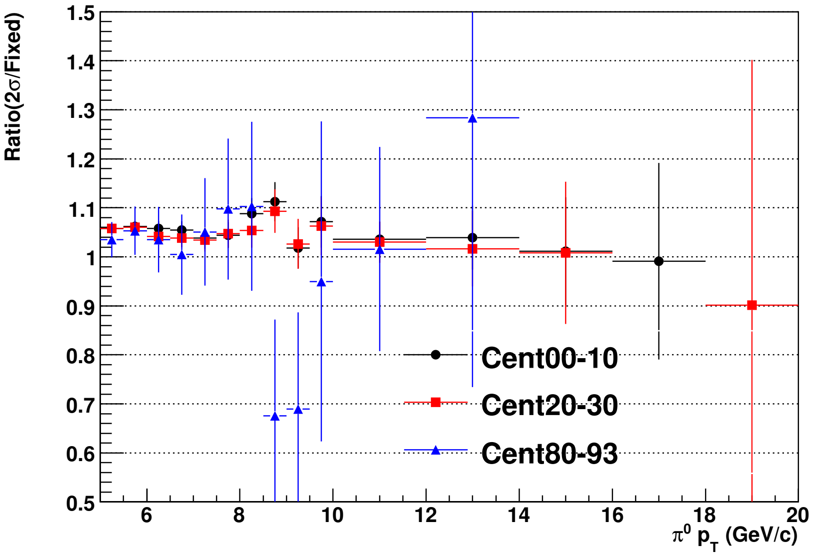

Figure 5.30: The ratio of the mass window for the two sigma and fixed mass window as a function of p_T at three centrality classes.

less than 0.5 %. The difference of the energy scale affects the yield of π^0. This uncertainty is evaluated with the power-law function which is an approximate to reproduce the p_T spectrum of π^0.

The power-law function, A/p_T^n, is shifted by ±0.5 % along the p_T direction, and the function shifted by 0.5 %, $f_{shift}(p_T)$ is given as,

$$f_{\mathrm{shift}}(p_T) = \frac{A}{(1.005 \cdot p_T)^n}, \tag{5.72}$$

where A and n denote an amplitude and power of the function, respectively. As taken the ratio of the power-law function to the shifted one, the difference of the yield is about 5 %. This is assigned to the systematic uncertainty from the energy scale.

Photon Identification

The shower shape cut is applied to the data to identify photons. The yields reconstructed with the shower shape cut ($\chi^2 < 3$) is compared to one with no shower shape cut (NoPID cut).

Figure 5.31 shows the ratio of the invariant yield with no shower shape cut to those with chi-square cut as a function of p_T for each 10 % centrality class. As shown in fig. 5.31, these ratios are p_T correlated. Assigned uncertainties are shown in Table 5.4.

π^0 Merging

As increasing p_T of π^0, the opening angle of the two decay photons decreases, and eventually they will be reconstructed as a single cluster. Due to the merging effect, the

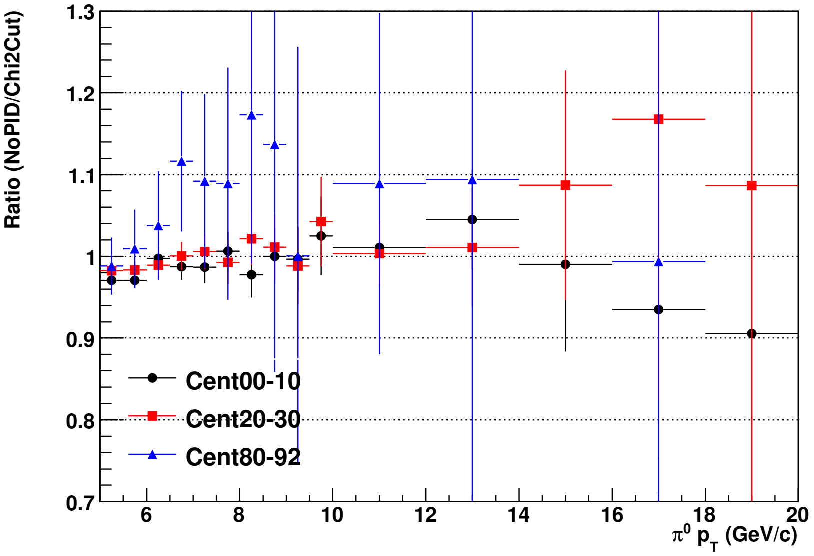

Figure 5.31: The ratio of invariant yield with no shower shape cut to those with chi-square cut ($\chi^2 < 3$) as a function of p_T for each 10 % centrality class.

detection efficiency of π^0s at high p_T decreases. Figure 5.32 shows the comparison to the cluster merging probability obtained from GEANT simulation and that from the beam test parametrization.

As shown in Fig. 5.32, such as a merging effect from π^0 starts in the PbSc at about p_T ~10-11 GeV/c, at 16 GeV/c already about 50 % of all π^0s are identified as a single cluster. The Merging which depends on the clustering algorithm itself has been studied extensively in the test beam and simulations, the measured and simulated efficiency curves have similar shape but are shifted by about 1 GeV. This evaluation for the merging effect is obtained from Ref. [77].

Geometrical Acceptance

The eight order polynomials is used to obtain the detection efficiency of π^0. The difference between the simulated data points in Fig. 5.27 and the eight order polynomials is assigned as the systematic uncertainty from the acceptance Figure 5.33 shows the ratio of the simulated data points to the function (8-th polynomials) as a function of p_T for each 10 % centrality class. As shown in Fig. 5.33, the difference is quite small (~ 1 %).

Reconstructed π^0 from Off-vertex

Two sources of π^0s not coming from the vertex (off-vertex π^0) are considered as a systematic uncertainty: products from hadrons interacting with detector materials and feed-down products from weak decay of higher mass hadrons. Based on simulation both types of background were found to be negligible (less than 1 % at $p_T > 2.0$ GeV/c) except for π^0s

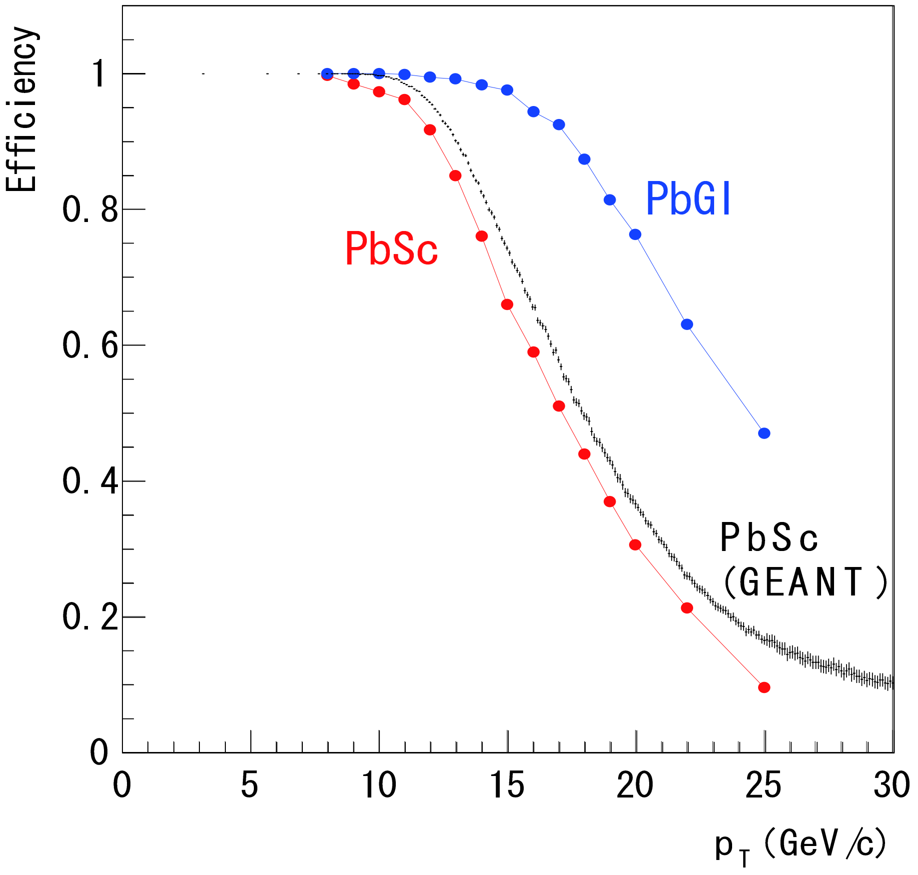

Figure 5.32: The probability that a π^0 is lost due to the cluster-merging inefficiency [78]. Red: PbSc, parameterization of the test beam data up to 7.5 GeV/c and points at 40 GeV/c in between were obtained from the fast Monte Carlo (shower parameterization). Black: PbSc, full GEANT simulation. Blue; PbGl, In all three cases, the energy asymmetry cut, $\alpha < 0.8$, is applied.

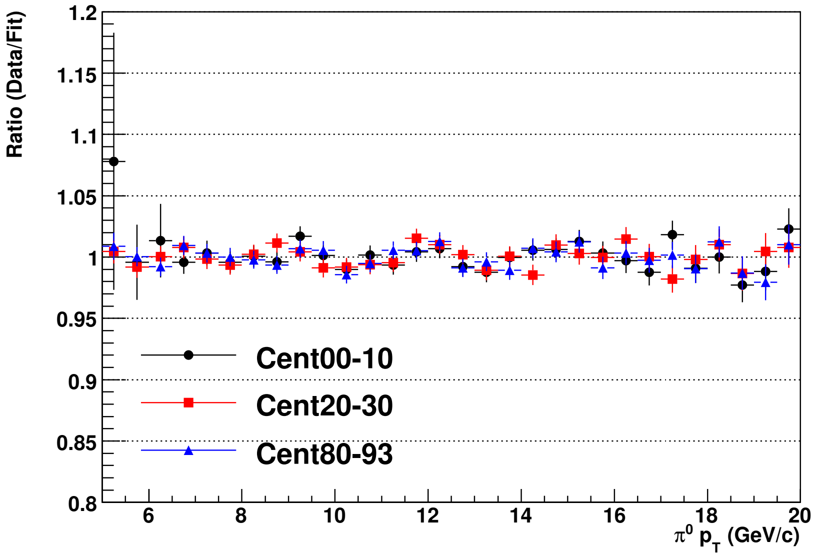

Figure 5.33: The ratio of the simulated data points to the 8-th polynomial function as a function of p_T for each 10 % centrality class.

from K_S^0 decay (3 % of π^0 yield for $p_T > 1$ GeV/c), which has been subtracted from the data. However, the contributions from K_S^0 survive at a constant 3 % level up to 6 GeV/c. The left panel of Fig. 5.34 shows the ratio of the primary to secondary reconstructed π^0 spectra as a function of p_T. Most of contributions come from K_S^0 particles at high-p_T region.

5.11 Summary of Systematic Uncertainty

The systematic uncertainties for the Glauber calculation and the measurement of azimuthal anisotropy and invariant yield of π^0 are summarized in Table 5.2, 5.3, and 5.4.

5.11.1 Systematic Uncertainty of Glauber Calculation

The average N_{part}, N_{coll}, $T_{\mathrm{Au+Au}}$, b and their systematic uncertainties for each centrality class are summarized.

5.11.2 Systematic Uncertainty of Azimuthal Anisotropy

The systematic uncertainty sources for measurement of the azimuthal anisotropy v_2 of neutral pion are summarized in Table 5.3. All systematic uncertainties are estimated at low p_T due to the low statistics at high p_T.

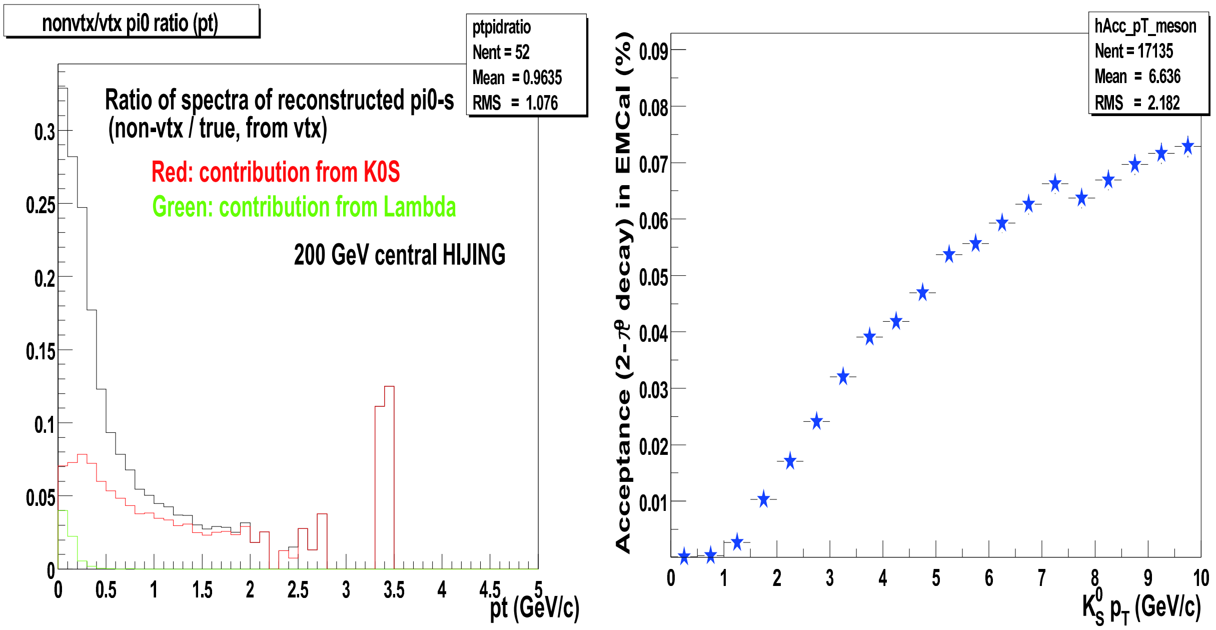

Figure 5.34: Left: Ratio of reconstructed secondary π^0s to all π^0s in HIJING events. Above 1 GeV/c, the ratio levels off at 3 % and is dominated by K^0_S decays. Right: the acceptance of inclusive two π^0 decay products as a function of p_T.

Centrality Class (%)	$\langle N_{part} \rangle$	$\langle N_{coll} \rangle$	T_{AuAu} (mb^{-1})	$\langle b \rangle$ (fm)
00-10	325.8±3.8	960.2±96.1	22.86±1.64	3.1±0.1
10-20	236.1±5.5	609.5±59.8	14.51±1.01	5.6±0.2
20-30	167.6±5.8	377.6±36.4	8.99±0.67	7.3±0.3
30-40	115.5±5.8	223.9±23.2	5.33±0.46	8.7±0.3
40-50	76.2±5.5	124.6±14.9	2.97±0.32	9.9±0.4
50-60	47.1±4.7	63.9±9.4	1.52±0.21	10.9±0.4
60-70	26.7±3.7	29.8±5.4	0.71±0.13	11.9±0.47
70-80	13.7±2.5	12.6±2.8	0.30±0.07	12.6±2.8
80-93	5.6±0.8	4.2±0.8	0.10±0.02	13.9±0.5

Table 5.2: N_{part}, N_{coll}, T_{AuAu}, and b by the Glauber calculation for Au+Au collisions at $\sqrt{s_{NN}}$ = 200 GeV. Errors are the systematic uncertainties.

	cent(00–10/10–20)	cent(20–30/30–40)	cent(40–50/50–60)	type
Yield extraction (%)	6.0	3.0	3.0	B
PID efficiency (%)	5.0	1.0	1.0	B
Event Plane (%)	10.0	5.0	10.0	C
Total (%)	12.7	5.9	10.5	

Table 5.3: Systematic uncertainties of the azimuthal anisotropy v_2 of neutral pion.

5.11.3 Systematic Uncertainty of Invariant Yield

The systematic uncertainty sources for measurement of neutral pion yield are summarized in Table 5.4.

	p_T indep.	6 GeV/c	8 GeV/c	10 GeV/c	16 GeV/c	type
Yield extraction (%)		5.0	2.0	2.0	2.0	B
Energy scale (%)		5.0	5.0	5.0	5.0	B
PID efficiency (%)		5.0	5.0	5.0	5.0	B
π^0 merging (%)				4.4	28.0	B
Acceptance (%)	1.0					B
Off-vertex π^0 (%)	1.5					C
Total (%)	1.8	8.6	7.3	8.6	28.9	

Table 5.4: Systematic uncertainties of the invariant yields of neutral pion.

Chapter 6

Results

6.1 Invariant Yield of Neutral Pion

Figure 6.1 shows the the invariant yield of neutral pion as a function of p_T for each 10 % centrality class, 0–5 % and minimum bias events in Au+Au collisions at $\sqrt{s_{NN}} = 200$ GeV. The invariant yields of π^0 were measured up to the p_T range of 20 GeV/c at mid-rapidity ($|y| < 0.35$).

6.2 $R_{AA}(p_T)$ of Neutral Pion

The yield of π^0 in $p + p$ collisions as a reference obtained at RHIC-Year2005 (Run5) is used to obtain the nuclear modification factor $R_{AA}(p_T)$. When the R_{AA} is calculated, the yields with Au+Au collisions are divided by the yields with $p + p$ for point-to-point. Since the cross section of π^0 in Run5 $p + p$ collisions is not available p_T range above 20GeV/c, the R_{AA} in RHIC-Year7 is also measured up to 20 GeV/c. Figure 6.2 shows the RHIC-Year7 and published R_{AA} for π^0 as a function of p_T for each centrality class. Red and black point show results obtained in this thesis and the published data [75] in PHENIX, respectively. Gray bands shows the global systematic uncertainties. The global systematic uncertainties are quadric sum of T_{AA}, $p + p$ normalization and π^0 from off-vertex uncertainties.

6.3 Azimuthal Anisotropy v_2 of Neutral Pion

The azimuthal anisotropy v_2 at mid-rapidity ($|y| < 0.35$) is obtained from the azimuthal angular distributions with the correction from the above event plane resolution. Figure 6.3 show the azimuthal anisotropy v_2 as a function of p_T. This have been measured by the author and the state University of New York at Stony Brook (SUNY). Open black circles and closed red circles show the SUNY's and the author's, respectively. The bands shows the systematic uncertainties. Both results are consistent within errors.

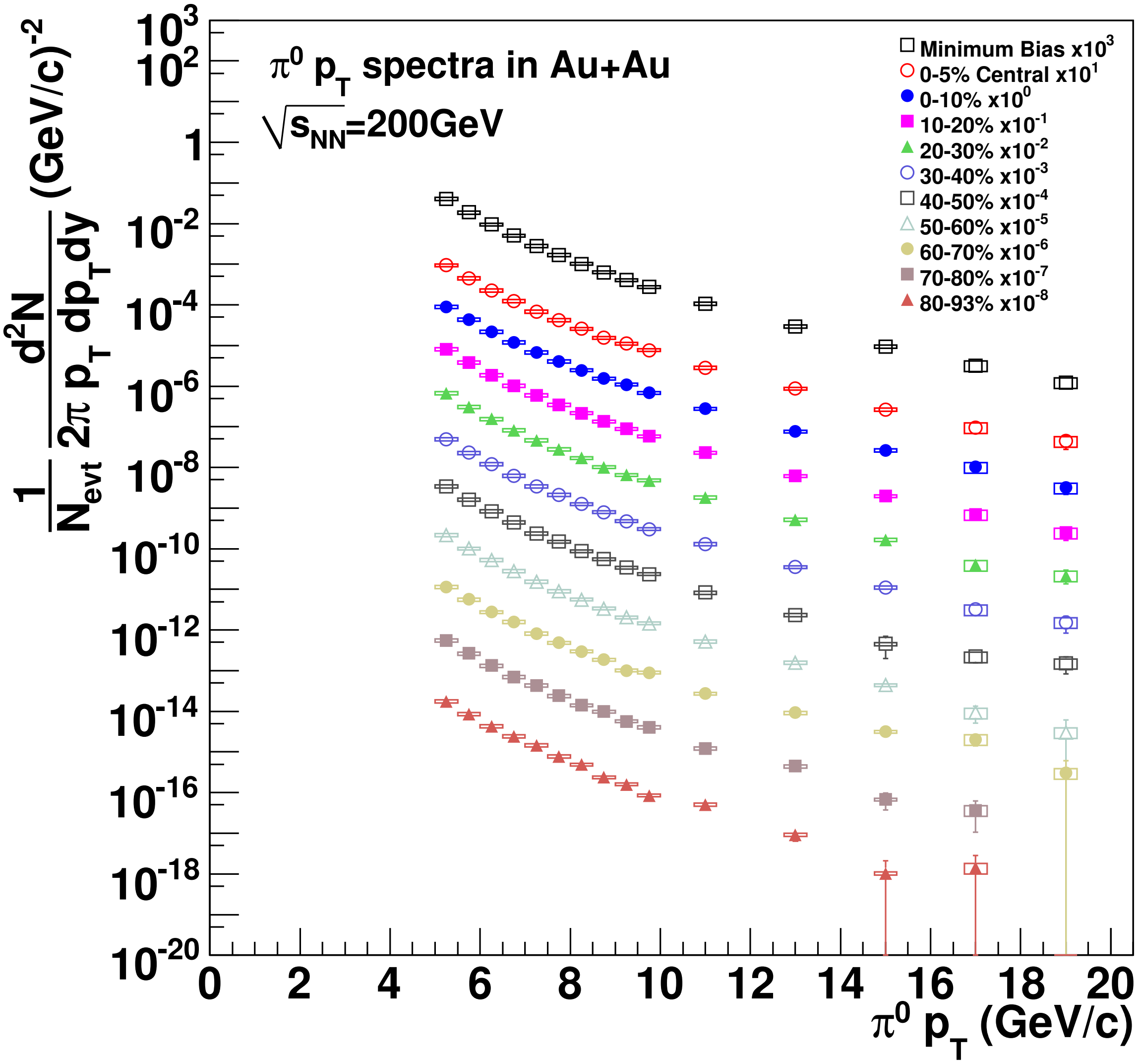

Figure 6.1: The invariant yield of π^0 as a function of p_T for each 10 % centrality class, 0–5 % centrality and minimum bias.

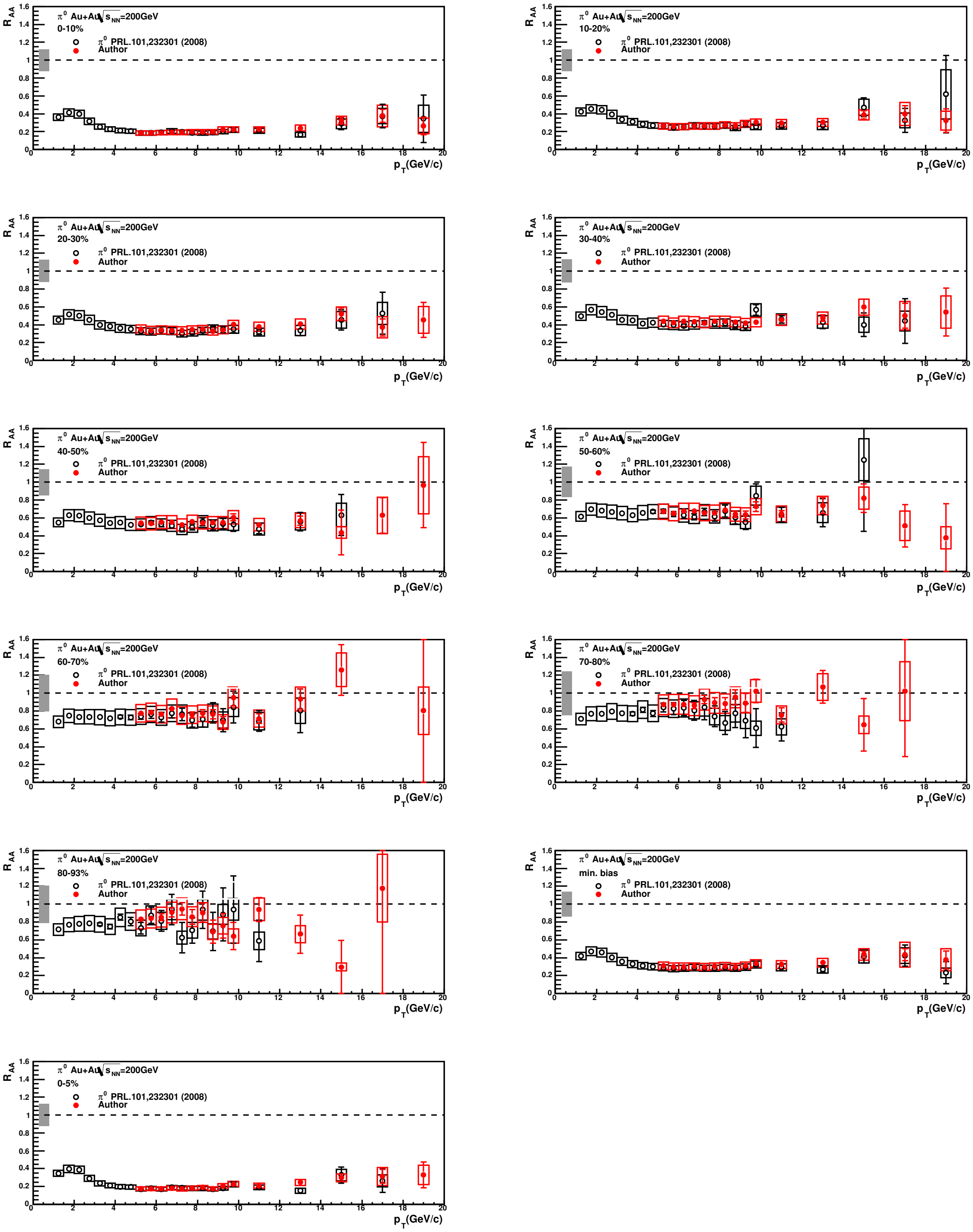

Figure 6.2: The nuclear modification factor of π^0 as a function of p_T for every 10 % centrality class, 0–5 % centrality and minimum bias. Red closed and black open circles are the results obtained in this thesis and the published data [75] at PHENIX.

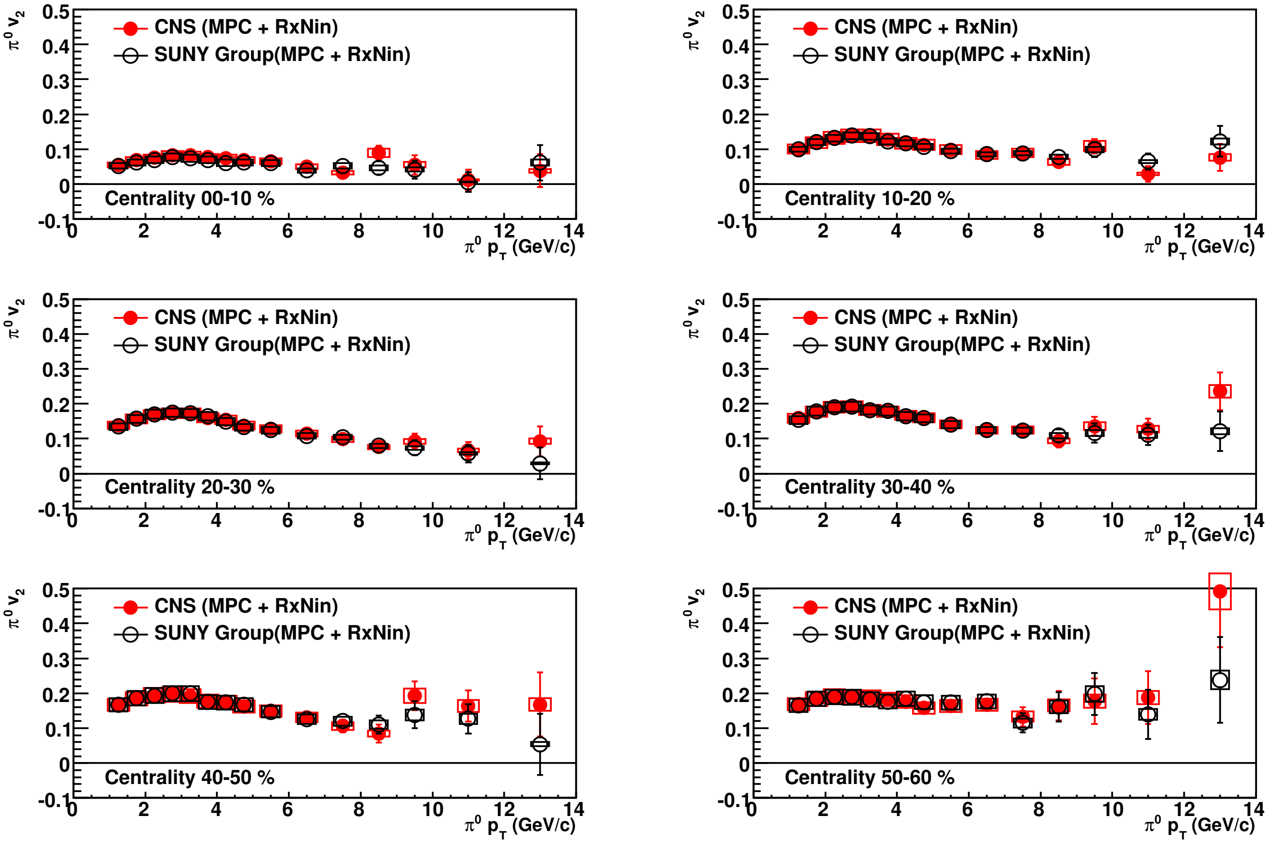

Figure 6.3: The azimuthal anisotropy v_2 of π^0 measured at mid-rapidity ($|y| < 0.35$) as a function of p_T for each 10 % centrality class.

6.4 $R_{AA}(p_T,\Delta\phi)$ of Neutral Pion

The transverse momentum and the number of participant dependence for the $R_{AA}(p_T, \Delta\phi)$ are described.

6.4.1 p_T Dependence for $R_{AA}(p_T, \Delta\phi)$

Figure 6.4 shows the $R_{AA}(p_T,\Delta\phi)$ as a function of p_T for each 10 % centrality class. Black (closed circle), red (closed square), green (closed triangle), blue (closed triangle), purple (open circle) and light green (open square) correspond to the $R_{AA}(p_T,\Delta\phi)$ of 0–15, 15–30, 30–45, 45–60, 60–75, and 75–90 degree. The systematic uncertainty of the $R_{AA}(p_T,\Delta\phi)$ is dropped from this figure. The gray band represent the systematic uncertainty of inclusive $R_{AA}(p_T)$.

6.4.2 N_{part} Dependence for $R_{AA}(p_T, \Delta\phi)$

Figure 6.5 shows the $R_{AA}(p_T, \Delta\phi)$ integrated into $6 < p_T < 10$ GeV/c as a function of N_{part}. Figure 6.6 shows the $R_{AA}(p_T, \Delta\phi)$ integrated into $p_T > 10$ GeV/c as a function of N_{part}. For both figures, red closed and blue circles are the in-plane and out-of-plane R_{AA} of π^0, respectively. The boxes are each systematic uncertainties in the measurement of the azimuthal anisotropy v_2, and the systematic uncertainties in the measurement of the $R_{AA}(p_T)$ are not shown in the figures.

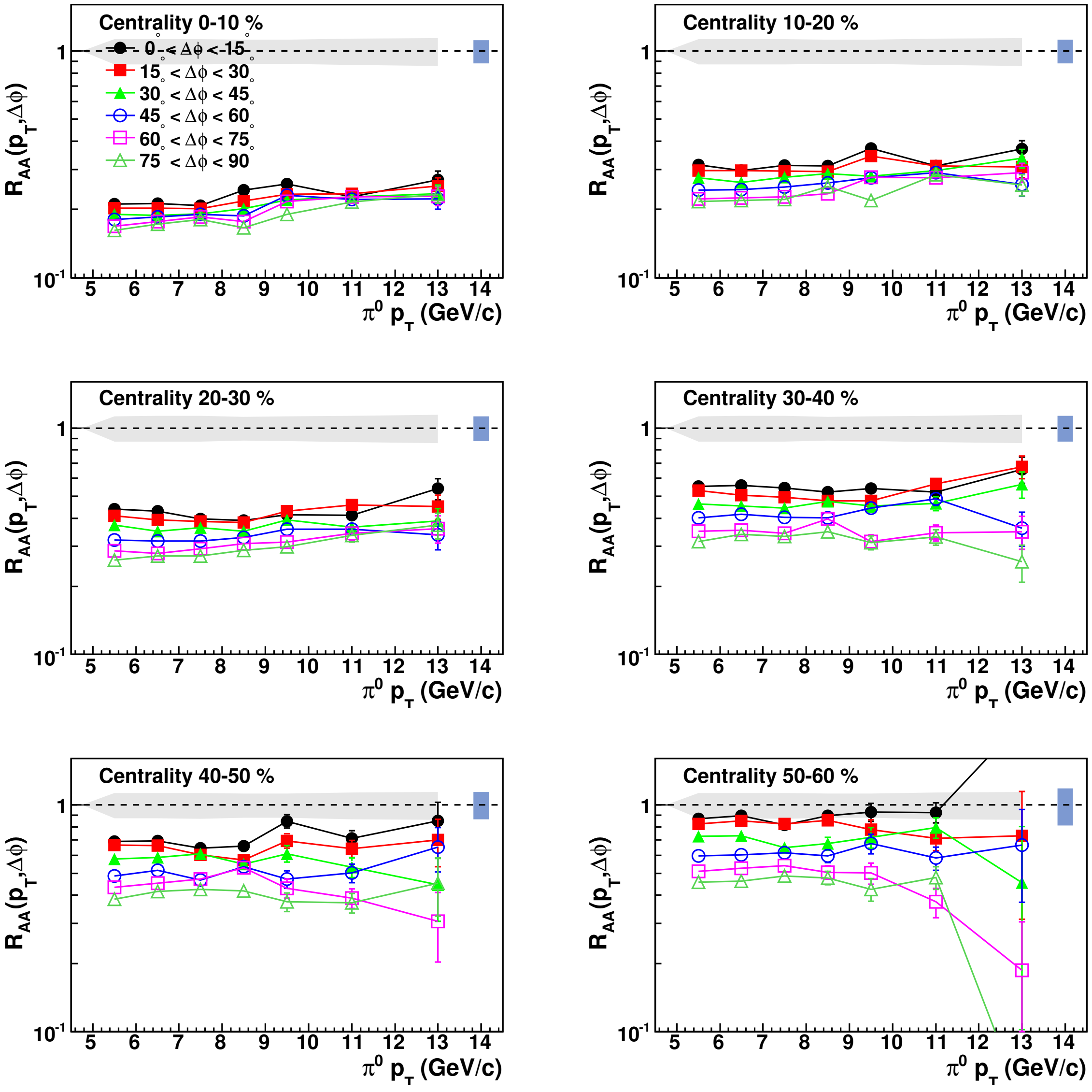

Figure 6.4: The $R_{AA}(p_T,\Delta\phi)$ as a function of p_T for each 10 % centrality class.

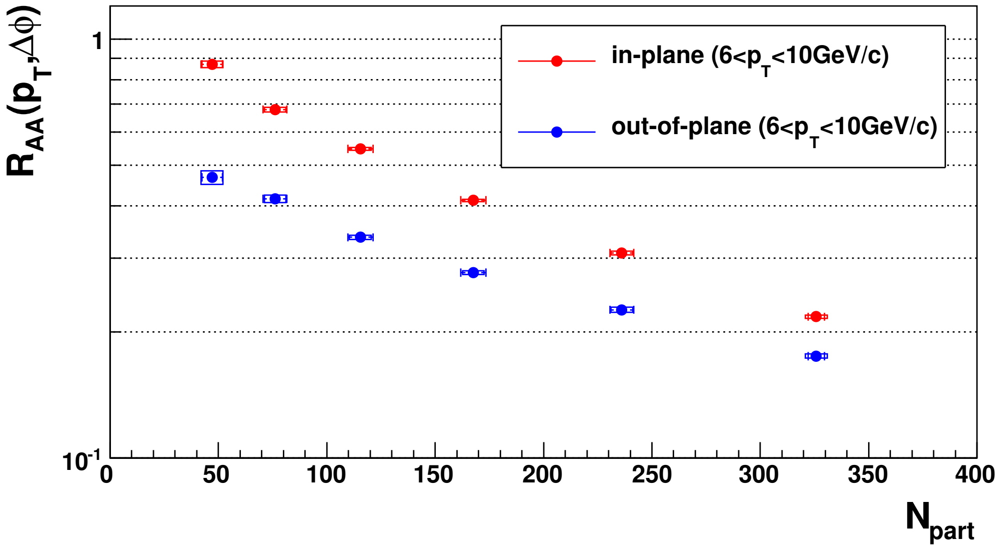

Figure 6.5: N_{part} dependence for the $R_{AA}(p_T, \Delta\phi)$ integrated into the p_T region of $6 < p_T < 10$ GeV/c of π^0.

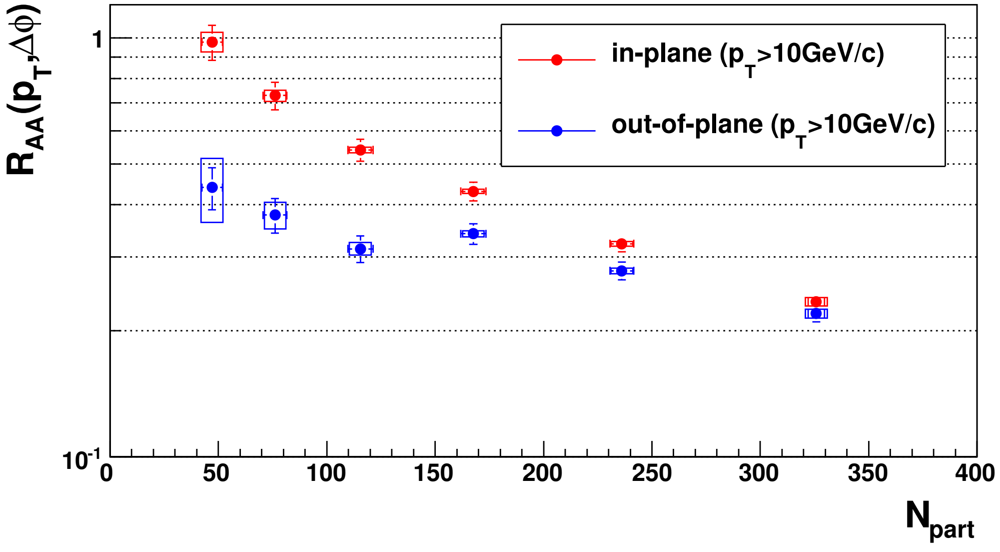

Figure 6.6: N_{part} dependence for the $R_{AA}(p_T, \Delta\phi)$ integrated into the p_T region of $p_T > 10$ GeV/c of π^0.

Chapter 7

Discussions

7.1 Recent Parton Energy Loss Models

The approaches to describe the parton energy loss in the hot/dense matter include:

- Recursive operator in opacity (GLV) [79]
- Higher twist (HT) [80]
- Finite temperature field theory approach (AMY) [81]
- Path Integral approach to the opacity expansion (BDMPS-Z/ASW) [82, 83]
- Hybrid of ASW and AdS/CFT correspondence [84]

7.1.1 GLV Formalism

The GLV formalism is proposed by M. Gyulassy, P. Lévai, and I. Vitev, and it is the perturbative treatment of the energy loss by an expansion in the opacity L/λ, where L is the path length which partons pass through and λ is the mean free path [79]. It is assumed in the GLV formalism that partons are lost by mainly radiative process.

A realistic transverse collision geometry and Bjorken 1-D expansion of the medium are taken into account in the model, and the energy loss is expressed in terms of the initial gluon density per unit rapidity dN^g/dy as follows:

$$\Delta E = \frac{9\pi C_R \alpha_s^3}{4}\Big(\frac{L}{\pi R^2}\frac{dN^g}{dy}\Big)\log\frac{E}{\mu}, \tag{7.1}$$

where C_R is the Casimir factor of parton, $C_R = C_A = 3$ for gluon, and $C_R = C_F = 4/3$, α is a coupling constant for QCD, and μ is the Debye screening mass in the plasma. This calculation incorporates the Cronin effect and the nuclear shadowing effect. Recent parton energy loss models are explained in Sec. 7.1. As shown in Eq. 7.1, one should note that the energy loss depends on the path length.

7.1.2 HT Formalism

The origin of the higher twist (HT) approximation scheme [80] lies in the calculations of medium-enhanced higher twist correction to the total cross section in deep inelastic scattering (DIS) off large nuclei [85]. The HT formalism incorporates only radiative energy loss process. Unlike the AMY and ASW formalism, the HT approach can directly calculate the medium-modified fragmentation function, and can obtain the final distribution of hadrons.

7.1.3 AMY Formalism

Arnold-Moore-Yaffe (AMY) proposed the calculation of the energy loss of the hard scattered partons induced by gluon bremsstrahlung in the deconfined phase [81]. The AMY formalism is considered in an extended medium in equilibrium at asymptotically high temperature, $T \to \infty$. The AMY approach incorporate not only radiative energy loss, but also collisional energy loss process. In contrast to the ASW and the HT approaches, the AMY approach includes flavor changing interactions in the medium. The AMY approach assumes a thermalized partonic medium and neglects the quenching of jets in the confined sector. In addition, interference between medium and vacuum radiation is not yet considered.

7.1.4 BDMPS-Z/ASW Formalism

The path integral approach for the energy loss of a hard jet propagation in a colored medium is Baier-Dokshitzer-Mueller-Peigne-Schiff (BDMPS-Z) scheme [82]. This approach are used by many theorists and is often referred to as Armest-Salgado-Wiedemann (ASW) scheme [83]. In this paper, this approach is called as ASW. The ASW approach includes only radiative energy loss process. This formalism assumes a model for the medium as an assembly of Debye screened heavy scattering centers which are well separated in the sense that the mean free path of a jet $\lambda \gg 1/\mu$ the color screening length of the medium.

The ASW approach to finite-length hot matter. The total energy loss ΔE in hot matter of the length L is given by the following expression.

$$\Delta E = \frac{\alpha_s C_R}{8} \frac{\mu^2}{\lambda_g} L^2 \ln\Big(\frac{L}{\lambda}\Big), \tag{7.2}$$

where R is the color representation of the incident parton.

7.1.5 ASW-AdS/CFT Formalism

M. Marquet and T. Renk proposed the energy loss model incorporating ASW formalism with Anti-de Sitter space/Conformal Field Theory (AdS/CFT) correspondence [84]. In this model, the hard process is treated perturbatively, and ASW formalism is used, while the soft process which is assumed to be strong coupling dynamics are used with the

AdS/CFT correspondence. This model has stronger path length dependence for the energy loss than standard ASW formalism.

The AdS/CFT correspondence represents the equivalence between $N = 4$ supersymmetric Yang-Mills (SYM) gauge theory and the string theory on 5-dimensional anti-de Sitter space [86]. Especially, the gauge theory at finite temperature in the string coupling limit corresponds to the classical gravity theory for the black hole on 5-dimensional anti-de Sitter space. The calculation of the gauge theory in the strong coupling is difficult due to its non-perturbative nature. Thus, this correspondence is expected to be one approach to the strong coupling gauge theory, and it might provide a clue to the treatment of strong coupling system.

One application for the AdS/CFT correspondence is the ratio of the shear viscosity η to the entropy density s, (η/s) which is used with AdS/CFT correspondence [87]. Another example is the energy loss of heavy quark. In the Ref. [88], the drag force on heavy quark in QGP is obtained by the single electron data and the calculation of relativistic Langevin equation and ideal hydrodynamics. The obtained value of the drag force agree with the the AdS/CFT approach for strongly interacting plasma.

7.2 Energy Loss Models in 3-D Hydrodynamics

The formalism of the energy loss describes the partonic process in the created matter. However, the formalism of the energy loss does not involve the variation of the density in the created matter and time which comes from the space-time evolution.

A three-dimensional (3D) relativistic hydrodynamics has been proposed to reproduce the effect of the space-time evolution by T. Hirano and Y. Nara [89]. The 3D hydrodynamics reproduced the results at RHIC, for example, the pseudo-rapidity and centrality dependence for the elliptic flow of charged hadrons, and the centrality and p_T dependence for the production of charged hadrons at low p_T region ($p_T <\sim 3$ GeV/c) [90]. Thus, the 3D hydrodynamics provide us with the matter involving the space-time evolution. In order to obtain the realistic parton energy loss model, the energy loss formalism should incorporate in 3D hydrodynamics.

S. Bass *et al.* proposed the parton energy loss models incorporating HT, AMY and BDMPS-Z/ASW in 3D hydrodynamics [91, 92, 93, 94].

7.2.1 Path Length Dependence for Parton Energy Loss

As described in Sec. 2.6, several parton energy loss models predict that the quantity of the energy loss in the medium depend on the path length L. If the collisional energy loss is a dominant process, the quantity of the energy loss is expected to be monotonically proportional to the path length.

If the radiative energy loss is a dominant process, energy loss models based on pQCD such as HT, AMY and ASW propose that the quantity of the energy loss is proportional to the square path length, L^2, static medium which does not consider the space-time evolution [83]. Additionally, the ASW model using AdS/CFT correspondence predict that the quantity of the energy loss is proportional to L^3 in static medium which does not consider the space-time evolution [84]. One should recognize that the expected power index of the path length would change in the medium with the time evolution for all proposed models.

7.3 Comparison to Parton Energy Loss Models

The measurement of neutral pion yields has been performed at RHIC-PHENIX. The result are compared to the several energy loss model based on pQCD which are introduced in previous sections. All parameters in all models incorporating the hydrodynamic evolution have been fixed so as to reproduce the soft observables which include elliptic flow, pseudo-rapidity distributions and low-p_T single particle spectra. The hydrodynamic model provides a space-time evolution of the temperature, energy density, flow velocity and QGP to hadron gas fraction. All hydrodynamic calculations are assumed to have an initial thermalization time of $\tau_0 = 0.6$ fm/c. All parameters in models are expressed as the transport coefficient, $\hat{q}$. The transport coefficient is defined as follows:

$$\hat{q} \equiv \frac{\mu^2}{\lambda} \ [\mathrm{GeV}^2/\mathrm{fm}], \tag{7.3}$$

where μ^2 is the average squared transverse momentum transferred from the medium to the parton per collision, and λ is the mean free path of partons. The transport coefficient involves the bulk properties of the medium. It should be noted that each $\hat{q}$ in all models has different relation to the bulk properties. AMY formalism is decidedly related to the temperature, while HT and ASW formalism is not directly related to the temperature. The $\hat{q}$ in ASW has been related to the energy density, ϵ, via $\epsilon^{3/4}$ scaling, while the $\hat{q}$ in HT has been related to the temperature, T, via T^3 or the entropy density, s, of the local medium.

7.3.1 Centrality Dependence for R_{AA}

The value of $\hat{q}$ in the three models is fixed so as to reproduce R_{AA} of π^0 at centrality 0–5 %. Figure 7.1 shows the comparison to the measured R_{AA} of π^0 as a function of p_T and the curves for AMY, HT and ASW models. The values of $\hat{q}_0$ defined as the $\hat{q}$ at $\tau = 0.6$ fm/c at the centrality 0–5 % events in AMY, HT and ASW are 4.1, 2.3 and 10 GeV^2/fm, respectively. The difference among the models are as much as a factor of five, while the models agree with the data well.

7.3.2 Transverse Momentum Dependence for $R_{AA}(p_T, \Delta\phi)$

Even though the quite large difference of $\hat{q}_0$ exits in models, all the models reproduce the p_T and centrality dependencies for the R_{AA}. Therefore, not only the R_{AA}, but also new

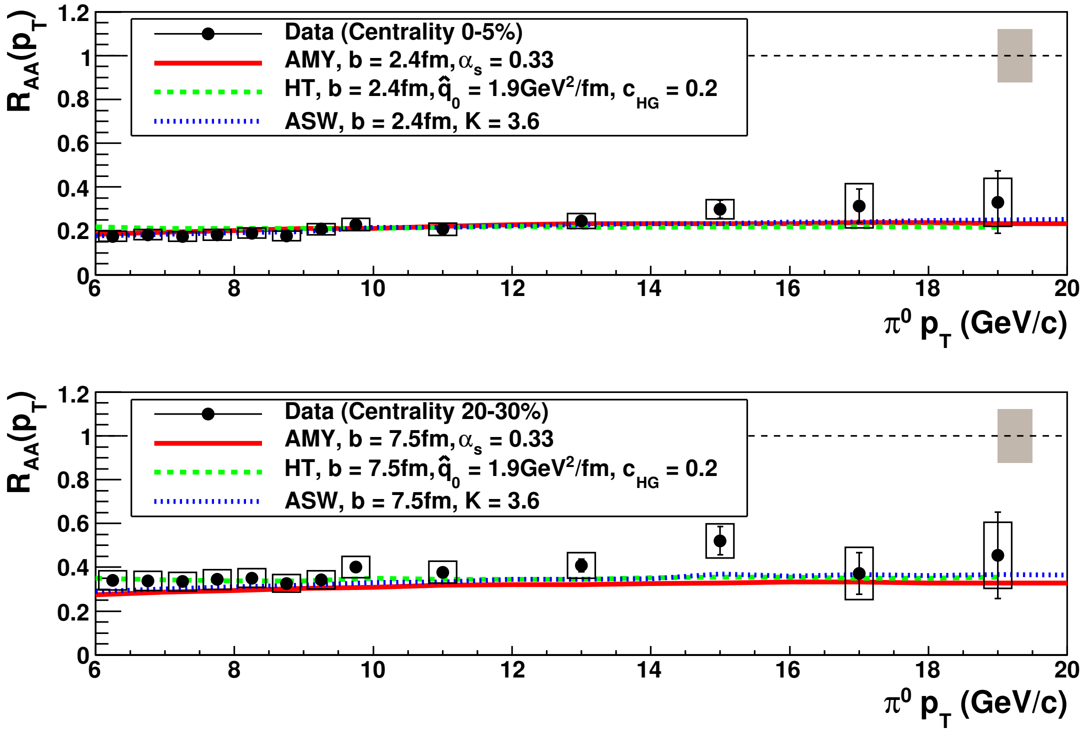

Figure 7.1: Upper panel: the nuclear modification factor of π^0 as a function of p_T at centrality 0–5 %. Red solid, green dashed and blue dotted-dashed curves are the expectations of AMY, HT and ASW models, respectively. Lower panel: the nuclear modification factor of π^0 as a function of p_T at centrality 20–30 %. The theoretical curves in both panels are obtained from Ref. [94].

observable for R_{AA} is needed to study parton energy loss mechanism. As described in the previous section, the energy loss may depend on the path length which partons pass through. The path length dependence for the R_{AA} appear as the variation of yields with respect to the azimuthal angle. In fact, AMY, HT and ASW models predict the different azimuthal angular dependence for the R_{AA}.

In order to look at the R_{AA} with a large difference of the path length, the measured in-plane (0–15 degree) and out-of-plane (75–90 degree) R_{AA}s as a function of p_T are compared to several energy loss models in centrality 20–30 % which corresponds to non-central collisions.

Figure 7.2, 7.3, 7.4, 7.5 shows the comparison to the measured in-plane, out-of-plane and average R_{AA} as a function of p_T at centrality 20–30 %. The gray band on the R_{AA} =1 corresponds to the systematic uncertainty of the average $R_{AA}(p_T)$ of π^0. The light-blue band corresponds to the systematic uncertainty of the number of T_{AA}. The bands on the data points are the systematic uncertainty of the $dN/d\phi$ including the anisotropy v_2. Black open, red closed circles and blue closed squares are the average π^0 $R_{AA}(p_T)$, in-plane R_{AA} and out-of-plane R_{AA}, respectively.

As shown in Fig. 7.2, HT model has small azimuthal angular dependence for the R_{AA}. This model can reproduce neither of in-plane R_{AA} nor out-of-plane R_{AA}. As shown in Fig. 7.3, AMY model has small azimuthal angular dependence for the R_{AA} similar to HT model. However, AMY model reproduce the only out-of-plane R_{AA}, while the in-plane R_{AA} has large difference between the prediction and the data. As shown in Fig. 7.4, ASW model has larger azimuthal angular dependence for the R_{AA} than those of HT and AMY models. In spite of larger azimuthal angular dependence, the in-plane R_{AA} can not be reproduced by the prediction. Even though the measured data have large errors, ASW model seems to be close to the data at $p_T > 10$ GeV/c. The compared theoretical predictions are based on pQCD. Figure 7.5 shows the model prediction using AdS/CFT correspondence. This model is different from other pQCD based models as for the nature of the medium interacting with partons. This model seem to reproduce both of in-plane and out-of-plane R_{AA} at wider p_T range ($5 < p_T < 14$ GeV/c) relative to other models.

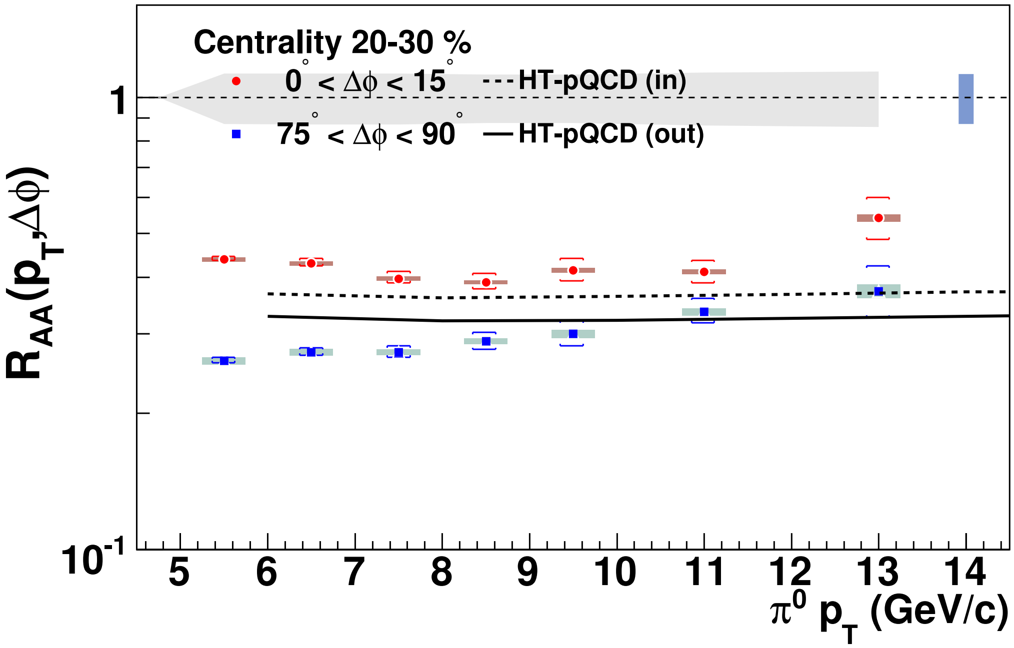

Figure 7.2: Comparison to HT model based in pQCD.

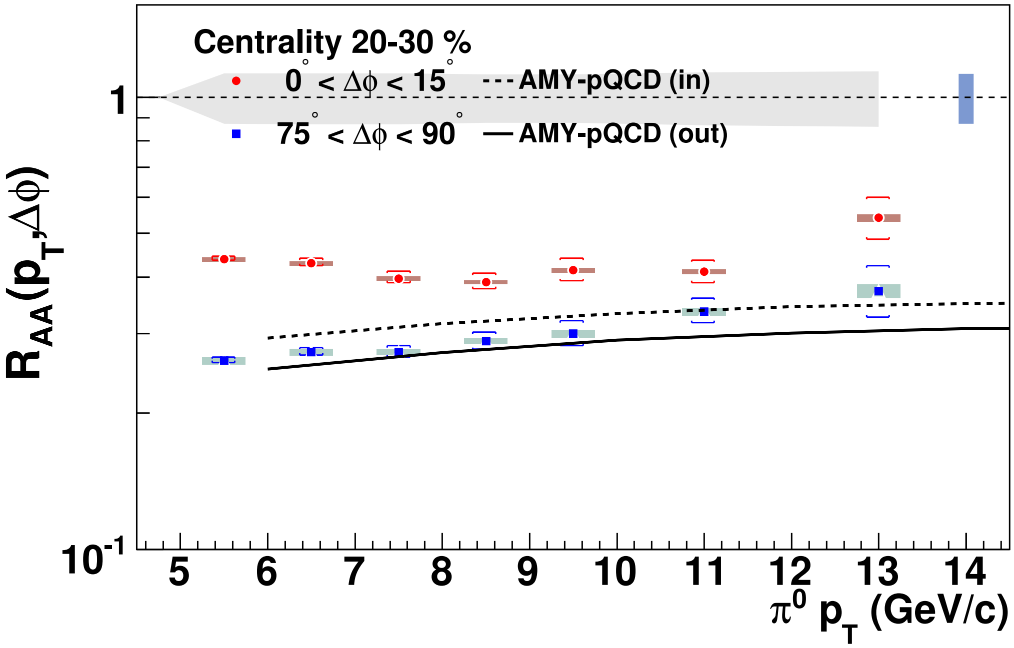

Figure 7.3: Comparison to AMY model based in pQCD.

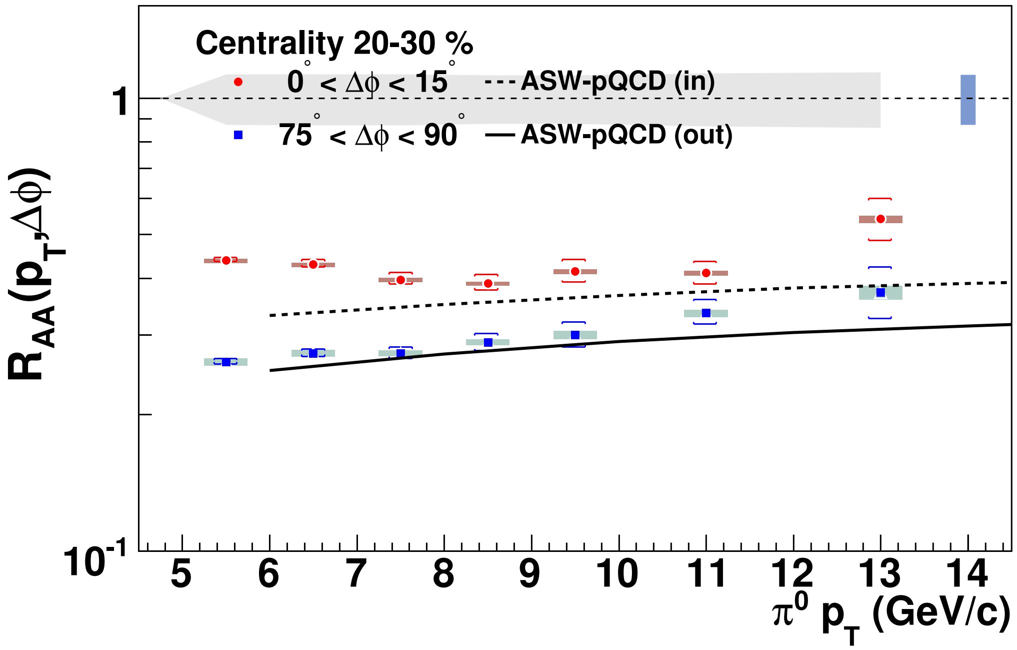

Figure 7.4: Comparison to ASW model based in pQCD.

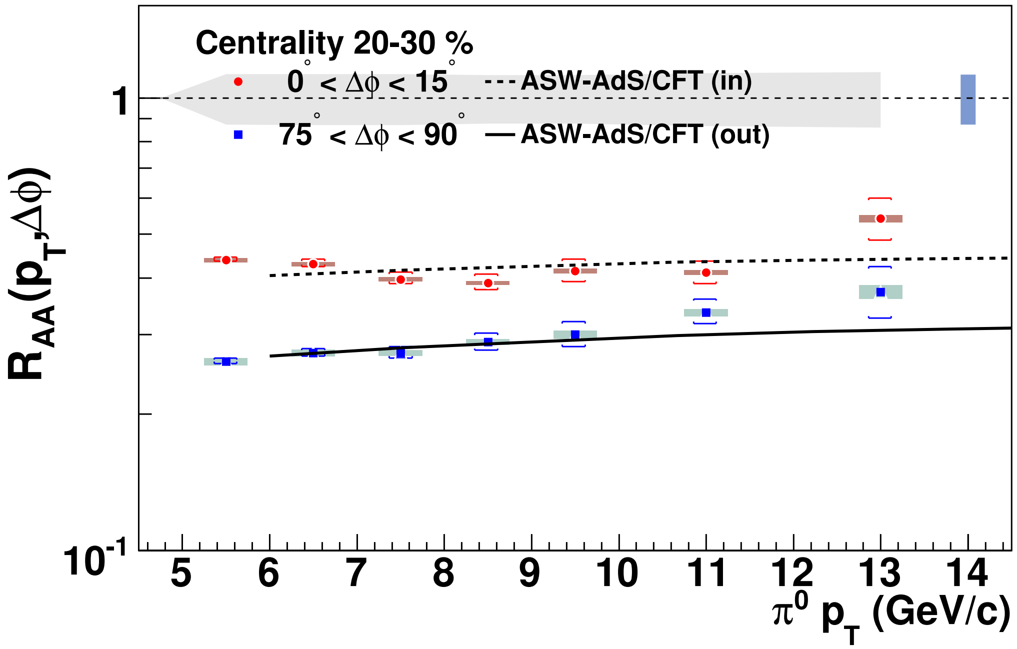

Figure 7.5: Comparison to ASW model using AdS/CFT correspondence.

Chapter 8

Conclusion

The invariant yield of neutral pion are measured up to the p_T of 20 GeV/c at mid-rapidity ($|y| < 0.35$) with RHIC-PHENIX in Au+Au collisions at $\sqrt{s_{NN}} = 200$ GeV. The measured yield of neutral pion in Au+Au collisions is compared to the binary scaled $p+p$ data using the nuclear modification factor, R_{AA}. It indicates that the binary scaling of high-p_T hadron production in heavy-ion collisions relative to $p+p$ collisions is well described by the Monte Carlo calculation with Glauber model.

In the most central collisions, the suppression of neutral pion yield at high p_T has been observed, compared to the yield in $p+p$ collisions at $\sqrt{s} = 200$ GeV scaled by the number of nucleon-nucleon collisions in Au+Au. The suppression is a factor of ~ 5 at p_T range of ∼5–20 GeV/c, while the yield of neutral pion in d+Au are not suppressed. Therefore the yield suppression in Au+Au is not initial state effect such as Cronin or Shadowing observed in d+Au collisions.

The strong suppression of neutral pion is interpreted as the consequence of parton energy loss through gluon bremsstrahlung in the created dense matter (jet quenching). The quantity of the energy loss in the created matter depends on the path length which partons pass through. This fact is supported by many parton energy loss models. The path length dependence for the energy loss has various predictions from different formalisms of parton energy loss.

Since the matter created in non-central collision has almond shape, path length is strongly associated with azimuthal angle of emitted particles. Some parton energy loss models predict different azimuthal angular dependence for the R_{AA} so that the measurement of the R_{AA} with respect to the azimuthal angle from the reaction plane enables us to understand parton energy loss mechanism more precisely.

In 2006 and 2007, detectors which can determine the reaction plane, MPC and RXNP were installed in RHIC-PHENIX experiment. The determination accuracy for reaction plane was improved by a factor of two than previous measurement at RHIC-PHENIX. The R_{AA} and azimuthal anisotropy v_2 of neutral pion are measured and compared to the some models.

The parton energy loss models based on pQCD are achieved a certain result that p_T and centrality dependence for the R_{AA} of neutral pion is well described, while their models can't reproduce the azimuthal angular dependence for the measured R_{AA}. This thesis is pointed out that pQCD might not be applicable to the strong-coupled dynamics in the hot and dense matter created at RHIC. Even though QCD in strong-coupled dynamics should be calculated, the calculation is of great difficulty. Thus, alternate approach which is applicable to the strong-coupled system is needed. One of frameworks to describe the strong-coupled system is AdS/CFT correspondence. The parton energy loss model with AdS/CFT correspondence can reproduce the azimuthal angular dependence for the R_{AA}, and it predicts that stronger path length dependence for the energy loss than models based on pQCD. However, one should recognize that the AdS/CFT correspondence is one of approaches to the strong-coupled system and CFT is different from QCD. The parton energy loss mechanism should eventually be clarified by QCD.

Acknowledgments

First of all, I would like to thank Prof. H. Hamagaki for his appropriate advice and discussion about the experiment, analysis, and physics. His entire support and fruitful knowledge guided me to the completion of this thesis.

I am obliged to Dr. G. David and Dr. T. Sakaguchi for their abundant knowledge and experiences in the photon analysis. I could learn a awful lot for the electromagnetic calorimeter from them. Their continuing support and encouragement have been instrumental in the progress I have made in this work. I am grateful to Dr. T. Gunji for his kind assistance, insightful comments, and valuable discussion for the analysis.

I wish to acknowledge Dr. H. Enyo and Prof. K. Ozawa, for continuous encouragement and support on this research. I could devote myself to conducting research at Japan and BNL thanks to them.

I wish to thank Dr. S. Oda, for his thoughtful help and valuable advice on the data analysis. I could learn the various basics of the data analysis from him. I wish to thank Dr. T. Isobe, for his abundant experience of the electromagnetic calorimeters in PHENIX. I could learn the technique of the photon analysis from him. I would like to thanks to Mr. Y. Ikeda, Dr. H. Masui, Dr. K. Miki and Dr. M. Shimomura, for excellent assistance. I could understand the characteristics of reaction plane detectors thanks to them.

This analysis was performed by the RHIC Computing Facility (RCF) and RIKEN Computing Center in Japan (CCJ), and I wish to express my thanks to all the staff of RCF and CCJ. Especially, I wish to express my obligation to the members of CCJ, Dr. S. Yokkaichi, Dr. T. Ichihara, Dr. Y. Watanabe, and Dr. T. Nakamura for marvelous assistance and steady operation of CCJ. I could increase my work efficiency and finish this research thanks to them. I wish to thank to Mr. S. Dairaku, Mr. K. Karatsu, Dr. Y. Morino, Dr. K. Okada, Mr. K. Shoji, and Dr. Y. Yamaguchi, for kind help on the computing environment at CCJ and the data analysis. I could have a cracking good time at BNL thanks to them.

I would like to thank to all the members of RIKEN Radiation Lab., RIKEN BNL Research Center, and PHENIX-J group, for their kind help.

I would like to express my acknowledgments to all the collaborators of the PHENIX experiment. I would like to give many thanks to the spokesperson, Prof. B. Jacak for her excellent leadership and continuous support. I would like to thank Dr. C. Vale, Dr. C. Pinkenburg, Dr. J. Michell, and Dr. N. Grau for productive cooperation in the analysis of π^0 production in RHIC Year-7 Au+Au Run. I would like to thank the members of Paper Preparation Group 110, Prof. B. Cole, Prof. J. Jia, Dr. R. Wei, and Dr. D. Winter, for appropriate advise and valuable discussion. I could improve the photon analysis technique through friendly competition.

I would like to express my thanks to all the past and present members of Hard/Photon Physics Working Group for fruitful discussion. Especially, I wish to express my thanks to Prof. J. Frantz, Prof. C. Ogilvie, Dr. M. Tannenbaum, and Dr. W. Wholzmann for valuable suggestions and insight comments on my analysis in the working group meeting. I could obtain the robust results in the thorough discussion.

I wish to express my appreciation to all the past and present members of Hamagaki's group, Dr. K. Kino, Dr. T. Horaguchi, Dr. F. Kajihara, Mr. Y. Tsuchimoto, Mr. N. Kurihara, Mr. S. Saito, Mr. S. Sano, Mr. A. Takahara, Mr. R. Akimoto, Mr. Y. Hori, Mr. K. Okada, Mr. T. Tsuji, Mr. S. Hayashi, and Mr. A. Nukariya for their helps, discussions, and the friendship. I could learn many things from their active work.

I wish to acknowledge all the members of the Center of Nuclear for Study, University of Tokyo. I wish to express to my institute secretariats, Ms. M. Hirano, Ms. I. Yamamoto, Ms. T. Endo, Ms. Y. Kishi, Ms. K. Takeuchi, Ms. T. Itagaki, Ms. M. Yamaguchi, Ms. Y. Fujiwara, and Ms. Y. Soma, for their helps. I could concentrate on the research with their support thanks to them.

I am obliged to Prof. H. Aihara, Prof. S. Komamiya, Prof. H. Sakurai, and Prof. K. Tokushuku for important comments and suggestions from the point of view of the measurement. I would like to thank to Prof. T. Hirano, for valuable advice and comments from the theorist's point of view.

The last, but not the least, my deepest appreciation goes to my parents, Yoichi and Toyomi, and my brother, Eiki, for continuous encouragement and support at my daily life. I could have invaluable experience thanks to them, and I could not continue my research without them.

Appendix A

Kinematic Variables

A.1 Transverse Momemtum

In this thesis, the z axis is chosen as the incoming beam direction. The transverse momentum, p_T, and transverse mass, m_T, are defined in terms of the energy momentum components of a particle.

$$p_T \equiv \sqrt{p_x^2 + p_y^2}, \tag{A.1}$$

$$m_T \equiv \sqrt{m^2 + p_T^2} = \sqrt{E^2 + p_z^2}, \tag{A.2}$$

where E, p_x, p_y, p_z and m are the energy, x, y and z components of the momentum and the mass of the particle, respectively.

A.2 Rapidity and Pseudo Rapidity

The rapidity , y, of the particle is defined as

$$y \equiv \frac{1}{2} \ln\Big(\frac{E + p_z}{E - p_z}\Big). \tag{A.3}$$

The rapidity is transformed under the Lorentz boost in the z direction with velocity of β as follows:

$$y \rightarrow y + \tanh^{-1} \beta \tag{A.4}$$

The particle energy and z component of the momentum p_z can be decribed in term of the rapidity y and transverse mass m_T as follows:

$$E = m_T \cosh y, \tag{A.5}$$

$$p_z = m_T \sinh y. \tag{A.6}$$

The pseudo rapidity, η, can be expressed in term of the angle, θ, between the particle momentum, $vecp$, and z axis as follows.

$$\eta \equiv \frac{1}{2} \ln\Big(\frac{|\vec{p}| + p_z}{|\vec{p}| - p_z}\Big) = \ln\Big(\tan\frac{\theta}{2}\Big). \tag{A.7}$$

Appendix B

Calibration of Event Plane

First, the event plane is calibrated by the re-centering method. After the re-centering calibration, most distortion of the event plane are corrected. In this thesis, the event plane is determiend by MPC and RXNin. Each flow vectors after the re-centering calibration is combined before the flattening calibration. Figure B.1 shows the angular distribution of the event plane measured with MPC (south and north) and RXNin (south and north). Black, blue, and red histograms corresponds to the angular distribution before the calibration, after re-centering calibration, and after re-centering and flattening calibrations.

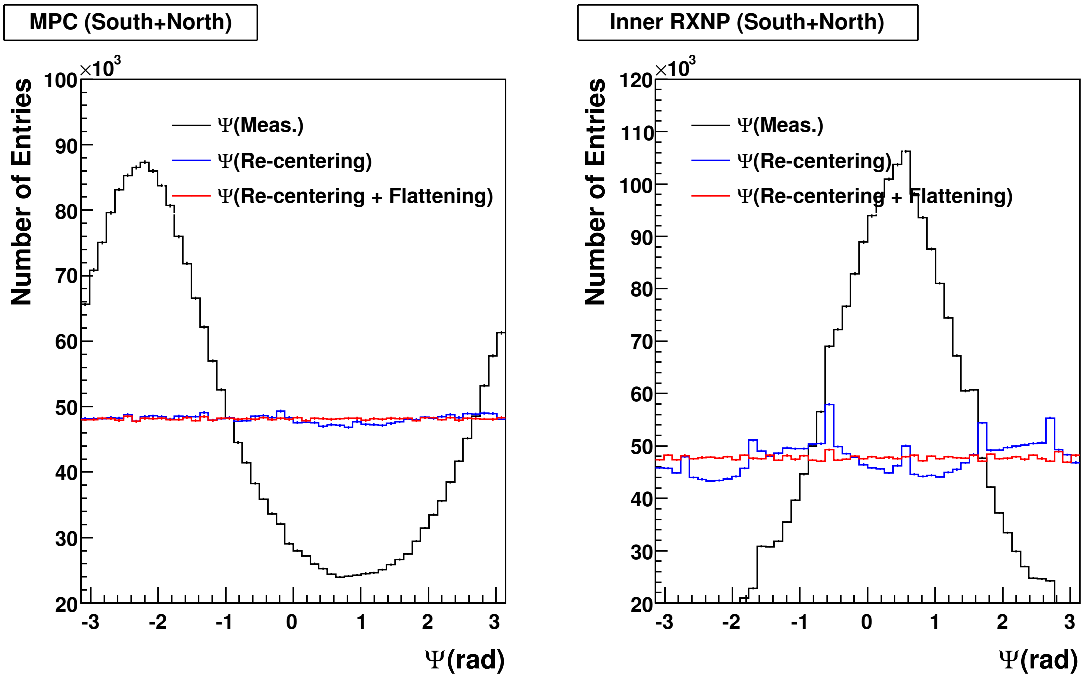

Figure B.1: A sample of the event plane calibration steps for MPC (left panel) and RXNin (right panel).

Appendix C

Fake v_2 with Jet Correlation Effect

In fact, the each azimuthal anisotropy measured with different reaction plane detectors is different at peripheral collisions and particles with high p_T. Figure C.1 shows the azimuthal anisotropy v_2 determined by MPC, RXNin, and RXNout as a function of N_{part}. Blue closed circles, red open triangles and black closed triangles are the azimuthal anisotropy v_2 from RXNout, RXNin, and MPC, respectively, and each band is their systematic uncertainties. The azimuthal anisotropy v_2 from RXNout is large relative to other detectors at high-p_T. It is considered to be due to the small rapidity gap between the EMCals in the central arm and RXNout, RXNin, and MPC located in the forward region. Therefore, the MPC and RXNin combined detectors are used for the determination of the event plane in this thesis. Each hit distribution measured by MPC and RXNin is combined before the calibration of the event plane.

As shown in Fig. C.1, the measurement of the azimuthal anisptropy v_2 at the peripheral collisions of above centrality 60 % has large uncertainty due to the jet correlation effect. In this thesis, the measurement of the azimuthal anisotropy v_2 has been performed at the centrality range of 0–60 %.

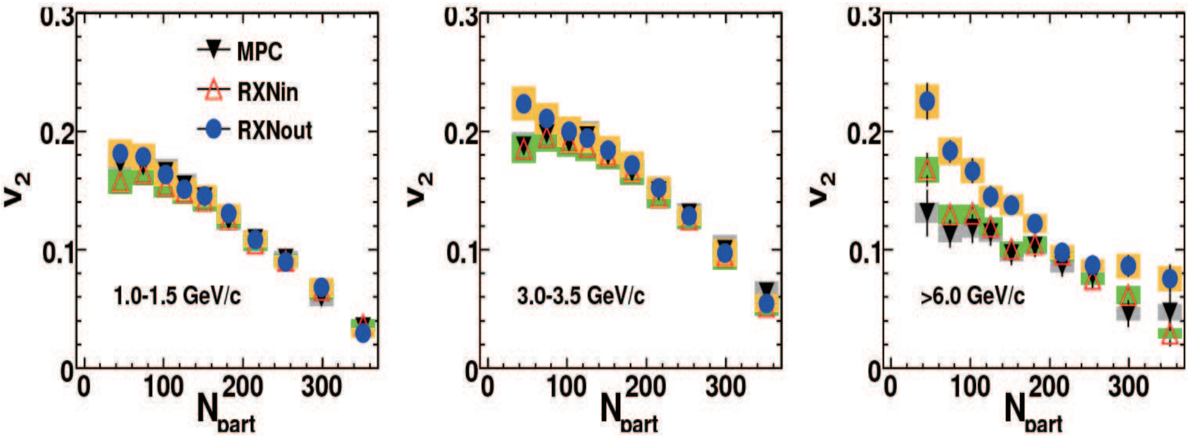

Figure C.1: The azimuthal anisotropy v_2 as a function of N_{part} at several p_T regions. Each azimuthal anisotropy v_2 is measured by three detector, MPC, RXNin and RXNout.

Appendix D

Azimuthal Anisotropy v_2 of Neutral Pion in $\sqrt{s_{NN}} = 200$ GeV Au+Au Collisions

p_T	v_2	Stat.	Rat. (%)	Syst.	Rat. (%)
1.25	5.4897e-02	2.8853e-03	5.26	7.1996e-03	13.1
1.75	6.8766e-02	1.7147e-03	2.49	9.0186e-03	13.1
2.25	7.5079e-02	1.8208e-03	2.43	9.8465e-03	13.1
2.75	8.3162e-02	2.2986e-03	2.76	1.0907e-02	13.1
3.25	8.2760e-02	3.0460e-03	3.68	1.0854e-02	13.1
3.75	7.6841e-02	4.0597e-03	5.28	1.0078e-02	13.1
4.25	7.4583e-02	5.3675e-03	7.2	9.7815e-03	13.1
4.75	6.9171e-02	7.0927e-03	10.3	9.0717e-03	13.1
5.5	6.5993e-02	7.0998e-03	10.8	8.6548e-03	13.1
6.5	5.0482e-02	1.0493e-02	20.8	6.6206e-03	13.1
7.5	3.2888e-02	1.4691e-02	44.7	4.3132e-03	13.1
8.5	8.9519e-02	2.0618e-02	23	1.1740e-02	13.1
9.5	5.5828e-02	2.7285e-02	48.9	7.3217e-03	13.1
11	1.2444e-02	2.8744e-02	231	1.6321e-03	13.1
13	3.8634e-02	4.7791e-02	124	5.0668e-03	13.1

Table D.1: Azimuthal anisotropy v_2 of neutral pion as a function of p_T at $|y| < 0.35$ (Centrality 0-10 %).

p_T	v_2	Stat.	Rat. (%)	Syst.	Rat. (%)
1.25	1.0118e-01	1.7849e-03	1.76	1.3270e-02	13.1
1.75	1.1856e-01	1.0586e-03	0.893	1.5549e-02	13.1
2.25	1.3279e-01	1.1168e-03	0.841	1.7415e-02	13.1
2.75	1.3872e-01	1.3904e-03	1	1.8192e-02	13.1
3.25	1.3840e-01	1.8251e-03	1.32	1.8152e-02	13.1
3.75	1.2795e-01	2.4494e-03	1.91	1.6780e-02	13.1
4.25	1.1694e-01	3.2878e-03	2.81	1.5337e-02	13.1
4.75	1.1213e-01	4.3689e-03	3.9	1.4706e-02	13.1
5.5	9.8750e-02	4.5033e-03	4.56	1.2951e-02	13.1
6.5	8.3699e-02	7.1250e-03	8.51	1.0977e-02	13.1
7.5	8.9528e-02	1.0536e-02	11.8	1.1741e-02	13.1
8.5	6.3865e-02	1.5022e-02	23.5	8.3758e-03	13.1
9.5	1.0915e-01	2.0447e-02	18.7	1.4315e-02	13.1
11	2.9590e-02	2.2269e-02	75.3	3.8807e-03	13.1
13	7.6455e-02	3.8938e-02	50.9	1.0027e-02	13.1

Table D.2: Azimuthal anisotropy v_2 of neutral pion as a function of p_T at $|y| < 0.35$ (Centrality 10-20 %).

p_T	v_2	Stat.	Rat. (%)	Syst.	Rat. (%)
1.25	1.3862e-01	2.1110e-03	1.52	1.0915e-02	7.87
1.75	1.5682e-01	1.2288e-03	0.784	1.2348e-02	7.87
2.25	1.6861e-01	1.2816e-03	0.76	1.3277e-02	7.87
2.75	1.7321e-01	1.5687e-03	0.906	1.3639e-02	7.87
3.25	1.7244e-01	2.0268e-03	1.18	1.3578e-02	7.87
3.75	1.5972e-01	2.6786e-03	1.68	1.2576e-02	7.87
4.25	1.5348e-01	3.5561e-03	2.32	1.2085e-02	7.87
4.75	1.3727e-01	4.7140e-03	3.43	1.0809e-02	7.87
5.5	1.2877e-01	4.8041e-03	3.73	1.0140e-02	7.87
6.5	1.1496e-01	7.5655e-03	6.58	9.0521e-03	7.87
7.5	9.8324e-02	1.1230e-02	11.4	7.7420e-03	7.87
8.5	7.6101e-02	1.6336e-02	21.5	5.9922e-03	7.87
9.5	9.2656e-02	2.2350e-02	24.1	7.2957e-03	7.87
11	6.6542e-02	2.4632e-02	37	5.2395e-03	7.87
13	9.2946e-02	4.3018e-02	46.3	7.3186e-03	7.87

Table D.3: Azimuthal anisotropy v_2 of neutral pion as a function of p_T at $|y| < 0.35$ (Centrality 20-30 %).

p_T	v_2	Stat.	Rat. (%)	Syst.	Rat. (%)
1.25	1.5870e-01	1.5448e-03	0.973	1.2496e-02	7.87
1.75	1.7747e-01	9.0378e-04	0.509	1.3974e-02	7.87
2.25	1.9046e-01	9.5803e-04	0.503	1.4997e-02	7.87
2.75	1.9170e-01	1.2007e-03	0.626	1.5095e-02	7.87
3.25	1.8288e-01	1.6044e-03	0.877	1.4400e-02	7.87
3.75	1.7734e-01	2.2106e-03	1.25	1.3964e-02	7.87
4.25	1.6683e-01	3.0611e-03	1.83	1.3136e-02	7.87
4.75	1.5995e-01	4.2152e-03	2.64	1.2594e-02	7.87
5.5	1.4159e-01	4.5573e-03	3.22	1.1149e-02	7.87
6.5	1.2365e-01	7.7585e-03	6.27	9.7364e-03	7.87
7.5	1.2491e-01	1.2272e-02	9.83	9.8351e-03	7.87
8.5	9.3622e-02	1.8031e-02	19.3	7.3718e-03	7.87
9.5	1.3605e-01	2.7000e-02	19.8	1.0713e-02	7.87
11	1.2760e-01	2.9492e-02	23.1	1.0047e-02	7.87
13	2.3579e-01	5.3418e-02	22.7	1.8566e-02	7.87

Table D.4: Azimuthal anisotropy v_2 of neutral pion as a function of p_T at $|y| < 0.35$ (Centrality 30-40 %).

p_T	v_2	Stat.	Rat. (%)	Syst.	Rat. (%)
1.25	1.6677e-01	2.6940e-03	1.62	1.7491e-02	10.5
1.75	1.8406e-01	1.5562e-03	0.845	1.9304e-02	10.5
2.25	1.9464e-01	1.6184e-03	0.831	2.0414e-02	10.5
2.75	1.9650e-01	1.9727e-03	1	2.0609e-02	10.5
3.25	1.9190e-01	2.5721e-03	1.34	2.0127e-02	10.5
3.75	1.7756e-01	3.4434e-03	1.94	1.8623e-02	10.5
4.25	1.7454e-01	4.6852e-03	2.68	1.8306e-02	10.5
4.75	1.6168e-01	6.3660e-03	3.94	1.6957e-02	10.5
5.5	1.4911e-01	6.7890e-03	4.55	1.5639e-02	10.5
6.5	1.3101e-01	1.1280e-02	8.61	1.3740e-02	10.5
7.5	1.0662e-01	1.7719e-02	16.6	1.1183e-02	10.5
8.5	8.4478e-02	2.6200e-02	31	8.8601e-03	10.5
9.5	1.9285e-01	4.1068e-02	21.3	2.0226e-02	10.5
11	1.6359e-01	4.4818e-02	27.4	1.7158e-02	10.5
13	1.6787e-01	9.2280e-02	55	1.7606e-02	10.5

Table D.5: Azimuthal anisotropy v_2 of neutral pion as a function of p_T at $|y| < 0.35$ (Centrality 40-50 %).

p_T	v_2	Stat.	Rat. (%)	Syst.	Rat. (%)
1.25	1.6891e-01	2.9430e-03	1.74	1.7716e-02	10.5
1.75	1.8369e-01	1.7281e-03	0.941	1.9265e-02	10.5
2.25	1.9124e-01	1.8612e-03	0.973	2.0058e-02	10.5
2.75	1.8909e-01	2.3745e-03	1.26	1.9831e-02	10.5
3.25	1.8786e-01	3.2220e-03	1.72	1.9703e-02	10.5
3.75	1.8201e-01	4.5141e-03	2.48	1.9089e-02	10.5
4.25	1.7619e-01	6.4061e-03	3.64	1.8479e-02	10.5
4.75	1.5780e-01	8.9133e-03	5.65	1.6550e-02	10.5
5.5	1.6434e-01	9.8194e-03	5.98	1.7236e-02	10.5
6.5	1.6711e-01	1.6870e-02	10.1	1.7527e-02	10.5
7.5	1.3340e-01	2.7554e-02	20.7	1.3991e-02	10.5
8.5	1.6515e-01	4.1957e-02	25.4	1.7321e-02	10.5
9.5	1.7723e-01	6.5695e-02	37.1	1.8588e-02	10.5
11	1.8763e-01	7.5711e-02	40.4	1.9679e-02	10.5
13	4.9149e-01	1.5965e-01	32.5	5.1547e-02	10.5

Table D.6: Azimuthal anisotropy v_2 of neutral pion as a function of p_T at $|y| < 0.35$ (Centrality 50-60 %).

Appendix E

Invariant Yields of Neutral Pion in $\sqrt{s_{NN}}$ = 200 GeV Au+Au Collisions

p_T	Yields	Stat.	Rat. (%)	p_T Corr.	Rat. (%)
5.25	8.9688e-05	5.6337e-07	0.628	7.8826e-06	8.79
5.75	4.3088e-05	3.3974e-07	0.788	3.7859e-06	8.79
6.25	2.1931e-05	2.1602e-07	0.985	1.9274e-06	8.79
6.75	1.1896e-05	1.4440e-07	1.21	1.0456e-06	8.79
7.25	6.7377e-06	1.0018e-07	1.49	5.9169e-07	8.78
7.75	4.0628e-06	7.2470e-08	1.78	3.5712e-07	8.79
8.25	2.4566e-06	5.2884e-08	2.15	1.8477e-07	7.52
8.75	1.5510e-06	3.9789e-08	2.57	1.1644e-07	7.51
9.25	1.0846e-06	3.1187e-08	2.88	8.1453e-08	7.51
9.75	6.7983e-07	2.3618e-08	3.47	5.1077e-08	7.51
11	2.7668e-07	6.6585e-09	2.41	2.4084e-08	8.7
13	7.6507e-08	3.2876e-09	4.3	6.6556e-09	8.7
15	2.6026e-08	2.0432e-09	7.85	2.2681e-09	8.71
17	1.0306e-08	1.4291e-09	13.9	2.9938e-09	29.1
19	3.1939e-09	1.0100e-09	31.6	9.2785e-10	29.1

Table E.1: Invariant yields of neutral pion as a function of p_T at $|y| < 0.35$ (Centrality 0-10 %).

p_T	Yields	Stat.	Rat. (%)	p_T Corr.	Rat. (%)
5.25	8.0529e-05	4.6079e-07	0.572	7.0801e-06	8.79
5.75	3.8055e-05	2.8164e-07	0.74	3.3475e-06	8.8
6.25	1.8819e-05	1.8054e-07	0.959	1.6540e-06	8.79
6.75	1.0311e-05	1.2273e-07	1.19	9.0611e-07	8.79
7.25	5.9243e-06	8.6818e-08	1.47	5.2013e-07	8.78
7.75	3.4688e-06	6.2494e-08	1.8	3.0521e-07	8.8
8.25	2.1608e-06	4.6738e-08	2.16	1.6196e-07	7.5
8.75	1.3449e-06	3.4631e-08	2.57	1.0093e-07	7.5
9.25	8.8438e-07	2.6976e-08	3.05	6.6394e-08	7.51
9.75	5.8378e-07	2.1145e-08	3.62	4.3788e-08	7.5
11	2.2996e-07	5.8760e-09	2.56	2.0001e-08	8.7
13	6.1407e-08	2.9031e-09	4.73	5.3302e-09	8.68
15	1.9708e-08	1.7253e-09	8.75	1.6923e-09	8.59
17	6.9531e-09	1.2517e-09	18	2.0200e-09	29.1
19	2.4896e-09	8.8020e-10	35.4	7.2326e-10	29.1

Table E.2: Invariant yields of neutral pion as a function of p_T at $|y| < 0.35$ (Centrality 10-20 %).

p_T	Yields	Stat.	Rat. (%)	p_T Corr.	Rat. (%)
5.25	6.6929e-05	3.8214e-07	0.571	5.8816e-06	8.79
5.75	3.0844e-05	2.3451e-07	0.76	2.7096e-06	8.78
6.25	1.5634e-05	1.5293e-07	0.978	1.3749e-06	8.79
6.75	8.2313e-06	1.0390e-07	1.26	7.2301e-07	8.78
7.25	4.6495e-06	7.2877e-08	1.57	4.0871e-07	8.79
7.75	2.7973e-06	5.3702e-08	1.92	2.4569e-07	8.78
8.25	1.7050e-06	3.9806e-08	2.33	1.2755e-07	7.48
8.75	1.0118e-06	2.9551e-08	2.92	7.5929e-08	7.5
9.25	6.5192e-07	2.2768e-08	3.49	4.8999e-08	7.52
9.75	4.7618e-07	1.8355e-08	3.85	3.5787e-08	7.52
11	1.8258e-07	5.2041e-09	2.85	1.5874e-08	8.69
13	5.1160e-08	2.6177e-09	5.12	4.4474e-09	8.69
15	1.6461e-08	1.5580e-09	9.46	1.4346e-09	8.71
17	3.9990e-09	8.7266e-10	21.8	1.1618e-09	29.1
19	2.1662e-09	8.1875e-10	37.8	6.2932e-10	29.1

Table E.3: Invariant yields of neutral pion as a function of p_T at $|y| < 0.35$ (Centrality 20-30 %).

p_T	Yields	Stat.	Rat. (%)	p_T Corr.	Rat. (%)
5.25	4.9597e-05	3.0165e-07	0.608	4.3596e-06	8.79
5.75	2.2939e-05	1.8939e-07	0.826	2.0149e-06	8.78
6.25	1.1943e-05	1.2623e-07	1.06	1.0501e-06	8.79
6.75	6.2652e-06	8.6569e-08	1.38	5.5027e-07	8.78
7.25	3.4487e-06	6.0807e-08	1.76	3.0288e-07	8.78
7.75	2.1188e-06	4.4973e-08	2.12	1.8599e-07	8.78
8.25	1.2664e-06	3.3365e-08	2.63	9.5113e-08	7.51
8.75	7.9201e-07	2.5431e-08	3.21	5.9168e-08	7.47
9.25	4.7334e-07	1.9137e-08	4.04	3.5495e-08	7.5
9.75	3.0244e-07	1.4615e-08	4.83	2.2732e-08	7.52
11	1.2965e-07	4.3353e-09	3.34	1.1267e-08	8.69
13	3.5372e-08	2.1518e-09	6.08	3.0825e-09	8.71
15	1.1171e-08	1.4617e-09	13.1	9.4924e-10	8.5
17	3.1951e-09	7.7492e-10	24.3	9.2821e-10	29.1
19	1.5310e-09	6.8466e-10	44.7	4.4476e-10	29.1

Table E.4: Invariant yields of neutral pion as a function of p_T at $|y| < 0.35$ (Centrality 30-40 %).

p_T	Yields	Stat.	Rat. (%)	p_T Corr.	Rat. (%)
5.25	3.3954e-05	2.3479e-07	0.691	2.9846e-06	8.79
5.75	1.6121e-05	1.5013e-07	0.931	1.4179e-06	8.8
6.25	8.3694e-06	1.0163e-07	1.21	7.3611e-07	8.8
6.75	4.4439e-06	7.0292e-08	1.58	3.9059e-07	8.79
7.25	2.3969e-06	4.9765e-08	2.08	2.1064e-07	8.79
7.75	1.4916e-06	3.6835e-08	2.47	1.3117e-07	8.79
8.25	8.6635e-07	2.7118e-08	3.13	6.4999e-08	7.5
8.75	5.5778e-07	2.0746e-08	3.72	4.1948e-08	7.52
9.25	3.4341e-07	1.5594e-08	4.54	2.5793e-08	7.51
9.75	2.3774e-07	1.2585e-08	5.29	1.7822e-08	7.5
11	8.3412e-08	3.4874e-09	4.18	7.2693e-09	8.71
13	2.3523e-08	1.8161e-09	7.72	2.0393e-09	8.67
15	4.5444e-09	2.5578e-09	56.3	3.9604e-10	8.71
17	2.2328e-09	6.4455e-10	28.9	6.4867e-10	29.1
19	1.5173e-09	6.7855e-10	44.7	4.4080e-10	29.1

Table E.5: Invariant yields of neutral pion as a function of p_T at $|y| < 0.35$ (Centrality 40-50 %).

p_T	Yields	Stat.	Rat. (%)	p_T Corr.	Rat. (%)
5.25	2.1474e-05	1.8003e-07	0.838	1.8876e-06	8.79
5.75	1.0070e-05	1.1549e-07	1.15	8.8514e-07	8.79
6.25	5.2528e-06	7.8868e-08	1.5	4.6160e-07	8.79
6.75	2.7852e-06	5.4229e-08	1.95	2.4475e-07	8.79
7.25	1.5351e-06	3.9046e-08	2.54	1.3494e-07	8.79
7.75	9.0183e-07	2.8486e-08	3.16	7.9311e-08	8.79
8.25	5.6282e-07	2.2159e-08	3.94	4.2181e-08	7.49
8.75	3.3522e-07	1.6446e-08	4.91	2.5091e-08	7.48
9.25	2.0410e-07	1.2729e-08	6.24	1.5341e-08	7.52
9.75	1.4587e-07	9.9880e-09	6.85	1.0903e-08	7.47
11	5.2699e-08	2.8136e-09	5.34	4.5821e-09	8.69
13	1.5633e-08	1.6567e-09	10.6	1.3624e-09	8.71
15	4.3870e-09	7.7552e-10	17.7	3.8231e-10	8.71
17	9.2881e-10	4.1538e-10	44.7	2.6983e-10	29.1
19	3.0298e-10	3.0298e-10	100	8.8020e-11	29.1

Table E.6: Invariant yields of neutral pion as a function of p_T at $|y| < 0.35$ (Centrality 50-60 %).

p_T	Yields	Stat.	Rat. (%)	p_T Corr.	Rat. (%)
5.25	1.1547e-05	1.2864e-07	1.11	1.0149e-06	8.79
5.75	5.6498e-06	8.4193e-08	1.49	4.9679e-07	8.79
6.25	2.7590e-06	5.6591e-08	2.05	2.4238e-07	8.79
6.75	1.5872e-06	4.0483e-08	2.55	1.3960e-07	8.79
7.25	8.1970e-07	2.7910e-08	3.4	7.2148e-08	8.8
7.75	4.8480e-07	2.0771e-08	4.28	4.2646e-08	8.8
8.25	2.9636e-07	1.5517e-08	5.24	2.2276e-08	7.52
8.75	1.8626e-07	1.2185e-08	6.54	1.3948e-08	7.49
9.25	1.0115e-07	9.1428e-09	9.04	7.5533e-09	7.47
9.75	8.9044e-08	8.1172e-09	9.12	6.6931e-09	7.52
11	2.7153e-08	1.9937e-09	7.34	2.3664e-09	8.71
13	9.2098e-09	1.0564e-09	11.5	8.0262e-10	8.71
15	3.1295e-09	6.5254e-10	20.9	2.7273e-10	8.71
17	2.0292e-09	6.1184e-10	30.2	5.8953e-10	29.1
19	3.0152e-10	3.0152e-10	100	8.7597e-11	29.1

Table E.7: Invariant yields of neutral pion as a function of p_T at $|y| < 0.35$ (Centrality 60-70 %).

p_T	Yields	Stat.	Rat. (%)	p_T Corr.	Rat. (%)
5.25	5.4859e-06	8.7174e-08	1.59	4.8280e-07	8.8
5.75	2.6506e-06	5.7248e-08	2.16	2.3307e-07	8.79
6.25	1.3305e-06	3.8546e-08	2.9	1.1709e-07	8.8
6.75	6.9625e-07	2.6358e-08	3.79	6.1331e-08	8.81
7.25	4.2925e-07	2.0255e-08	4.72	3.7660e-08	8.77
7.75	2.4038e-07	1.5481e-08	6.44	2.1106e-08	8.78
8.25	1.4239e-07	1.0798e-08	7.58	1.0647e-08	7.48
8.75	9.7968e-08	8.2504e-09	8.42	7.3639e-09	7.52
9.25	5.6286e-08	6.5798e-09	11.7	4.2308e-09	7.52
9.75	4.0444e-08	4.9783e-09	12.3	3.0400e-09	7.52
11	1.2124e-08	1.2374e-09	10.2	1.0566e-09	8.71
13	4.4482e-09	7.3128e-10	16.4	3.8765e-10	8.71
15	6.7624e-10	3.0243e-10	44.7	5.8932e-11	8.71
17	3.6625e-10	2.5898e-10	70.7	1.0640e-10	29.1
19	—	—	—	—	—

Table E.8: Invariant yields of neutral pion as a function of p_T at $|y| < 0.35$ (Centrality 70-80 %).

p_T	Yields	Stat.	Rat. (%)	p_T Corr.	Rat. (%)
5.25	1.7481e-06	4.2854e-08	2.45	1.5379e-07	8.8
5.75	8.5053e-07	2.8207e-08	3.32	7.4837e-08	8.8
6.25	4.3444e-07	1.9596e-08	4.51	3.8260e-08	8.81
6.75	2.4514e-07	1.3560e-08	5.53	2.1473e-08	8.76
7.25	1.4599e-07	1.0224e-08	7	1.2800e-08	8.77
7.75	7.7269e-08	7.2323e-09	9.36	6.8066e-09	8.81
8.25	4.8739e-08	5.6114e-09	11.5	3.6636e-09	7.52
8.75	2.3739e-08	4.4393e-09	18.7	1.7844e-09	7.52
9.25	1.5991e-08	2.8268e-09	17.7	1.2020e-09	7.52
9.75	8.4724e-09	1.9970e-09	23.6	6.3686e-10	7.52
11	5.0405e-09	6.9899e-10	13.9	4.3927e-10	8.71
13	9.2302e-10	2.9188e-10	31.6	8.0441e-11	8.71
15	1.0384e-10	1.0384e-10	100	9.0493e-12	8.71
17	1.4071e-10	1.4071e-10	100	4.0879e-11	29.1
19	—	—	—	—	—

Table E.9: Invariant yields of neutral pion as a function of p_T at $|y| < 0.35$ (Centrality 80-93 %).

p_T	Yields	Stat.	Rat. (%)	p_T Corr.	Rat. (%)
5.25	4.0376e-05	1.0327e-07	0.256	3.5490e-06	8.79
5.75	1.8800e-05	6.2823e-08	0.334	1.6525e-06	8.79
6.25	9.4645e-06	4.0517e-08	0.428	8.3204e-07	8.79
6.75	5.0475e-06	2.7377e-08	0.542	4.4355e-07	8.79
7.25	2.8210e-06	1.9172e-08	0.68	2.4782e-07	8.79
7.75	1.6876e-06	1.3970e-08	0.828	1.4834e-07	8.79
8.25	1.0220e-06	1.0343e-08	1.01	7.6670e-08	7.5
8.75	6.3105e-07	7.7628e-09	1.23	4.7333e-08	7.5
9.25	4.0748e-07	5.9821e-09	1.47	3.0597e-08	7.51
9.75	2.7441e-07	4.6909e-09	1.71	2.0599e-08	7.51
11	1.0729e-07	1.3153e-09	1.23	9.3339e-09	8.7
13	2.9684e-08	6.5882e-10	2.22	2.5810e-09	8.69
15	9.4537e-09	3.9716e-10	4.2	8.1855e-10	8.66
17	3.2078e-09	2.5969e-10	8.1	9.3191e-10	29.1
19	1.2240e-09	2.0122e-10	16.4	3.5558e-10	29.1

Table E.10: Invariant yields of neutral pion as a function of p_T at $|y| < 0.35$ (Centrality 0-93 %).

p_T	Yields	Stat.	Rat. (%)	p_T Corr.	Rat. (%)
5.25	9.3942e-05	8.6757e-07	0.924	8.2524e-06	8.78
5.75	4.5241e-05	5.1663e-07	1.14	3.9763e-06	8.79
6.25	2.2734e-05	3.2479e-07	1.43	1.9987e-06	8.79
6.75	1.2533e-05	2.1669e-07	1.73	1.1019e-06	8.79
7.25	6.8618e-06	1.4735e-07	2.15	6.0245e-07	8.78
7.75	4.1642e-06	1.0610e-07	2.55	3.6639e-07	8.8
8.25	2.5978e-06	7.8155e-08	3.01	1.9547e-07	7.52
8.75	1.5449e-06	5.7515e-08	3.72	1.1616e-07	7.52
9.25	1.1183e-06	4.4668e-08	3.99	8.3916e-08	7.5
9.75	7.6839e-07	3.5421e-08	4.61	5.7694e-08	7.51
11	2.8374e-07	9.6036e-09	3.38	2.4699e-08	8.7
13	8.6849e-08	4.9366e-09	5.68	7.5684e-09	8.71
15	2.6588e-08	3.0437e-09	11.4	2.3169e-09	8.71
17	9.5467e-09	1.9487e-09	20.4	2.7733e-09	29
19	4.4495e-09	1.6818e-09	37.8	1.2926e-09	29

Table E.11: Invariant yields of neutral pion as a function of p_T at $|y| < 0.35$ (Centrality 0-5 %).

Appendix F

$R_{AA}(p_T)$ of Neutral Pion in $\sqrt{s_{NN}} =$ 200 GeV Au+Au Collisions

p_T	R_{AA}	p_T Uncorr.	Rat. (%)	p_T Corr.	Rat. (%)	Global	Rat. (%)
5.25	1.8594e-01	1.3671e-03	0.735	2.3778e-02	12.8	2.2616e-02	12.2
5.75	1.8552e-01	1.7548e-03	0.946	2.3775e-02	12.8	2.2564e-02	12.2
6.25	1.8822e-01	2.2771e-03	1.21	2.4177e-02	12.8	2.2893e-02	12.2
6.75	1.9223e-01	2.9342e-03	1.53	2.4752e-02	12.9	2.3381e-02	12.2
7.25	1.9077e-01	3.6067e-03	1.89	2.4619e-02	12.9	2.3203e-02	12.2
7.75	1.9671e-01	4.5438e-03	2.31	2.5472e-02	12.9	2.3925e-02	12.2
8.25	1.9897e-01	5.6201e-03	2.82	2.4210e-02	12.2	2.4200e-02	12.2
8.75	1.9700e-01	6.6363e-03	3.37	2.4062e-02	12.2	2.3961e-02	12.2
9.25	2.2411e-01	8.8675e-03	3.96	2.7472e-02	12.3	2.7258e-02	12.2
9.75	2.2495e-01	1.0915e-02	4.85	2.7650e-02	12.3	2.7361e-02	12.2
11	2.2526e-01	7.6901e-03	3.41	3.0172e-02	13.4	2.7398e-02	12.2
13	2.4026e-01	1.5137e-02	6.3	3.3934e-02	14.1	2.9222e-02	12.2
15	3.2436e-01	3.6734e-02	11.3	4.8494e-02	15	3.9451e-02	12.2
17	3.7630e-01	7.2167e-02	19.2	1.2121e-01	32.2	4.5769e-02	12.2
19	2.6386e-01	9.9973e-02	37.9	8.7229e-02	33.1	3.2093e-02	12.2

Table F.1: R_{AA} of neutral pion as a function of p_T at $|y| < 0.35$ (Centrality 0-10 %).

p_T	R_{AA}	p_T Uncorr.	Rat. (%)	p_T Corr.	Rat. (%)	Global	Rat. (%)
5.25	2.6303e-01	1.8098e-03	0.688	3.3642e-02	12.8	3.1671e-02	12
5.75	2.5814e-01	2.3387e-03	0.906	3.3100e-02	12.8	3.1082e-02	12
6.25	2.5446e-01	3.0254e-03	1.19	3.2686e-02	12.8	3.0639e-02	12
6.75	2.6251e-01	3.9579e-03	1.51	3.3797e-02	12.9	3.1609e-02	12
7.25	2.6427e-01	4.9517e-03	1.87	3.4100e-02	12.9	3.1820e-02	12
7.75	2.6460e-01	6.1485e-03	2.32	3.4278e-02	13	3.1860e-02	12
8.25	2.7572e-01	7.8097e-03	2.83	3.3505e-02	12.2	3.3199e-02	12
8.75	2.6913e-01	9.0856e-03	3.38	3.2867e-02	12.2	3.2406e-02	12
9.25	2.8791e-01	1.1763e-02	4.09	3.5287e-02	12.3	3.4667e-02	12
9.75	3.0434e-01	1.5093e-02	4.96	3.7384e-02	12.3	3.6645e-02	12
11	2.9496e-01	1.0383e-02	3.52	3.9495e-02	13.4	3.5516e-02	12
13	3.0381e-01	2.0055e-02	6.6	4.2874e-02	14.1	3.6581e-02	12
15	3.8696e-01	4.6316e-02	12	5.7567e-02	14.9	4.6594e-02	12
17	4.0000e-01	8.9403e-02	22.4	1.2885e-01	32.2	4.8163e-02	12
19	3.2404e-01	1.3303e-01	41.1	1.0712e-01	33.1	3.9017e-02	12

Table F.2: R_{AA} of neutral pion as a function of p_T at $|y| < 0.35$ (Centrality 10-20 %).

p_T	R_{AA}	p_T Uncorr.	Rat. (%)	p_T Corr.	Rat. (%)	Global	Rat. (%)
5.25	3.5279e-01	2.4238e-03	0.687	4.5113e-02	12.8	4.3422e-02	12.3
5.75	3.3766e-01	3.1151e-03	0.923	4.3270e-02	12.8	4.1559e-02	12.3
6.25	3.4115e-01	4.1083e-03	1.2	4.3836e-02	12.8	4.1990e-02	12.3
6.75	3.3820e-01	5.2932e-03	1.57	4.3532e-02	12.9	4.1626e-02	12.3
7.25	3.3471e-01	6.5420e-03	1.95	4.3214e-02	12.9	4.1197e-02	12.3
7.75	3.4436e-01	8.3213e-03	2.42	4.4574e-02	12.9	4.2384e-02	12.3
8.25	3.5110e-01	1.0412e-02	2.97	4.2634e-02	12.1	4.3214e-02	12.3
8.75	3.2676e-01	1.1915e-02	3.65	3.9903e-02	12.2	4.0218e-02	12.3
9.25	3.4250e-01	1.5157e-02	4.43	4.1997e-02	12.3	4.2156e-02	12.3
9.75	4.0062e-01	2.0558e-02	5.13	4.9246e-02	12.3	4.9308e-02	12.3
11	3.7795e-01	1.4135e-02	3.74	5.0599e-02	13.4	4.6519e-02	12.3
13	4.0848e-01	2.8125e-02	6.89	5.7679e-02	14.1	5.0276e-02	12.3
15	5.2161e-01	6.5192e-02	12.5	7.7985e-02	15	6.4200e-02	12.3
17	3.7127e-01	9.4778e-02	25.5	1.1959e-01	32.2	4.5696e-02	12.3
19	4.5502e-01	1.9645e-01	43.2	1.5043e-01	33.1	5.6004e-02	12.3

Table F.3: R_{AA} of neutral pion as a function of p_T at $|y| < 0.35$ (Centrality 20-30 %).

p_T	R_{AA}	p_T Uncorr.	Rat. (%)	p_T Corr.	Rat. (%)	Global	Rat. (%)
5.25	4.4084e-01	3.1664e-03	0.718	5.6378e-02	12.8	5.7412e-02	13
5.75	4.2344e-01	4.1374e-03	0.977	5.4260e-02	12.8	5.5146e-02	13
6.25	4.3944e-01	5.5768e-03	1.27	5.6461e-02	12.8	5.7230e-02	13
6.75	4.3407e-01	7.2185e-03	1.66	5.5870e-02	12.9	5.6530e-02	13
7.25	4.1864e-01	8.8532e-03	2.11	5.4028e-02	12.9	5.4521e-02	13
7.75	4.3982e-01	1.1350e-02	2.58	5.6917e-02	12.9	5.7280e-02	13
8.25	4.3974e-01	1.4103e-02	3.21	5.3478e-02	12.2	5.7269e-02	13
8.75	4.3130e-01	1.6747e-02	3.88	5.2581e-02	12.2	5.6169e-02	13
9.25	4.1934e-01	2.0429e-02	4.87	5.1374e-02	12.3	5.4612e-02	13
9.75	4.2906e-01	2.5320e-02	5.9	5.2745e-02	12.3	5.5878e-02	13
11	4.5256e-01	1.8683e-02	4.13	6.0575e-02	13.4	5.8938e-02	13
13	4.7623e-01	3.6342e-02	7.63	6.7308e-02	14.1	6.2022e-02	13
15	5.9690e-01	9.2052e-02	15.4	8.8490e-02	14.8	7.7736e-02	13
17	5.0019e-01	1.3823e-01	27.6	1.6112e-01	32.2	6.5141e-02	13
19	5.4226e-01	2.6761e-01	49.4	1.7927e-01	33.1	7.0620e-02	13

Table F.4: R_{AA} of neutral pion as a function of p_T at $|y| < 0.35$ (Centrality 30-40 %).

p_T	R_{AA}	p_T Uncorr.	Rat. (%)	p_T Corr.	Rat. (%)	Global	Rat. (%)
5.25	5.4217e-01	4.2834e-03	0.79	6.9338e-02	12.8	7.9321e-02	14.6
5.75	5.3460e-01	5.7088e-03	1.07	6.8546e-02	12.8	7.8213e-02	14.6
6.25	5.5324e-01	7.7608e-03	1.4	7.1091e-02	12.8	8.0940e-02	14.6
6.75	5.5311e-01	1.0136e-02	1.83	7.1216e-02	12.9	8.0921e-02	14.6
7.25	5.2270e-01	1.2451e-02	2.38	6.7478e-02	12.9	7.6472e-02	14.6
7.75	5.5623e-01	1.5979e-02	2.87	7.2041e-02	13	8.1377e-02	14.6
8.25	5.4045e-01	1.9592e-02	3.63	6.5699e-02	12.2	7.9068e-02	14.6
8.75	5.4568e-01	2.3534e-02	4.31	6.6692e-02	12.2	7.9834e-02	14.6
9.25	5.4655e-01	2.8924e-02	5.29	6.7000e-02	12.3	7.9962e-02	14.6
9.75	6.0590e-01	3.8079e-02	6.28	7.4411e-02	12.3	8.8645e-02	14.6
11	5.2305e-01	2.5272e-02	4.83	7.0096e-02	13.4	7.6524e-02	14.6
13	5.6896e-01	5.1153e-02	8.99	8.0255e-02	14.1	8.3240e-02	14.6
15	4.3622e-01	2.4810e-01	56.9	6.5218e-02	15	6.3819e-02	14.6
17	6.2795e-01	1.9945e-01	31.8	2.0228e-01	32.2	9.1870e-02	14.6
19	9.6547e-01	4.7647e-01	49.4	3.1918e-01	33.1	1.4125e-01	14.6

Table F.5: R_{AA} of neutral pion as a function of p_T at $|y| < 0.35$ (Centrality 40-50 %).

p_T	R_{AA}	p_T Uncorr.	Rat. (%)	p_T Corr.	Rat. (%)	Global	Rat. (%)
5.25	6.6913e-01	6.1648e-03	0.921	8.5572e-02	12.8	1.1418e-01	17.1
5.75	6.5167e-01	8.2129e-03	1.26	8.3530e-02	12.8	1.1120e-01	17.1
6.25	6.7756e-01	1.1231e-02	1.66	8.7031e-02	12.8	1.1562e-01	17.1
6.75	6.7646e-01	1.4583e-02	2.16	8.7089e-02	12.9	1.1543e-01	17.1
7.25	6.5326e-01	1.8283e-02	2.8	8.4342e-02	12.9	1.1147e-01	17.1
7.75	6.5625e-01	2.2857e-02	3.48	8.4998e-02	13	1.1198e-01	17.1
8.25	6.8512e-01	2.9741e-02	4.34	8.3252e-02	12.2	1.1691e-01	17.1
8.75	6.3994e-01	3.4364e-02	5.37	7.8072e-02	12.2	1.0920e-01	17.1
9.25	6.3385e-01	4.3123e-02	6.8	7.7724e-02	12.3	1.0816e-01	17.1
9.75	7.2547e-01	5.5419e-02	7.64	8.8996e-02	12.3	1.2379e-01	17.1
11	6.4485e-01	3.7804e-02	5.86	8.6333e-02	13.4	1.1003e-01	17.1
13	7.3783e-01	8.5261e-02	11.6	1.0428e-01	14.1	1.2590e-01	17.1
15	8.2173e-01	1.6000e-01	19.5	1.2285e-01	15	1.4022e-01	17.1
17	5.0973e-01	2.3775e-01	46.6	1.6419e-01	32.2	8.6978e-02	17.1
19	3.7620e-01	3.8430e-01	102	1.2437e-01	33.1	6.4193e-02	17.1

Table F.6: R_{AA} of neutral pion as a function of p_T at $|y| < 0.35$ (Centrality 50-60 %).

p_T	R_{AA}	p_T Uncorr.	Rat. (%)	p_T Corr.	Rat. (%)	Global	Rat. (%)
5.25	7.7264e-01	9.1000e-03	1.18	9.8806e-02	12.8	1.5736e-01	20.4
5.75	7.8509e-01	1.2398e-02	1.58	1.0065e-01	12.8	1.5990e-01	20.4
6.25	7.6421e-01	1.6569e-02	2.17	9.8148e-02	12.8	1.5564e-01	20.4
6.75	8.2782e-01	2.2461e-02	2.71	1.0662e-01	12.9	1.6860e-01	20.4
7.25	7.4905e-01	2.6962e-02	3.6	9.6768e-02	12.9	1.5256e-01	20.4
7.75	7.5756e-01	3.4308e-02	4.53	9.8131e-02	13	1.5429e-01	20.4
8.25	7.7468e-01	4.2964e-02	5.55	9.4239e-02	12.2	1.5778e-01	20.4
8.75	7.6356e-01	5.2660e-02	6.9	9.3171e-02	12.2	1.5551e-01	20.4
9.25	6.7455e-01	6.3670e-02	9.44	8.2512e-02	12.2	1.3738e-01	20.4
9.75	9.5094e-01	9.2479e-02	9.72	1.1690e-01	12.3	1.9368e-01	20.4
11	7.1348e-01	5.5163e-02	7.73	9.5615e-02	13.4	1.4531e-01	20.4
13	9.3343e-01	1.1539e-01	12.4	1.3193e-01	14.1	1.9011e-01	20.4
15	1.2588e+00	2.8186e-01	22.4	1.8820e-01	15	2.5637e-01	20.4
17	2.3914e+00	7.8757e-01	32.9	7.7034e-01	32.2	4.8706e-01	20.4
19	8.0396e-01	8.2128e-01	102	2.6578e-01	33.1	1.6374e-01	20.4

Table F.7: R_{AA} of neutral pion as a function of p_T at $|y| < 0.35$ (Centrality 60-70 %).

p_T	R_{AA}	p_T Uncorr.	Rat. (%)	p_T Corr.	Rat. (%)	Global	Rat. (%)
5.25	8.7012e-01	1.4221e-02	1.63	1.1134e-01	12.8	2.1285e-01	24.5
5.75	8.7313e-01	1.9402e-02	2.22	1.1194e-01	12.8	2.1358e-01	24.5
6.25	8.7360e-01	2.6043e-02	2.98	1.1229e-01	12.9	2.1370e-01	24.5
6.75	8.6078e-01	3.3547e-02	3.9	1.1095e-01	12.9	2.1056e-01	24.5
7.25	9.2983e-01	4.5199e-02	4.86	1.1994e-01	12.9	2.2745e-01	24.5
7.75	8.9040e-01	5.8816e-02	6.61	1.1524e-01	12.9	2.1781e-01	24.5
8.25	8.8234e-01	6.8828e-02	7.8	1.0712e-01	12.1	2.1584e-01	24.5
8.75	9.5200e-01	8.2823e-02	8.7	1.1633e-01	12.2	2.3288e-01	24.5
9.25	8.8981e-01	1.0679e-01	12	1.0911e-01	12.3	2.1766e-01	24.5
9.75	1.0239e+00	1.3071e-01	12.8	1.2587e-01	12.3	2.5045e-01	24.5
11	7.5518e-01	7.9215e-02	10.5	1.0120e-01	13.4	1.8473e-01	24.5
13	1.0687e+00	1.8246e-01	17.1	1.5104e-01	14.1	2.6142e-01	24.5
15	6.4479e-01	2.9312e-01	45.5	9.6400e-02	15	1.5773e-01	24.5
17	1.0232e+00	7.3607e-01	71.9	3.2958e-01	32.2	2.5029e-01	24.5
19	—	—	—	—	—	—	—

Table F.8: R_{AA} of neutral pion as a function of p_T at $|y| < 0.35$ (Centrality 70-80 %).

p_T	R_{AA}	p_T Uncorr.	Rat. (%)	p_T Corr.	Rat. (%)	Global	Rat. (%)
5.25	8.2983e-01	2.0588e-02	2.48	1.0617e-01	12.8	1.7305e-01	20.9
5.75	8.3848e-01	2.8150e-02	3.36	1.0753e-01	12.8	1.7485e-01	20.9
6.25	8.5371e-01	3.8972e-02	4.57	1.0977e-01	12.9	1.7803e-01	20.9
6.75	9.0704e-01	5.0871e-02	5.61	1.1660e-01	12.9	1.8915e-01	20.9
7.25	9.4643e-01	6.7196e-02	7.1	1.2205e-01	12.9	1.9737e-01	20.9
7.75	8.5658e-01	8.1155e-02	9.47	1.1103e-01	13	1.7863e-01	20.9
8.25	9.0385e-01	1.0537e-01	11.7	1.0995e-01	12.2	1.8849e-01	20.9
8.75	6.9039e-01	1.2998e-01	18.8	8.4364e-02	12.2	1.4397e-01	20.9
9.25	7.5655e-01	1.3531e-01	17.9	9.2771e-02	12.3	1.5777e-01	20.9
9.75	6.4190e-01	1.5285e-01	23.8	7.8913e-02	12.3	1.3386e-01	20.9
11	9.3962e-01	1.3227e-01	14.1	1.2592e-01	13.4	1.9595e-01	20.9
13	6.6368e-01	2.1209e-01	32	9.3802e-02	14.1	1.3840e-01	20.9
15	2.9631e-01	2.9729e-01	100	4.4300e-02	15	6.1791e-02	20.9
17	1.1764e+00	1.1867e+00	101	3.7895e-01	32.2	2.4533e-01	20.9
19	—	—	—	—	—	—	—

Table F.9: R_{AA} of neutral pion as a function of p_T at $|y| < 0.35$ (Centrality 80-93 %).

p_T	R_{AA}	p_T Uncorr.	Rat. (%)	p_T Corr.	Rat. (%)	Global	Rat. (%)
5.25	3.1047e-01	1.4276e-03	0.46	3.9706e-02	12.8	4.3782e-02	14.1
5.75	3.0023e-01	1.8622e-03	0.62	3.8483e-02	12.8	4.2338e-02	14.1
6.25	3.0128e-01	2.4782e-03	0.823	3.8706e-02	12.8	4.2486e-02	14.1
6.75	3.0253e-01	3.2450e-03	1.07	3.8949e-02	12.9	4.2662e-02	14.1
7.25	2.9625e-01	4.0024e-03	1.35	3.8238e-02	12.9	4.1776e-02	14.1
7.75	3.0306e-01	5.1066e-03	1.68	3.9244e-02	12.9	4.2738e-02	14.1
8.25	3.0701e-01	6.4169e-03	2.09	3.7320e-02	12.2	4.3294e-02	14.1
8.75	2.9729e-01	7.4500e-03	2.51	3.6299e-02	12.2	4.1924e-02	14.1
9.25	3.1230e-01	9.6474e-03	3.09	3.8280e-02	12.3	4.4040e-02	14.1
9.75	3.3679e-01	1.2778e-02	3.79	4.1382e-02	12.3	4.7493e-02	14.1
11	3.2398e-01	8.7928e-03	2.71	4.3385e-02	13.4	4.5686e-02	14.1
13	3.4575e-01	1.7682e-02	5.11	4.8825e-02	14.1	4.8757e-02	14.1
15	4.3700e-01	4.0117e-02	9.18	6.5192e-02	14.9	6.1625e-02	14.1
17	4.3444e-01	6.7447e-02	15.5	1.3994e-01	32.2	6.1264e-02	14.1
19	3.7505e-01	9.9637e-02	26.6	1.2399e-01	33.1	5.2889e-02	14.1

Table F.10: R_{AA} of neutral pion as a function of p_T at $|y| < 0.35$ (Centrality 0-93 %).

p_T	R_{AA}	p_T Uncorr.	Rat. (%)	p_T Corr.	Rat. (%)	Global	Rat. (%)
5.25	1.7528e-01	1.7519e-03	0.999	2.2410e-02	12.8	2.1445e-02	12.2
5.75	1.7531e-01	2.2016e-03	1.26	2.2471e-02	12.8	2.1447e-02	12.2
6.25	1.7560e-01	2.7955e-03	1.59	2.2560e-02	12.8	2.1483e-02	12.2
6.75	1.8227e-01	3.5744e-03	1.96	2.3472e-02	12.9	2.2300e-02	12.2
7.25	1.7485e-01	4.2741e-03	2.44	2.2563e-02	12.9	2.1392e-02	12.2
7.75	1.8145e-01	5.3353e-03	2.94	2.3507e-02	13	2.2200e-02	12.2
8.25	1.8936e-01	6.6669e-03	3.52	2.3045e-02	12.2	2.3167e-02	12.2
8.75	1.7661e-01	7.6220e-03	4.32	2.1583e-02	12.2	2.1606e-02	12.2
9.25	2.0798e-01	1.0048e-02	4.83	2.5486e-02	12.3	2.5444e-02	12.2
9.75	2.2883e-01	1.3090e-02	5.72	2.8120e-02	12.3	2.7996e-02	12.2
11	2.0791e-01	8.6523e-03	4.16	2.7848e-02	13.4	2.5436e-02	12.2
13	2.4546e-01	1.7960e-02	7.32	3.4692e-02	14.1	3.0030e-02	12.2
15	2.9822e-01	4.1929e-02	14.1	4.4586e-02	15	3.6485e-02	12.2
17	3.1373e-01	7.6345e-02	24.3	1.0106e-01	32.2	3.8383e-02	12.2
19	3.3084e-01	1.4284e-01	43.2	1.0937e-01	33.1	4.0475e-02	12.2

Table F.11: R_{AA} of neutral pion as a function of p_T at $|y| < 0.35$ (Centrality 0-5 %).

Appendix G

$R_{AA}(p_T, \Delta\phi)$ in $\sqrt{s_{NN}} = 200$ GeV Au+Au Collisions

Cent	$\Delta\phi$(deg.)	p_T	R$_{AA}(p_T, \Delta\phi)$	p_T Uncorr. (abs.)	Rat. (%)	p_T Corr. (abs.)	Rat. (%)
00-10	00-15	5.5	2.1059e-01	2.5714e-03	1.22	3.2471e-03	1.54
00-10	00-15	6.5	2.1232e-01	3.8022e-03	1.79	3.0186e-03	1.42
00-10	00-15	7.5	2.0838e-01	5.2922e-03	2.54	3.0833e-03	1.48
00-10	00-15	8.5	2.4342e-01	8.1221e-03	3.34	5.8920e-03	2.42
00-10	00-15	9.5	2.5864e-01	1.1879e-02	4.59	6.5645e-03	2.54
00-10	00-15	11	2.2709e-01	1.1661e-02	5.13	6.0167e-03	2.65
00-10	00-15	13	2.7021e-01	2.5564e-02	9.46	1.1247e-02	4.16
00-10	15-30	5.5	2.0243e-01	2.5081e-03	1.24	2.3615e-03	1.17
00-10	15-30	6.5	2.0289e-01	3.7217e-03	1.83	2.1734e-03	1.07
00-10	15-30	7.5	2.0110e-01	5.2489e-03	2.61	2.2276e-03	1.11
00-10	15-30	8.5	2.1771e-01	7.8998e-03	3.63	4.0524e-03	1.86
00-10	15-30	9.5	2.3283e-01	1.1247e-02	4.83	4.4898e-03	1.93
00-10	15-30	11	2.3419e-01	1.1844e-02	5.06	4.5857e-03	1.96
00-10	15-30	13	2.5367e-01	2.2680e-02	8.94	7.9502e-03	3.13
00-10	30-45	5.5	1.9045e-01	2.3798e-03	1.25	8.6325e-04	0.453
00-10	30-45	6.5	1.8840e-01	3.5488e-03	1.88	7.7792e-04	0.413
00-10	30-45	7.5	1.9154e-01	5.0537e-03	2.64	8.0793e-04	0.422
00-10	30-45	8.5	2.0146e-01	7.3324e-03	3.64	1.5024e-03	0.746
00-10	30-45	9.5	2.2042e-01	1.0831e-02	4.91	1.6630e-03	0.754
00-10	30-45	11	2.2712e-01	1.1560e-02	5.09	1.6550e-03	0.729
00-10	30-45	13	2.3411e-01	2.1940e-02	9.37	2.8230e-03	1.21
00-10	45-60	5.5	1.8075e-01	2.2604e-03	1.25	8.8173e-04	0.488
00-10	45-60	6.5	1.8519e-01	3.4350e-03	1.85	8.1417e-04	0.44
00-10	45-60	7.5	1.9063e-01	4.9262e-03	2.58	8.4277e-04	0.442
00-10	45-60	8.5	1.8734e-01	6.9920e-03	3.73	1.5652e-03	0.835

Next page

Cent	$\Delta\phi$(deg.)	p_T	R$_{AA}(p_T, \Delta\phi)$	p_T Uncorr. (abs.)	Rat. (%)	p_T Corr. (abs.)	Rat. (%)
00-10	45-60	9.5	2.3043e-01	1.0528e-02	4.57	1.8848e-03	0.818
00-10	45-60	11	2.2081e-01	1.1482e-02	5.2	1.6405e-03	0.743
00-10	45-60	13	2.2218e-01	2.1359e-02	9.61	2.8434e-03	1.28
00-10	60-75	5.5	1.6892e-01	2.1482e-03	1.27	2.4099e-03	1.43
00-10	60-75	6.5	1.7669e-01	3.2891e-03	1.86	2.2471e-03	1.27
00-10	60-75	7.5	1.8537e-01	4.7654e-03	2.57	2.3350e-03	1.26
00-10	60-75	8.5	1.7631e-01	6.5519e-03	3.72	4.4824e-03	2.54
00-10	60-75	9.5	2.1633e-01	1.0234e-02	4.73	5.2037e-03	2.41
00-10	60-75	11	2.2775e-01	1.1205e-02	4.92	4.7017e-03	2.06
00-10	60-75	13	2.2886e-01	2.0934e-02	9.15	8.4395e-03	3.69
00-10	75-90	5.5	1.6152e-01	2.0791e-03	1.29	3.2809e-03	2.03
00-10	75-90	6.5	1.7227e-01	3.2187e-03	1.87	3.0972e-03	1.8
00-10	75-90	7.5	1.8046e-01	4.6921e-03	2.6	3.1830e-03	1.76
00-10	75-90	8.5	1.6554e-01	6.2753e-03	3.79	6.1462e-03	3.71
00-10	75-90	9.5	1.9001e-01	9.8132e-03	5.16	6.5256e-03	3.43
00-10	75-90	11	2.1603e-01	1.1059e-02	5.12	6.1525e-03	2.85
00-10	75-90	13	2.3309e-01	2.0185e-02	8.66	1.2117e-02	5.2

Table G.1: $R_{AA}(p_T, \Delta\phi)$ of neutral pion at $|y| < 0.35$ (Centrality 0-10 %).

Cent	$\Delta\phi$(deg.)	p_T	R$_{AA}(p_T, \Delta\phi)$	p_T Uncorr. (abs.)	Rat. (%)	p_T Corr. (abs.)	Rat. (%)
10-20	00-15	5.5	3.1514e-01	3.2549e-03	1.03	6.4437e-03	2.04
10-20	00-15	6.5	2.9629e-01	4.9089e-03	1.66	5.3310e-03	1.8
10-20	00-15	7.5	3.1298e-01	7.4767e-03	2.39	6.0566e-03	1.94
10-20	00-15	8.5	3.1085e-01	1.0622e-02	3.42	4.9213e-03	1.58
10-20	00-15	9.5	3.7210e-01	1.6657e-02	4.48	8.8792e-03	2.39
10-20	00-15	11	3.1160e-01	1.6018e-02	5.14	4.3930e-03	1.41
10-20	00-15	13	3.6986e-01	3.2729e-02	8.85	9.1892e-03	2.48
10-20	15-30	5.5	2.9680e-01	3.1200e-03	1.05	4.6435e-03	1.56
10-20	15-30	6.5	2.9673e-01	4.7803e-03	1.61	4.0636e-03	1.37
10-20	15-30	7.5	2.9474e-01	7.1514e-03	2.43	4.3553e-03	1.48
10-20	15-30	8.5	2.9294e-01	1.0355e-02	3.53	3.5148e-03	1.2
10-20	15-30	9.5	3.4317e-01	1.5969e-02	4.65	6.3196e-03	1.84
10-20	15-30	11	3.1071e-01	1.6366e-02	5.27	3.2792e-03	1.06
10-20	15-30	13	3.0790e-01	3.2812e-02	10.7	5.8837e-03	1.91
10-20	30-45	5.5	2.7526e-01	2.9184e-03	1.06	1.7101e-03	0.621
10-20	30-45	6.5	2.6242e-01	4.4562e-03	1.7	1.4127e-03	0.538
10-20	30-45	7.5	2.7778e-01	6.8460e-03	2.46	1.6236e-03	0.584
10-20	30-45	8.5	2.8701e-01	1.0013e-02	3.49	1.3423e-03	0.468
10-20	30-45	9.5	2.7985e-01	1.4183e-02	5.07	2.0815e-03	0.744

Next page

Cent	$\Delta\phi$(deg.)	p_T	$\mathrm{R}_{AA}(p_T, \Delta\phi)$	p_T Uncorr. (abs.)	Rat. (%)	p_T Corr. (abs.)	Rat. (%)
10-20	30-45	11	2.9668e-01	1.5426e-02	5.2	1.1923e-03	0.402
10-20	30-45	13	3.3668e-01	3.1729e-02	9.42	2.5773e-03	0.766
10-20	45-60	5.5	2.4378e-01	2.6723e-03	1.1	1.6792e-03	0.689
10-20	45-60	6.5	2.4435e-01	4.2175e-03	1.73	1.4382e-03	0.589
10-20	45-60	7.5	2.5110e-01	6.4346e-03	2.56	1.6183e-03	0.644
10-20	45-60	8.5	2.6127e-01	9.4379e-03	3.61	1.3206e-03	0.505
10-20	45-60	9.5	2.7585e-01	1.3613e-02	4.93	2.3293e-03	0.844
10-20	45-60	11	2.9103e-01	1.5728e-02	5.4	1.2258e-03	0.421
10-20	45-60	13	2.5726e-01	2.9167e-02	11.3	2.2039e-03	0.857
10-20	60-75	5.5	2.2222e-01	2.4931e-03	1.12	4.6165e-03	2.08
10-20	60-75	6.5	2.2470e-01	3.9564e-03	1.76	3.9308e-03	1.75
10-20	60-75	7.5	2.2745e-01	6.0352e-03	2.65	4.3955e-03	1.93
10-20	60-75	8.5	2.3422e-01	8.8391e-03	3.77	3.4761e-03	1.48
10-20	60-75	9.5	2.7728e-01	1.3147e-02	4.74	7.2413e-03	2.61
10-20	60-75	11	2.7536e-01	1.4816e-02	5.38	3.3040e-03	1.2
10-20	60-75	13	2.9110e-01	2.7779e-02	9.54	7.5723e-03	2.6
10-20	75-90	5.5	2.1631e-01	2.3967e-03	1.11	6.5306e-03	3.02
10-20	75-90	6.5	2.1921e-01	3.8433e-03	1.75	5.5185e-03	2.52
10-20	75-90	7.5	2.2182e-01	5.8323e-03	2.63	6.2048e-03	2.8
10-20	75-90	8.5	2.5259e-01	9.0552e-03	3.58	5.3510e-03	2.12
10-20	75-90	9.5	2.1941e-01	1.1926e-02	5.44	8.4695e-03	3.86
10-20	75-90	11	2.8484e-01	1.5206e-02	5.34	4.7854e-03	1.68
10-20	75-90	13	2.5683e-01	2.7178e-02	10.6	9.7382e-03	3.79

Table G.2: $R_{AA}(p_T, \Delta\phi)$ of neutral pion at $|y| < 0.35$ (Centrality 10-20 %).

Cent	$\Delta\phi$(deg.)	p_T	$\mathrm{R}_{AA}(p_T, \Delta\phi)$	p_T Uncorr. (abs.)	Rat. (%)	p_T Corr. (abs.)	Rat. (%)
20-30	00-15	5.5	4.3774e-01	5.0278e-03	1.15	5.2053e-03	1.19
20-30	00-15	6.5	4.2896e-01	7.5524e-03	1.76	4.7705e-03	1.11
20-30	00-15	7.5	3.9712e-01	1.0744e-02	2.71	4.1609e-03	1.05
20-30	00-15	8.5	3.8991e-01	1.5343e-02	3.93	4.0504e-03	1.04
20-30	00-15	9.5	4.1443e-01	2.3052e-02	5.56	5.3476e-03	1.29
20-30	00-15	11	4.1098e-01	2.4252e-02	5.9	5.3141e-03	1.29
20-30	00-15	13	5.4062e-01	5.8062e-02	10.7	1.0809e-02	2
20-30	15-30	5.5	4.0861e-01	4.7886e-03	1.17	3.7613e-03	0.921
20-30	15-30	6.5	3.9187e-01	7.2389e-03	1.85	3.3627e-03	0.858
20-30	15-30	7.5	3.8705e-01	1.0561e-02	2.73	3.1214e-03	0.806
20-30	15-30	8.5	3.8307e-01	1.5111e-02	3.94	3.0540e-03	0.797
20-30	15-30	9.5	4.2949e-01	2.2386e-02	5.21	4.2981e-03	1
20-30	15-30	11	4.5707e-01	2.5561e-02	5.59	4.5379e-03	0.993

Next page

Cent	$\Delta\phi$(deg.)	p_T	R$_{AA}(p_T, \Delta\phi)$	p_T Uncorr. (abs.)	Rat. (%)	p_T Corr. (abs.)	Rat. (%)
20-30	15-30	13	4.5058e-01	5.5644e-02	12.3	7.0479e-03	1.56
20-30	30-45	5.5	3.7235e-01	4.3903e-03	1.18	1.3932e-03	0.374
20-30	30-45	6.5	3.5075e-01	6.6065e-03	1.88	1.2155e-03	0.347
20-30	30-45	7.5	3.6299e-01	9.8370e-03	2.71	1.1760e-03	0.324
20-30	30-45	8.5	3.5045e-01	1.3987e-02	3.99	1.1150e-03	0.318
20-30	30-45	9.5	3.9182e-01	2.2055e-02	5.63	1.5970e-03	0.408
20-30	30-45	11	3.6472e-01	2.2644e-02	6.21	1.4451e-03	0.396
20-30	30-45	13	3.8891e-01	5.1992e-02	13.4	2.5160e-03	0.647
20-30	45-60	5.5	3.2018e-01	3.9497e-03	1.23	1.3732e-03	0.429
20-30	45-60	6.5	3.1725e-01	6.0893e-03	1.92	1.2484e-03	0.393
20-30	45-60	7.5	3.1709e-01	9.1339e-03	2.88	1.1570e-03	0.365
20-30	45-60	8.5	3.2840e-01	1.3456e-02	4.1	1.1641e-03	0.354
20-30	45-60	9.5	3.5780e-01	2.0170e-02	5.64	1.6701e-03	0.467
20-30	45-60	11	3.5667e-01	2.1834e-02	6.12	1.5720e-03	0.441
20-30	45-60	13	3.3809e-01	4.8548e-02	14.4	2.5504e-03	0.754
20-30	60-75	5.5	2.8766e-01	3.5767e-03	1.24	3.8598e-03	1.34
20-30	60-75	6.5	2.7949e-01	5.5968e-03	2	3.4035e-03	1.22
20-30	60-75	7.5	2.9238e-01	8.4910e-03	2.9	3.2704e-03	1.12
20-30	60-75	8.5	3.0850e-01	1.2727e-02	4.13	3.3079e-03	1.07
20-30	60-75	9.5	3.1340e-01	1.8674e-02	5.96	4.5513e-03	1.45
20-30	60-75	11	3.4270e-01	2.1989e-02	6.42	4.5541e-03	1.33
20-30	60-75	13	3.5987e-01	4.9134e-02	13.7	8.5808e-03	2.38
20-30	75-90	5.5	2.6106e-01	3.3741e-03	1.29	5.2225e-03	2
20-30	75-90	6.5	2.7294e-01	5.3362e-03	1.96	4.9168e-03	1.8
20-30	75-90	7.5	2.7299e-01	8.0953e-03	2.97	4.4852e-03	1.64
20-30	75-90	8.5	2.8888e-01	1.2320e-02	4.26	4.5050e-03	1.56
20-30	75-90	9.5	2.9988e-01	1.7627e-02	5.88	6.4518e-03	2.15
20-30	75-90	11	3.3533e-01	2.0985e-02	6.26	6.4630e-03	1.93
20-30	75-90	13	3.7207e-01	4.8854e-02	13.1	1.3266e-02	3.57

Table G.3: $R_{AA}(p_T, \Delta\phi)$ of neutral pion at $|y| < 0.35$ (Centrality 20-30 %).

Cent	$\Delta\phi$(deg.)	p_T	R$_{AA}(p_T, \Delta\phi)$	p_T Uncorr. (abs.)	Rat. (%)	p_T Corr. (abs.)	Rat. (%)
30-40	00-15	5.5	5.5275e-01	5.6351e-03	1.02	7.0826e-03	1.28
30-40	00-15	6.5	5.5789e-01	9.4163e-03	1.69	6.6225e-03	1.19
30-40	00-15	7.5	5.4375e-01	1.4271e-02	2.62	6.8804e-03	1.27
30-40	00-15	8.5	5.2061e-01	2.0911e-02	4.02	6.4784e-03	1.24
30-40	00-15	9.5	5.3997e-01	3.1719e-02	5.87	9.0537e-03	1.68
30-40	00-15	11	5.2083e-01	3.5007e-02	6.72	9.0027e-03	1.73

Next page

Cent	$\Delta\phi$(deg.)	p_T	R$_{AA}(p_T, \Delta\phi)$	p_T Uncorr. (abs.)	Rat. (%)	p_T Corr. (abs.)	Rat. (%)
30-40	00-15	13	6.5679e-01	8.6595e-02	13.2	1.6776e-02	2.55
30-40	15-30	5.5	5.2841e-01	5.4012e-03	1.02	5.2643e-03	0.996
30-40	15-30	6.5	5.0614e-01	8.8909e-03	1.76	4.6528e-03	0.919
30-40	15-30	7.5	4.9475e-01	1.3814e-02	2.79	4.8688e-03	0.984
30-40	15-30	8.5	4.7672e-01	2.0040e-02	4.2	4.5933e-03	0.964
30-40	15-30	9.5	4.7732e-01	2.9605e-02	6.2	6.3273e-03	1.33
30-40	15-30	11	5.6757e-01	3.4922e-02	6.15	7.7491e-03	1.37
30-40	15-30	13	6.7381e-01	7.6910e-02	11.4	1.4201e-02	2.11
30-40	30-45	5.5	4.6271e-01	4.9405e-03	1.07	1.8907e-03	0.409
30-40	30-45	6.5	4.5240e-01	8.2286e-03	1.82	1.6917e-03	0.374
30-40	30-45	7.5	4.4216e-01	1.2755e-02	2.88	1.7851e-03	0.404
30-40	30-45	8.5	4.7521e-01	1.9340e-02	4.07	1.8592e-03	0.391
30-40	30-45	9.5	4.5312e-01	2.8184e-02	6.22	2.5440e-03	0.561
30-40	30-45	11	4.6415e-01	3.2410e-02	6.98	2.6771e-03	0.577
30-40	30-45	13	5.6410e-01	7.4723e-02	13.2	5.5295e-03	0.98
30-40	45-60	5.5	4.0139e-01	4.4040e-03	1.1	1.9053e-03	0.475
30-40	45-60	6.5	4.1610e-01	7.6475e-03	1.84	1.7853e-03	0.429
30-40	45-60	7.5	4.0291e-01	1.1707e-02	2.91	1.8887e-03	0.469
30-40	45-60	8.5	4.0116e-01	1.7614e-02	4.39	1.7904e-03	0.446
30-40	45-60	9.5	4.4416e-01	2.7096e-02	6.1	3.0245e-03	0.681
30-40	45-60	11	4.8702e-01	3.1854e-02	6.54	3.3884e-03	0.696
30-40	45-60	13	3.6206e-01	6.2041e-02	17.1	5.0171e-03	1.39
30-40	60-75	5.5	3.5079e-01	3.9991e-03	1.14	5.2898e-03	1.51
30-40	60-75	6.5	3.5331e-01	6.9096e-03	1.96	4.7456e-03	1.34
30-40	60-75	7.5	3.4230e-01	1.0752e-02	3.14	5.0871e-03	1.49
30-40	60-75	8.5	3.9630e-01	1.7149e-02	4.33	5.4822e-03	1.38
30-40	60-75	9.5	3.1463e-01	2.2919e-02	7.28	7.1069e-03	2.26
30-40	60-75	11	3.4430e-01	2.7948e-02	8.12	7.8840e-03	2.29
30-40	60-75	13	3.4885e-01	5.7955e-02	16.6	1.9534e-02	5.6
30-40	75-90	5.5	3.1573e-01	3.7119e-03	1.18	7.1779e-03	2.27
30-40	75-90	6.5	3.3987e-01	6.6324e-03	1.95	6.8080e-03	2
30-40	75-90	7.5	3.3187e-01	1.0254e-02	3.09	7.4179e-03	2.24
30-40	75-90	8.5	3.4741e-01	1.5804e-02	4.55	7.1037e-03	2.04
30-40	75-90	9.5	3.1139e-01	2.2119e-02	7.1	1.0902e-02	3.5
30-40	75-90	11	3.2991e-01	2.6287e-02	7.97	1.1634e-02	3.53
30-40	75-90	13	2.5671e-01	4.7790e-02	18.6	2.6133e-02	10.2

Table G.4: $R_{AA}(p_T, \Delta\phi)$ of neutral pion at $|y| < 0.35$ (Centrality 30-40 %).

Cent	$\Delta\phi$(deg.)	p_T	$\mathrm{R}_{AA}(p_T, \Delta\phi)$	p_T Uncorr. (abs.)	Rat. (%)	p_T Corr. (abs.)	Rat. (%)
40-50	00-15	5.5	6.9079e-01	9.1463e-03	1.32	1.6415e-02	2.38
40-50	00-15	6.5	6.9329e-01	1.4959e-02	2.16	1.5344e-02	2.21
40-50	00-15	7.5	6.4373e-01	2.2221e-02	3.45	1.3406e-02	2.08
40-50	00-15	8.5	6.5846e-01	3.3791e-02	5.13	1.4612e-02	2.22
40-50	00-15	9.5	8.4794e-01	5.9095e-02	6.97	2.9445e-02	3.47
40-50	00-15	11	7.1378e-01	5.8114e-02	8.14	2.4461e-02	3.43
40-50	00-15	13	8.5157e-01	1.7380e-01	20.4	4.5842e-02	5.38
40-50	15-30	5.5	6.6635e-01	8.7035e-03	1.31	1.2342e-02	1.85
40-50	15-30	6.5	6.6103e-01	1.4560e-02	2.2	1.1356e-02	1.72
40-50	15-30	7.5	6.0172e-01	2.2350e-02	3.71	9.6872e-03	1.61
40-50	15-30	8.5	5.7075e-01	3.1164e-02	5.46	9.7633e-03	1.71
40-50	15-30	9.5	6.9537e-01	5.0412e-02	7.25	1.9381e-02	2.79
40-50	15-30	11	6.4111e-01	5.5263e-02	8.62	1.7536e-02	2.74
40-50	15-30	13	6.9913e-01	1.6501e-01	23.6	3.0502e-02	4.36
40-50	30-45	5.5	5.7853e-01	7.9052e-03	1.37	4.4176e-03	0.764
40-50	30-45	6.5	5.8616e-01	1.3247e-02	2.26	4.1154e-03	0.702
40-50	30-45	7.5	6.0826e-01	2.0442e-02	3.36	3.9670e-03	0.652
40-50	30-45	8.5	5.4795e-01	2.9911e-02	5.46	3.7710e-03	0.688
40-50	30-45	9.5	6.0975e-01	5.0980e-02	8.36	7.4440e-03	1.22
40-50	30-45	11	5.3117e-01	5.1640e-02	9.72	6.2776e-03	1.18
40-50	30-45	13	4.4364e-01	1.3642e-01	30.8	8.5996e-03	1.94
40-50	45-60	5.5	4.8625e-01	6.9537e-03	1.43	4.3465e-03	0.894
40-50	45-60	6.5	5.1450e-01	1.2115e-02	2.35	4.1724e-03	0.811
40-50	45-60	7.5	4.6586e-01	1.8103e-02	3.89	3.4603e-03	0.743
40-50	45-60	8.5	5.3499e-01	2.8307e-02	5.29	4.1440e-03	0.775
40-50	45-60	9.5	4.7111e-01	4.2125e-02	8.94	7.3779e-03	1.57
40-50	45-60	11	5.0104e-01	4.5975e-02	9.18	7.4039e-03	1.48
40-50	45-60	13	6.5142e-01	1.4460e-01	22.2	1.6344e-02	2.51
40-50	60-75	5.5	4.3307e-01	6.2190e-03	1.44	1.2408e-02	2.87
40-50	60-75	6.5	4.5072e-01	1.0787e-02	2.39	1.1528e-02	2.56
40-50	60-75	7.5	4.6961e-01	1.6970e-02	3.61	1.0813e-02	2.3
40-50	60-75	8.5	5.2887e-01	2.7621e-02	5.22	1.2513e-02	2.37
40-50	60-75	9.5	4.2882e-01	4.1069e-02	9.58	2.3963e-02	5.59
40-50	60-75	11	3.8790e-01	3.8072e-02	9.82	1.9715e-02	5.08
40-50	60-75	13	3.0690e-01	1.0437e-01	34	2.7361e-02	8.92
40-50	75-90	5.5	3.8443e-01	5.7288e-03	1.49	1.6714e-02	4.35
40-50	75-90	6.5	4.1499e-01	1.0236e-02	2.47	1.5912e-02	3.83
40-50	75-90	7.5	4.2465e-01	1.5827e-02	3.73	1.4466e-02	3.41
40-50	75-90	8.5	4.1758e-01	2.3462e-02	5.62	1.4457e-02	3.46
40-50	75-90	9.5	3.7374e-01	3.4716e-02	9.29	3.4327e-02	9.18

Next page

Cent	$\Delta\phi$(deg.)	p_T	R$_{AA}(p_T, \Delta\phi)$	p_T Uncorr. (abs.)	Rat. (%)	p_T Corr. (abs.)	Rat. (%)
40-50	75-90	11	3.7007e-01	3.7164e-02	10	2.9956e-02	8.09
40-50	75-90	13	4.5231e-01	1.2997e-01	28.7	6.5539e-02	14.5

Table G.5: $R_{AA}(p_T, \Delta\phi)$ of neutral pion at $|y| < 0.35$ (Centrality 40-50 %).

Cent	$\Delta\phi$(deg.)	p_T	R$_{AA}(p_T, \Delta\phi)$	p_T Uncorr. (abs.)	Rat. (%)	p_T Corr. (abs.)	Rat. (%)
50-60	00-15	5.5	8.6803e-01	1.2553e-02	1.45	2.2794e-02	2.63
50-60	00-15	6.5	8.9581e-01	2.2049e-02	2.46	2.5344e-02	2.83
50-60	00-15	7.5	8.1512e-01	3.2817e-02	4.03	2.4581e-02	3.02
50-60	00-15	8.5	8.9773e-01	5.3125e-02	5.92	3.5252e-02	3.93
50-60	00-15	9.5	9.3134e-01	8.4002e-02	9.02	4.9303e-02	5.29
50-60	00-15	11	9.2661e-01	9.5523e-02	10.3	5.4250e-02	5.85
50-60	00-15	13	2.3348e+00	5.3169e-01	22.8	1.8752e-01	8.03
50-60	15-30	5.5	8.2617e-01	1.1909e-02	1.44	1.7020e-02	2.06
50-60	15-30	6.5	8.4925e-01	2.0855e-02	2.46	1.8938e-02	2.23
50-60	15-30	7.5	8.2542e-01	3.2450e-02	3.93	1.9550e-02	2.37
50-60	15-30	8.5	8.5445e-01	5.0280e-02	5.88	2.6793e-02	3.14
50-60	15-30	9.5	7.7639e-01	8.5375e-02	11	3.3179e-02	4.27
50-60	15-30	11	7.1095e-01	8.1941e-02	11.5	3.3790e-02	4.75
50-60	15-30	13	7.2944e-01	4.1681e-01	57.1	5.1897e-02	7.11
50-60	30-45	5.5	7.2641e-01	1.0798e-02	1.49	6.2519e-03	0.861
50-60	30-45	6.5	7.2944e-01	1.8526e-02	2.54	6.8595e-03	0.94
50-60	30-45	7.5	6.4821e-01	2.8414e-02	4.38	6.4126e-03	0.989
50-60	30-45	8.5	6.7624e-01	4.5121e-02	6.67	9.1581e-03	1.35
50-60	30-45	9.5	7.2103e-01	7.4888e-02	10.4	1.3588e-02	1.88
50-60	30-45	11	7.9395e-01	8.3370e-02	10.5	1.6832e-02	2.12
50-60	30-45	13	4.5298e-01	3.5075e-01	77.4	1.7766e-02	3.92
50-60	45-60	5.5	5.9497e-01	9.3094e-03	1.56	6.1149e-03	1.03
50-60	45-60	6.5	6.0237e-01	1.6201e-02	2.69	6.8536e-03	1.14
50-60	45-60	7.5	6.1495e-01	2.6132e-02	4.25	7.2234e-03	1.17
50-60	45-60	8.5	5.9506e-01	3.9727e-02	6.68	1.0045e-02	1.69
50-60	45-60	9.5	6.7554e-01	6.8055e-02	10.1	1.6325e-02	2.42
50-60	45-60	11	5.8326e-01	6.8718e-02	11.8	1.6127e-02	2.76
50-60	45-60	13	6.6376e-01	2.9138e-01	43.9	5.1907e-02	7.82
50-60	60-75	5.5	5.0923e-01	8.0905e-03	1.59	1.7169e-02	3.37
50-60	60-75	6.5	5.2503e-01	1.4187e-02	2.7	1.9874e-02	3.79
50-60	60-75	7.5	5.3896e-01	2.3513e-02	4.36	2.0498e-02	3.8
50-60	60-75	8.5	5.0499e-01	3.4940e-02	6.92	2.9153e-02	5.77
50-60	60-75	9.5	5.0076e-01	5.3941e-02	10.8	4.2657e-02	8.52
50-60	60-75	11	3.7313e-01	5.5587e-02	14.9	3.7098e-02	9.94

Next page

Cent	$\Delta\phi$(deg.)	p_T	R$_{AA}(p_T,\Delta\phi)$	p_T Uncorr. (abs.)	Rat. (%)	p_T Corr. (abs.)	Rat. (%)
50-60	60-75	13	1.8596e-01	1.1949e-01	64.3	1.1936e-01	64.2
50-60	75-90	5.5	4.5670e-01	7.4158e-03	1.62	2.3773e-02	5.21
50-60	75-90	6.5	4.6042e-01	1.2943e-02	2.81	2.7171e-02	5.9
50-60	75-90	7.5	4.8503e-01	2.2025e-02	4.54	2.8106e-02	5.79
50-60	75-90	8.5	4.7615e-01	3.2381e-02	6.8	4.3566e-02	9.15
50-60	75-90	9.5	4.2366e-01	4.8495e-02	11.4	5.8423e-02	13.8
50-60	75-90	11	4.7881e-01	5.5473e-02	11.6	7.8236e-02	16.3
50-60	75-90	13	4.8731e-02	2.7627e-02	56.7	3.0169e-01	619

Table G.6: $R_{AA}(p_T,\Delta\phi)$ of neutral pion at $|y| < 0.35$ (Centrality 50-60 %).

Appendix H

η/π^0 Ratio in $\sqrt{s_{NN}} = 200$ GeV Au+Au Collisions

In the measurement of η/π^0, the η are used for the data obtained at the same year.

Figure H.1 shows the ratio of η to π^0 at minimum bias as a function of p_T. The open and closed magenta circles are the data in RHIC-Year2004 (Run4) and in RHIC-Year2007 (Run7), the closed triangles and the dashed line are the data in d+Au collisions at RHIC-Year2003 (Run3) and the expectation from $p+p$ event generator, PYTHIA 6.131 (default setting). The η/π^0 at low pT region below 5 GeV/c is complemented by the Run4 dataset (Au+Au collisions). The boxes around the data points are the p_T correlated systematic uncertainties, the light blue band on the $\eta/\pi^0 = 1$ is the type-C (global) systematic uncertainty from the measurement of the invariant yield of neutral pion. The ratios don't show the significant difference among collision species. For collision species, the ratios are not significant difference.

Figure H.2 shows the centrality dependence for the ratio of η to π^0 as a function of p_T. The closed black circles, blue triangles, red squares, magenta circles, and the dashed line are the ratio at centrality 0–20, 20–60, 60–93, minimum bias, and PYTHIA 6.131. The boxes around the data points are the p_T correlated systematic uncertainties, the light blue band on the $\eta/\pi^0 = 1$ is the type-C (global) systematic uncertainty from the measurement of the invariant yield of neutral pion. The ratios don't show the significant difference among the centrality classes, and the PYTHIA agrees with the data.

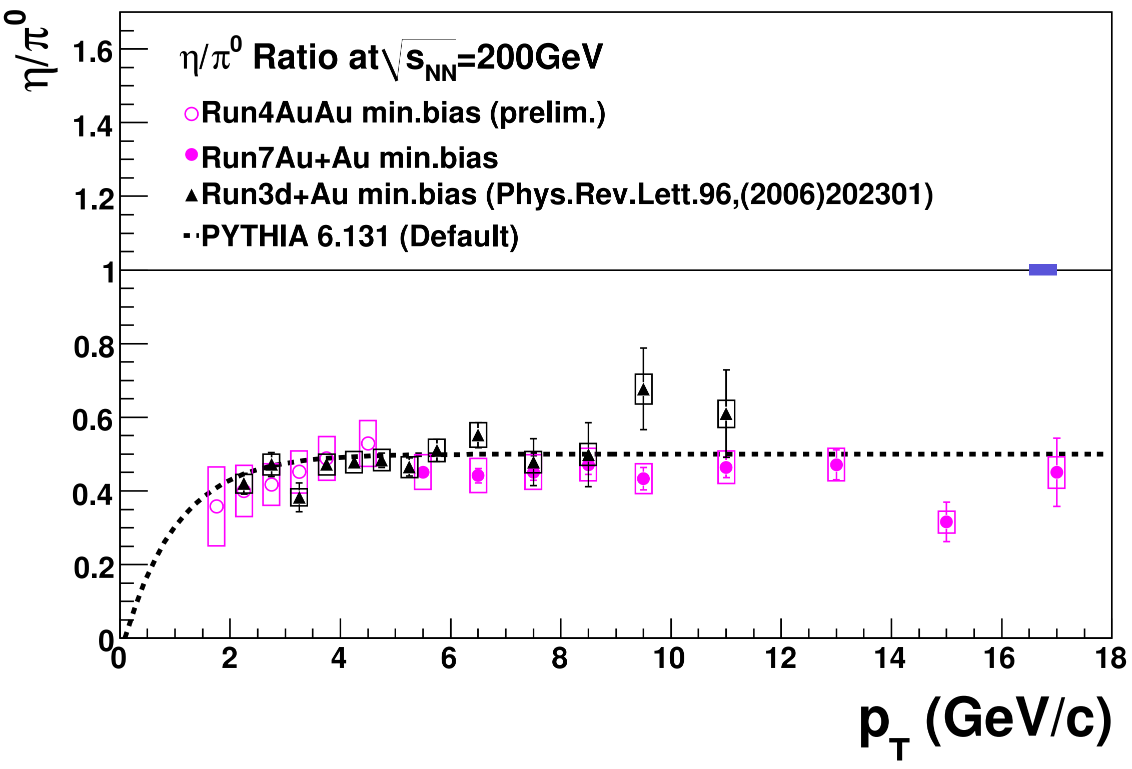

Figure H.1: The ratio of η to π^0 as a function of p_T at minimum bias measured in Au+Au collisions at Run7 and Run4, in d+Au at Run3, and PYTHIA 6.131.

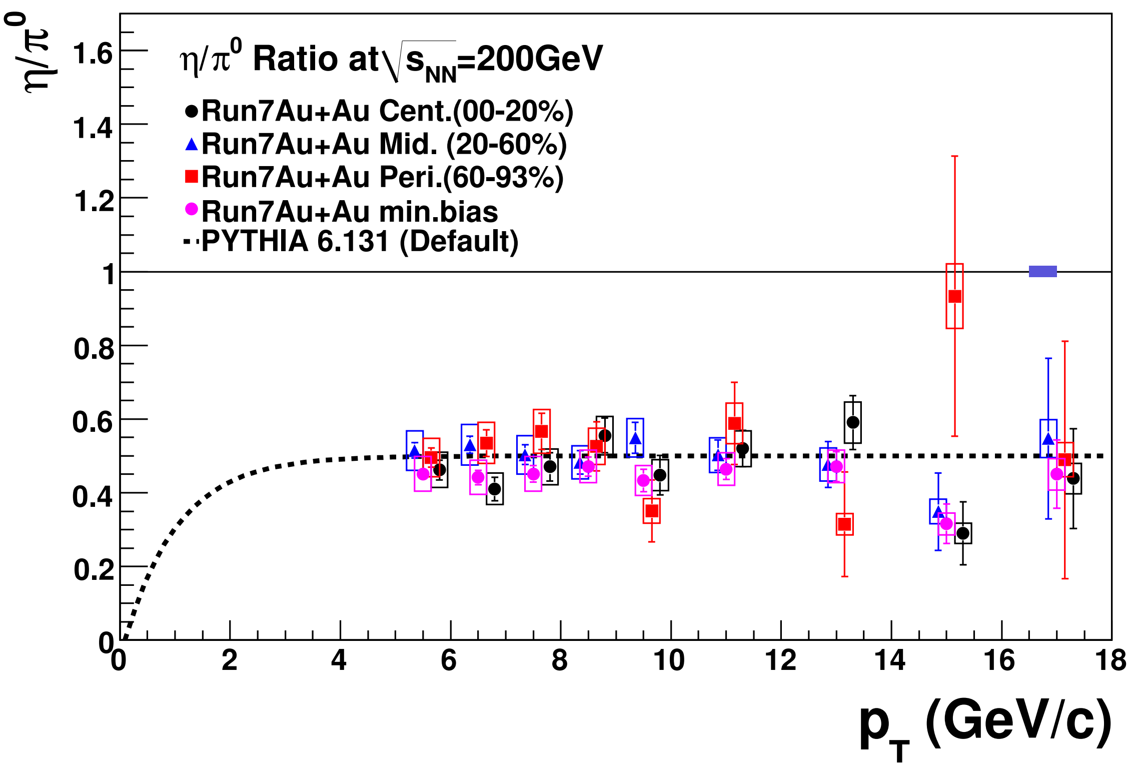

Figure H.2: The centrality dependence for the ratio of η to π^0 as a function of p_T and the expectation from PYTHIA 6.131.

p_T	η/π^0	p_T Uncorr.	Rat. (%)	p_T Corr.	Rat. (%)	p_T TypeC	Rat. (%)
5.5	4.6194e-01	2.6834e-02	5.81	4.8098e-02	10.4	6.9292e-03	1.5
6.5	4.1051e-01	3.1577e-02	7.69	4.2743e-02	10.4	6.1577e-03	1.5
7.5	4.7024e-01	3.9008e-02	8.3	4.8961e-02	10.4	7.0536e-03	1.5
8.5	5.5552e-01	4.7200e-02	8.5	5.2187e-02	9.39	8.3328e-03	1.5
9.5	4.4789e-01	5.3741e-02	12	4.2076e-02	9.39	6.7184e-03	1.5
11	5.1979e-01	4.9027e-02	9.43	4.8830e-02	9.39	7.7969e-03	1.5
13	5.9078e-01	7.3435e-02	12.4	5.5498e-02	9.39	8.8617e-03	1.5
15	2.8979e-01	8.5438e-02	29.5	2.7223e-02	9.39	4.3468e-03	1.5
17	4.3909e-01	1.3536e-01	30.8	4.1248e-02	9.39	6.5863e-03	1.5

Table H.1: η/π^0 ratio as a function of p_T at $|y| < 0.35$ (Centrality 0-20 %).

p_T	η/π^0	p_T Uncorr.	Rat. (%)	p_T Corr.	Rat. (%)	p_T TypeC	Rat. (%)
5.5	5.1477e-01	2.0629e-02	4.01	5.3598e-02	10.4	7.7216e-03	1.5
6.5	5.3073e-01	2.3336e-02	4.4	5.5260e-02	10.4	7.9609e-03	1.5
7.5	5.0308e-01	2.6865e-02	5.34	5.2381e-02	10.4	7.5462e-03	1.5
8.5	4.8272e-01	3.2162e-02	6.66	4.5347e-02	9.39	7.2407e-03	1.5
9.5	5.4920e-01	4.1658e-02	7.59	5.1592e-02	9.39	8.2379e-03	1.5
11	5.0214e-01	4.0903e-02	8.15	4.7172e-02	9.39	7.5322e-03	1.5
13	4.7711e-01	6.2042e-02	13	4.4820e-02	9.39	7.1566e-03	1.5
15	3.4917e-01	1.0502e-01	30.1	3.2802e-02	9.39	5.2376e-03	1.5
17	5.4718e-01	2.1836e-01	39.9	5.1403e-02	9.39	8.2077e-03	1.5

Table H.2: η/π^0 ratio as a function of p_T at $|y| < 0.35$ (Centrality 20-60 %).

p_T	η/π^0	p_T Uncorr.	Rat. (%)	p_T Corr.	Rat. (%)	p_T TypeC	Rat. (%)
5.5	4.9549e-01	2.5516e-02	5.15	5.1591e-02	10.4	7.4324e-03	1.5
6.5	5.3510e-01	3.6166e-02	6.76	5.5714e-02	10.4	8.0264e-03	1.5
7.5	5.6639e-01	4.8791e-02	8.61	5.8972e-02	10.4	8.4958e-03	1.5
8.5	5.2617e-01	6.6206e-02	12.6	4.9429e-02	9.39	7.8925e-03	1.5
9.5	3.5097e-01	8.3621e-02	23.8	3.2971e-02	9.39	5.2646e-03	1.5
11	5.8799e-01	1.1170e-01	19	5.5237e-02	9.39	8.8199e-03	1.5
13	3.1457e-01	1.4200e-01	45.1	2.9551e-02	9.39	4.7186e-03	1.5
15	9.3319e-01	3.8026e-01	40.7	8.7665e-02	9.39	1.3998e-02	1.5
17	4.8976e-01	3.2213e-01	65.8	4.6008e-02	9.39	7.3463e-03	1.5

Table H.3: η/π^0 ratio as a function of p_T at $|y| < 0.35$ (Centrality 60-93 %).

p_T	η/π^0	p_T Uncorr.	Rat. (%)	p_T Corr.	Rat. (%)	p_T TypeC	Rat. (%)
5.5	4.5098e-01	1.7699e-02	3.92	4.6956e-02	10.4	6.7646e-03	1.5
6.5	4.4166e-01	1.9400e-02	4.39	4.5985e-02	10.4	6.6249e-03	1.5
7.5	4.5101e-01	2.2266e-02	4.94	4.6959e-02	10.4	6.7652e-03	1.5
8.5	4.7148e-01	2.5916e-02	5.5	4.4292e-02	9.39	7.0722e-03	1.5
9.5	4.3320e-01	3.0154e-02	6.96	4.0695e-02	9.39	6.4980e-03	1.5
11	4.6443e-01	2.8441e-02	6.12	4.3629e-02	9.39	6.9665e-03	1.5
13	4.7134e-01	4.0469e-02	8.59	4.4279e-02	9.39	7.0701e-03	1.5
15	3.1563e-01	5.3707e-02	17	2.9651e-02	9.39	4.7344e-03	1.5
17	4.5006e-01	9.2687e-02	20.6	4.2279e-02	9.39	6.7509e-03	1.5

Table H.4: η/π^0 ratio as a function of p_T at $|y| < 0.35$ (Centrality 0-93 %).

Bibliography

[1] D.J. Gross *et al.*, Phys. Rev. Lett., **30**, 1343 (1973).

[2] H.D. Polizer et al., Phys. Rev. Lett., **30**, 1346 (1973).

[3] F. Karsh, Lect. Notes Phys. **583**, 209 (2002).

[4] K. Karsch, Nucl. Phys. A**698**, 447 (2002).

[5] A. Adare *et al.*, Phys. Rev. C**82**, 011902 (2010).

[6] A. Adare *et al.*, Phys. Rev. Lett. **105**, 142301 (2010).

[7] R.J. Glauber, in: Lectures in theoretocal physics, ed. W.E. Brittin *et al.*, (Interscience Publishers, New York, 1958) vol. I, 315.

[8] J.D. Bjorken, Phys. Rev. D**27**, 140 (1983).

[9] T. Alber *et al.*, Phys. Rev. Lett., **75**, 3814 (1995).

[10] S.S. Adler *et al.*, Phys. Rev. C**71**, 034908 (2005).

[11] J. Pumplin *et al.*, J. High Energy Phys. **07**, 012 (2002).

[12] M. Gluck *et al.*, Z. Phys. Rev. D**51** 1427 (1995).

[13] S.S. Adler *et al.*, Phys. Rev. Lett. **91** 241803 (2003).

[14] J.W. Cronin *et al.*, Phys. Rev. D**11** 3105 (1975).

[15] M.D. Nagra *et al.*, Nucl. Phys. B**127**, 1 (1977).

[16] J.J. Aubert *et al.*, Phys. Rev. Lett., **33**, 1404 (1974).

[17] M. Arneodo *et al.*, Nucl. Phys. B**441**, 12 (1995).

[18] R. Albrecht *et al.*, Eur. Phys. J. C**5**, 255 (1998).

[19] M.M. Aggarwal *et al.*, Eur. Phys. K. C**23**, 225 (2002).

[20] X.-N. Wang *et al.*, Phys. Rev. Lett. **86**, 2655 (1998).

[21] A.L.S. Angelis *et al.*, Phys. Lett. B**185**, 213 (1987).

[22] D. d'Enterria, Phys. Lett. B**576**, 32 (2004).

[23] K. Adcox *et al.*, Nucl. Phys. A**757**, 184 (2005).

[24] K. Adcox *et al.*, Phys. Rev. Lett., **88**, 192303 (2002).

[25] S.S. Adler *et al.*, Phys. Rev. Lett., **91**, 072301 (2003).

[26] S.S. Adler *et al.*, Phys. Rev. Lett., **91**, 072303 (2003).

[27] I. Vitev *et al.*, Phys. Rev. Lett., **89**, 252301 (2002).

[28] X.-N. Wang *et al.*, Nucl. Phys. A**715**, 775 (2003).

[29] D. Kharzeev *et al.*, Phys. Lett. B**561**, 93 (2003).

[30] K. Gallmeister *et al.*, Phys. Rev. C**62**, 044905 (2003).

[31] M. Gyulassy *et al.*, Phys. Lett. B**243**, 432 (1990).

[32] X.-N. Wang *et al.*, Phys. Rev. Lett., **68**, 1480 (1992).

[33] R. Baier *et al.*, Ann. Rev. Nucl. Part. Sci., **50**, 37 (2000).

[34] J.D. Bjorken., FERMILAB-PUB-82-059-THY, (1982).

[35] X.-N. Wang *et al.*, Phys. Rev. Lett., **68**, 1480 (1992).

[36] M. Gyulassy *et al.*, Nucl. Phys. B**420**, 583 (1994).

[37] R. Baier *et al.*, Nucl. Phys. B**483**, 291 (1997).

[38] R. Baier *et al.*, Phys. Rev. C**58**, 1706 (1998).

[39] R. Baier *et al.*, Phys. Lett. B**345**, 277 (1995).

[40] X.-N. Wang *et al.*, Phys. Rev. D**51**, 3436 (1995).

[41] X.-N. Wang *et al.*, Phys. Rev. C**58**, 2321 (1998).

[42] D.T. Haar, *Collected Paper of L.D. Landau.*, Gordon and Breach (1965).

[43] J.D. Bjorken, Phys. Rev. D**27**, 140 (1983).

[44] R. Baier *et al.*, Nucl. Phys. B**484**, 265 (1997).

[45] S. Voloshin *et al.*, Phys. Rev. C**70**, 665 (1997).

[46] S.S. Adler, *et al.*, Phys. Rev. Lett., **91**, 182301 (2003).

[47] H. Hahn *et al.*, Nucl. Instr. Meth., A**499**, 245 (2003).

[48] A. Drees *et al.*, Proc. of PAC07, 722 (2007).

[49] K. Adcox *et al.*, Nucl. Instr. Meth., A**499**, 469 (2003).

[50] M. Allen *et al.*, Nucl. Instr. Meth., A**499**, 549 (2003).

[51] C. Adler *et al.*, Nucl. Instr. Meth., A**499**, 433 (2003).

[52] K. Adcox *et al.*, Nucl. Instr. Meth., A**499**, 489 (2003).

[53] M. Aizawa *et al.*, Nucl. Instr. Meth., A**499**, 508 (2003).

[54] L. Aphecetche *et al.*, Nucl. Instr. Meth., A**499**, 521 (2003).

[55] S.S. Adler *et al.*, Nucl. Instr. Meth., A**499**, 560 (2003).

[56] T.C. Awes *et al.*, Nucl. Instr. Meth., A**311**, 130 (1992).

[57] M.M. Aggarwal *et al.*, Phys. Rev. Lett., **85**, 3595 (2000).

[58] M.S. Emery *et al.*, IEEE Trans. Nucl. Sci., **44**, 374 (1997)

[59] Letter of Intent for PHENIX Muon Piston Calorimeter (2005).

[60] Letter of Intent for PHENIX Reaction Plane Detector (2006)

[61] K. Homma *et al.*, PHENIX Analysis Note 107.

[62] J. Nagle *et al.*, PHENIX Analysis Note 113.

[63] J. Nagle *et al.*, PHENIX Analysis Note 387.

[64] X.-N. Wang *et al.*, Phys. Rev. D **44**, 3501 (1991).

[65] R. Brun and F. Carminati, CERN Program Library Long Writeup W**5013**, (1993).

[66] S.S. Adler *et al.*, Phys. Rev. C**75**, 024909 (2007).

[67] J. Barrette *et al.*, Phys. Rev. C**55**, 1420 (1997).

[68] H. de Vries *et al.*, Atomic Data and Nuclear Data Table **36**, 495 (1987).

[69] H. Brown *et al.*, Philos. Mag. **45**, 27 (1956).

[70] G. Goldhaber *et al.*, Phys. Rev. Lett. **3**, 181 (1959).

[71] J.-Y. Ollitraut, Phys. Rev. D**46**, 229 (1992).

[72] A.M. Poskanzer *et al.*, Phys. Rev. C**58**, 1671 (1998).

[73] A.V. Bazilevsky *et al.*, Instr. Exp. Tech., **42**, 167 (1999).

[74] G. David *et al.*, PHENIX Analysis Note 352.

[75] A. Adare *et al*, Phys. Rev. Lett. **101**, 232301 (2008).

[76] C. Klein-Bösing, Doctoral thesis, Univ. of Münster, 2004

[77] T. Isobe, Doctoral thesis, Univ. of Tokyo, 2007

[78] S. Bazilevsky *et al.*, PHENIX Analysis Note 224.

[79] M. Gyulassy et al., Nucl. Phys. B**571**, 197 (2000).

[80] X.-N. Wang *et al.*, Nucl. Phys. A**696**, 788 (2001).

[81] P. Arnold *et al.*, J. High Energy Phys. **11**, 057 (2001).

[82] R. Baier *et al.*, Nucl. Phys. B**483**, 291 (1997).

[83] C.A. Salgado and U.A. Wiedemann, Phys. Rev. D**68**, 014008 (2003).

[84] C. Marquet *et al.*, Phys. Lett. B**685**, 270 (2010).

[85] J.-W. Qiu *et al.*, Nucl. Phys. B**353**, 105 (1991).

[86] J.M. Maldacena, Adv. Theor. Math. Phys. **2**, 231 (1998).

[87] D.T. Son *et al.*, Annu. Rev. Nucl. Part. Sci. **57**, 95 (2007).

[88] Y. Akamatsu *et al.*, Phys. Rev. C**79**, 054907 (2009).

[89] T. Hirano *et al.*, Phys. Rev. C**66**, 041901(R) (2002).

[90] C. Nonaka *et al.*, Phys. Rev. C**75**, 014902 (2007).

[91] A. Madjumder *et al.*, Phys Rev. C**76**, 041902(R) (2007).

[92] G.-Y. Qin *et al.*, Phys. Rev. C**76**, 064907(R) (2007).

[93] T. Renk *et al.*, Phys. Rev. C**75**, 031902(R) (2007).

[94] S. Bass *et al.*, Phys. Rev. C**79**, 024901 (2009).